University of Pennsylvania
ScholarlyCommons

Publicly Accessible Penn Dissertations

1-1-2014

Mechanochemical Control of Stem Cell Biology in Development and Disease: Experimental and Theoretical Models

Polimyr Caesar Dave Pelisco Dingal
University of Pennsylvania, davedingal@gmail.com

Follow this and additional works at: http://repository.upenn.edu/edissertations

Part of the Biomedical Commons, Biophysics Commons, and the Cell Biology Commons

Recommended Citation

Dingal, Polimyr Caesar Dave Pelisco, "Mechanochemical Control of Stem Cell Biology in Development and Disease: Experimental and Theoretical Models" (2014). *Publicly Accessible Penn Dissertations*. 1260.
http://repository.upenn.edu/edissertations/1260

This paper is posted at ScholarlyCommons. http://repository.upenn.edu/edissertations/1260
For more information, please contact libraryrepository@pobox.upenn.edu.

Mechanochemical Control of Stem Cell Biology in Development and Disease: Experimental and Theoretical Models

Abstract

Whether a stem cell remains or egresses away from its physiological niche is a function of mechanical and soluble factors in a time-dependent manner, which implicates a `memory' of prior mechanochemical conditioning. Virtually every organ in the body contains resident stem or progenitor cells that contribute to organ homeostasis or repair. The wound healing process in higher vertebrate animals is spatiotemporally complex and usually leads to scarring. Limitations for the use of stem cells as regenerative therapy include the lack of expansion capabilities *in vitro* as well as materials issues that complicate traditional biochemical protocols. A minimal `scar in a dish' model is developed to clarify the kinetics of tension-sensitive proteins in mesenchymal stem cells (MSCs), which possess plasticity to mechanochemical changes of the microenvironment that are typical of scars. The organization and expression of such proteins implicates transcription factors that ultimately steer cell fate. In contrast to classic mechano-transducers of matrix mechanics such as actin assembly-dependent serum response factor (SRF) signaling, a novel mechano-repressive role of NKX2.5 is implicated in maintaining intracellular tension in long-term stem cell cultures on stiff matrices via nucleo-cytoplasmic shuttling — ultimately setting up a 'mechanical memory'. Core gene circuits with known roles in stem cell mechanobiology are modeled based on the 'use it or lose it' concept: tension inhibits turnover of structural proteins such as extracellular collagens, cytoskeletal myosins and nucleoskeletal lamins. This theoretical approach is tested in a variety of processes *in vitro* and *in vivo* that involve forces including cardiac development, osteogenic commitment of MSCs, and fibrosis therapy. With the sophistication of the science and technology of biomaterials relevant to stem cell biology and medicine, matrix mechanics can thus be rigorously combined with biochemical instructions in order to maximize therapeutic utility of stem cells.

Degree Type

Dissertation

Degree Name

Doctor of Philosophy (PhD)

Graduate Group

Chemical and Biomolecular Engineering

First Advisor

Dennis E. Discher

Keywords

Biomaterials, Extracellular Matrix, Mechanobiology, Mechanorepressor, Stem Cell

Subject Categories

Biomedical | Biophysics | Cell Biology

This dissertation is available at ScholarlyCommons: http://repository.upenn.edu/edissertations/1260

MECHANOCHEMICAL CONTROL OF STEM CELL BIOLOGY IN DEVELOPMENT AND DISEASE: EXPERIMENTAL AND THEORETICAL MODELS

Polimyr Caesar Dave P. Dingal

A DISSERTATION
in
Chemical and Biomolecular Engineering
Presented to the Faculties of the University of Pennsylvania
in
Partial Fulfillment of the Requirements for the
Degree of Doctor of Philosophy
2014

Supervisor of Dissertation

____

Dennis E. Discher, Professor of Chemical and Biomolecular Engineering

Graduate Group Chairperson

____

Raymond J. Gorte, Professor of Chemical and Biomolecular Engineering

Dissertation Committee
Scott L. Diamond, Professor of Chemical and Biomolecular Engineering
Rebecca G. Wells, Associate Professor of Medicine
Kathleen J. Stebe, Professor of Chemical and Biomolecular Engineering

Dedicated to

my family and friends

ACKNOWLEDGMENTS

These 5 years have been an adventure to the other side of the world. There are not enough words to fully acknowledge all the persons that influenced my foray into academic enterprise.

To my advisor who never stops working and whom I never call by his first name (to his face), I am grateful for the opportunities to pick your brain and to contribute to your academic endeavors. The works that are presented here used to be riddled with his red ink, but are now undoubtedly presentable.

To the Lamin Team (circa 2013-2014), I have enjoyed our sharing of personal stories and scientific manuscripts as we share our meals.

To the University of Pennsylvania Glee Club (circa 2011-2013), thank you for filling my nights and my head with music and for the unforgettable memories (Brothership Tour 2012!).

Most importantly, to my friends and family back home, thank you for always reminding me to never forget where I am from and the endless possibilities to where I can go.

ABSTRACT

MECHANOCHEMICAL CONTROL OF STEM CELL BIOLOGY IN DEVELOPMENT AND DISEASE: EXPERIMENTAL AND THEORETICAL MODELS

Polimyr Caesar Dave P. Dingal

Dennis E. Discher

Whether a stem cell remains or egresses away from its physiological niche is a function of mechanical and soluble factors in a time-dependent manner, which implicates a ‘memory’ of prior mechanochemical conditioning. Virtually every organ in the body contains resident stem or progenitor cells that contribute to organ homeostasis or repair. The wound healing process in higher vertebrate animals is spatiotemporally complex and usually leads to scarring. Limitations for the use of stem cells as regenerative therapy include the lack of expansion capabilities *in vitro* as well as materials issues that complicate traditional biochemical protocols. A minimal ‘scar in a dish’ model is developed to clarify the kinetics of tension-sensitive proteins in mesenchymal stem cells (MSCs), which possess plasticity to mechanochemical changes of the microenvironment that are typical of scars. The organization and expression of such proteins implicates transcription factors that ultimately steer cell fate. In contrast to classic mechano-transducers of matrix mechanics such as actin assembly-dependent serum response factor (SRF) signaling, a novel mechano-repressive role of NKX2.5 is implicated in maintaining intracellular tension in long-term stem cell cultures on stiff matrices *via* nucleo-cytoplasmic shuttling – ultimately setting up a ’mechanical memory’. Core gene circuits with known roles in stem cell mechanobiology are modeled based on the ’use it or lose it’ concept: tension inhibits turnover of structural proteins such as extracellular collagens, cytoskeletal myosins and nucleoskeletal lamins. This theoretical approach is tested in a variety of processes *in vitro* and *in vivo* that involve forces including cardiac development, osteogenic commitment of MSCs, and fibrosis therapy. With the sophistication of the science and technology of biomaterials relevant

to stem cell biology and medicine, matrix mechanics can thus be rigorously combined with biochemical instructions in order to maximize therapeutic utility of stem cells.

Table of Contents

ACKNOWLEDGMENTS iii

ABSTRACT v

Table of Contents vi

List of Tables ix

List of Figures x

1 Matrix mechanics and soluble factors combine to steer stem cell fate 1
- 1.1 Introduction 2
- 1.2 Lessons from the niche 2
  - 1.2.1 Hematopoietic stem cell niche 3
  - 1.2.2 Muscle stem cell niche 4
  - 1.2.3 Neurogenic niche 5
  - 1.2.4 Multifunctional mesenchymal stem cells 6
- 1.3 Soluble factors with contrasting function 7
- 1.4 Harnessing pluripotency 10

2 A minimal 'scar in a dish' model reveals mechano-temporal effects of matrix stiffness on stem cell fate 18
- Abstract 19
- 2.1 Introduction 19
- 2.2 Results and Discussion 21
  - 2.2.1 Hydrogels with scar-like collagen fiber heterogeneity and regional rigidity 21
  - 2.2.2 'Scar in a dish' impairs cardiomyocyte beating consistent with heart failure 23
  - 2.2.3 MSCs durotax to the 'scar in a dish' 24
  - 2.2.4 Effective stiffness of 'scar in a dish' can be deduced from cell shape and cytoskeleton 26
  - 2.2.5 Stiffness of 'scar in a dish' increases lamin A and MSC osteo-commitment 27
  - 2.2.6 Lamin-A & MMP9 in progenitor-derived macrophages also increase with matrix stiffness 28
- 2.3 Conclusion 29
- 2.4 Materials and Methods 31

2.4.1 Synthesis and functionalization of conventional and scar-like hydrogels for cell culture . . . 31
2.4.2 Surface characterization and microrheology of hydrogels . . . 32
2.4.3 Cell culture, manipulation, and treatments . . . 33
2.4.4 Proteomics analyses of mouse tissue . . . 34
2.4.5 Bulk rheology . . . 35
2.4.6 3D reconstruction & photobleaching in confocal microscopy . . . 35
2.4.7 Decellularized Embryonic Heart Matrix . . . 36
2.4.8 Time-lapse Microscopy . . . 36
2.4.9 Histological analyses of osteogenic commitment . . . 37
2.4.10 Combined Fluorescence *In Situ* Hybridization (FISH) and Immunofluorescence Microscopy . . . 38
2.4.11 Gelatin Zymography . . . 39

3 Role of a matrix stiffness-sensitive repressor, NKX2.5, in stem cell plasticity 58
Abstract . . . 59
3.1 Introduction . . . 59
3.2 Results and Discussion . . . 61
3.2.1 MSCs downregulate collagen-1 synthesis as they become more contractile 61
3.2.2 Matrix stiffness modulates NKX2.5 localization . . . 62
3.2.3 A long-term rigid-matrix phenotype: nuclear exit of NKX2.5 . . . 64
3.2.4 Crosstalk of NKX2.5 and SRF with TGF-β pathway decouples SMA & collagen-1 expression . . . 65
3.2.5 Other modifications of NKX2.5 . . . 66
3.3 Conclusion . . . 67
3.4 Materials and Methods . . . 68
3.4.1 Transcriptional profiling by DNA microarrays . . . 68
3.4.2 Promoter binding analyses . . . 68
3.4.3 Isolation of embryonic cardiomyocytes . . . 68

4 Systems Mechanobiology: Tension-inhibited protein turnover is sufficient to physically control gene circuits 90
4.1 Introduction . . . 91
4.2 Results and Discussion . . . 94
4.2.1 Tension-inhibited degradation of coiled-coil proteins . . . 94
4.2.2 Mechanical coupling of coiled-coil modules in series . . . 96
4.2.3 Logistic coupling between collagen and myosin in cardiac development . 99
4.3 Conclusion . . . 101
4.4 Methods . . . 102

5 Future challenges in characterization and mechanochemical control of stem cell fate 109
Abstract . . . 110
5.1 Introduction . . . 110
5.2 Soft matter control . . . 112
5.2.1 Synthesis, Functionalization and Characterization . . . 113

5.2.2 Advances in Soft Matter Research 114
5.3 Hard matter approaches 117
5.4 Conclusion 118

A Supplementary Information for Chapter 2 **119**
A.1 Adhesion and Thin-film Corrections for scar-like$_{0.3kPa}$ gel 119
A.2 Theoretical analysis of lateral pulling curves 122

B Supplementary Information for Chapter 4 **123**
B.1 Mechanobiological gene circuits: systems of ordinary differential equations 123
B.1.1 Single-module gene circuits: reaction-order stability 124
B.1.2 Two-Module Gene Circuit 127
B.1.3 Two-Module, Tissue-level Mechanobiological Gene Circuit 128
B.2 Analytical Solution for Single-Module Gene Circuit 129
B.3 Numerical Solution for Two-Module Gene Circuit 130
B.4 Numerical Solution for Tissue-level Coupled Gene Circuit 131

C Standard biological laboratory protocols and reagents used **132**
C.1 Cell culture 132
C.2 Quantitative Immunofluorescence Microscopy 132
C.3 Cell Morphometrics 133
C.4 Transfection protocol 134
C.5 Western Blotting and Analysis 134
C.6 Statistical Analyses 135

Bibliography **138**

List of Tables

1.1 Glossary of factors and proteins 13

3.1 Promoter analysis of transcription factor binding to ACTA2 and COL1A2 70

C.1 Polyacrylamide gel precursor formulations 136
C.2 Primary antibody specifications 137

List of Figures

1.1 The insoluble and soluble milieus in a stem cell niche 15
1.2 Matrix and soluble factors converge to control lamin-A levels 16
1.3 Stem cells have a time-dependent 'memory' of prior conditioning 17

2.1 Mechanics, transcriptomic, proteomic profiling of muscular dystrophy tissue . . . 40
2.2 Synthesis and characterization of a 'scar in a dish' 41
2.3 Embedded collagen is stable but does not induce cell spreading 42
2.4 Bulk and surface rheology, and functionalization of PA gel 43
2.5 Lateral pulling microscopy 44
2.6 Stem cell-derived cardiomyocytes beat less on scar-like gel 45
2.7 Synthesis of a scar-like gradient gel 46
2.8 MSCs durotax on a gradient of scar-like fibers 47
2.9 Human MSCs home toward a 'scar in a dish' and crosslinked heart matrix *ex vivo* 48
2.10 Matrix composition of decellularized embryonic chick heart 49
2.11 Scar-like$_{0.3kPa}$ gel exhibits matrix stiffness-dependent MSC response 50
2.12 Local matrix stiffening couples lamin-A and α-smooth muscle actin upregulation 51
2.13 Matrix stiffness, but not retinoic acid, induces MSC osteogenesis 52
2.14 Mechanochemical control of monocyte-derived macrophage differentiation . . . 53
2.15 Matrix stiffness, but not RA, induces lamin A in monocytes/macrophages 54
2.16 Matrix stiffness, but not RA, also induces MMP9 in monocytes/macrophages . . 55
2.17 Summary of transcription factor binding scores from ENCODE database 56
2.18 Retinoic acid, through RARα, reduced lamin A & MMP9 in monocyte/macrophage 57

3.1 Genes relevant to mechanobiology in development 71
3.2 Transcriptomic and proteomic profiles of MSCs on gels 72
3.3 Matrix stiffness downregulates collagen-I matrix synthesis in MSCs 73
3.4 Stiff gels coated with collagen-2 reduced collagen-1 in MSCs 74
3.5 TGF-β is sufficient but not necessary for α-smooth muscle actin expression . . 75
3.6 NKX family of transcription factors: *ACTA2*-promoter binding & gene abundance 76
3.7 Matrix stiffness modulates Nkx2.5 expression in embryonic cardiomyocytes . . . 77
3.8 MSCs express NKX2.5 with some modifications 78
3.9 Matrix stiffness modulates NKX2.5 localization in MSCs 79
3.10 NKX2.5 is a slow-acting mechanorepressor of α-smooth muscle actin 80
3.11 Subcellular localization of Nkx2.5 by mutating its nuclear localization signal . . . 81
3.12 NKX2.5 can reprogram the stiff phenotype of MSCs 82

3.13 Extranuclear localization of NKX2.5 83
3.14 Blebbistatin rescues NKX2.5 depletion from the nucleus 84
3.15 NKX2.5 decreases with long-term stiff-substrate cultures of MSCs 85
3.16 TGF-β inhibition recapitulates matrix stiffness-induced nuclear exit of NKX2.5 . 86
3.17 Crosstalk of NKX2.5 and Serum Response Factor with TGF-β signaling 87
3.18 Post-translational modifications of NKX2.5 in MSCs 88
3.19 NKX2.5 is independent of retinoic acid/Lamin-A/SRF axis 89

4.1 Systems-level view of structural molecules involved in mechanotransduction . . 103
4.2 Feedback-based gene circuit for lamin A exhibits polymer physics scaling if cell tension suppresses protein turnover 104
4.3 Dynamic behavior of collagen-1 produced by mesenchymal stem cells 105
4.4 Matrix stiffness-coupled lamin A and myosin turnover 106
4.5 Sensitivity analysis of coupled structural modules 107
4.6 Cardiomyocytes and fibroblasts balance contraction and matrix production during heart development 108

Chapter 1

Matrix mechanics and soluble factors combine to steer stem cell fate

This chapter appears in *Nature Materials* 13, 532-537 (2014) as a Commentary piece in a focus issue on Cell Culture.

1.1 Introduction

The broad promise of stem cells for regenerative medicine is founded on decades of clinical success already achieved with bone marrow transplantation of hematopoietic stem cells. Current capabilities to induce pluripotency with any person's terminally differentiated cells could also revolutionize therapies for repairing or replacing many other damaged tissues. Yet direct implantation of such cells causes teratomas — that is, tumors with regions of disorganized fat, bone, epithelium or other tissues. Expansion of stem cells with at least partial lineage specification *in vitro* through optimal control of the physicochemical milieu is therefore essential to success in therapeutic applications. We highlight some key aspects of the interplay between mechanical factors and soluble factors (**Table 1.1**) in both the physiological and *in vitro* milieu of stem cells. We provide examples of how soluble-factor control of stem cell fate is modulated by the physical microenvironment, and we discuss aspects of mechanobiological mechanisms and potential research avenues requiring more attention and rigor.

1.2 Lessons from the niche

Stem and progenitor cells in adult organisms can maintain their multipotent state because of 'signals' that they receive in the protected, tissue-specific environment that is the stem cell niche (**Figure 1.1**; Schofield, 1983). Signaling factors include soluble cytokines, cell–cell contacts, and insoluble extracellular matrices with characteristic structure and physicochemical properties (such as stiffness and softness) that define a cell orientation (O'Brien, 2013). Apical–basal polarity is common, and seems to poise a stem cell for asymmetric division — that is, the generation of one differentiated cell with the stem cell remaining in its niche. Otherwise, niches vary with tissue type, as discussed below for soluble and insoluble microenvironments of four distinct adult stem cells.

1.2.1 Hematopoietic stem cell niche

Haematopoietic stem cells (HSCs) remain the best described somatic stem cells, but how they are maintained in their adult niche(s) within the bone marrow or otherwise how they egress into the circulation remains an active area of research. Embryonic niches for these cells are distinct and precede establishment of bone. One niche for adult HSCs comprises nestin-positive mesenchymal stem cells (MSCs) and endothelial cells that are spatially associated near the perivascular microenvironment (Mendez-Ferrer et al., 2010); yet proximity to trabecular bone and bone cells also seems important in another HSC niche (Morrison and Scadden, 2014). All of these bone marrow cells, as well as factors present near the bone surface, could help to promote HSC quiescence, with key niche cytokines including stem cell factor (SCF) and stromal cell-derived factor 1 (SDF-1) (Morrison and Scadden, 2014; Peled et al., 2000). MSCs and other stromal cells play an important role in the homing of HSCs to the niche – especially after myeloablative therapy, that is, the depletion of bone marrow cells by means of chemo- or radiotherapy before transplantation — perhaps chemoctactically driven via SDF-1. For example, SDF-1-induced expression of matrix metalloproteinase-9 (MMP9) in bone marrow cells can enzymatically release matrix-bound SCF, which can then permit the recruitment of repopulating cells and also promote the proliferation of normally quiescent HSCs (Heissig et al., 2002).

The ability of stem cells to divide asymmetrically is a characteristic niche process that maintains stemness under homeostatic or inflammatory conditions to replenish blood cells. The mobilization of HSCs through the induction of granulocyte colony-stimulating factor (G-CSF; another soluble niche factor) was first demonstrated in the early 1990s, yet little is known about HSC trafficking within the bone marrow before egress into the bloodstream, particularly towards lineage specification and possibly to other sub-niches. Physiologically, HSC mobilization follows circadian oscillations (Mendez-Ferrer et al., 2008), yet relations to local pressure, flow and other circulating factors remain obscure; oxygen certainly regulates the behavior of stem cells (Keith and Simon, 2007).

The expansion of haematopoietic stem and progenitor cells is also biophysically regulated (as suggested by Lichtman and Kearney in the 1970s, who anticipated key roles for “contracting-relaxing [. . .] macromolecules in motile cells”). In blood cells, a major impediment to migration is the nucleus, and regulation of its deformability probably modulates hematopoietic cell trafficking and lineage. Indeed, nucleoskeletal-lamin (Shin et al., 2013) and cytoskeletal-myosin (Shin et al., 2014) isoforms differentially regulate egress and lineage maturation of HSCs. In particular, myosin IIB promotes cell polarization to generate more blood progenitors, whereas myosin IIA supports a more symmetric division. Interestingly, reversible inhibition of myosin II, and soft matrices that mimic the compliance of marrow (and also tend to suppress myosin II), both favor long-term HSC reconstitution (Shin et al., 2014). Tropoelastin, which is also highly compliant, has an additive effect with serum-free cytokine cocktails (of IL-3, IL-6 and SCF) in supporting repopulating HSCs *in vitro*; yet stiffening of tropoelastin by glutaraldehyde crosslinking abrogated the effect (Holst et al., 2010). The myosin-II inhibition strategy also enriches for megakaryocytes of high ploidy (Shin et al., 2013) and pro-platelet generation (Shin et al., 2011), and thus seems to be key in directing at least some lineage programs. On the whole, the tight regulation of HSC niche components plays a crucial role in stem cell quiescence, with feedback and feed-forward mechanisms between cells and soluble and insoluble factors.

1.2.2 Muscle stem cell niche

Host muscle fibre, interstitial cells, basal lamina and a nearby blood circulation seem to be the main components of the niche for muscle stem cells (also known as satellite cells) (Kuang et al., 2007). In satellite-cell homing during development, canonical Notch signals that occur asymmetrically at cell–cell contacts — which control multiple cell differentiation processes — stimulate emerging satellite cells to assemble their own basal-lamina matrix (Brohl et al., 2012). Integrin binding to laminin in this extracellular matrix localizes to the basal side of satellite cells, whereas M-cadherin localizes to the apical side for attachment to the host muscle fibre (Kuang et al., 2007). It has been hypothesized that the basal adhesion regulates stem cell quiescence through inhibition of caveolin-mediated endocytosis of soluble factors, and that the polarized distribution of adhesion molecules determines the asymmetric fate of daughter cells after division (Kuang and Rudnicki, 2008). The one daughter cell that maintains contact with the basal lamina maintains a self-renewal capacity, whereas the other is pushed into the host myofibre and presumably differentiates (Kuang and Rudnicki, 2008).

On injury, activated satellite cells remodel their niche through autologous expression of fibronectin, feeding back to Wnt7a signaling (a pathway known to be implicated in developmental processes), which in turn induces symmetric expansion of satellite cells (Bentzinger et al., 2013). Collagen VI is also produced by satellite cells, with collagen-VI knockout mice showing impaired muscle regeneration with decreased muscle stiffness (from 12 kPa to 7 kPa) (Urciuolo et al., 2013). Consistent with this, *in vitro* satellite cell maintenance and subsequent muscle engraftment is maximal when culturing on substrates that match normal muscle tissue stiffness (∼12 kPa; Engler et al., 2004a; Gilbert et al., 2010). Nonetheless, such cell cultures exhibited lower regenerative capacity *in vivo* than cells freshly isolated from muscle, which suggests that some combination of biophysical and biochemical elements of the muscle stem cell niche have yet to be identified for optimal cell culture.

1.2.3 Neurogenic niche

The relatively recent discovery of adult neural stem cells (NSCs) and of the signals regulating adult neurogenesis illustrates differences with the early development of the brain. In embryonic neurogenesis, all cells derive from neuroepithelial cells that divide symmetrically at first (Chenn and McConnell, 1995). In adults, however, the NSC niche is restricted to the ventricular–subventricular zone of the lateral ventricle and to the subgranular zone at the interface of the hilus and dentate gyrus in the hippocampus (Alvarez-Buylla and Lim, 2004). As with satellite cells, canonical Notch signaling is highly active and regulates maintenance of both developing and adult brains (Imayoshi et al., 2010). More importantly, the neocortical niche architecture is maintained by integrin-based adhesion of NSCs to laminin along the apical (ventricular) surface (Loulier et al., 2009). Similar to the HSC niche, SDF-1 secretion by ependymal cells at the apical surface maintains NSC quiescence, whereas SDF-1 secreted by endothelial cells of the vascular basal region results in chemotaxis by both activated NSCs and progenitors in an integrin-$\alpha_6\beta_1$-dependent manner. Transition from progenitors to neuroblasts is marked by β_1-integrin downregulation, enabling egress from the niche (Kokovay et al., 2010). The process seems to prompt asymmetric cell division, with the NSC staying in its niche and the resulting daughter cell moving into more differentiated basal regions of the niche. The highly polarized NSC niche thus allows for compartmentalization of multiple signals derived from cell–cell and/or cell–matrix adhesions as well as of soluble factor gradients that combine to maintain NSC polarity and stemness (Fuentealba et al., 2012).

1.2.4 Multifunctional mesenchymal stem cells

MSCs can take on lineage characteristics of various soft- and hard-tissue cell types (such as neurons, adipocytes, chondrocytes, osteoblasts, skeletal myoblasts and smooth muscle cells), and thus they are an attractive choice for autologous transplantation (Pittenger et al., 1999). Among the various types of adult stem cell, MSCs (from the bone marrow or other sources) that have been isolated through strong adhesion to plastic seem to have the broadest lineage potential (Colter et al., 2000); also, they expand for prolonged periods on tissue-culture plastic while maintaining some degree of multipotency (Abdallah and Kassem, 2009). Other materials might do better, but traditional plastic has allowed MSCs to be used in additional *in vitro* systems to identify soluble and insoluble cues that induce differentiation.

By mimicking the characteristic stiffnesses of different tissues (for instance, brain tissue is always soft; bone tissue is rigid) with inert hydrogels functionalized with collagen I, it was shown that matrix elasticity can direct MSC lineage specification from soft brain to stiff bone and that myosin II has a key role in pulling on and feeling matrix elasticity (Engler et al., 2006). Microarray analyses also indicated significant increases in some key factors of the transforming growth factor beta (TGF-β) superfamily such as bone morphogenetic proteins (BMP) and myostatin (also known as growth differentiation factor 8; GDF8) (Engler et al., 2006). MSCs respond to such TGF-β-family growth factors (Wang et al., 2004), as expected of mesenchymal cells, which means that growth factors could have key autocrine/paracrine signaling roles and that these are triggered by matrix elasticity. For example, MSC injection into scars (which tend to be stiff) such as those resulting from myocardial infarcts has sometimes led to bone formation in the scar; in this case, matrix stiffness may trigger an increase in BMP, which is likely to be the proximal cause for osteogenesis (Breitbach et al., 2007). Such potent growth factors may thus contribute to lineage-inducing signals, even if differences in their expression or activation imparted by physical features of the microenvironment such as matrix elasticity are small (say, at the picomolar level). With respect to three-dimensional culture models (Khetan et al., 2013; Huebsch et al., 2010), many questions arise that should be rigorously addressed, including how cell-secreted growth factors and extracellular matrix binds or not to the surrounding scaffold or gel, whether the various soluble serum or induction factors added to cultures permeate the gel (including oxygen gradients studied decades ago in three-dimensional cultures; Colton, 1995), and also how far the cells reside above a rigid substrate that they might feel. Understanding the various triggering mechanisms in two dimensions as well as three dimensions is likely to be important in physiological conditions, yet it is also possible that adding a growth factor such as BMP to cultures of cells in microenvironments with different stiffnesses will yield different cell phenotypes.

1.3 Soluble factors with contrasting function

The main TGF-β reservoir in serum resides in platelets, and TGF-β is secreted on platelet activation in a matrix-binding, latent complex form (Ahamed et al., 2008), from which it can be released by high fluid shear. Evidence for TGF-β release resulting from cell tension was first obtained with contractile myofibroblasts, the characteristic cell type in stiff, fibrotic tissue (Wipff et al., 2007). Following release, TGF-β_1 binds membrane receptors that activate ubiquitous transcription factors (such as SMADs), which enter the nucleus to promote matrix synthesis and the expression of contractility proteins such as α-smooth muscle actin during fibrotic wound healing by myofibroblasts. Although intracellular processes are probably modulated by the microenvironment, an interplay with TGF-β_1 release mechanisms seems likely to occur *in vivo*. For example, in patients with coronary artery disease an increase in active, but not total, TGF-β_1 in plasma correlates with the number of constricted vessels in the patient (Wang et al., 1997); hence, constricted or stenotic vessels have higher shear stresses and thus higher concentrations of active TGF-β (the release kinetics of active TGF-β with shear stress and time characterizes the forced unfolding of a protein, and the unfolding seems to be roughly linear with shear stress and lacks a threshold; Tenney and Discher, 2009). Given its subnanomolar concentrations in serum, however, TGF-β activation at low stress would take a long time. In the marrow niche where flow is minimal, glial cells of the autonomic nervous system (known as non-myelinating Schwann cells) produce TGF-β and activate it via integrin β_8 to help maintain HSC dormancy (Yamazaki et al., 2011).

Unlike most protein-based growth factors, which cannot cross cell membranes, retinoic acid (RA) is a much smaller molecule that readily permeates cell membranes and regulates ubiquitous transcription factors that shuttle between the cytoplasm and the nucleus (oxygen is another example). In adults, RA is converted in the liver from ingested vitamin A and circulates in serum ($\sim$10 nM). RA signaling seems somehow primed in adult HSCs in part by the niche stroma (Ghiaur et al., 2013), and it is essential for the generation of early embryonic HSCs from the haemogenic endothelium (Chanda et al., 2013). In HSCs, RA receptor-γ (RARγ) regulates the balance of HSC self-renewal and differentiation (Purton et al., 2006), with RARα promoting granulocyte commitment. Indeed, RA suppresses erythropoiesis (Labbaye et al., 1994) and enhances neutrophil differentiation (Shin et al., 2013). Although RARs regulate expression of many genes (up or down), its downregulation of at least the nuclear structure protein lamin A proved revealing: neutrophils have soft, floppy nuclei with low levels of lamin A, which allow these cells to easily crawl through endothelial pores from marrow into blood, and also to enter distal tissues. In contrast, erythroblasts normally maintain high levels of lamin A in their stiff, condensed nuclei; these nuclei are easily ejected in final differentiation and retained in the marrow, with the enucleated cell entering circulation as a red blood cell.

Lamin A is an intermediate filament protein related to keratins in nails, hair, beaks and horns. In addition to controlling nuclear deformability, lamin A has a role in maintaining DNA stability, and is also mechanoresponsive, as we have recently shown (Swift et al., 2013b). Its levels scale with the stiffness of primary tissue (0.1–40 kPa), and in cultured MSCs the levels increase with the stiffness of hydrogel substrates. Lamin-A levels in MSCs on stiff matrix are also modulated by RA levels, with more RARγ entering the nucleus in cells on stiff matrices than in cells on soft substrates (**Figure 1.2**). Brain is low in RARγ, but has other RARs (Swift et al., 2013b); in serum-free NSC cultures adhering to a narrow range of flexible substrates (10–1,000 Pa) and even under strong pro-neuronal conditions (1 μM RA), commitment to specific lineages is stiffness-dependent (Saha et al., 2008). Similar observations were made with NSCs encapsulated within alginate hydrogels of stiffness matching that of brain tissue (Banerjee et al., 2009).

The regulation of the nuclear entry of transcription factors by matrix elasticity might actually be general. Other transcription factors whose nuclear entry is also known to be regulated by matrix stiffness include the YAP/TAZ co-activators (Swift et al., 2013b; Dupont et al., 2011; Yang et al., 2014) and key lineage-specific factors for muscle (MyoD) and bone (core-binding factor alpha 1; CBFA1) (Engler et al., 2006). Some of these participate in signaling pathways (such as the Hippo pathway for YAP/TAZ) that are also regulated by soluble factors (such as lipopolysaccharide). Nucleo-cytoplasmic shuttling of glucocorticoid receptors for natural and synthetic glucocorticoids such as dexamethasone need to be studied thoroughly as a function of matrix properties because glucocorticoids are frequently used in differentiation cocktails (Grigoriadis et al., 1988). Target genes in these pathways that are differentially expressed as a function of matrix properties and soluble-factor levels provide key evidence of functional nuclear entry or exit of a transcription factor. Epigenetic memory is also key to stem cell responses. For example, if MSCs are grown for one to three weeks on soft matrices (1 kPa) that tend to induce expression of a neurogenic marker, and then an osteoinduction cocktail is added, one finds that the neurogenic expression is largely reversed in the one-week cultures but not in the three-week cultures (Engler et al., 2006) (**Figure 1.3**). A lineage choice can be likened to a fork in a road going downhill that does not require much steering to choose, but the further down a chosen fork, the more difficult it is to reverse the fate/choice. Recent studies of the nuclear localization of YAP/TAZ in MSCs cultured on stiffness-switchable hydrogels confirm the idea of a matrix memory (Yang et al., 2014). How such transcriptional regulators are preferentially sequestered in the cytoplasm rather than the nucleus is generally unknown, but immunoprecipitation of the factors followed by mass spectrometry can help identify validatable binding partners in the cytoplasm and nucleus, as recently shown for RARγ (Swift et al., 2013b). Far better characterized in this respect is the actin-regulated serum response factor pathway (Miralles et al., 2003; Swift et al., 2013b), which couples directly to the mechanosensitive assembly of the actin–myosin cytoskeleton.

1.4 Harnessing pluripotency

Responses of embryonic stem cells (ESCs) to mechanical stress and stiffness are beginning to be clarified. The softness of embryos ($\sim$400 Pa) results from a relative lack of extracellular matrix even when compared with the earliest beating heart (Majkut et al., 2013). The softness of ESCs dictates the threshold for stress-driven, myosin-II dependent spreading and differentiation of mouse ESCs, but not of ESC-differentiated cells that are ten times stiffer (Chowdhury et al., 2010b). Similar to the matrix-modulated differentiation of MSCs, soft substrates that match the intrinsic softness of ESCs (600 Pa) suppress cell–matrix tractions and maintain the ESCs' self-renewal potential (Chowdhury et al., 2010a).

Inhibition of Rho-associated protein kinase (ROCK), an effector of myosin contractility, dramatically enhances survival of dissociated human ESCs (hESCs), with no effects on ESC differentiation (Watanabe et al., 2007). Decreased cell–cell contact has also been shown to reduce survival of dissociated hESCs (Chen et al., 2010) because of irreparably disrupted E-cadherin signaling (Xu et al., 2010). Enhancing cell attachment immediately after dissociation greatly improves survival, and is suggested to be partly a consequence of the synergy between integrin signaling and growth-factor signaling (Xu et al., 2010). Mechanical straining of hESCs on stiff substrates synergizes with soluble factors to inhibit the differentiation of pluripotent cells and to enhance their self-renewal (Saha et al., 2006; the physiological relevance of the strain needed, about 10%, is however unclear). Soft substrates might nonetheless be combined with externally imposed strains and suitable biochemical signals to maximize pluripotent cell numbers. For therapeutic applications, ESC expansion should be done without the usual underlying feeder cells (commonly, fibroblasts), which introduce biological variation and sources of immune rejection. The standard for ESC culture involves mouse tumor-derived Matrigel ($\sim$1 kPa) to increase cell adhesion, and high concentrations of TGF-β and basic fibroblast growth factor to antagonize differentiation (Rao and Zandstra, 2005). Current research is however focused on synthetic surface-engineered surfaces for xeno-free human pluripotent stem cell (hPSC) culture under chemically defined conditions, which should allow for scalability without the risks of cellular or pathogenic contamination. Examples include ultraviolet-treated spatial patterns (Saha et al., 2011) and peptide-decorated acrylate surfaces (Melkoumian et al., 2010). A high-throughput study on biomaterials development also found acrylate surfaces to be optimal for clonal growth of hPSCs (Mei et al., 2010). Materials that can accelerate hPSC expansion (Celiz et al., 2014) are needed for regenerative-medicine applications.

The discovery and development of human induced pluripotent stem cells (hiPSCs; Takahashi et al., 2007) was immediately followed by a flurry of research into therapeutic applications, in particular neurological diseases. A recent kinome-wide study of iPSCs highlighted the role of actomyosin polymerization through kinase-mediated phosphorylation of cofilin (a protein that disassembles actin filaments) as one major barrier to efficient reprogramming to iPSCs (Sakurai et al., 2014). It is then not surprising that NSC profiles are more similar to ESCs than to NSC-derived differentiated cells (Ramalho-Santos et al., 2002), not only because of default neurulation tendencies of ESCs (brain development is very early; Tropepe et al., 2001) but also perhaps because of the similarity in softness of embryos and the neural microenvironment relative to other tissues such as embryonic heart (Majkut et al., 2013). Indeed, hPSCs integrate readily into the motor cortex and undergo cortical neurogenesis without added morphogens (Espuny-Camacho et al., 2013). However, direct implantation of hESCs into various other tissue sites produces heterogeneous teratomas (Prokhorova et al., 2009). Reprogramming *in vivo* also produces teratomas as well as iPSCs with totipotency features that are not possible in standard *in vitro* reprogramming (Abad et al., 2013).

Since the first bone marrow reconstitution after myeloablative therapy decades ago, functional tissue regeneration with other types of stem cell has been the vision of many. Enabling technologies include cell phenotyping by flow cytometry with antibodies against lineage-distinctive arrays of cell-surface receptors. However, HSC transplantation is successful because of the intrinsic ability of HSCs to ‘home’ to the bone marrow and find their niche(s). The promise of iPSC technology to produce all diverse cell types in a given solid tissue is tempered by a poor understanding of microenvironmental factors that direct stem cell fate, as well as of lineage phenotyping and uncertainty over how to control the mobility and engraftment of cells (Yu et al., 2013). Commitment to a lineage *in vitro* before implantation seems essential and necessarily brings culture materials into a protocol, but also complicates the various efforts.

Yamanaka and Gurdon’s 2012 Nobel prize in Physiology or Medicine has largely fixed the trajectory of most of the currently envisaged stem cell-based therapies into using iPSCs generated from suitably matched donors. Yet high-efficiency reprogramming and tissue specification remains a major challenge, as does delivery and survival *in vivo*. Therapies with any type of stem cell should eventually be compared to normal tissue, but technologies to ascertain cell integration and contributions to diseased tissue require more rigor than is typical with decades-old histological methods. For example, putting human cells in immunodeficient mice is the current standard in the HSC field; however, for similar studies with solid tissues, human versus mouse proteomics (Swift et al., 2013b) and RNA-sequencing can be used to reveal the contributions of stem-cell-derived xenografts to obtain systems-level views of the myriad of factors that come into play for fully functional transplants. With the wide range of material and analytical technologies emerging to help the translation from *in vitro* to *in vivo*, challenges in concepts and applications seem increasingly addressable with suitable rigor and reproducibility for translation into humans.

Table 1.1. Glossary of factors and proteins most relevant to stem cell mechanobiology

Growth Factors	
SCF, stem cell factor	transmembrane or soluble cytokine produced by fibroblasts and endothelial cells that binds to the c-Kit receptor (CD117) to help HSC in homing to and maintenance of the niche
SDF-1, stromal cell-derived factor	soluble chemotactic cytokine for HSC homing to the marrow
G-CSF, granulocyte colony-stimulating factor	soluble glycoprotein that promotes stem cell granulopoiesis
TGF-β/BMP, Transforming growth factor-β / Bone morphogenetic protein	soluble or matrix-bound growth factors that promote cell growth, differentiation and matrix synthesis
bFGF, basic Fibroblast growth factor	soluble or matrix-bound factor, used as supplement in culture medium for ESC maintenance
RA, Retinoic acid	membrane-permeable vitamin-A metabolite with roles in neutrophil differentiation; implicated in nucleus deformability
IL, Interleukin	membrane-bound or matrix-bound cytokines produced mostly by the immune system to regulate production, differentiation and function of blood cells
Transcription factors	
RAR, Retinoic acid receptor	on binding of RA, RAR heterodimerizes with retinoid X receptor (RXR) to bind to a retinoic acid response element (RARE) on a target gene, such as *LMNA*
SRF, Serum response factor	binds to serum response element (SRE) of genes responsible for controlling cytoskeletal structures involved in, for example, cell spreading, adhesion and contractility
SMAD, Sma and Mad related family	TGF-β/BMP family of ligands bind to their receptors, which in turn activate SMAD signaling and bind to SMAD-binding elements (SBE) in target genes, such as *COL1A1*
YAP/TAZ, Yes-associated protein / Transcriptional co-activator of PDZ-binding motif	involved in the Hippo signaling pathway, responsible for cell-size control; recently shown to be crucial in transducing mechanical signals from ECM to nucleus, in an actomyosin and Rho-dependent manner and independent of the Hippo pathway
Matrix, adhesion, and cyto-/nucleoskeletal proteins	
Collagen	the most abundant protein in animals; it confers the majority of tissue structure and stiffness
Fibronectin	usually found as a provisional matrix component in embryonic development and wound healing

Table 1.1. (continued)

Matrix, adhesion, and cyto-/nucleoskeletal proteins	
Laminin	basement membrane protein that helps maintain the apical–basal polarity of stem cell niches
Integrin	transmembrane heterodimeric protein that binds to the extracellular matrix
Cadherin	transmembrane protein that mediates cell–cell adhesion
Actin	highly abundant protein that forms microfilaments (a major cytoskeletal structure); essential for migration, contractility, and cell division
Myosin	provides the basis for cell contraction by binding to actin filaments in an ATP-dependent manner
Lamin	a class of intermediate filaments (a major cytoskeletal structure) found in the nuclear envelope; provides structural function and transcriptional regulation
Nestin	a class of intermediate filaments expressed mostly in nerve cells; also found in mesenchymal stem cells and newly formed endothelial cells
Examples of synergy between soluble and insoluble factors	
Tropoelastin & serum-free cytokine cocktail (IL-3, IL-6 and SCF)	HSCs repopulate on soft tropoelastin but not on stiff, crosslinked tropoelastin even with the presence of cocktail
Matrix-bound SCF and SDF-1 induced MMP9 expression	MMP9 releases SCF and permit HSC repopulation and proliferation of quiescent HSCs
Matrix-bound TGF-β	activated with shear flow or cell-derived force; implicated in progressive fibrosis
Mechanosensitive lamin A and retinoic acid signaling	lamin A increases with tissue stiffness, and primes RARγ to enter nucleus and to promote RA signaling
Soft substrate and retinoic acid in NSC cultures	NSCs commit to neurons only on very soft substrates even under strong pro-neuronal conditions
Matrigel, TGF-β and bFGF	maintains ESC pluripotent state

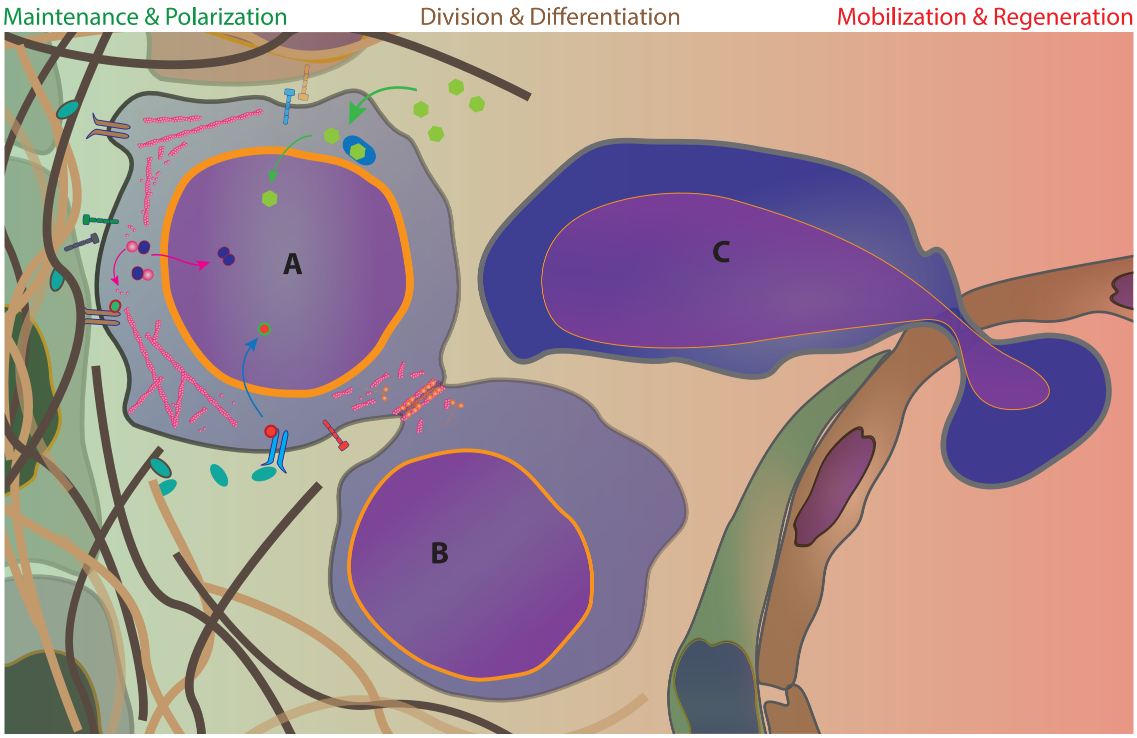
Maintenance & Polarization
Division & Differentiation
Mobilization & Regeneration
A
B
C

Figure 1.1. Lessons from the niche. A, The insoluble and soluble milieus in a stem cell niche specify apical–basal polarity and help maintain stemness. Signaling factors include cell–cell (segmented rods) and cell–matrix contacts (wiggly lines represent the matrix; rod-shaped dimers at the cell boundary represent membrane-bound integrins), membrane-permeable molecules (green hexagons; green, purple and red circles) and matrix-bound factors (blue ovals). **B**, Asymmetric cell division results in differentiating daughter cells. **C**, Migration out of the niche is affected by both extrinsic barriers (such as other cells or the matrix in, for example, endothelial pores; green and brown semi-circular structures, right) and intrinsic factors, such as the nuclear lamina (orange line encircling cell nuclei). For example, neutrophils have very low lamin-A (that is, softer nuclei) and can thus easily enter the circulatory system (red region, lower right).

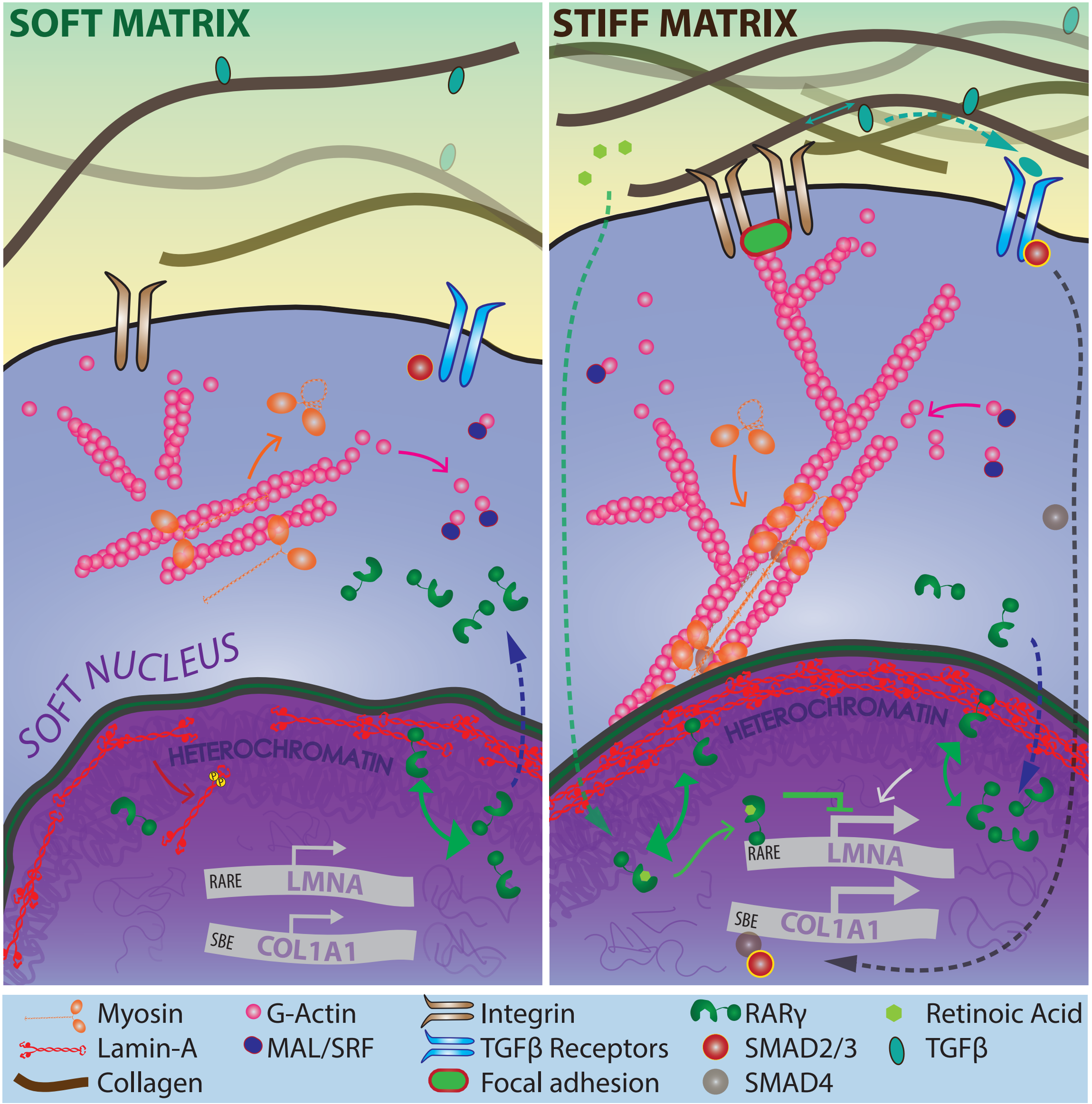
SOFT MATRIX
STIFF MATRIX
SOFT NUCLEUS
HETEROCHROMATIN
RARE
LMNA
SBE
COL1A1
Myosin
Lamin-A
Collagen
G-Actin
MAL/SRF
Integrin
TGFβ Receptors
Focal adhesion
RARγ
SMAD2/3
SMAD4
Retinoic Acid
TGFβ

Figure 1.2. Matrix and soluble factors converge to control lamin-A levels. Left, in soft tissues, collagen is low, cells do not contract, and the nucleus is not tensed. Lamin A is turned over and RARγ is mostly cytoplasmic, with no appreciable soluble agonist effects. **Right**, as collagen content increases (as in stiffer tissues or in fibrosis), a cell forms stable focal adhesions, a stable actomyosin cytoskeleton, and a tension-stabilized nucleus. Tension-mediated activation of matrix-bound TGF-β leads to collagen and lamin-A production, and to RARγ nuclear localization. This primes the stem cell to respond to RA, which in turn represses lamin-A transcription.

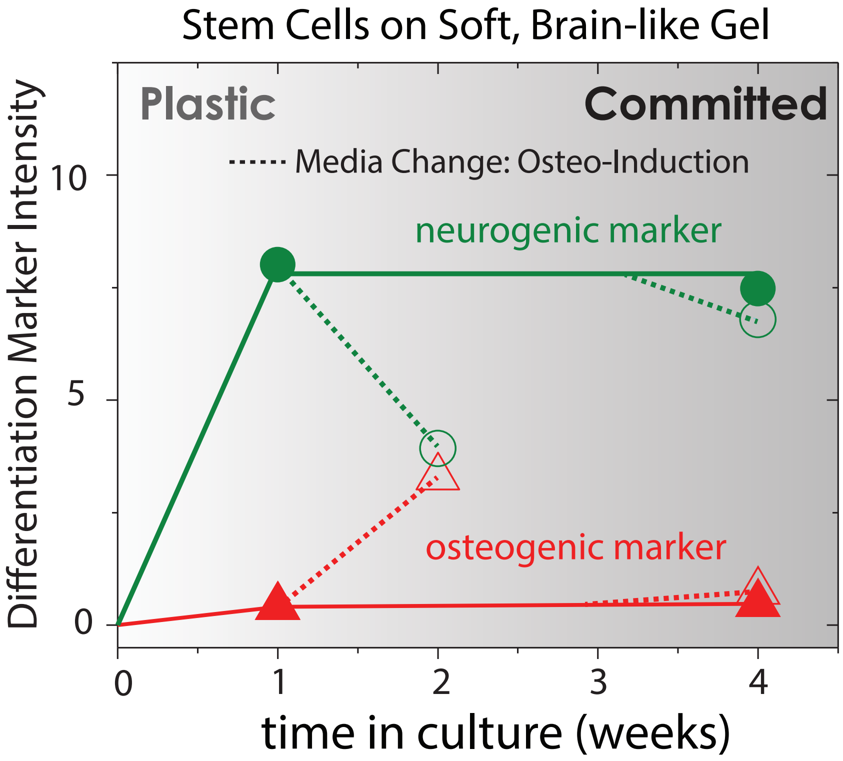

Figure 1.3. Stem cells have a time-dependent 'memory' of prior conditioning. MSCs grown on soft, neurogenic matrix in standard media are induced towards neurogenic lineage (green), yet can be challenged by osteoinduction media that redirects them towards an osteogenic lineage (red) during the first 1-2 weeks after initial induction by the matrix. Figure adapted from Engler et al. (2006).

Chapter 2

A minimal ‘scar in a dish’ model reveals mechano-temporal effects of matrix stiffness on stem cell fate

Portions of this work are under peer-review in *Nature Materials*.

3D decellularized heart models were performed by Dr. Matthew Raab.
Proteomics analyses of mouse tissue were performed by Dr. Joe Swift.

Abstract

Scarring in higher animals compromises tissue function and is highly complex, which motivates the development of culture systems that clarify cellular mechanisms and that might also help identify therapeutics. Co-polymerization of collagen-I with polyacrylamide produced scar-like, crosslinked fiber bundles that segregated heterogenously atop the hydrogel and directed the fate of multiple cell types towards scar-like phenotypes. As with scars, the gels stain non-uniformly with Sirius Red dye and are regionally stiff. Cardiomyocytes derived from pluripotent stem cells do not beat on scar-like gels, consistent with defective beating of scarred hearts. Mesenchymal stem cells (MSCs), which traffic to injured sites, 'durotax' towards mimetic scars, undergo osteogenesis consistent with ossification of some scars, and upregulate tension-sensitive proteins. Within hours, myosin IIB polarized rearward in stress fibers and nucleoskeletal lamin-A levels increased as cells and nuclei spread, but 1-2 days were required to upregulate the 'scar marker' α-smooth muscle actin. Agonists to one pathway involving retinoic acid receptors inhibited scar-induced differentiation, with similar effects evident in the mechano-regulated fates of progenitor-derived macrophages that remodel scars. Mechanobiological gene circuits are modeled mathematically, illustrating how key features of scars in soft tissues can be usefully studied in culture.

2.1 Introduction

Scarring is an unavoidable consequence in mature higher vertebrates of survivable injuries that range from external trauma to acute events such as myocardial infarction and various chronic diseases (Gurtner et al., 2008). Fibrotic, heterogeneous matrix is the defining feature of a scar and consists predominantly of excessive, crosslinked collagen-I bundles, which displace cells and less oriented matrix and thereby limit tissue function (Martin, 1997). Across striated muscle diseases, for example, collagen-I expression increases up to ten-fold or more relative to normal levels (Bakay et al., 2002), and scarred tissue also tends to be stiffer (Engler et al., 2004b;

Tomita et al., 1999). An increase in tissue stiffness is predictable because collagen-I, being the most abundant protein in animals, makes key structural networks (Munster et al., 2013), and this is seen in most fibrotic tissues (**Figure 2.1**). However, many additional changes in scarred tissue can be detected, including proportional increases in the nuclear structure protein lamin A versus collagen-I (Figure 2.1B,C). For normal tissues, we have shown recently that lamin-A levels scale with collagen-I and are mechanosensitive *in vitro* (Swift et al., 2013b), but given the complexity of scars *in vivo* in terms of diverse cell types, matrix, and soluble factors, it is unclear whether lamin A and the transcription factors it regulates are responsive in any given cell type to a heterogeneous scarring microenvironment.

Cell therapies for many types of scarred tissues are being pursued with a wide range of cell types, and the list will no doubt grow with the emergence of various stem cells, including pluripotent cells (Boiani and Scholer, 2005) and adult mesenchymal stem cells (MSCs; Pittenger et al., 1999). Whether stem cell-derived lineages are plastic and change phenotype when engrafted into scars is a critical question for cell therapy, particularly for MSCs that are multipotent as well as immunomodulatory. A mechanochemical gradient is also likely wherever normal tissue transitions to scar (Tomita et al., 1999; Pfeffer and Braunwald, 1990), and an impact on cell trafficking into scars will likely affect cell and tissue fate (Orlic et al., 2001).

Matrix ligand type and density provide signals complementary to matrix mechanics (Engler et al., 2004b) in influencing cell behavior such as MSC differentiation (Engler et al., 2006; Huebsch et al., 2010; Trappmann et al., 2012; Khetan et al., 2013), but recent studies of matrix tethering (Trappmann et al., 2012), topography (McNamara et al., 2010), crosslinking, and in three-dimensional (3D) models (Huebsch et al., 2010; Khetan et al., 2013; Liu et al., 2012; Ulrich et al., 2009; Levental et al., 2009) have stirred debate on the influence of matrix mechanical properties in cell-fate decisions. Stiffness of scars (e.g. in skin) measured in the macroscopic (in MPa; Corr et al., 2009) versus microscopic (in kPa; Achterberg et al., 2014) scales yield vastly different numbers. A clear relationship to specific tissue parameters is an important goal of new cell-culture material systems (MacQueen et al., 2013). Here we focused on microscale elasticity of tissues (and gels) since cells sense on the same scale. With heterogeneous scar-like culture platforms here, we make a range of comparisons to scarred tissue (Figure 2.1) and ultimately show that the effective stiffness of a scar is key to cell fate signals.

2.2 Results and Discussion

2.2.1 Hydrogels with scar-like collagen fiber heterogeneity and regional rigidity

Starting with an allylsilane-modified ‘bottom’ coverslip that anchors polyacrylamide (PA) chains, we discovered that mixing collagen-I (Col1) heterotrimers into the PA precursor solution promotes Col1 fibril formation with segregation to within $\sim$10 microns of the gel interface during free-radical polymerization (**Figure 2.2**A,B). Importantly, the embedded Col1 gels stain positively but heterogeneously for the histochemical dye, Sirius Red (Figure 2.2C), which is widely used to assess tissue fibrosis (Turgeman et al., 2008; Mann et al., 2011; Georges et al., 2007). Sirius Red staining was not observed, in contrast, with Col1 coated (CC) conventionally on the PA gel surface (Figure 2.2C) via a standard sulfo-SANPAH-mediated covalent reaction widely used for culture substrates (Dembo and Wang, 1999). The embedded Col1 was varied to approximate the Sirius Red area fraction visible in typical sections of scarred tissue (20–30%, Figure 2.1). Surprisingly, initial studies of cells cultured on the embedded Col1 gels showed that ligand density on fiber bundles was below the threshold needed for cell adhesion, and so the conventional ‘CC’ modification was used to obtain cell-adhesive scar-like$_{0.3kPa}$ gels with bundles of collagen that were stable for at least 7 days in cell culture (**Figure 2.3**). This minimal matrix model of a scar provides separate control over matrix elasticity and ligand density, which is not possible in pure collagen gels where ligand density changes with collagen density. Furthermore, collagen gels exhibit non-linear elasticity (Storm et al., 2005) and stiffen under strain induced by incorporating cells (Vader et al., 2009), which complicate matrix-mechanical effects on cell responses.

Consistent with interfacial formation of fibril bundles, the embedding of Col1 (0.04%

w/v) showed no significant effect on the gel's bulk modulus ($E \approx 2.9G' =$ 0.3 kPa; 3% acrylamide, 0.07% bis-acrylamide w/v), and for all gels, the elastic modulus dominated the viscous modulus (**Figure 2.4**A). Unlike PA gels, collagen fiber networks typically show non-linear strain stiffening independent of crosslinking (Munster et al., 2013), which becomes insignificant in the embedded system here that is predominantly elastomeric. However, because a surface-adherent cell feels only a few microns deep into a gel (Buxboim et al., 2010), the surface microelasticity E_{surf} seemed critical to measure. We started with conventional micro-indentation by atomic force microscopy (AFM; Engler et al., 2007), with results for pristine or CC gels identical to bulk rheology (Figure 2.4Bi). Microelasticity maps of scar-like$_{0.3kPa}$ gel surfaces proved to be far more heterogeneous than those of CC gels, consistent with Sirius Red imaging, and the scar-like$_{0.3kPa}$ gels also appeared 2–3-fold stiffer than the same gels without collagen fibers (Figure 2.4Bii). However, such a nominal shift for a stratified material is indicative of a stiffer material on top of a softer bulk. We calculated therefore a suitable thin-film correction and also measured gel tackiness for a second estimation of E_{surf} (see section A.1, Appendix A). Both measurements suggested E_{surf} ~10 kPa, which is far stiffer than the bulk gel. A recent report showed that extracellular matrix tethering, by varying sulfo-SANPAH concentration, could influence stem cell fate regardless of hydrogel stiffness (Trappmann et al., 2012). However, we found that reducing Sulfo-SANPAH reduced Col1 coating density (Figure 2.4C), which may complicate the reported matrix-tethering effects as they may also be attributed to cell responses to ligand-density variation (Engler et al., 2004a).

Cells apply tractions predominantly along the matrix surface (Dembo and Wang, 1999), whereas the AFM probes primarily normal to the substrate. Lateral pulling of the gel surface with a glass microprobe at constant displacement was therefore used to apply a constant force on scar-like$_{0.3kPa}$ gels (**Figure 2.5**). Displacements of microbeads embedded in the gels exhibited the expected Boussinesq-like profiles (Figure 2.5B,C; also see section A.2, Appendix A). Displacement profiles far from a fiber bundle were strikingly similar to those for homogeneous 0.3-kPa gels, whereas profiles closer to fiber bundles appeared similar to those for homogeneous 10 kPa gels (Figure 2.5Cii). We estimated therefore that $E_{surf} \sim$ 0.3

to 10 kPa for scar-like$_{0.3kPa}$ gels, which highlights the regional rigidity near the fiber bundles. The imaging and physical measurements therefore suggest that the scar-like matrix is a stiff fibrous meshwork within a background of otherwise soft, tissue-like matrix. Whether cells would respond in a scar-like manner, despite matrix heterogeneity, was the next critical question.

2.2.2 'Scar in a dish' impairs cardiomyocyte beating consistent with heart failure

Following a heart attack, regions of necrotic myocardium that result from acute ischemic injury are replaced by scars that are too rigid for the heart to contract, causing large decreases in cardiac output and eventual heart failure. This is a major clinical problem today, and there is great interest in using cardiomyocytes differentiated from pluripotent stem cells to help replace damaged myocardium (Laflamme et al., 2007). However, how such cells respond to a scar-like matrix when engrafting is crucial to understand. Stem cell-derived cardiomyocytes were therefore seeded onto CC$_{3kPa}$ or scar-like$_{3kPa}$ gels, with 3 kPa chosen as the nominal stiffness because embryonic heart is mostly collagenous matrix and is ∼1–6 kPa in stiffness (Majkut et al., 2013; Engler et al., 2008). Collagen-coated tissue culture polystyrene (CC-TCP) was used as a standard control. After 10 days of culture, the number of beating cells was minimal on scar-like$_{3kPa}$ gels compared to CC$_{3kPa}$ gels (28% vs 100%) with large differences likewise in beating frequencies (0.24 $\pm$ 0.03 Hz vs. 0.61 $\pm$ 0.06 Hz) (**Figure 2.6**A). Results for CC-TCP were the same as scar-like$_{3kPa}$ gels, consistent with expectations that heart cells simply cannot contract rigid matrices and will eventually stop beating.

The handful of cardiomyocytes that beat at high rates on the stiff scar-like$_{3kPa}$ and CC-TCP substrates exhibited informative beating patterns. TCP is too rigid to contract, but local regions of some cells did appear to twitch at the normal rate. Likewise, on scar-like$_{3kPa}$ gels, any cardiomyocyte that was half-attached to a scar-like fiber bundle showed no measurable contraction on the fibers, while the other half of the same cell beat normally on the CC part of the substrate (Figure 2.6Bi-iii). Given the sensitivity of beating to substrates, the evident nuclear beating (Figure 2.6Biv) suggested that nuclear phenotypes could also emerge in scar-like cultures. Ultimately, individual cardiomyocytes could not beat when the matrix was too rigid. These initial findings with cells confirm our physical measurements showing scar-like gels are regionally soft or rigid, but they also suggest that the overall cell response is dominated by the rigid regions.

2.2.3 MSCs durotax to the 'scar in a dish'

MSCs show some therapeutic utility in heart repair (Berry et al., 2006; Hare et al., 2009), and although mechanisms remain unclear, there is also evidence of homing to the injury site (Orlic et al., 2001). MSC migration towards a site of injury within tissue will typically involve a large gradient in stiffness, such as in an infarct border zone (∼9 kPa/mm; Berry et al., 2006; Tse and Engler, 2011). In several other homogeneous gel systems, various cell types including MSCs have been reported to 'durotax' from soft to stiff matrix (Tse and Engler, 2011; Isenberg et al., 2009; Raab et al., 2012; Lo et al., 2004). A gradient of increasing scar-like fiber bundles was therefore made here to resemble a transition from homogeneous soft tissue to a heterogeneous scar (**Figure 2.7**A). A PA gel precursor solution was mixed with or without Col1, and drops of each solution were deposited next to each other; Sirius Red staining confirmed such a gradient of scar-like fibers over a length scale (2–4 mm) that ultimately saturates to a 20–30% area fraction (Figure 2.7B), similar to that seen in diseased tissue (Pfeffer and Braunwald, 1990; Turgeman et al., 2008; Mann et al., 2011).

Live cell imaging allowed us to track cells on either side of the transition zone (**Figure 2.8**A). Net displacements of cell centroids every 15 min towards either the CC half or scar-like half were used to calculate a Durotaxis Index (Raab et al., 2012), by counting the net number of steps a cell takes to move towards the scar-like region. Strikingly, only MSCs migrating in the transition region exhibited strongly positive net displacements (Figure 2.8B) and Durotaxis Index (**Figure 2.8**C) towards the scar-like$_{0.3kPa}$ region. Far from the gradient and in both CC$_{0.3kPa}$ and scar-like$_{0.3kPa}$ regions, MSCs showed no observable migration bias. A monotonic increase in Durotaxis Index with the underlying elasticity contrast (ΔE) was previously documented for vascular smooth muscle cells (Isenberg et al., 2009), and a very similar relationship for MSCs implies that scar-like$_{0.3kPa}$ gels have an effective $E_{surf} \sim$ 10–14 kPa (Figure 2.8Ciii). This E_{surf} estimated from cell motility agrees with the maximum E_{surf} obtained from our physical measurements (Figure 2.5). Heterogeneity of our matrices did not obscure durotaxis probably because the turnover and hysteresis of cytoskeletal structures (e.g. myosin IIB) takes hours (Raab et al., 2012), suggesting a short-term memory (rather than long-term memory; Yang et al., 2014) in the crawling cells as they average over matrix heterogeneities and 'remember' only the stiffer fiber bundles. Moreover, the minimum area fraction of 'scar' for imparting a memory seems low since MSCs durotax into an increasingly heterogeneous scar-like region with migration results that fit well to findings for homogeneous gels.

Knockdown of myosin IIB (MIIB) in MSCs eliminated durotaxis (Figure 2.8Ci,ii), consistent with our recent demonstration that MIIB polarizes rearward only on stiff matrices and is needed for durotaxis where persistent migration increases from soft to stiff (Raab et al., 2012). Immunostaining and imaging of MSCs on both ends of the soft-to-scar gradient confirmed the expected MIIB polarization differences as well as increasing expression of α-smooth muscle actin expression (SMA; **Figure 2.9**A), which is a myogenic marker for intracellular tension that is commonly elevated in scarred tissue (Hinz, 2007). However, results for day-1 versus day-2 showed that MIIB polarization preceded SMA upregulation on the scar-like matrix (Figure 2.9Aii). Thus, the 'scar marker' SMA is not required for early stiffness sensing, consistent with studies of chemically induced liver fibrosis (Georges et al., 2007). Rearward nucleus polarization during cell migration on stiffer matrices (Figure 2.9Ai) is also suggestive of higher contractility in the rear, consistent with MIIB polarization seen recently (Raab et al., 2012). Among myosin-II isoforms (A, B and C), MIIB accounts for only 5–10% of total myosin-II in MSCs (Raab et al., 2012), and cell traction forces do not change drastically with MIIB knockdown (Cai et al., 2006). Interestingly, a cell size-dependent 'attraction' to the underlying scar-like fibers was evident (Figure 2.9B), consistent with a local, myosin-dependent durotaxis in which well-spread cells exert higher, myosin-IIA-dominated traction forces. Haptotaxis did not contribute because

MSCs did not spread on scar-like fibers without the additional collagen coating (Figure 2.3A).

To confirm and extend these findings, an additional model for scarred heart matrix was made. Ventricular myocardium was decellularized and half of the collagen-I-dominated matrix (Majkut et al., 2013; **Figure 2.10**) was stiffened by chemical crosslinking (Figure 2.9C). The apparent E of this 3D matrix determined by AFM (Figure 2.9Cii) approximates the results above from AFM for CC$_{0.3kPa}$ and scar-like$_{0.3kPa}$ gels (0.3–1 kPa; Figure 2.4Bii). Seeding of MSCs (transduced with GFP for visualization) showed a uniform distribution along the entire heart matrix, as verified 4 hrs post-seeding. After 1–2 days, cell numbers were depleted in the gradient region as a wave of MSCs accumulated in the crosslinked, stiff region (Figure 2.9Ciii). The findings are consistent with the net effect of durotaxis-based accumulation as illustrated with the simpler ‘scar in a dish’.

2.2.4 Effective stiffness of ‘scar in a dish’ can be deduced from cell shape and cytoskeleton

Systematic analyses of cell morphologies and key markers of cytoskeleton uniformly indicate the scar-like matrix is $\sim$10–14 kPa with respect to the cell. Most cells spread more on stiffer substrates (Engler et al., 2006; Rehfeldt et al., 2012), and by fitting a characteristic hyperbola in response to matrix *E* (Rehfeldt et al., 2012; Zemel et al., 2010), the scar-like$_{0.3kPa}$ gel has an effective elasticity (E_{eff}) of $\sim$12 kPa (R^2 = 0.98), which is similar to the estimate obtained from analyses of cell aspect ratio (**Figure 2.11**Ai,ii). The latter also proved sensitive to myosin-II inhibition, even on the scar-like matrix. Nuclear shapes also respond similarly to matrix rigidity-induced contraction (Figure 2.11Aii). Localization of MIIB to the rear of the cell (Raab et al., 2012) and the expression of SMA are both hyperbolic with E ($R^2 \geq 0.97$), and once again indicate that the scar-like$_{0.3kPa}$ gel has an $E_{eff} \sim 12$ kPa (Figure 2.11B,C). SMA incorporation into stress fibers as well as its increased expression is sustained up to 7 days on stiff matrices (Figure 2.11Cii,iii), suggestive of commitment to a scar-like phenotype (Tomita et al., 1999).

2.2.5 Stiffness of 'scar in a dish' increases lamin A and MSC osteo-commitment

Our analyses of striated muscle diseases prone to scarring revealed an increase in lamin A (Figure 2.1), which is a nucleoskeletal protein implicated in various differentiation and maturation processes (Swift et al., 2013b; Majkut et al., 2013; Shin et al., 2013). Measurements of lamin A here likewise showed an increase on stiffer matrices (**Figure 2.12**A) as early as 24 hours (Figure 2.12B), which is also consistent with our recent report that lamin A is mechanosensitive to matrix stiffness (Swift et al., 2013b), likely through cytoskeletal stress exerted on the nucleus (Swift et al., 2013b; Liu et al., 2014). Knockdown of lamin A followed by in situ hybridization shows that lamin-A protein levels increase with *LMNA* transcript numbers (Figure 2.12C). Lamin A is highly expressed in bone (Swift et al., 2013b), and MSCs injected into infarcted hearts have sometimes been found to form ossified structures (Breitbach et al., 2007) that would be detrimental for the beating heart. Lamin A regulates nuclear entry of a retinoic acid (RA) receptor (RARγ) transcription factor (Swift et al., 2013b) that is known to promote bone formation (Shimono et al., 2011), while SMA is a product of the serum response factor (SRF) pathway that also contributes to osteogenesis (Chen et al., 2012). Studies of osteogenesis on the scar-like matrix were thus strongly motivated. A mechanobiological gene circuit (MGC) is proposed to formalize the various pathways in Chapter 4 (Figure 2.12D), starting with matrix stiffness that induces cytoskeletal tension (e.g. myosin II or SMA) that is, in turn, applied to the nucleus, specifically regulating the stability of lamin A. RARγ-dependent lamin-A expression is upstream of SMA via SRF (Swift et al., 2013b), while positive mechanical feedback by SMA-rich stress fibers on lamin A leads to fold changes of both proteins in response to matrix E — as modeled by the MGC (Figure 2.12A).

Compared to MSCs on CC$_{0.3kPa}$ gel, culturing MSCs for a week on both scar-like$_{0.3kPa}$ and CC$_{40kPa}$ gels with osteogenic induction media (OIM) increased Alkaline Phosphatase (ALP) activity, which is an early marker of osteogenic commitment (**Figure 2.13**A). Calcification was also evident on the stiffer matrices based on staining with Alizarin Red (Figure 2.13B). The lack of significant Alizarin-Red staining on scar-like$_{0.3kPa}$ gels conforms to the observations that its E_{eff} is well below what is needed for MSC osteogenesis either *in vitro* (Engler et al., 2006) or *in vivo* (Berry et al., 2006; Breitbach et al., 2007). In all cases, RA treatment inhibited both ALP activity and Alizarin-Red staining that is likely due to reduction of stress-stabilized lamin A (Swift et al., 2013b). The results indicate that the scar-like matrix tends to be osteogenic, and that even though the vitamin-A derivative RA is normally nM in serum, higher doses of RA agonists show therapeutic promise for inhibiting calcification of scar tissue.

2.2.6 Lamin-A & MMP9 in progenitor-derived macrophages also increase with matrix stiffness

Monocyte-derived macrophages are essential in solid tissue remodeling, as exemplified by regeneration of salamander limbs (Godwin et al., 2013), liver (Ramachandran et al., 2012) and, to a more limited extent, skeletal muscle (Tidball and Wehling-Henricks, 2007). Distinct macrophage subtypes and plasticity complicate our understanding of repair (Ramachandran et al., 2012; Tidball and Wehling-Henricks, 2007; Nahrendorf et al., 2007), and specialized resident macrophages in various tissue compartments exhibit a spectrum of activation states (Mosser and Edwards, 2008) that seem, in part, mechanically regulated (Yang et al., 2000; McWhorter et al., 2013). We hypothesized therefore a differentiation circuit for macrophages that depends on matrix stiffness and RA (**Figure 2.14**A) and affects not only lamin-A levels but also proteases known for roles in liver repair (Ramachandran et al., 2012).

Monocytes differentiate to surface-adherent macrophages by addition of phorbol esters (PMA) that induce expression of lamin A (Olins et al., 2001) and matrix metalloproteinases (MMP; Worley et al., 2003), which RA inhibits (Olins et al., 2001; Worley et al., 2003; Figure 2.14B). As a function of increasing matrix stiffness, PMA increased protein levels of lamin A and MMP9 (but not of lamin B or MMP2), and subsequent RA treatment generally suppressed expression (**Figs. 2.15 and 2.16**). Chromatin immunoprecipitation followed by sequencing (ChIP-Seq) for the relevant transcription factors (**Figure 2.17**) confirms binding of

RA-regulated transcription factors to the *LMNA* and *MMP9* promoters but not to *LMNB1/2* nor *MMP2* genes (Allenby et al., 1993). Interestingly, the protein changes versus matrix stiffness are well-fit by the same hyperbolic responses as those for MSCs (Figure 2.11). This not only implicates the same underlying gene circuit with respect to matrix sensitivity but also that the scar-like$_{0.3kPa}$ matrix exhibits — for a cell type distinct from an MSC — an effective stiffness of E_{eff} = 10–14 kPa.

2.3 Conclusion

All three cell systems studied here (striated myocytes, MSCs, and macrophages) are not only relevant to scarring of at least one major human tissue type, striated muscle, but more importantly all three cell types respond to our heterogeneous scar-like gels as if they are on much stiffer matrix. The 3D ex vivo decellularized heart matrices developed here exhibit similar rheological profiles as 2D scar-like gels (Figs. 2.5 and 2.9C), and MSCs durotax on both, reminiscent of MSC accumulation into scarred tissues (Orlic et al., 2001). MSC migration, morphology, and protein responses to matrix E indeed reveal a high effective *E* of the scar-like$_{0.3kPa}$ gel (Figs. 2.8, 2.9 and 2.11), consistent with the maximum E determined in suitably analyzed micromechanical measurements (Figure 2.5). ECM micro-architecture is thereby important to the mechanochemical control of cell fate.

Heterotopic ossification occurs in many tissue contexts, including muscle disease (Mu et al., 2013) and hip replacement surgery where it is problematic (Kocic et al., 2010). MSC injection into infarcts (but not normal muscle) can cause calcification (Figure 2.13; Breitbach et al., 2007), but MSC injection can also improve cardiac performance due to direct repression of fibrosis (Berry et al., 2006) or indirect immunomodulation (Tomita et al., 1999). MMP secretion by MSCs is far below that of macrophages, but the changes in phenotype of engrafted MSCs could help to recruit and modulate reparative macrophages that effectively repress fibrosis. Therapeutic utility has indeed been shown with macrophages activated *ex vivo* and injected into infarcted hearts (Leor et al., 2006), and MMP9 is specifically implicated in blood stem cell recruitment for muscle repair (Lolmede et al., 2009). MMP-mediated softening of stiff, fibrotic matrix seems likely, and co-cultures of MSCs and macrophages in scar-like gel systems and gradients made here could help clarify mechanistic aspects of the interplay of such important cells.

The fact that scarring occurs only in mature stages of higher animals (Gurtner et al., 2008), such as *Homo sapiens*, likely reflects an evolved need to generate a sufficiently stiff tissue that sustains the large stresses in mature tissues. Tissue injuries initiate broad chemical and mechanical changes that also serve as homing cues for highly plastic MSCs and monocytes/macrophages, among other cell types. Lamin-A changes in scarred tissues and scar-like gels (Figs. 2.1, 2.12 and 2.15) illustrate the plasticity of at least one nuclear protein that regulates several transcription factors in normal differentiation. For example, lamin-A's positive regulation of actomyosin proteins via SRF (Swift et al., 2013b) should help MSCs contract wounds that myofibroblasts usually close (Hinz, 2007) and also make macrophages more phagocytic (Tsai and Discher, 2008), which is conducive to resolving fibrosis at least in liver (Ramachandran et al., 2012). In MSCs, lamin-A levels regulate nuclear entry of RARG, promoting osteogenesis (Swift et al., 2013b). However, monocytes express RARA as the major RAR isoform (Hashimoto et al., 1990; Zhu et al., 2001), and so a panel of RAR specific drugs was tested, revealing that PMA-induced levels of lamin A and MMP9 were significantly repressed via RARA (Figure 2.18). Such findings can guide novel application of specific compounds to limit calcification and matrix remodeling in scars.

2.4 Materials and Methods

2.4.1 Synthesis and functionalization of conventional and scar-like hydrogels for cell culture

Circular glass coverslips (18-mm diameter, Fisher Scientific) were pre-treated in boiling ethanol, then RCA solution at 70°C (1:1:3 of 30% H_2O_2:15N NH_4OH:distilled H_2O) for 10 minutes each, and functionalized in chloroform solution with 0.1% allyltrichlorosilane and 0.1% triethylamine for 30 minutes. Varying ratios of N,N'-methylene-bis-acrylamide (Sigma) and acrylamide solution (40%, Sigma) in distilled H_2O were formulated to tune polyacrylamide (PA) hydrogel stiffness. The PA precursor solution (20 μL) was pipetted on allylsilanated coverslips with 0.1% ammonium persulfate and 0.1% N,N,N',N'-tetramethylethylenediamine to initiate polymerization. To make a 0.3-kPa PA gel, precursor solution consists of 3% acrylamide and 0.07% bis-acrylamide; a 40-kPa PA gel comprises 10% acrylamide and 0.3% bis-acrylamide (for other formulations, see Table C.1, Appendix C). To create PA gels with embedded collagen (e.g. scar-like$_{0.3kPa}$), type I rat-tail collagen (BD Biosciences) was diluted in the PA precursor solution to a final concentration of 0.4 mg/mL in 50 mM HEPES buffer (pH 8). Gradient gels were prepared by juxtaposing 2 drops (10 μL) of different precursor solutions on a coverslip. For MSC durotaxis on CC$_{0.3kPa}$/scar-like$_{0.3kPa}$ hybrid gel (Figure 2.7), the formulation for 0.3-kPa PA gel was used on both sides, but with pre-mixed collagen-I on the scar-like side as described above. In order to delineate the regions under the microscope, fluospheres (1-μm diameter, Invitrogen) were supplemented 0.005% by weight in the soft side, while collagen fibers in the embedded collagen region were fluorescently immunolabeled. During polymerization, the gel precursor drop(s) was sandwiched with another pretreated coverslip until the gel polymerizes. To functionalize the polymerized PA gel, 300 μL of sulfo-SANPAH (Thermo Scientific, 0.5 mg/mL in HEPES), was added to the gel and exposed for 7 min under 365-nm UV light (0.7 A, Spectroline Model XX-15A), and was washed twice in distilled H_2O. Collagen-I was diluted to 0.1 mg/mL in HEPES and incubated with the functionalized PA gel at 37°C overnight on a shaker. Excess collagen was removed and the gel was equilibrated in PBS. Cells were plated onto the gels within 24 hours of collagen attachment. Preliminary studies on the efficacy of sulfo-SANPAH as a collagen-PA gel crosslinker reveal that the collagen-1 concentration (0.1 mg/mL) used in all experiments here, as suggested by previous studies (Engler et al., 2004a; Lo et al., 2004), saturates all available reactive moieties on the PA gel and are covalently tethered to the PA gel (Figure 2.4C). These studies altogether indicate saturation of matrix ligands for cells, thus eliminating the possibility of cell rounding due to low ligand density.

2.4.2 Surface characterization and microrheology of hydrogels

Sirius Red dye (0.1% in H2O, Direct Red 80, Sigma) was stained (for 1 h, rinsed twice in 0.5% acetic acid) on embedded collagen fibers in the gel to determine their scar-mimesis. Elasticity of the gel surface, E_{surf}, was quantified with an Asylum MFP-3D Atomic Force Microscope (Asylum Research, Santa Barbara), equipped with a microscope stage micromanipulator to move across the gel during AFM probing. The spatial AFM resolution used here is 1 μm, which emulates cellular length scales in matrix sensing. A silicon nitride cantilever probe with pyramidal tip and spring constant of 30–100 pN/nm (MCST, Veeco) was used to indent the gels. To determine E_{surf}, the Hertz cone model was used to fit probe deflection curves (up to 1 μm indentation; Domke and Radmacher, 1998). In lateral pulling experiments (Figure 2.5), glass micropipettes were formed from glass capillaries (1-mm inner diameter, World Precision Instruments, Sarasota, FL) using a Flaming-Brown Micropipette Puller (Sutter Instrument, Novato, CA). Pulled micropipettes were tapered at the base, were reopened to a final inner diameter of 10 μm, and were used to probe the surface of gels, embedded with microbeads (1-μm diameter FluoSpheres, Invitrogen) as fiduciary markers. The glass probe was constantly displaced 20 μm parallel to the gel surface, and fluorescent bead displacements were acquired with a Nikon Eclipse TE300 inverted microscope equipped with Cascade Photometric CCD camera. Particle Image Velocimetry, an ImageJ plugin, was used to quantify fiduciary bead displacements after probe pulls. Analysis of displacement profiles is detailed in section A.2 of Appendix A.

2.4.3 Cell culture, manipulation, and treatments

R1 mouse embryonic stem cells (mESCs) with cardiac-specific puromycin resistance were kindly provided by Dr. Rong (University of Pennsylvania, Philadelphia). Fetal bovine serum (FBS) used in ESC growth and differentiation media was purchased from Hyclone. The mESCs were cultured on mitomycin-treated mouse embryonic fibroblast (MEF) feeder layers in supplemented Dulbecco Modified Eagle Medium (DMEM with 4.5 g/L glucose, 100 mM sodium pyruvate, 100 mM non-essential amino acids; 0.1 beta-mercaptoethanol; 15% Hyclone FBS; Leukemia Inhibitory Factor, LIF, 1000 u/L). Stem cells were spontaneously differentiated in embryoid bodies (EB) made from hanging drops of 600 cells per 20 μL in the same DMEM without LIF. After 2 days in hanging drops, EBs were transferred to rotating cultures for five days and were then seen to beat spontaneously. To isolate single cardiomyocytes (CMs) from EBs, 0.05% trypsin-EDTA (Gibco) was used to enzymatically dissociate EBs; the resulting cell suspension was quenched with differentiation media, pelleted, resuspended, plated on PA gels. After 24 hr, mESC-derived CMs were further purified by addition of 2.5 μg/mL puromycin in differentiation media for 7 days.

Racemic blebbistatin (EMD Biosciences) was used at 50 μM for 30 min. For knockdown experiments, Lipofectamine 2000 (Invitrogen) with 30 nM siRNA was used according to manufacturer's instructions. The level of knockdown was assessed by Western blotting after 48 hrs. Myosin-IIB siRNA duplex sequences were obtained from Raab et al. (2012) and were synthesized by Dharmacon, Inc. Scrambled siRNA was siGENOME Non-Targeting siRNA #1 (Dharmacon). To minimize experimental variability in durotaxis experiments, both scrambled and MIIB siRNA-treated MSCs were simultaneously seeded on the hybrid gels and their migrations were visually discriminated by prior minimal labeling with hydrophobic PKH26 and PKH67 dyes, respectively, according to manufacturer's (Sigma-Aldrich) instructions. Prior to plating into decellularized heart matrices, MSCs were transduced at passage 2 (50% confluency) with 300 PFU of lentivirus per cell for 24 hrs to stably express GFP. For osteogenesis experiments, sparsely-seeded MSCs ($\sim$2000 cells/cm^2) were allowed to reach

$\sim$70% confluency in normal media prior to addition of osteogenic induction media (OIM, StemXVivo Osteogenic/Adipogenic Base Media and Supplement, R&D Systems). Osteogenic cultures, with fresh media every 3–4 days, were done for 1 week or 4 weeks and evaluated for Alkaline-Phosphatase activity or Alizarin-Red staining, respectively (further details in Section 2.4.9).

Human THP-1 monocyte suspensions were maintained between 3×10^5–1.5×10^6 cells/mL in RPMI 1640 Medium (Gibco) with 10% FBS and 1% P/S. Differentiation of THP-1 cells into adherent macrophages was induced by addition of 100 ng/mL phorbol 12-myristate 13-acetate (PMA) for 2 days. Culture medium (without PMA) is freshly replaced every 2–3 days. Transition from suspended to surface-adhesive phenotype was concomitant with upregulation of nuclear lamins and matrix metalloproteinases (Figs. 2.15, 2.16 and 2.18).

Retinoic Acid Receptor (RAR) isoform-selective drugs used for cell treatment were: Adapalene and CD2665 (Santa Cruz Biotechnology), respective agonist and antagonist drugs for RARβ and γ isoforms only. All-trans retinoic acid (RA, Fisher Scientific) is a pan-RAR agonist; AGN-193109 (AGN, Santa Cruz Biotechnology) is a pan-RAR antagonist. Cell-on-gel cultures were treated with either control solution (0.15% ethanol, 0.15% DMSO in culture media), or with solution with 1 μM drug.

2.4.4 Proteomics analyses of mouse tissue

Mouse tissue was prepared for analysis as described by Swift et al. (2013b). Approximately 1 mm^3 of frozen muscle tissue was ground on dry ice and solubilized in 100 μL 1× NuPAGE LDS sample buffer (Invitrogen); samples were sonicated on ice before addition of 1% β-mercaptoethanol, followed by heating to 80 °C for 10 min. SDS-PAGE gels (NuPAGE 4-12% Bis-Tris, Invitrogen) were loaded with matched quantities of protein (determined by Coomassie densitometry), with separations run at 100 V for 10 min. followed by 160 V for 25 min. Gel bands were excised for mass spectrometry (MS) analysis between 60–150 kDa. Details of protein quantification by label-free MS are described by Swift et al. (2013a), with Elucidator software

(Rosetta Biosystems) set to search for the hydroxylation modifications that are common in matrix proteins (proline, asparagine, aspartic acid and lysine, Δ = +15.995 Da).

2.4.5 Bulk rheology

A cone-and-plate Bohlin rheometer (Malvern Instruments, Worcestershire, UK) was used to measure the viscoelastic spectrum (elastic modulus, G' and viscous modulus, G'') of the hydrogels as a function of frequency. In order to confirm polymerization had come to completion, a time sweep test was also performed for 20 minutes with a controlled absolute strain of 1% at an angular frequency of 1 rad/s. PBS was then added to allow complete swelling of the gel before a frequency test was conducted from 8 Hz down to 0.0008 Hz at 1.0% strain.

2.4.6 3D reconstruction & photobleaching in confocal microscopy

To visualize both PA gel and collagen-1 (Figure 2.2A), the gel precursor was doped with 0.02% w/v allylamine (Sigma) for subsequent fluorescein isothiocyanate (FITC, Thermo Scientific) conjugation, while collagen-1 coating covalently crosslinked with sulfo-SANPAH on the gel surface is indirectly immunolabeled (Alexa-647 fluorophore, Life Technologies). To delineate registration of collagen coating on polyacrylamide gels, a confocal microscope (FV1000, Olympus) equipped with a 40× objective (UPLFLN40XO, N.A. 1.3) was used. Pinhole size was set at 125 μm to generate an optimal slice thickness of 0.76 μm. Collagen coat is $\sim$5 μm on a fully hydrated hydrogel of $\sim$60–80-μm thickness as determined by 3D confocal stack reconstruction.

Fluorescence photobleaching was also performed (Figure 2.4Cii) to determine the extent of immobilization of the collagen-I coating on the gel surface. Fluorescence of the gel surface was imaged prior to bleaching. The confocal plane was localized on the gel surface as determined by collagen-I immunofluorescence, and the laser power was increased to maximum possible amount to photobleach a circular region of interest (ROI) for 60 seconds. Gel surface with the photobleached ROI was re-acquired for another 5 minutes. Even without sulfo-SANPAH crosslinking, photobleached collagen-1 remains relatively stable perhaps due to interpenetration into the porous gel surface.

2.4.7 Decellularized Embryonic Heart Matrix

Hearts were removed from chicken embryos at embryonic-day 14 (E14) and the left ventricle wall was isolated and immersed in 1% SDS in deionized water for decellularization. After shaking overnight at room temperature (RT), the decellularized tissue was placed into 1% Triton-X in deionized water for 30 min and then equilibrated in PBS with 100 μg/mL penicillin and 100 μM streptomycin until used for experiments. To make a gradient of crosslinks in the matrix, the decellularized tissue was fixed on a coverslip and then placed into a chamber such that approximately one half is immersed in 100% glycerol. After allowing glycerol to penetrate into the matrix for 30 min, 3 mM of genipin (a fluorescent crosslinker, Sigma) in PBS was added on top of the glycerol to immerse the other half of the matrix, and was then incubated in the dark at 37°C for 2 hours. Glycerol was then added to replace the top genipin solution, and the resulting matrix with a crosslink gradient was washed and stored in PBS with antibiotics prior to use.

2.4.8 Time-lapse Microscopy

Beating cardiomyocytes were quickly imaged (< 1 h) under HEPES-buffered (10 mM) phenol-red free DMEM (with 10% FBS and 1% P/S, Gibco) on a temperature-controlled (37 °C) microscope stage with an inverted microscope (IX-71, Olympus) equipped with a 20× LCACh objective (N.A. 0.40) and a Cascade CCD camera (Photometrics). Image sequences were acquired every 0.2 s.

Imaging of MSC migration was done using an inverted Olympus IX-71 microscope with a 10× objective enclosed in a humidified chamber at 37 °C and 5% CO_2, 300 W xenon lamp illumination, and a high-resolution CCD camera (Photometrics CoolSnap HQ). Deltavision Softworx software was used for image acquisition at 10-min intervals. ImageJ was used to track the center of MSC nuclei in movie sequences, and the summed contour distance traveled divided by the time was used as our measurement of mean speed. This measurement only reflects total distance traversed but does not reflect cell persistence. We quantified the bias of the time-dependent number of steps to the left (L, soft CC$_{0.3kPa}$ region) and to the right (R, scar-like$_{0.3kPa}$ region) by using the equation adapted from Isenberg et al. (2009):

$$\text{Durotaxis Index} = (R - L)/(R + L).$$

If Durotaxis Index = 0, there is no bias to cell migration. If Durotaxis Index = 1, all of the steps are toward the stiff side. Cells that underwent mitosis and those that migrated out of the trackable region were included only prior to such events.

To verify the hypothesis that MSCs with spread areas greater than 5000 μm^2 (i.e. high myosin content) sense and track the underlying scar-like fibers (Figure 2.9B), the angle difference between fitted ellipses that best approximate MSC and collagen fiber shape was calculated in ImageJ. In time-lapse sequences where MSCs overlap with an immunolabeled fiber, cells were discriminated based on average spread area during period of overlap and the respective angles were measured and tracked over time.

2.4.9 Histological analyses of osteogenic commitment

After 1 or 4 weeks in culture with osteogenic induction media (OIM), MSCs on gels were fixed at RT with 3.7% paraformaldehyde for 20 min and washed thrice in 10 mM Tris buffer (pH 7.2). For 1-week cultures, Alkaline Phosphatase (ALP, early osteogenic biomarker) activity was visualized by Fast Blue staining. While cells were being fixed, 2 mL of naphthol-AS-MX phosphate and one pre-weighed capsule of Fast Blue RR Salt (Sigma) were dissolved with stirring in 48 mL distilled water in the dark (Fast Blue Solution). Fixed cultures were then immersed in Fast Blue Solution for 30 min, subsequently washed in distilled water twice, and imaged immediately or mounted in aqueous mounting media for storage.

For 4-week cultures with OIM, Alizarin Red (late osteogenic biomarker) staining was performed. Cultures were fixed with 10% paraformaldehyde for 10 min, washed with PBS twice, and stained with 2% Alizarin Red S (Sigma) solution for 15 min, all at RT. Staining-solution pH was pre-adjusted to ∼4.1–4.3 with 0.5% ammonium hydroxide. Samples were then washed with distilled water and imaged immediately (or stored accordingly). Samples were imaged using an inverted microscope (IX-71, Olympus) with a 4× objective and a USB-compatible digital color camera (DC2000M; World Precision Instruments, Inc.) attached to the microscope c-mount tube. Color images were acquired using ScopePhoto software (ScopeTek) and were processed in ImageJ by converting to 32-bit black and white images, inverting, and measuring raw intensities. Osteogenic indices for images from both ALP and Alizarin Red-stained samples were calculated from these raw intensities, and normalized to cell cultures under serum-only conditions.

2.4.10 Combined Fluorescence *In Situ* Hybridization (FISH) and Immunofluorescence Microscopy

This method was developed with multiple singly-labeled fluorescent RNA probes by Dr. Arjun Raj (University of Pennsylvania) adapted here to simultaneously detect lamin-A expression in the mRNA and protein levels *in situ*. Reagents were kindly provided by Dr. Raj. Detailed probe-synthesis and hybridization protocols were developed by Raj et al. (2008). Labeled samples were visualized in the same setup as time-lapse microscopy movie sequences, but with a 100× objective with high numerical aperture to achieve a narrow depth of field and discriminate diffraction-limited mRNA spots during image processing. Roughly 40 z-stack images per cell were obtained to fully encompass cell height. Spot counting was performed in ImageJ, by manually thresholding spot intensities and counting speckles that are in the expected diffraction limited range of 0.2–0.5 microns in diameter. Counts of mRNA spots reported here may be an overestimate due to the choice of imaging and image processing. Nonetheless, good mRNA-protein correlations in LMNA-knockdown experiments (Figure 2.12B) validated the technique. LMNA siRNA was obtained from Harada et al. (2014) and transfected into MSC cultures with Lipofectamine as per manufacturer's instructions.

2.4.11 Gelatin Zymography

To detect matrix metalloproteinase (MMP) secretion during PMA-induced THP-1 differentiation, gelatin zymogram gels (Life Technologies) were loaded with conditioned media samples harvested from THP-1 cultures at desired time points and treatments. Prior to loading conditioned medium was diluted 1:1 with Tris-Glycine loading buffer (Life Technologies), and immediately loaded into a well. Loaded gels were run in Tris-Glycine running buffer (Life Technologies) for 120 min. Cell number was used as normalization.

To visualize MMPs, samples in gels were renatured and developed according to manufacturer's instructions (Life Technologies). Finally, gels were stained with SimplyBlue SafeStain (Life Technologies) and scanned for image processing in ImageJ software. MMP bands on the gels appeared light on a blue background, where enzymatic degradation of embedded gelatin occurred.

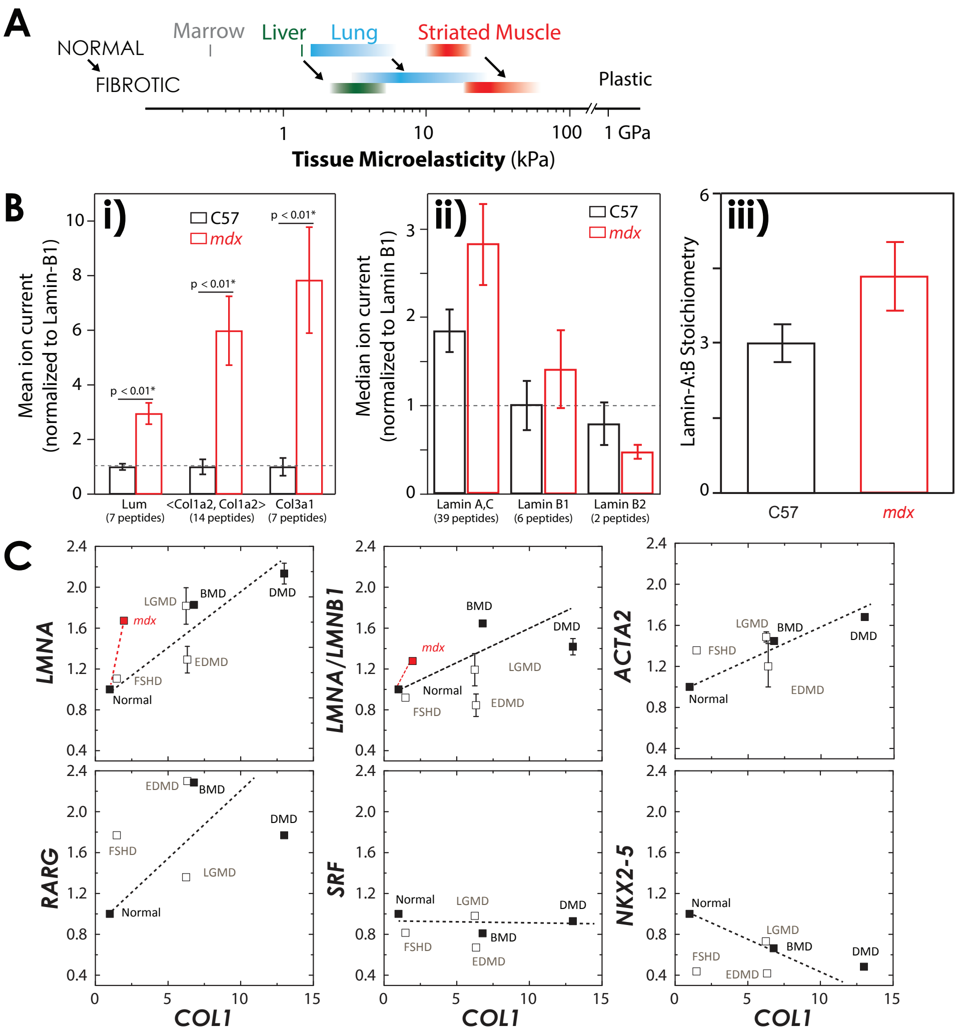

Figure 2.1. Mechanics, transcriptional and proteomic profiling of muscular dystrophy tissue. **A**, Fibrosis-associated stiffening and heterogeneity is consistently seen across tissues with abundant collagen such as liver (Georges et al., 2007), lung (Liu et al., 2010) and striated muscle (Berry et al., 2006; Engler et al., 2007). **B**, Consistent with earlier findings in adult mouse tissue (Swift et al., 2013b) and developing chick embryo (Majkut et al., 2013), correlations were observed between lamin A in the nucleus and the composition of the ECM. Quantification of matrix proteins in mouse muscle tissue by label-free mass spectrometry (MS). i) The signal strength of each ECM protein was normalized by lamin B1 to account for cell-density variations between samples; mdx mouse tissue is shown relative to a control of C57 mouse tissue (y-axis shows fold-change). A Kruskal-Wallis location equivalence test showed the mdx mouse to have significantly more lumican, collagen-1 and collagen-3 than the control ($p < 0.01$; $n = 4$). ii) MS measurements also suggested that *mdx* mice had correspondingly higher lamin A,C and iii) lamin A-to-B stoichiometry ($n = 4$, not significant). **C**, At the transcript level, tissue samples from patients with muscular dystrophy and mouse muscular dystrophy models showed higher mean *COL1* and (Top) correspondingly higher *LMNA*, even when normalized to *LMNB1*, another nuclear envelope gene; *ACTA2*, a cytoskeleton gene, is expectedly upregulated in response to stiffening. Bottom, Transcription factors relevant in mechanotransduction pathways either scale with (*RARG*), scale against (*NKX2-5*), or does not scale (*SRF*) with *COL1*.

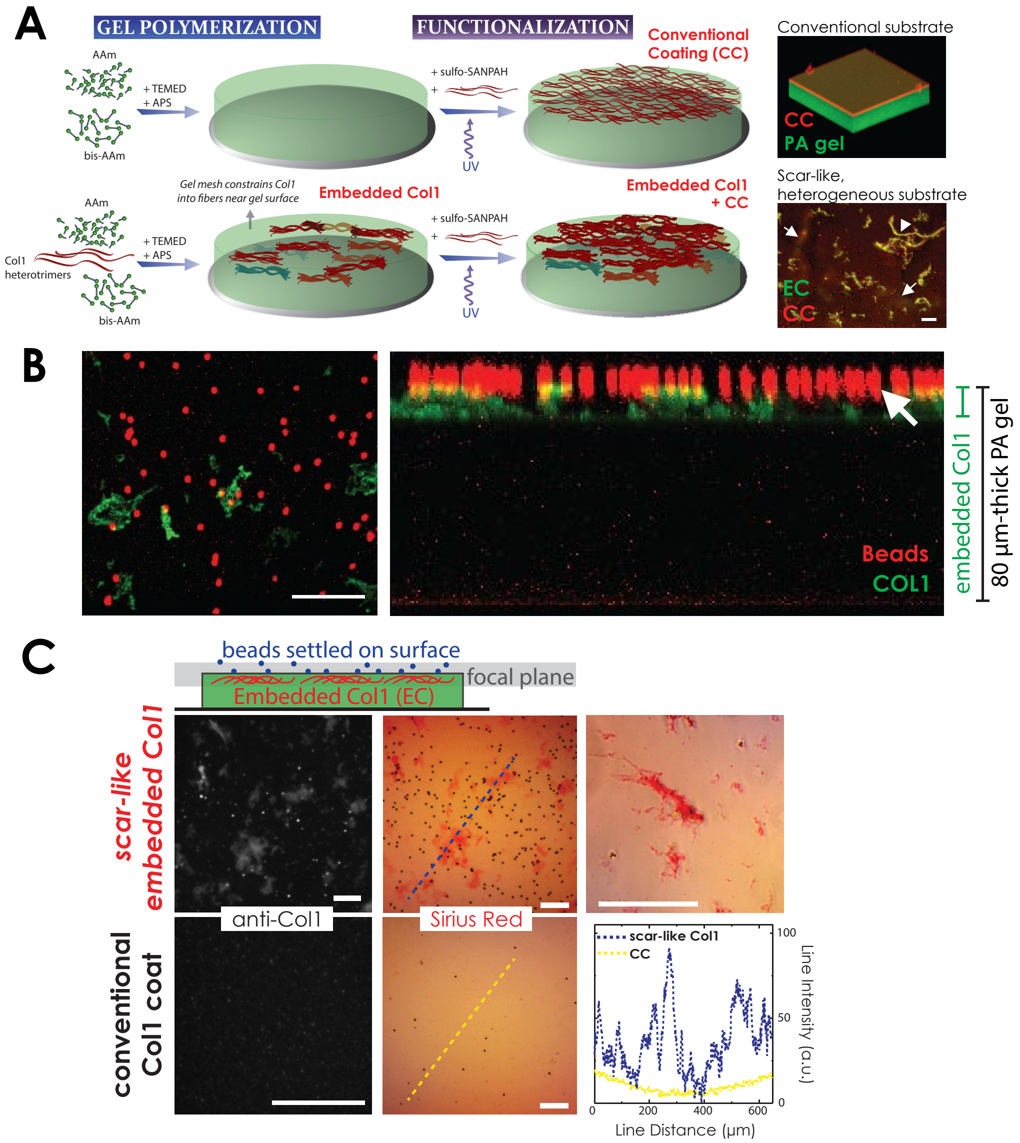
A
GEL POLYMERIZATION
FUNCTIONALIZATION
Conventional Coating (CC)
Conventional substrate
AAm
+TEMED
+APS
bis-AAm
+ sulfo-SANPAH
+
UV
CC
PA gel
Gel mesh constrains Col1 into fibers near gel surface
Embedded Col1
Embedded Col1 + CC
Scar-like, heterogeneous substrate
Col1 heterotrimers
EC
CC
B
Beads
COL1
embedded Col1
80 µm-thick PA gel
C
beads settled on surface
focal plane
Embedded Col1 (EC)
scar-like embedded Col1
conventional Col1 coat
anti-Col1
Sirius Red
scar-like Col1
CC
Line Intensity (a.u.)
100
50
0
0
200
400
600
Line Distance (µm)

Figure 2.2. Synthesis and characterization of a 'scar in a dish'. A, (Top panel) Schematic of free radical polymerization of a polyacrylamide (PA) hydrogel and functionalization with collagen-I (Col1) matrix. (Top, right) PA gel (green) with coated Col1 (CC, red) reconstructed from confocal image stacks (365 μm × 365 μm surface, ~80 μm height). (Bottom panel) Incorporating 400 μg/mL of Col1 during polymerization creates an embedded-Col1 (EC) PA gel that mimics a scar-like matrix. (Bottom, right) Pore-size directed fibrillogenesis of EC (green) in CC (red) PA gel. Most Col1 fibers localize near the surface (arrowhead), while some are embedded (arrows). **B**, (Left) Top view of EC-PA gel with 1-μm fluorescent beads (red) to delineate gel surface. (Right) EC fibers (green) localize as a heterogeneous thin film within ~10 μm near the gel surface (arrow). **C**, Schematic: EC fibers in the same focal plane as beads settled on the gel surface. Immunolabeled EC fibers (top, left) stain positive for Sirius Red (top, middle). Higher magnification of Sirius Red-positive EC fibers (top, right). CC gels (bottom) have no significant Sirius Red staining, as revealed by line intensity scans (bottom, right). Scale bars, 100 μm.

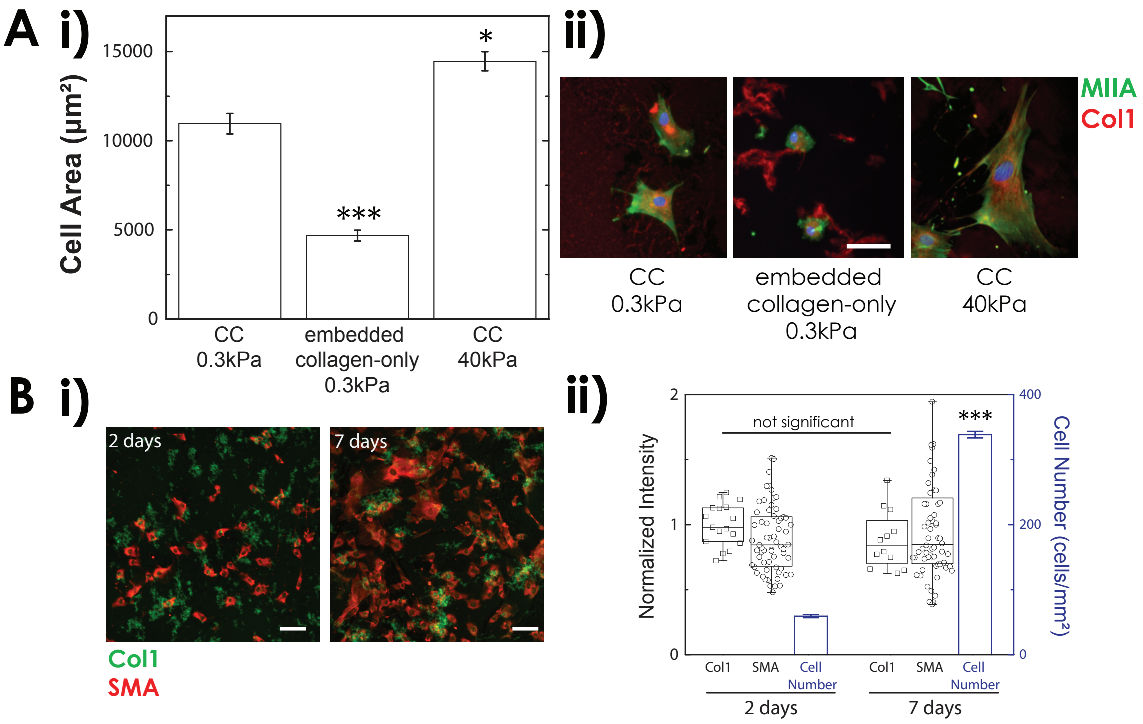

Figure 2.3. Embedded collagen is stable but does not induce cell spreading alone on soft gel. **A**, i) MSC cell area (mean ± s.e.m.) on soft ($\text{CC}_{0.3kPa}$) and stiff (CC_{40kPa}) gels are significantly higher than on scar-like EC gel without CC (EC-only 0.3kPa gel). ii) Myosin IIA (MIIA, green) and Collagen-1 (Col1, red) immunofluorescence of MSCs on gels. $^{*}p < 0.05$, $^{***}p < 0.001$, compared to cells on $\text{CC}_{0.3kPa}$ gel. **B**, i) Immunofluorescence images of α-smooth muscle actin (SMA, red) in MSCs on $\text{scar-like}_{0.3kPa}$ gel cultured for 2 (left) and 7 (right) days show that EC (green) is stable in the gel. ii) Cell number (blue) increases from 2 to 7 days, while SMA/cell and embedded Col1 remains the same. $^{***}p < 0.001$, compared to 2 days on $\text{scar-like}_{0.3kPa}$ gel. Scale bars, 100 μm.

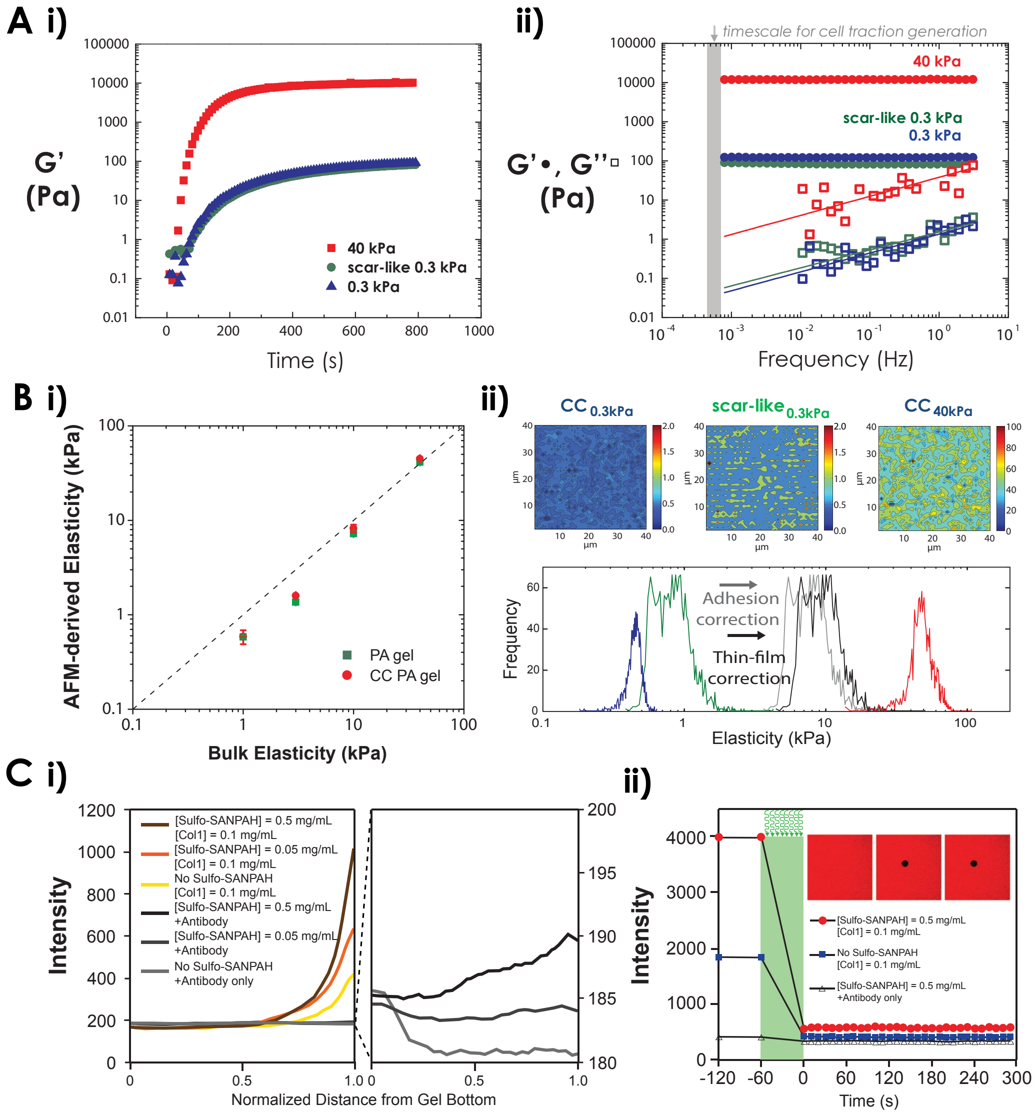

Figure 2.4. Bulk and surface rheology, and functionalization of PA gel. **A**, i) Time-sweep measurements of bulk elastic moduli of various PA gels; embedding collagen-1 (0.4 mg/mL; scar-like$_{0.3kPa}$, green) did not augment the nominal elastic modulus of 0.3 kPa (blue). ii) Bulk elastic (G') and viscous (G'') moduli of PA gels measured via cone-plate rheometry at frequencies (0.0008–8 Hz) and strain (1%) that mimic cell traction forces (grey area; Engler et al., 2004a). **B**, Atomic force microscopy (AFM) measurements of i) E of bare PA (green) and CC-PA (red) gels. ii) (Top panel) AFM-derived elasticity maps (40 μm×40 μm) of gel surfaces. (Bottom) E values of CC$_{0.3kPa}$ gels (blue), scar-like$_{0.3kPa}$ (mean $E \approx$ 0.8 kPa, green), and CC$_{40kPa}$ (red) gels. Adhesion (grey) and thin-film corrections (black) predict an order-of-magnitude higher stiffness (see Appendix A.1). **C**, i) (Left) Covalent Col1 attachment on a 3-kPa PA gel depends on Sulfo-SANPAH. Bound Col1 is measured via immunofluorescence from confocal stacks through the gel. (Right) Absence of Col1 (only Col1 Antibody) shows some Sulfo-SANPAH binding and diffusion of fluorescent antibodies in the gel. ii) Photobleaching of immunolabeled Col1 coated via covalent crosslinking (red) or pure adsorption (blue) showed no recovery.

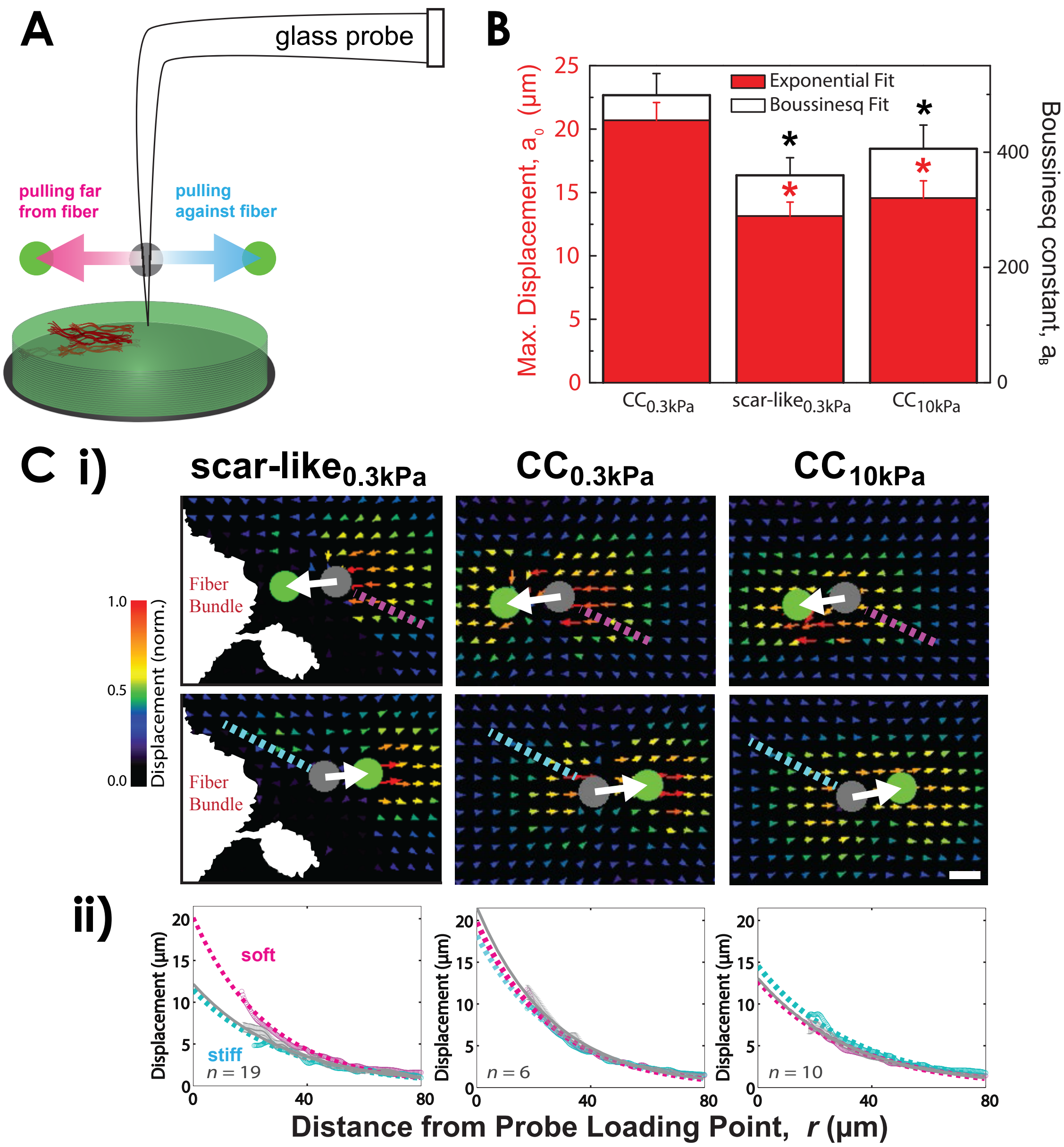

Figure 2.5. Lateral pulling microscopy reveals the heterogeneity of scar-like$_{0.3kPa}$ gel. **A**, Lateral pulling in scar-like EC gels indicate heterogeneous Boussinesq-like displacement profiles by tracking movement of embedded microbeads in the gels. **B**, Fit constants of surface pulling profiles assuming exponential decay (red, $a_0 e^{-br}$) or classic Boussinesq decay (black, a_B/r; Landau and Lifshitz, 1986). Pulling profiles of scar-like$_{0.3kPa}$ fibers behave similar to those of CC$_{10kPa}$ gels. $^*p < 0.001$ (red), 0.05 (black); compared to CC$_{0.3kPa}$ gel. **C**, i) Representative lateral pulls on scar-like$_{0.3kPa}$ (left), CC$_{0.3kPa}$ (middle) and CC$_{10kPa}$ (right) gels. ii) Pulling against an EC fiber bundle in scar-like$_{0.3kPa}$ gel shows smaller bead displacements (left, cyan and grey) similar to a stiffer 10-kPa gel (right). Pulling far from a bundle (left, magenta) has a displacement profile similar to a 0.3-kPa gel (center). Grey curves are averaged profiles from n pullings. Scale bar, 10 μm.

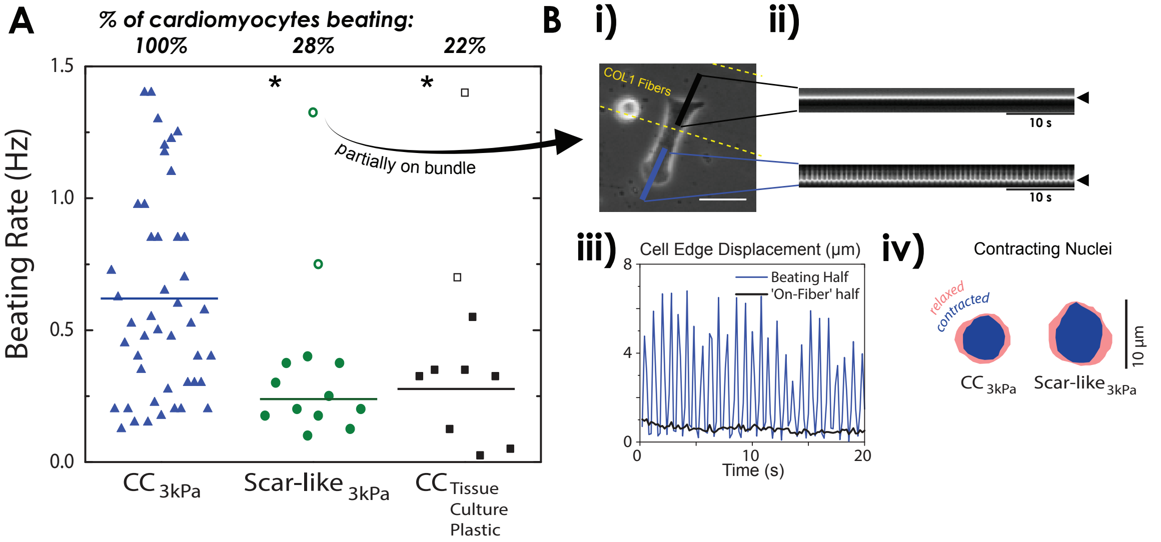

Figure 2.6. Stem cell-derived cardiomyocytes beat less on scar-like gel. A, Decreased beating rate of embryonic stem cell-derived cardiomyocytes (SCD-CM) on scar-like$_{3kPa}$ and CC-Tissue Culture Plastic versus CC$_{3kPa}$ PA gel (n = 13–40 cells, $^*p < 0.05$ when compared to CC$_{3kPa}$ gel). Unfilled data points indicate cells are only partially beating. Solid lines indicate means, excluding unfilled points. **B**, i) A half-beating SCD-CM on scar-like$_{3kPa}$ gel, standard deviation of movement (red) shows only the bottom half is beating, away from the region of scar-like fibers (yellow). Scale bar, 20 μm. ii) Kymographs along solid lines drawn on beating (blue) and non-beating (black) halves of the cell. iii) Cell edge displacement cycles over time on the beating half (blue), while it remains static on fiber-rich half (black). iv) Nuclei also contract, which could change nuclear phenotype.

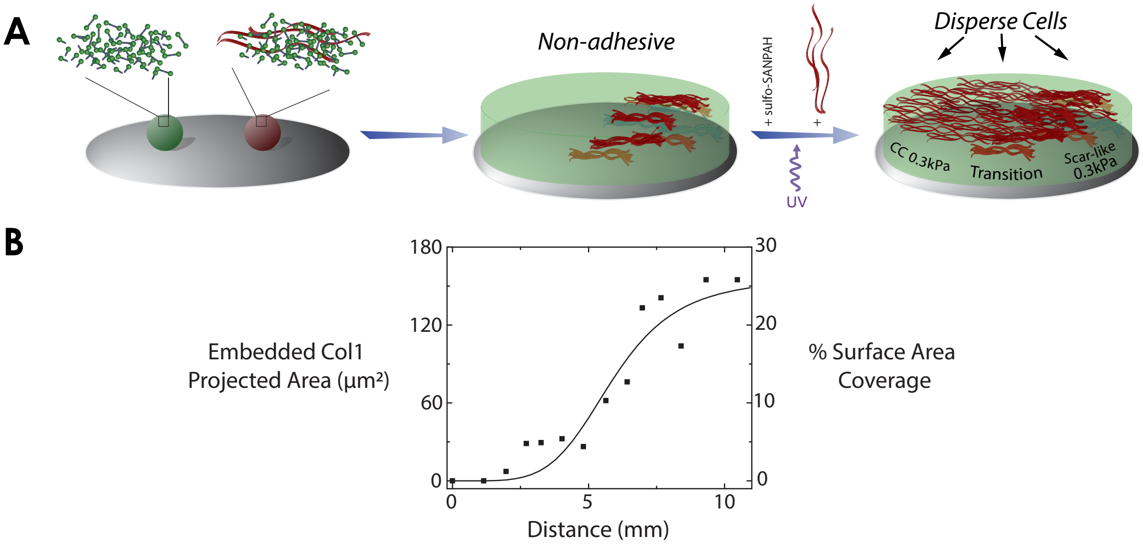
A
Non-adhesive
+ sulfo-SANPAH
+
UV
Disperse Cells
CC 0.3kPa
Transition
Scar-like 0.3kPa
B
Embedded Col1 Projected Area (μm²)
% Surface Area Coverage
180
120
60
0
30
20
10
0
0
5
10
Distance (mm)

Figure 2.7. Synthesis of a scar-like gradient gel. **A**, Schematic of making a hybrid CC$_{0.3kPa}$/scar-like$_{0.3kPa}$ gel with both nonfibrillar and scar-like regions, as an *in vitro* system to study MSC durotaxis. **B**, Quantification of Sirius Red staining along the transition region of CC$_{0.3kPa}$/scar-like$_{0.3kPa}$ hybrid gel shows a 2–3 mm gradient of fiber bundles that saturates to a 20–30% surface coverage.

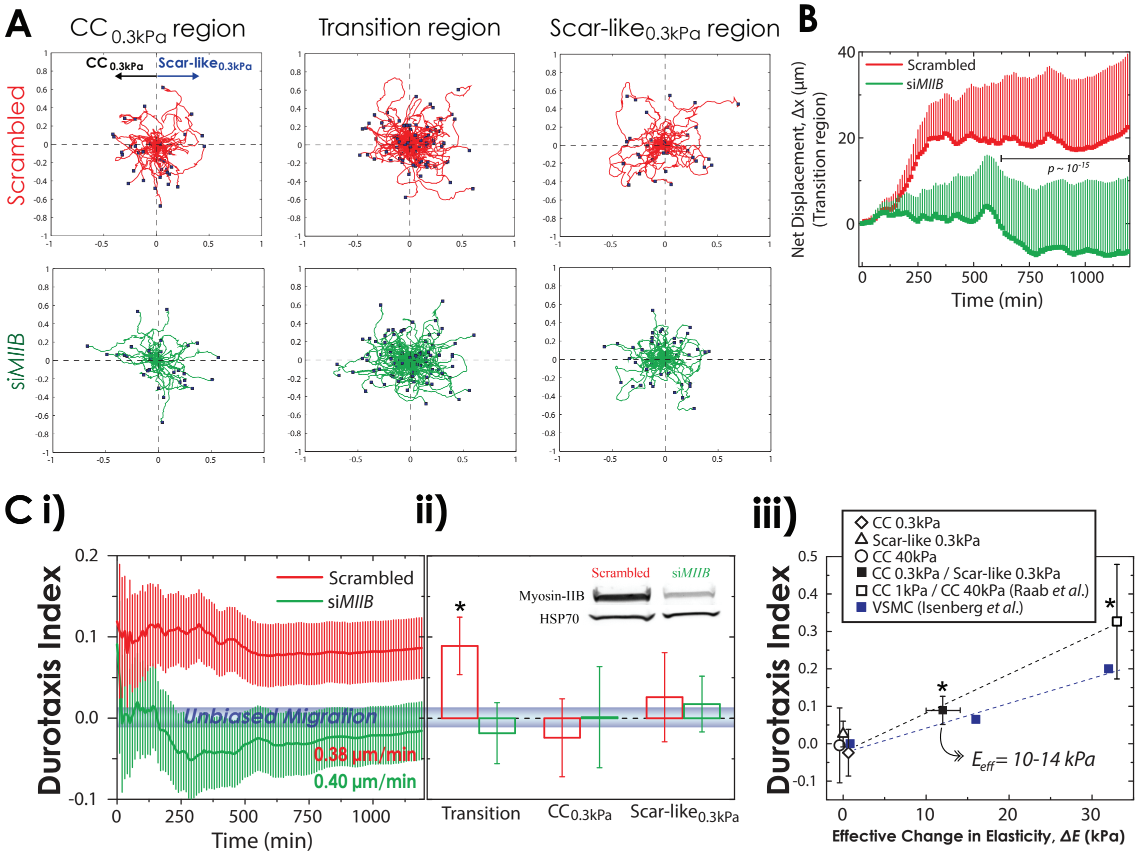

Figure 2.8. MSC durotaxis on a gradient of scar-like fibers. **A**, Normalized migration trajectories and final positions (squares) of scrambled or myosin IIB-siRNA–treated MSCs on $\text{CC}_{0.3kPa}$/scar-like$_{0.3kPa}$ hybrid gel after 20 hrs of imaging. Durotaxis occurs if more cells move to scar-like$_{0.3kPa}$ side (right) more than the $\text{CC}_{0.3kPa}$ side (left). **B**, Net positive displacement (mean $\pm$ s.e.m.) of MSC migration in the transition region toward scar-like$_{0.3kPa}$ region over time. Statistical difference between scrambled (green) and myosin-IIB knockdown (red) was determined by two-way analysis of variance with Tukey's HSD test at α = 0.05 significance level. **C**, i) Durotaxis index over time of MSCs treated with either scrambled (red) or nonmuscle myosin-IIB siRNA (siMIIB, green) on the 'Transition' region of the hybrid gel. No significant change in mean speed was seen in both scrambled (0.38 μm/min) and siMIIB-treated MSCs (0.40 μm/min). ii) Average durotaxis indices (mean $\pm$ s.e.m.) of scrambled and siMIIB-treated MSCs on various regions of the hybrid gel ($^*p < 0.05$, when compared to siMIIB). Inset: Western blot of siRNA-treated cells indicating 75% reduction of myosin IIB. iii) Durotaxis index versus effective elasticity change ΔE on the different hybrid hydrogel systems. The monotonic increase of Durotaxis Index with increasing gradient strength has been found previously for vascular smooth muscle cells (VSMC, Isenberg et al., 2009); thus, ΔE for $\text{CC}_{0.3kPa}$/scar-like$_{0.3kPa}$ hybrid gel fits around ~10–14 kPa.

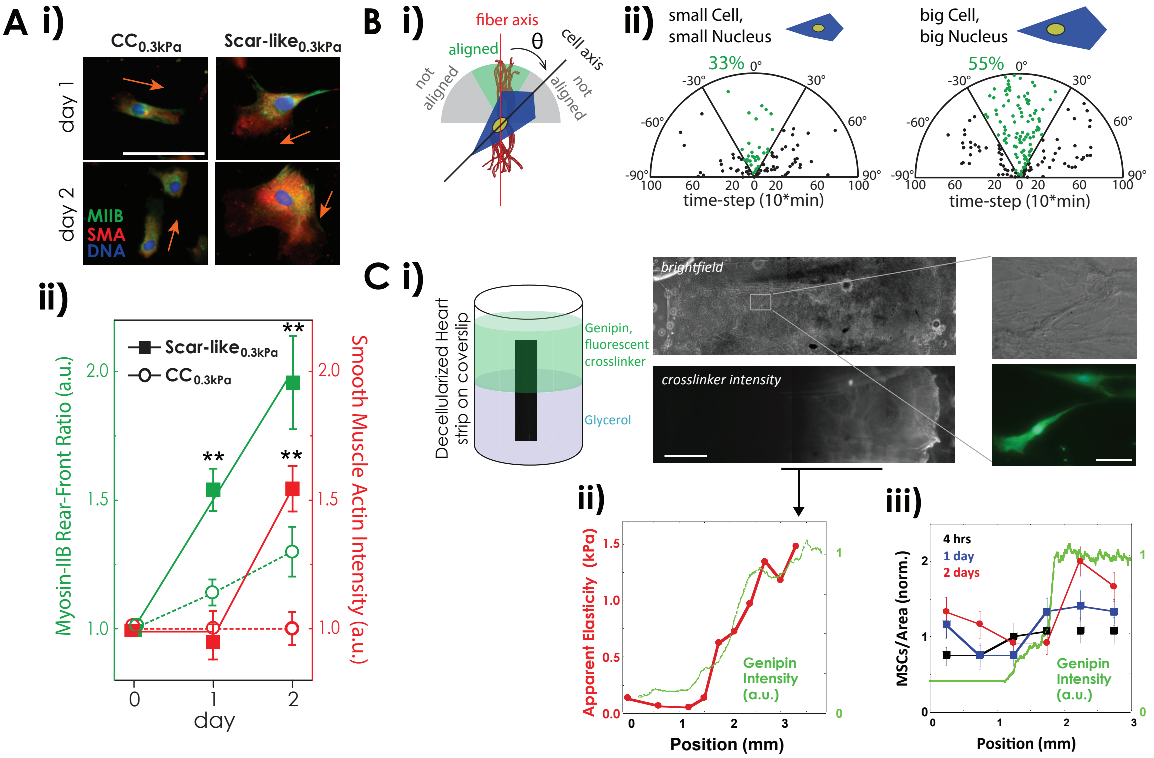

Figure 2.9. Human MSCs home toward a 'scar in a dish' and crosslinked heart matrix *ex vivo*. **A**, i) Immunofluorescence images of myosin IIB (MIIB, green) and α-smooth muscle actin (SMA, red) at 1 and 2 days after seeding MSCs on the hybrid gel. DNA, blue. ii) Kinetics of SMA (red) and MIIB rearward polarization (green) of MSCs on CC$_{0.3kPa}$ (circle) or scar-like$_{0.3kPa}$ (square) side of the transition region (n = 34–89 cells). $^{**}p < 0.01$, when compared to CC$_{0.3kPa}$ side of the gradient. **B**, i) Alignment between a migrating MSC and an EC fiber based on the angle difference, θ, of their respective major axes. ii) Real-time tracking of θ in small MSCs (mean cell/nuclear spread area <5000/<400 μm^2, n = 8 cells) and iii) big MSCs (>5000/>400 μm^2, n = 8 cells). **C**, i) (Left) Decellularized strip of a chick embryonic day-13 left ventricular wall supported on a coverslip, is half-dipped in a solution of a fluorescent protein-crosslinker, Genipin. (Right) MSCs expressing GFP (green) migrate within the matrix. Scale bar, 50 μm. ii) Gradient in Genipin-fluorescence intensity for the indicated region matches the measured gradient in apparent matrix elasticity measured by AFM. iii) MSCs in the *ex vivo* matrix are plated homogeneously, but after 1–2 days, cells accumulate on the highly cross-linked side of the matrix.

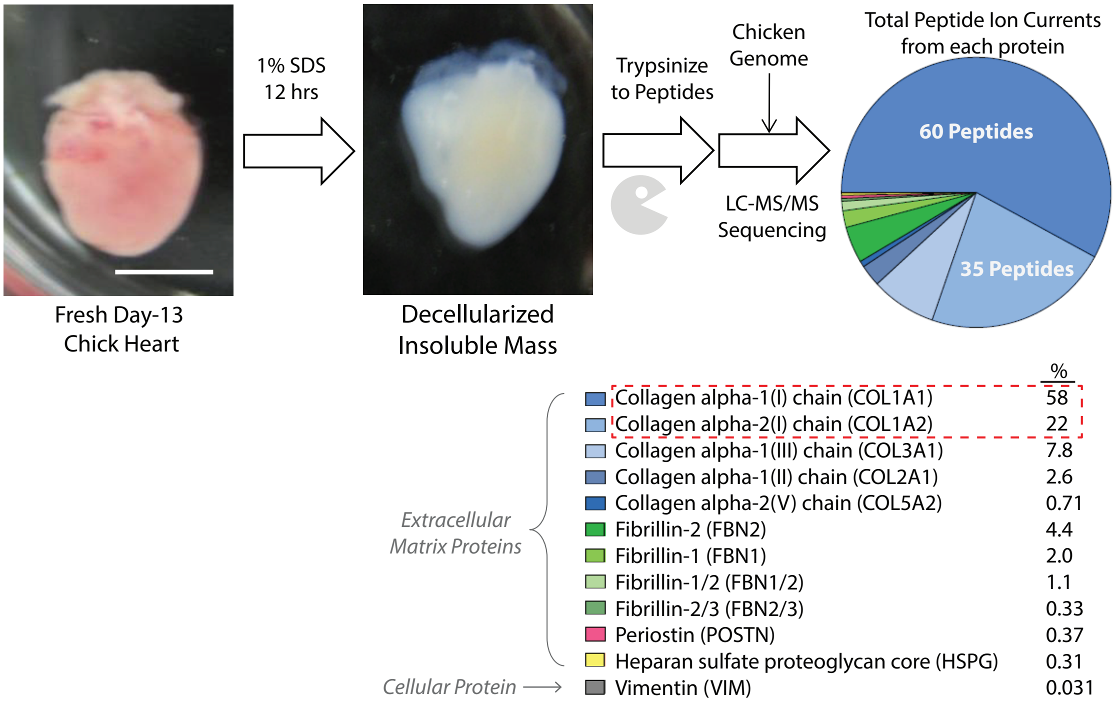

		%
🟦	Collagen alpha-1(I) chain (COL1A1)	58
🟦	Collagen alpha-2(I) chain (COL1A2)	22
🟦	Collagen alpha-1(III) chain (COL3A1)	7.8
🟦	Collagen alpha-1(II) chain (COL2A1)	2.6
🟦	Collagen alpha-2(V) chain (COL5A2)	0.71
🟩	Fibrillin-2 (FBN2)	4.4
🟩	Fibrillin-1 (FBN1)	2.0
🟩	Fibrillin-1/2 (FBN1/2)	1.1
🟩	Fibrillin-2/3 (FBN2/3)	0.33
🟥	Periostin (POSTN)	0.37
🟨	Heparan sulfate proteoglycan core (HSPG)	0.31
⬛	Vimentin (VIM)	0.031

Figure 2.10. Matrix composition of decellularized embryonic chick heart. Decellularized day-13 embryonic chick heart that was trypsin-digested and sequenced in Mass Spectrometry revealed the compositional breakdown of extracellular matrix proteins, which was dominated by Collagen-1 based on total peptide ion current. Scale bar, 2 mm.

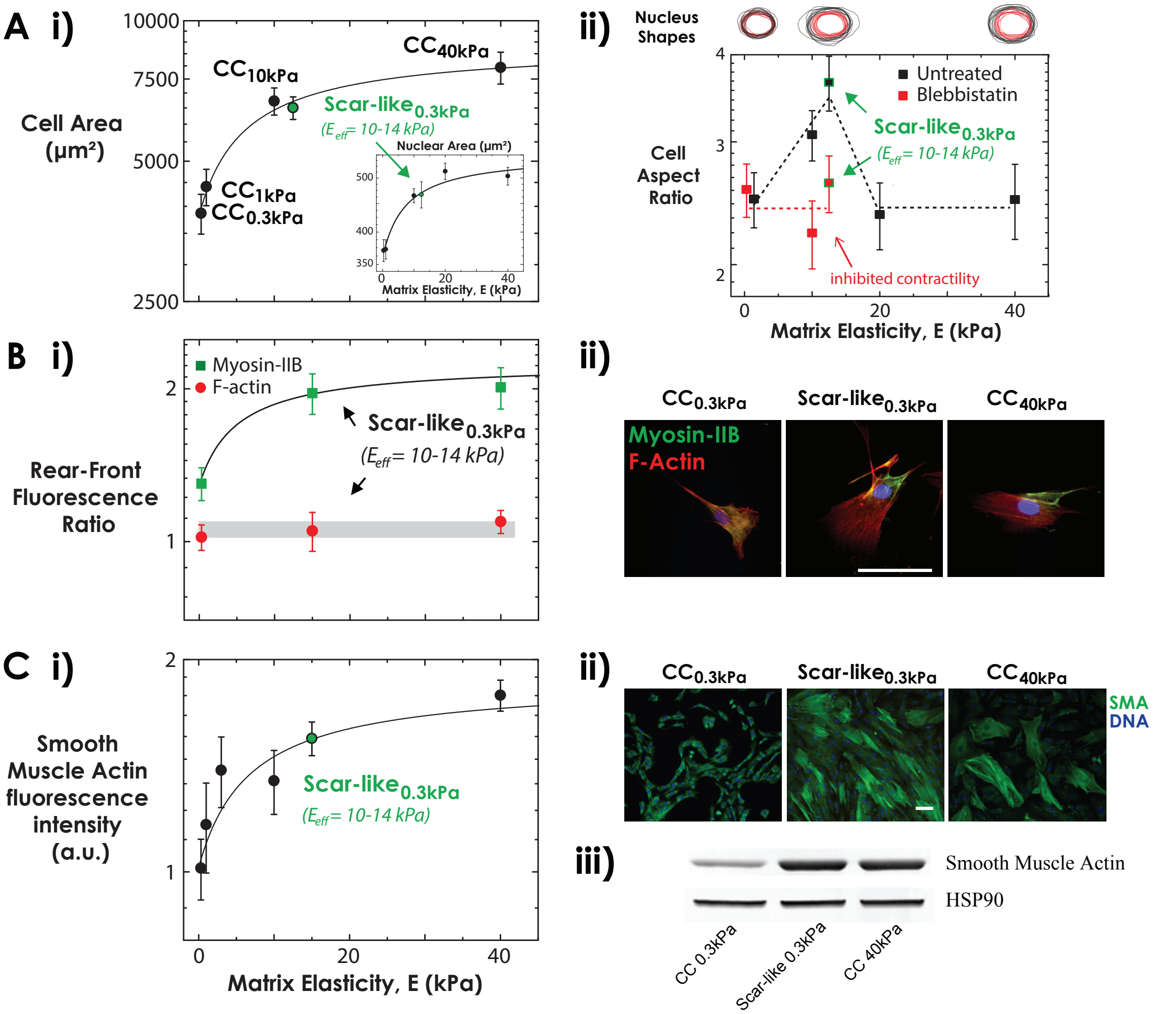

Figure 2.11. Scar-like$_{0.3kPa}$ gel exceeds the threshold for matrix stiffness-dependent MSC response despite heterogeneity. Morphological and cytoskeletal effects of matrix elasticity, E, are fitted with a hyperbolic equation: $A + BE/(E_m + E)$ using a characteristic elasticity constant, E_m = 9.2 kPa (Rehfeldt et al., 2012). **A**, i) Matrix elasticity-dependent cell (A = 3797 μm^2, B = 5064) and nuclear (inset; A = 360 μm^2, B = 191) spread area and ii) aspect ratio are quantified (mean $\pm$ s.e.m.) from myosin-IIA immunofluorescence staining of MSCs cultured for 2 days on gels. Nucleus shapes (top) are derived from DNA-stained nuclei. Myosin-II ATPase activity was inhibited with blebbistatin (50 μM, red) for 30 minutes prior to fixation. **B**, i) Quantification of rear/front immunofluorescence intensity (mean $\pm$ s.e.m.) of myosin IIB (MIIB; A = 1.29, B = 0.96) and F-actin. ii) MIIB polarizes toward the rear of a migrating MSC on both scar-like$_{0.3kPa}$ and CC$_{40kPa}$ gels, while F-actin (red) remains ubiquitous and non-polarized. **C**, i) Quantification of immunofluorescence staining (mean $\pm$ s.e.m.) of α-smooth muscle actin (SMA; A = 1, B = 1.17) 2 days after cell seeding. ii) SMA (green) incorporates into stress fibers over 7 days on both scar-like$_{0.3kPa}$ and CC$_{40kPa}$, but not on CC$_{0.3kPa}$. DNA, blue. iii) Western blot of SMA in MSCs cultured for 7 days on the gels. Goodness of fits, R^2 $\geq$ 0.95. Scale bars, 100 μm.

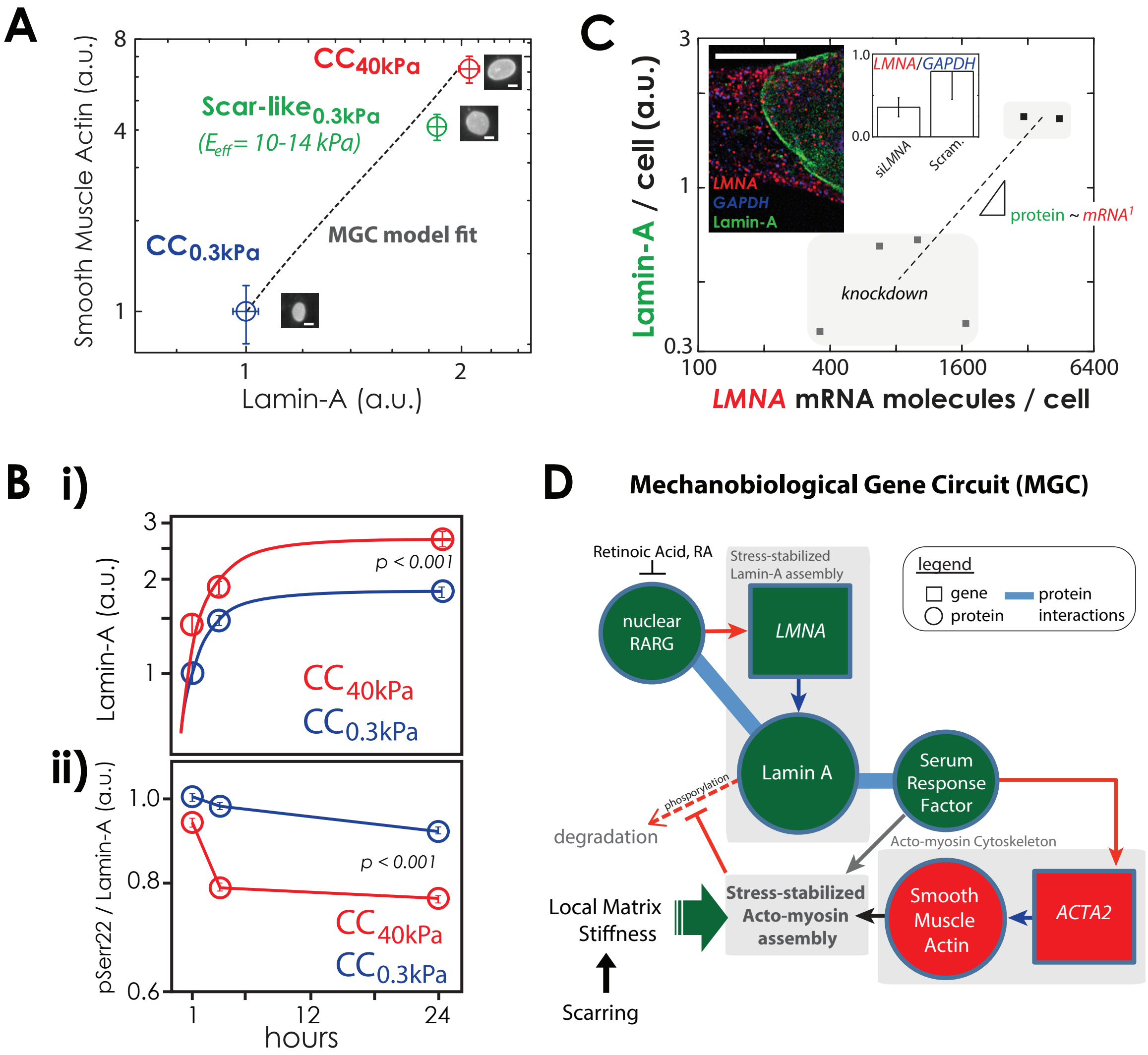

Figure 2.12. Local matrix stiffening couples lamin-A and α-smooth muscle actin (SMA) upregulation, as modeled in the Mechanobiological Gene Circuit. **A**, Quantitative immunofluorescence of SMA and lamin-A expression in MSCs cultured for 7 days on gels (mean ± s.e.m.) revealed tight coupling of cytoskeletal and nucleoskeletal tension as predicted by the Mechanobiological Gene Circuit (MGC) model (dashed line, see Chapter 4). Inset: Representative immunofluorescence images of lamin A. **B**, Kinetics of i) total lamin-A and ii) serine-22 phosphorylation levels (pSer22/Lamin-A) on soft vs stiff gels. **C**, Combined fluorescence *in situ* hybridization (FISH) and immunofluorescence (inset image) of MSCs showed lamin-A mRNA (*LMNA*, red) spot counts correlate with protein expression (green). (Inset plot) *LMNA* normalized to *GAPDH* mRNA spots (blue) indicate extent of knockdown. Scale bars, 10 μm. **D**, MGC predicts that scarring, which leads to local increases in matrix stiffness, can couple and stress-stabilize cytoskeletal and nucleoskeletal tension. Retinoic acid (RA) disrupts stress-stabilized lamin-A (and downstream-SMA) assembly through retinoic acid receptor-γ (RARG) (Swift et al., 2013b; Figure 2.13).

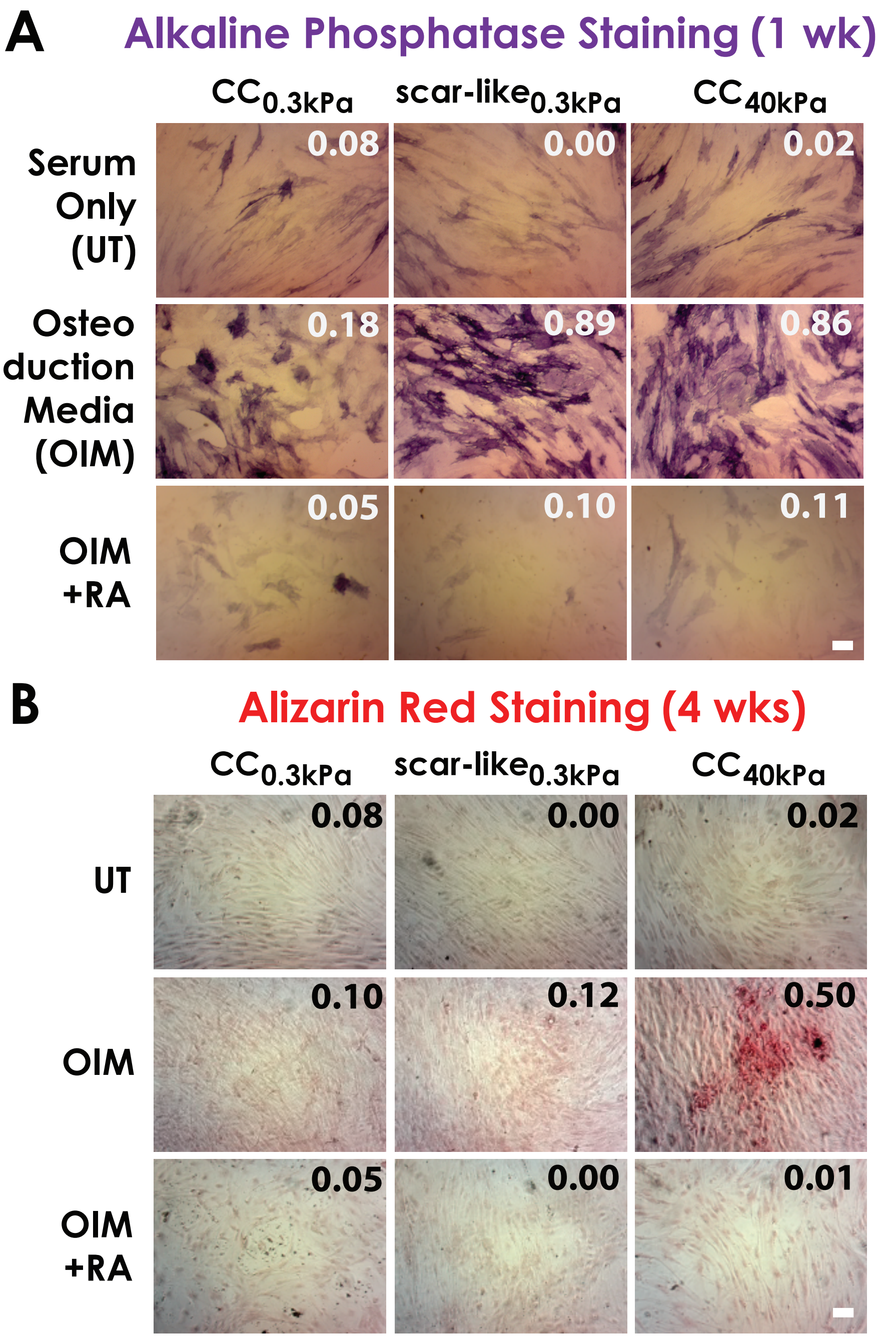
A
Alkaline Phosphatase Staining (1 wk)
CC0.3kPa
scar-like0.3kPa
CC40kPa
Serum Only (UT)
0.08
0.00
0.02
Osteo Induction Media (OIM)
0.18
0.89
0.86
OIM +RA
0.05
0.10
0.11
B
Alizarin Red Staining (4 wks)
CC0.3kPa
scar-like0.3kPa
CC40kPa
UT
0.08
0.00
0.02
OIM
0.10
0.12
0.50
OIM +RA
0.05
0.00
0.01

Figure 2.13. Matrix stiffness, but not retinoic acid (RA), induces MSC osteogenesis. A, MSCs on gels cultured in osteogenic induction media (OIM) with or without RA (1 μM) for 1 wk and stained for Alkaline Phosphatase (ALP), an early marker of osteogenic commitment. **B**, MSCs on gels cultured for 4 wks and stained for Alizarin Red, a late marker for bone. Osteogenic indices (see Section 2.4.9 of Materials and Methods) are relative to serum only-treated (UT) scar-like$_{0.3kPa}$ gels. Scale bars, 100 μm.

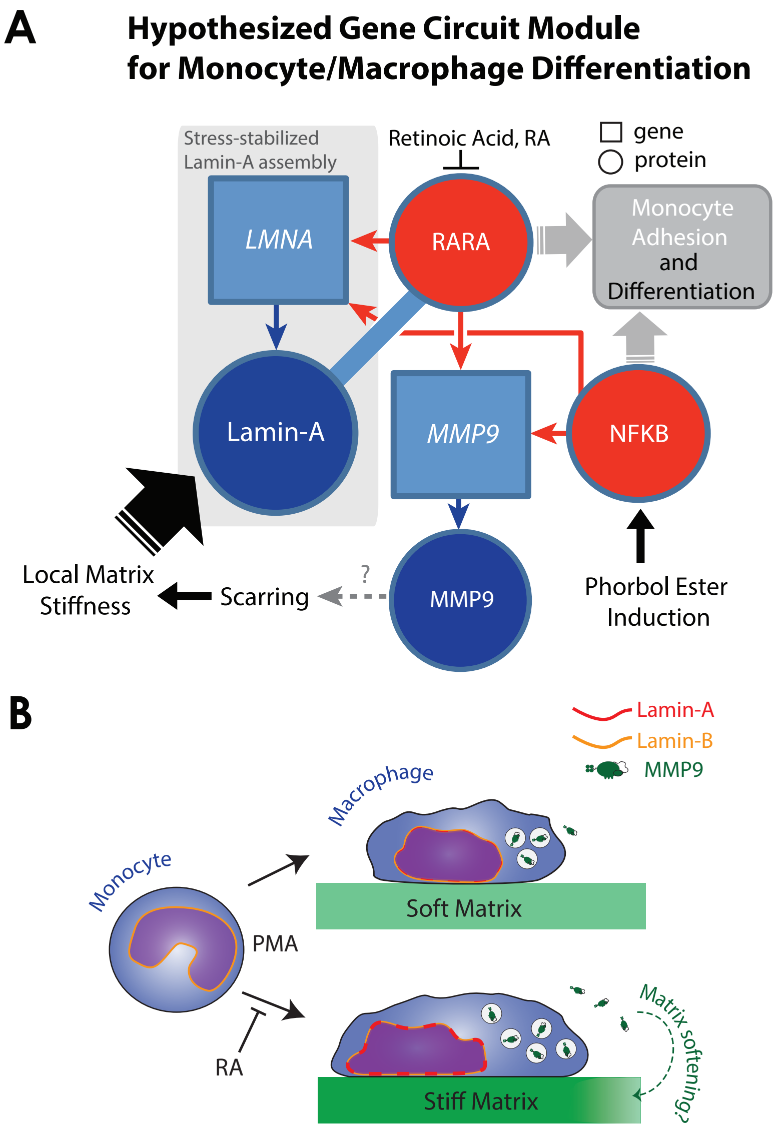
A
Hypothesized Gene Circuit Module
for Monocyte/Macrophage Differentiation
Stress-stabilized
Lamin-A assembly
Retinoic Acid, RA
☐ gene
○ protein
LMNA
RARA
Monocyte
Adhesion
and
Differentiation
Lamin-A
MMP9
NFKB
Local Matrix
Stiffness
Scarring
?
MMP9
Phorbol Ester
Induction
B
Lamin-A
Lamin-B
MMP9
Macrophage
Monocyte
PMA
RA
Soft Matrix
Matrix softening?
Stiff Matrix

Figure 2.14. Mechanochemical control of monocyte-derived macrophage differentiation. **A**, THP-1 monocyte integrates retinoic acid (RA) response through its major receptor isoform-α (RARA) that, in turn, controls lamin-A expression during PMA-induced differentiation into MMP-expressing macrophages. **B**, Schematic of how lamin-A and MMP9 might increase with PMA stimulation and matrix stiffness.

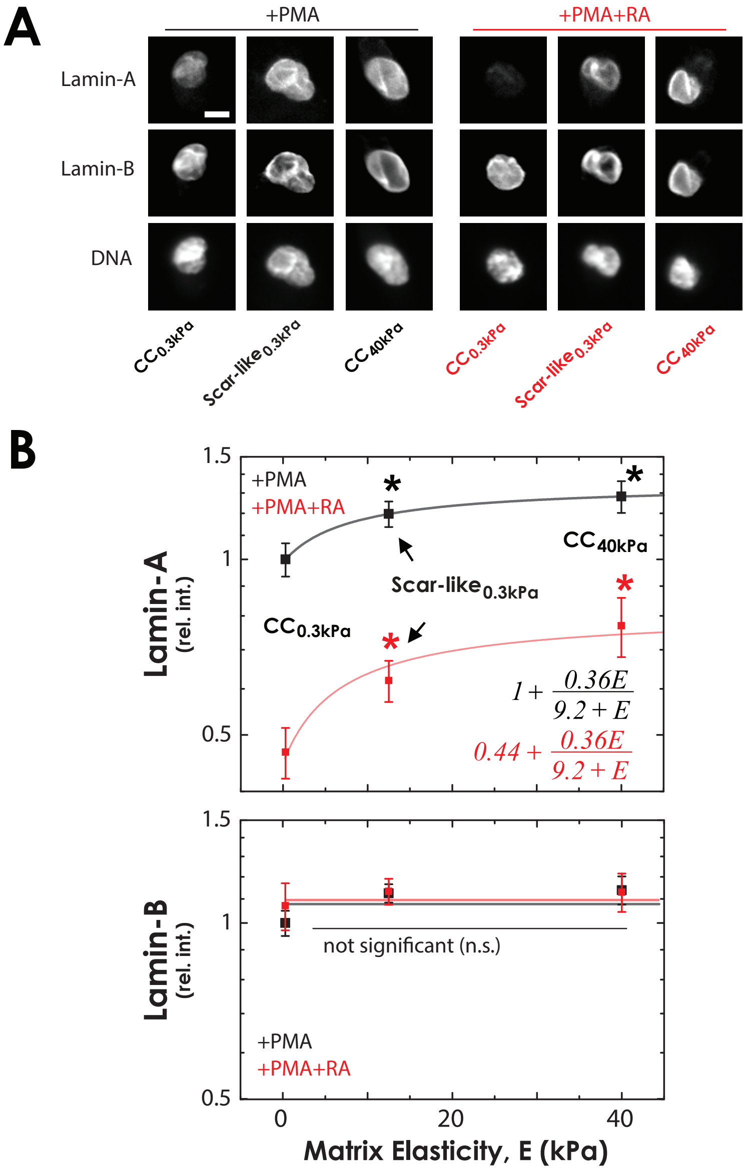

Figure 2.15. Matrix stiffness, but not Retinoic Acid (RA), induces lamin A during monocyte/macrophage differentiation. **A**, Immunofluorescence images of lamin-A, lamin-B and DNA in THP-1 monocytes stimulated for 2 days with PMA (100 ng/mL) and cultured for 7 days on various matrix stiffness without RA (+PMA) or with RA (1 μM; +PMA+RA). Scale bar, 10 μm. **B**, Quantification of immunofluorescence intensities (mean $\pm$ s.e.m.) reveals hyperbolic stiffness and RA response of lamin A (top) but not of lamin B (bottom). $^*p < 0.05$, when compared to CC$_{0.3kPa}$ gel. Hyperbolic curves fit well using half-maximal elasticity, E_m = 9.2 kPa (goodness of fits, $R^2 \geq$ 0.95).

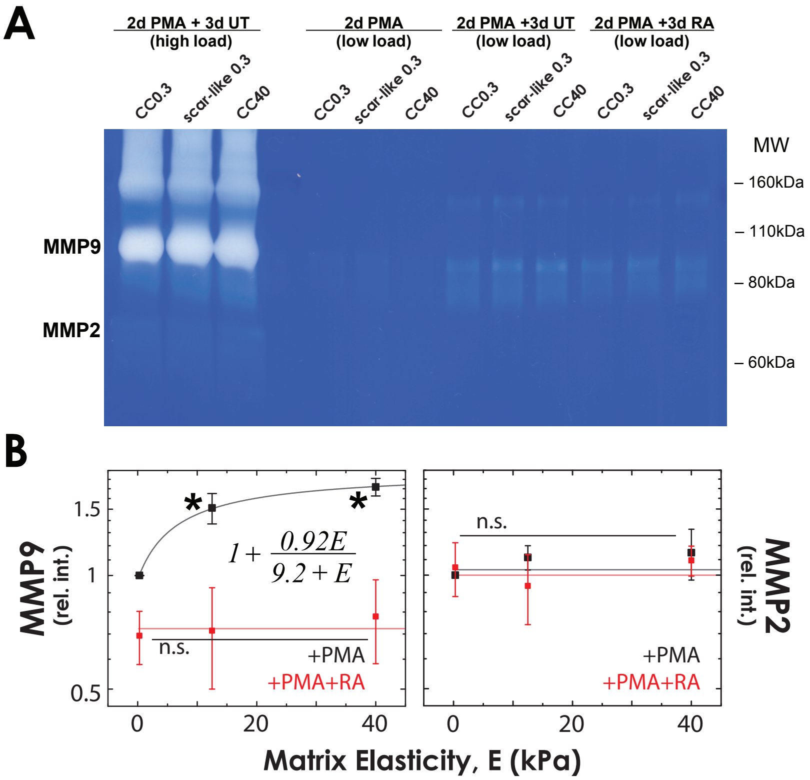

Figure 2.16. Matrix stiffness, but not Retinoic Acid (RA), also induces MMP9 in monocytes/macrophages. **A**, Gelatin zymography of conditioned media collected from 2-day PMA-stimulated THP-1 cells and conditioned media spiked with or without RA (1 μM) from day 3–5. **B**, MMP9 enzyme (92 kDa), but not MMP2 (72 kDa), is upregulated upon PMA stimulation in a stiffness-dependent manner and is reduced upon RA addition. $^*p < 0.05$, when compared to CC$_{0.3kPa}$ gel. Hyperbolic curves fit well using half-maximal elasticity, E_m = 9.2 kPa (goodness of fits, R$^2 \geq$ 0.95).

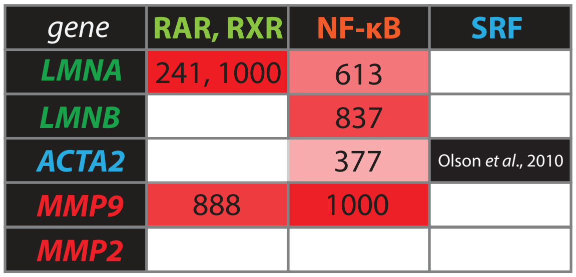

gene	RAR, RXR	NF-κB	SRF
LMNA	241, 1000	613	
LMNB		837	
ACTA2		377	Olson *et al.*, 2010
MMP9	888	1000	
MMP2			

Figure 2.17. Summary of transcription factor binding scores based on chromatin immunoprecipitation sequencing (ChIP-seq) data in ENCODE database (Kent et al., 2002; `https://genome.ucsc.edu/ENCODE/`). SRF interaction with *ACTA2* derived from Olson and Nordheim (2010).

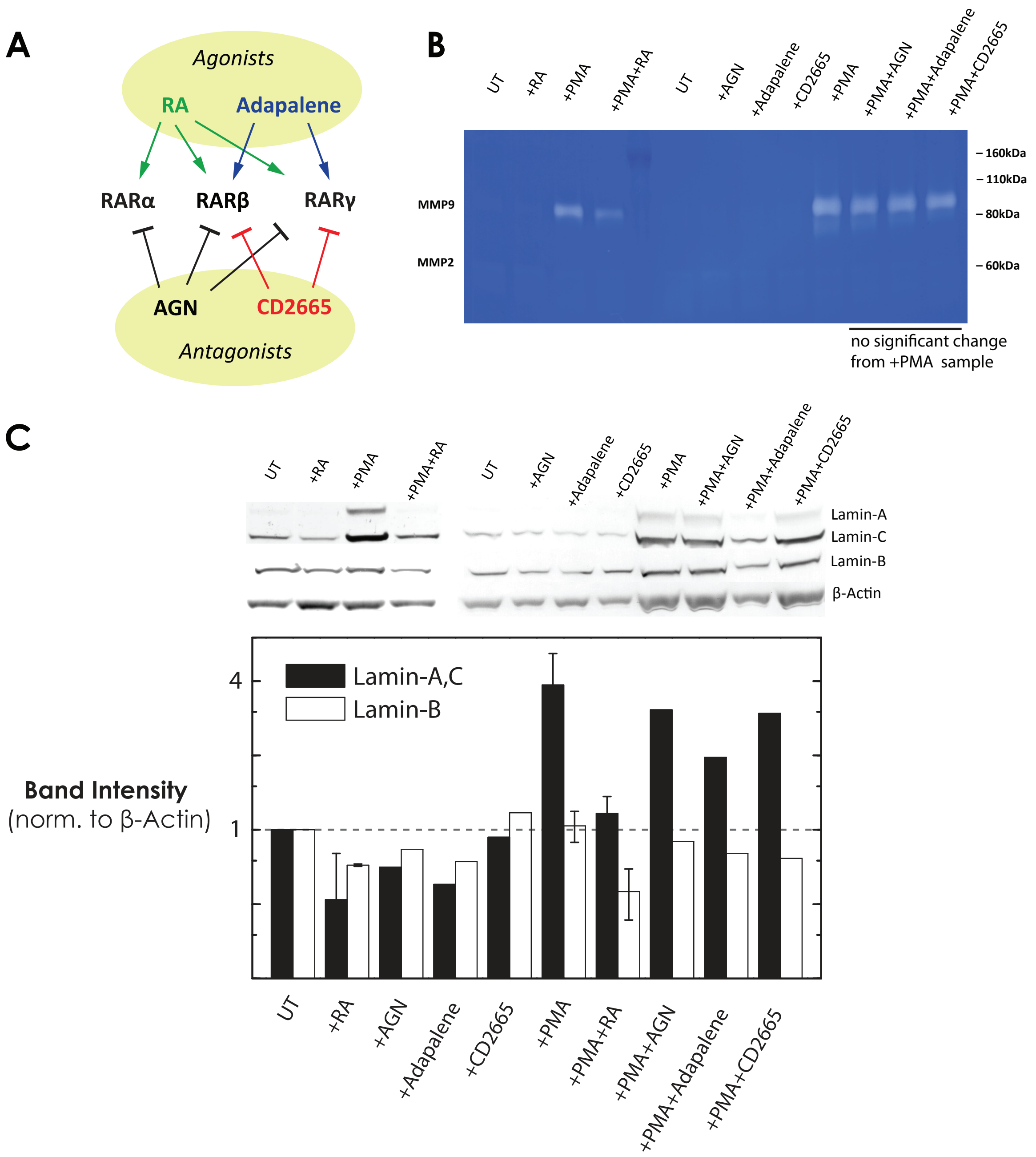

Figure 2.18. Retinoic Acid (RA), through RARα isoform, reduced lamin A,C and MMP9 in monocyte-derived macrophages. **A**, A panel of RAR agonists and antagonists were used to deduce RAR-isoform specific regulation. THP-1 monocytes were induced to differentiate (or left untreated, UT) with PMA (100 ng/mL) for 2 days with or without RAR specific drugs. **B**, Gelatin zymogram gel of conditioned media from different conditions to determine matrix metalloproteinase (MMP) expression as THP-1 differentiates. MMP9 was significantly upregulated after 2-day PMA induction but is reduced with RA treatment, via RARγ. MMP2 remained at basal activity. **C**, Lamin-protein levels were checked by Western blotting, implicating RARα as the major isoform that regulates lamin A,C but not lamin B.

Chapter 3

Role of a matrix stiffness-sensitive repressor, NKX2.5, in stem cell plasticity

Portions of this work are under peer-review in *Nature Materials*.

Proteomics analyses of cell lysates were performed by Sangkyun Cho.
Microarray analyses of cell-on-gel cultures were performed by Dr. Amnon Buxboim.

Abstract

An adherent cell responds to matrix stiffness by activating mechanotransduction pathways to turn on genes that support mechanical stress. Here, we show a novel role of NKX2.5 as a mechanosensitive repressor of α-smooth muscle actin (SMA), a common fibrosis and cell-tension marker. A repressor of SMA transcription, NKX2.5, translocates slowly from nucleus to cytoplasm in response to matrix rigidity, but nuclear-localized mutants of NKX2.5 override matrix-stiffness sensing with suppression of SMA and cell spreading. MSCs cultured for weeks or longer on rigid substrate reinforce a 'mechanical memory' by decreasing NKX2.5, thus stabilizing an SMA-high, scar-like phenotype. Interestingly, matrix stiffness also downregulated collagen-1 synthesis as it upregulated contractility in MSCs. This phenytopic response was also observed by inhibiting the TGF-β signaling pathway, which is known to modulate matrix synthesis. TGF-β inhibition accelerated NKX2.5 nuclear exit and degradation, illustrating how matrix synthesis and contractility is decoupled and how mechanical memory is developed in MSCs.

3.1 Introduction

Morphological tissue changes during development are often accompanied, if not because of, mechanical changes. Living cells that comprise tissue are capable of actively sensing and responding to forces from its microenvironment, by which mechanotransduction of these signals into the cell ultimately affects cell and tissue fate. Tracking the transcriptomic changes from pluripotent stem cells (embryonic or induced) to terminally differentiated fibroblasts indicates systemic increases in structural genes of the extracellular matrix, cytoskeleton, and the nuclear lamina (**Figure 3.1**). The multilineage plasticity of stem cells, even after *in vitro* culture (Pittenger et al., 1999), has provided a platform to elucidate a milieu of factors that control differentiation. For example, MSCs can be directed to a specific lineage on matrix-functionalized hydrogels that mimic the typical stiffness of a mature tissue (Engler et al., 2006). Induced pluripotent stem cells have gained increasing utility over embryonic counterparts not only in tissue regeneration efforts – particularly for soft tissues like brain (Karumbayaram et al., 2009; Wang et al., 2011) and liver (Sullivan et al., 2010; Liu et al., 2011b) – but also in elucidating the pathogenesis of aging disorders (Liu et al., 2011a).

Cell-based therapies, such as injecting autologous MSCs into myocardial infarcts (Tomita et al., 1999; Orlic et al., 2001; Berry et al., 2006), are promising perhaps in their immunomodulatory properties, but they also pose some risks (Breitbach et al., 2007) due to a lack of understanding in their unique response to the mechanochemical milieu of a fibrotic scar. In contrast to embryonic healing, TGF-β signaling is dysregulated in adult tissue injury (Leask and Abraham, 2004). Resident fibroblasts are activated to myofibroblasts upon TGF-β-induced nuclear translocation of SMAD2/3, which binds to collagen and SMA genes (among many others) to generate a highly tensed cellular phenotype (Heldin et al., 1997). Cellular tension and a stiff matrix synergize to activate TGF-β from its latent, matrix-bound complex (Wipff et al., 2007), creating a positive feedback loop of matrix hypersecretion and hypercontractility – ultimately leading to a stiff, fibrotic scar. Therapeutic interventions that inhibit TGF-β signaling via neutralizing antibodies (Hinz et al., 2001; Biswas et al., 2007) or pharmacological treatments (Leask and Abraham, 2004) lead to decreases in SMA and collagen production by fibroblasts.

Ubiquitous (SRF, YAP/TAZ, RARG) and tissue-specific (MYOD, NKX2-5, CBFA1) transcription factors known to potentiate mechanotransduction did not significantly change mRNA levels during development (Figure 3.1) or with matrix stiffness, at least in MSCs (**Figure 3.2**A). SRF (Miralles et al., 2003) and YAP/TAZ (Dupont et al., 2011) has been shown to modulate cell spreading and adhesion on stiffer matrices, while NKX2.5 is largely implicated in the specification of the contractile machinery in cardiac tissue (Kasahara and Izumo, 1999). TGF-β-dependent signaling has also been implicated in enhancing cardiac-specific activity of NKX2.5 (Lien et al., 2002). A transcription factor that does not change its expression levels, while its downstream targets do in response to matrix stiffness, hints at intracellular processes such as posttranslational or structural modifications that affect its function. For example, nuclear SRF binds effectively on its DNA target only when MAL/MKL1 is released upon actin assembly and translocates into the nucleus to associate with SRF (Miralles et al., 2003). More recently, nuclear entry of RARG in MSCs on stiff matrices has been implicated to modulate levels of the mechanosensitive nucleoskeletal lamin A protein (Swift et al., 2013b).

In both disease and development, mechanical changes feed back into cell fate. But cells can also remodel their immediate microenvironment, which complicate various *in vitro* efforts, especially three-dimensional models where factors that cells secrete are hard to characterize. Here, we used hydrogel substrates with a well-defined adhesive matrix to elucidate the effects of matrix stiffness on the matrix-synthetic and contractile abilities of MSCs. Through bioinformatics analysis of matrix versus cytoskeletal genes, we uncovered a novel role of NKX2.5 as a mechanosensitive repressor of matrix stiffness-directed stem-cell response, especially in long-term mechanical memory induction.

3.2 Results and Discussion

3.2.1 MSCs downregulate collagen-1 synthesis as they become more contractile

First, systems-level profiling of the effects of matrix stiffness on contractility and matrix-synthetic ability of MSCs was performed. Transcriptomic analyses of MSCs cultured on stiff (40 kPa) versus soft (0.3 kPa) collagen-1-coated gels revealed a negative correlation between cytoskeleton and matrix genes. Genes that are relevant to cytoskeletal contractility are generally more abundant than the extracellular matrix genes (Figure 3.2A, left column). Furthermore, intracellular tension markers such as *ACTA2* and *CALD1* (for proteins, SMA and caldesmon, respectively) are upregulated 2-fold on stiffer gels, while matrix genes for collagens type 1 and type 6 decreased (Figure 3.2A, right column). The observation that collagen synthesis is downregulated as MSCs become contractile on stiff gels was then confirmed with mass spectrometry analysis in the 110-160 kDa range (Figure 3.2B) as well as with Western blot (**Figure 3.3**A) and immunofluorescence (Figure 3.3B). This was also observed independent of matrix type (**Figure 3.4**). Contractile proteins detected in MS (e.g. actinins) that fall within the 110–160 kDa range were also found to be upregulated (Figure 3.2B), consistent with transcriptome profiling (Figure 3.2A).

Consistent with the role of stem cells in tissue homeostasis, a less matrix-synthetic yet contractile phenotype might be beneficial, particularly in wound healing, as mimicked by the scar-like$_{0.3kPa}$ gel described in Chapter 2. In contrast, fibrosis is principally due to activated fibroblasts (i.e. myofibroblasts) that concomitantly increase SMA expression and collagen matrix deposition, both of which can be downregulated by inhibition of TGF-β signaling (Kapoun et al., 2006). Indeed, MSCs treated with TGF-β_1 increased in SMA and collagen-1; yet unlike myofibroblasts, MSCs treated with a TGF-β receptor inhibitor (SB505124, 10 μM) almost completely abrogated collagen-1 but did not affect SMA (**Figure 3.5**) — a phenotypic equivalent to the response of MSCs to matrix stiffness (Figs. 3.2 and 3.3). Therefore, TGF-β is sufficient but not necessary for SMA expression in MSCs. This response is also seen in hepatic stellate cells (Olsen et al., 2011), which also possess stem-cell characteristics.

3.2.2 Matrix stiffness modulates NKX2.5 localization

We looked into transcription factors that bind differentially to contractility- and matrix-related genes that could explain this decoupling response. Through bioinformatics-based comparative promoter analysis of representative genes for cytoskeleton (*ACTA2*) and matrix (*COL1A2*) (**Table 3.1**A), we found transcription-factor families with the highest binding to *ACTA2* promoter (but not to *COL1A2* promoter) that contained homeodomains and POU domains; SMADs of the TGF-β pathway and SRF are common to both promoters (Table 3.1B). Homeodomain-containing NKX2.5 ranked highest among transcription factors that bind only on *ACTA2* but not on *COL1A2* promoter. In the first $\sim$1200 base-pairs upstream of *ACTA2* transcription start site, there are at least 4 predicted binding sites for the NKX family, and 5 sites for the SRF family (**Figure 3.6**A). Among the NKX family of transcription factors, NKX2.5 is also the most abundantly expressed in the body (Kasahara et al., 1998) and particularly in MSCs

(Figure 3.6B); it is also moderately expressed relative to other genes (Figure 3.2A).

To determine whether NKX2.5 plays a role in the matrix-stiffness response of cells, embryonic chick cardiomyocytes beating on soft or stiff gels were immunostained and imaged for Nkx2.5, which was predominantly nuclear (**Figure 3.7**). However, total Nkx2.5 increased in highly striated cardiomyocytes found on stiff-gel cultures, largely due to increased cytoplasmic levels (Figure 3.7B). We looked into the predicted abundance of NKX2.5 in human MSCs (Figure 3.6) and observed post-translational modifications as evidenced by band shifts from the expected 35 kDa band (**Figure 3.8**A). To confirm that this was not an artifactual effect of a polyclonal antibody that detects mouse, chick and human versions, we overexpressed Nkx2.5 (mouse) in an A549 human cell line and detected highly abundant peptides unique to Nkx2.5 (Figure 3.8B,C). As with endogenous NKX2.5 in MSCs, overexpressed Nkx2.5 was also post-translationally modified (Figure 3.8B).

NKX2.5 was likewise nuclear-localized in MSCs on soft gels, but unlike cardiomyocytes, it was predominantly cytoplasmic on stiff gels (**Figure 3.9**). We have also uncovered an interesting matrix-stiffness response of NKX2.5 that spans several days. Unlike myosin IIB (Figure 2.9Aii) and lamin A (Figure 2.12B) that respond in <1 day to matrix stiffness, SMA only increased significantly (by 2-fold) in two-day MSC cultures on stiff matrix compared to soft matrix (Fig. 2.9Ai and Fig. 2.11C), while prolonged 7-day cultures led to further SMA upregulation (up to 8-fold) on stiff matrix, which was not observed on soft matrix (Figure 2.12A, **Figure 3.10**). Nuclear exit of NKX2.5 in MSCs appeared slower than typical SRF mechano-activation, which can respond within minutes (Esnault et al., 2014), suggesting that SRF could drive initial expression of SMA while NKX2.5 is involved in the maintenance of SMA expression for longer cultures. Transcript profiling of MSCs cultured for 1 day (Figure 3.2A) revealed stiffness-driven increases in *ACTA2* and *CALD1* but not *NKX2-5* or *SRF* (which also promotes its own expression). Total NKX2.5 protein levels also did not change with matrix stiffness up to 7 days (Figure 3.10, inset), highlighting an important role for transcription-factor localization rather than its abundance.

3.2.3 A long-term rigid-matrix phenotype: nuclear exit of NKX2.5

Given the decreases in *NKX2-5* levels in chronic diseases such as muscular dystrophies (Figure 2.1C), we hypothesized that cytoplasmic enrichment of NKX2.5 in MSCs on rigid substrates would be followed by its degradation (**Figure 3.11**A). First, to determine whether NKX2.5 is functionally sufficient to repress SMA's response to matrix stiffness, we overexpressed wild-type or mutant forms of Nkx2.5. Shuttling of Nkx2.5 to the nucleus has been shown to be controlled by a putative nuclear localization sequence (NLS) near the homeodomain region of the protein (Kasahara and Izumo, 1999); mutations to the NLS of Nkx2.5 determine its subcellular localization (Figure 3.11B). We overexpressed wild-type and NLS-mutant NKX2.5 in A549 cells and observed that only the NLS3 mutant, with alanine replacement of all residues, prevented nuclear localization (Figure 3.11C). More importantly, overexpression of the nuclear-localized wild-type, NLS1, or NLS2 mutants in MSCs repressed SMA, reduced stress fibers, and ultimately reduced cell and nuclear spread areas on rigid substrate (**Figure 3.12**). In clear contrast, the cytoplasmic NLS3 mutant maintained the rigid-substrate phenotype.

An endogenous NLS sequence in NKX2.5 implies that its nuclear exit on rigid matrix must be an active process. NKX2.5 in stress fibers (**Figure 3.13**A) and in lamellipodia co-localized with myosin phosphatase-1 (MYPT1; Figure 3.13B) supports recent evidence of MYPT1-dependent nuclear exit of NKX2.5 in embryonic stem cells (Ryan et al., 2013). It has been suggested that nuclear exit of Nkx2.5 requires ROCK-induced phosphorylation of MYPT1 (Ryan et al., 2013), which prevents myosin-IIA filament disassembly (Eto et al., 2005) that is induced, for example, by matrix stiffness (Raab et al., 2012). Thus, direct binding of phosphorylated MYPT1 to NKX2.5 may account for the observed nuclear exit and subsequent stress-fiber localization. The effect of cytoskeletal tension in NKX2.5 translocation from nucleus to cytoplasm was tested by inhibiting myosin-generated cytoskeletal forces with blebbistatin. Within several hours, nuclear levels of NKX2.5 increased and SMA subsequently decreased (**Figure 3.14**A). Transcript profiles following 24-h blebbistatin treatment of MSCs on rigid substrates (CC$_{11kPa}$ and tissue culture plastic, TCP) further showed the expected repression of *ACTA2* but in the absence of reproducible changes in cardiac-specific transcripts downstream of NKX2.5 (Figure 3.14B). As expected (Swift et al., 2013b; Dupont et al., 2011), blebbistatin also decreased YAP1 and SRF target genes (slightly), with the latter likely to also contribute to the >50% decrease in SMA at both protein and transcript levels.

Finally, on rigid substrates where drugs such as blebbistatin rescue nuclear depletion of NKX2.5, the long-term trend is a major decrease in NKX2.5, as observed in high-passage MSCs (**Figure 3.15**). SMA might increase slightly, but it certainly does not decrease (Figure 3.15B, rightmost bar). One other study that has described NKX2.5 in MSCs focused on the cardiogenic potential of MSCs grown on either TCP or gel-bound matrix derived from healthy or infarcted hearts (Sullivan et al., 2014), and the authors described a tendency in immunoblots (that show an atypical high molecular weight band) for decreased NKX2.5 in MSCs on stiffer substrates (25 kPa > 40 kPa > TCP). Functional significance of NKX2.5 in MSCs has not been examined previously, and any possible relation to NKX2.5 to SMA in MSCs has not been suggested – especially since SMA is not part of the cardiogenic program. Because we show that translocation of NKX2.5 out of the nucleus can be modulated by cytoskeletal interactions, including stress fibers, the long-term effects of matrix stiffness (e.g. fibrosis) ultimately favor degradation of NKX2.5 and maintenance of an SMA-high phenotype as a form of ’mechanical memory’.

3.2.4 Crosstalk of NKX2.5 and SRF with TGF-β pathway decouples SMA & collagen-1 expression

Inhibiting TGF-β with SB505124 for 1 day also reduced nuclear-NKX2.5 levels on both soft and stiff gels (**Figure 3.16**A). Plotting SMA intensity with nuclear localization of NKX2.5 suggested a universal repressor-inhibition curve (Figure 3.16B). Interestingly, sustained TGF-β inhibition (3 days) decreased total NKX2.5 levels, concomitant with an increased SMA expression (Figure 3.16C), which further demonstrated the equivalent effects of matrix stiffness and TGF-β

inhibition.

Tissue stiffening is typically accompanied by elevated TGF-β signaling, as in fibrosis. It has been suggested that serum-induced SRF is a nuclear repressor of TGF-β signaling, by inhibiting the DNA binding of Smad3/Smad4 complex (Lee et al., 2007). Matrix stiffness-induced actin polymerization also increases SRF activity (Swift et al., 2013b; Miralles et al., 2003), with SRF upregulating contractility genes like *ACTA2* (Esnault et al., 2014). Here, cell-on-gel cultures have basal serum-derived TGF-β and SRF activity; on stiffer matrices, however, a higher SRF activity (Swift et al., 2013b) coupled to a cytoplasmic NKX2.5 (Figure 3.9) may have inhibited TGF-β-induced expression of collagen-1 (Figure 3.3), whilst promoting SMA transcription and translation (**Figure 3.17**A). TGF-β has also been shown to modulate NKX2.5 expression in MSCs via SMAD (Li et al., 2008). Indeed, inhibiting TGF-β signaling reduced nuclear levels (Figure 3.9) and when sustained, total NKX2.5 levels as well (Figure 3.10) – effectively promoting a highly contractile, yet low matrix-synthetic phenotype in MSCs (Figure 3.17B).

3.2.5 Other modifications of NKX2.5

We have also observed NKX2.5 in the Golgi apparatus (via co-localization with fluorescent wheat germ agglutinin, WGA), but not in the endoplasmic reticulum (via co-localization with procollagen-1) (**Figure 3.18**A). WGA stains for proteins modified with O-linked N-acetylglucosamine (O-GlcNAc, 203 Da) typically seen in the Golgi apparatus. O-GlcNAc modifications, in general, have been implicated as a rapid stress sensor (Hart et al., 2007). O-GlcNAcylation of Nkx2.5 could affect its function and turnover and was recently linked to diabetic cardiomyopathy (Kim et al., 2012), which is characterized by excessive O-GlcNAcylation (Clark et al., 2003). This modification, however, does not account for the multiple molecular weight shifts observed in Western blots (Figure 3.8).

Other studies have suggested that Nkx2.5 activity can be regulated by the attachment of small ubiquitin-like modifier-1 (SUMO-1, ∼11.5 kDa) on lysine residue-51 (Wang et al., 2008), whereas preventing such leads to congenital heart defects during development (Kim et al., 2011). In MSCs, cells that had smaller spread area (and hence, nuclear-localized NKX2.5) also had higher nuclear SUMO-1 intensities (Figure 3.18B). Whether localization mutants of NKX2.5 have varying SUMO-1 levels and whether nucleocytoplasmic shuttling of Nkx2.5 involves SUMOylation pathway warrant further investigation.

3.3 Conclusion

Matrix stiffness and TGF-β inhibition induced similar phenotypes in MSCs, in terms of contractility and matrix synthesis. Through comparative promoter analysis, the decoupled contractility/synthesis response uncovered NKX2.5 as a mechanosensitive transcription factor with slow-acting repressive effects on cell tension, particularly on SMA expression. As discussed in Chapter 2, Lamin-A is known to regulate *SRF*, while SRF regulates *ACTA2*; however, a 60% knockdown of *LMNA* only led to 40% reduction of *ACTA2* (**Figure 3.19**A). Furthermore, while retinoic acid treatment greatly reduced lamin A levels (Swift et al., 2013b), it did not completely abrogate SMA expression on long-term stiff-matrix cultures (Figure 3.19B). These suggest that the NKX2.5 mechanorepressor pathway is largely independent of the RA/Lamin-A/SRF signaling axis (Figure 3.19C).

As with activators like SRF (Miralles et al., 2003), YAP/TAZ (Dupont et al., 2011) and RARG (Swift et al., 2013b), nuclear entry/exit seems to be the last step in converting mechanical signals to an effective cellular response. Posttranslational modifications should also shed light into the details of the nucleocytoplasmic shuttling of NKX2.5, with initial correlations shown here with SUMO-1 (Figure 3.18). In classical signal transduction pathways, kinases (unlike phosphatases) are evolutionarily optimized to react on short timescales. A striking parallel is observed here with NKX2.5 (much like a phosphatase) slowly acting on longer timescales than, say, SRF (much like a kinase) in response to matrix stiffness. These findings may benefit novel applications of specific compounds that target such factors to optimize stem cell therapy in fibrotic diseases.

3.4 Materials and Methods

3.4.1 Transcriptional profiling by DNA microarrays

Total RNA was extracted from cells using Trizol and purified by RNeasy (Qiagen) with on-column DNase digestion according to manufacturer's protocol. Adherent cells were gently scraped in Trizol. Total RNA was amplified and converted to cDNA using WT-Ovation Pico kit (NuGen). Fragmented and biotin-labeled ST-cDNA was generated using WT-Ovation Exon Module (NuGen). Samples were tested with Human Gene 1.0 ST DNA microarrays (Affymetrix), used according to the manufacturer's instructions. Expression data sets were analyzed by standard Robust Multi-array Averaging (RMA) methods.

3.4.2 Promoter binding analyses

The Genomatix software suite (`www.genomatix.de`) curates a library of transcription factor binding site matrices and DNA sequences of promoter regions such as of *ACTA2* (IDs: GXP_236533, GXP_236534) and *COL1A2* (GXP_94473). The MatInspector algorithm (Cartharius et al., 2005) was used to scan promoter sequences for potential transcription-factor binding sites based on weighted matrix patterns specific to a transcription factor. Core similarity and matrix similarity scores that range from 0–1 were calculated (Cartharius et al., 2005), and reach a value of 1 only if the test sequence matches to the most conserved nucleotide at each position of the matrix. Transcription factor families, with core and matrix similarity scores $\geq$ 0.80, that differentially bind to *ACTA2* and *COL1A2* were compiled in Table 3.1.

3.4.3 Isolation of embryonic cardiomyocytes

White Leghorn chicken eggs (Charles River Laboratories) were incubated at 37°C, rotated once per day, until the desired developmental stage was reached. Embryos were extracted at room temperature by windowing eggs, removing extraembryonic membranes with forceps and cutting major blood vessels to the embryonic disc tissue to free the embryo. The embryo was placed in a dish containing PBS and quickly decapitated. For E2–E5 embryos, whole heart tubes (HTs) were extracted by severing the conotruncus and sino venosus. All tissues were incubated at 37°C in pre-warmed chick heart media (alpha-MEM supplemented with 10% FBS and 1% Penicillin/Streptomycin, Gibco, 12571-063) until ready for use.

Cell isolation from heart tissue was performed by dicing it to sub-millimeter pieces and then digesting them with trypsin/EDTA (Gibco, 25200-072). To digest, we incubated tissue pieces at 37°C in approximately 1 mL trypsin per HT for 13 min with rotation, then for another 2 min upright to let large tissue pieces settle before carefully removing supernatant and replacing with an equal volume of fresh trypsin for a final 15-min shake. We stopped digestion by adding an equal volume of chick heart media. Cells were plated at concentrations of approximately 2×10^5 cells/cm^3 directly on collagen-1-coated PA gels of varying stiffness.

Table 3.1. Promoter analysis of transcription factor binding to ACTA2 and COL1A2

A. Promoter sequences for comparative transcription factor binding analysis

Gene (Promoter ID)	Gene Position	Transcription Start Site	Promoter Position
ACTA2 (GXP_236533, GXP_236534)	Chr10:90694831-90712530 (-)	Chr10:90712580/-30/-29/-04	Chr10:90707633-90708233, Chr10:90712404-90713080
COL1A2 (GXP_94473)	Chr7:94023873-94060544 (+)	Chr7:94023873	Chr7:94022989-94024379

B. Top transcription factor binding sites

Matrix Family	Transcription Factor	Strand	Core Sim.	Matrix Sim.	Binding Motif
Binding to ACTA2 promoter					
V$SMAD	Sma- and Mad-related proteins	+	1.00	0.97	tctGTCTgaat
V$CEBP	CCAAT/enhancer binding protein beta	+	1.00	0.97	tttattagGAAAtgg
V$SRFF	Serum response factor	-	1.00	0.87	gccctgTATGgttaa
V$NKXH	Homeodomain factor Nkx-2.5/Csx	+	1.00	1.00	cctcaAGTGgttattt
V$NKX6	NK6 homeobox 1	+	1.00	1.00	tcttTTAAttacccg
V$NKXH	Homeodomain protein Nkx-3.2	+	1.00	0.99	gggtaAGTGgcgc
V$NKX1	NK1 homeobox 2, Sax1-like	-	1.00	0.91	cgggtAATTaaaag
V$NKXH	NK2 homeobox 4, NKX 2 DELTA	+	1.00	0.88	attccAGTGgctcttt
V$HOMF	Homeobox protein HMX3/Nkx5.1	+	1.00	0.97	gaagcAAGTggga
V$HOXF	Homeobox C8 / Hox-3alpha	+	1.00	0.99	cttttaATTAcccggt
V$HOXF	Hox-1.3, vertebrate homeobox protein	+	1.00	0.87	ctgacTAATttaggc
V$HOXC	Meis homeobox 1	+	1.00	0.98	aacttGATTtataaa
V$ABDB	Homeobox B9	-	1.00	0.96	gacccaTAAAatag
V$OCT1	Octamer-binding factor 1 (OCT1)	-	1.00	0.95	agcATGCaaagaa
V$STEM	Octamer-binding factor 3/4 (OCT3/4)	+	1.00	0.93	ttctttGCATgctacc
V$BRN5	POU class 6 homeobox 1 (POU6F1)	-	1.00	0.86	aaatcATTAaggtg
Binding to COL1A2 promoter					
V$SMAD	Sma- and Mad-related proteins	-	1.00	1.00	cttGTCTggat
V$SRFF	Serum response factor	-	1.00	0.82	ccgacATGGgcag
V$NKXH	Homeodomain protein Nkx-3.2	+	1.00	0.91	gtctAAGTgctagac
V$HOMF	Homeobox protein HMX3/Nkx5.1	+	1.00	0.93	cctacAAGTggcct
V$HOXF	Hox-1.3, vertebrate homeobox protein	-	1.00	0.85	aaaTAATaaagccc
V$HOXC	Meis homeobox 1	-	1.00	0.88	gtctgGATTtaccag
V$ABDB	Homeobox B9	+	1.00	0.89	aactggTAAAtcca
V$OCT1	Octamer-binding factor 1 (OCT1)	+	0.75	0.85	gatCTGCaaattct
V$STEM	Octamer-binding factor 3/4 (OCT3/4)	+	1.00	0.97	gagtctGCATgtcta

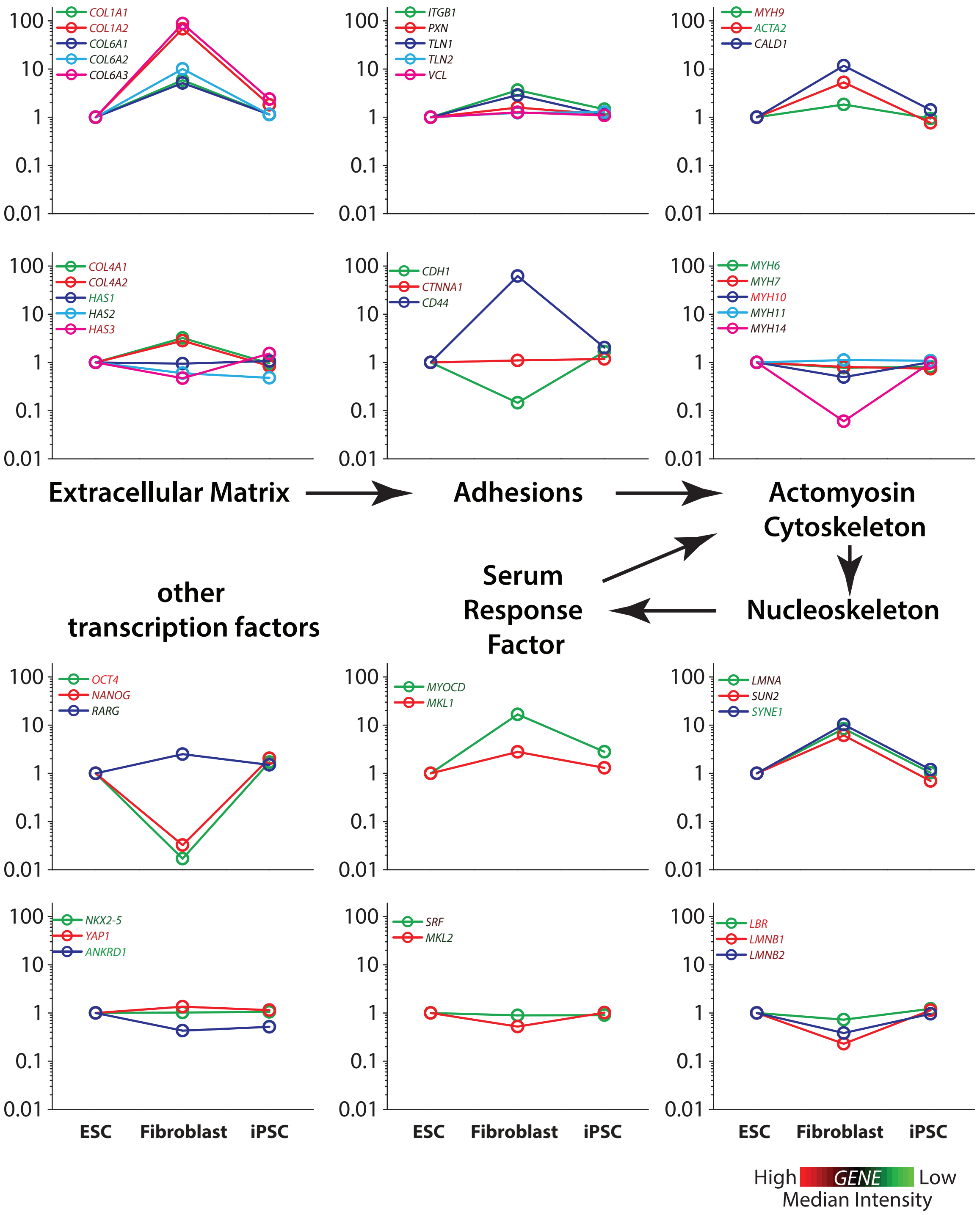

Figure 3.1. Genes relevant to mechanobiology in development. Relative expression levels of genes relevant to mechanobiology in development, from extracellular matrix proteins to transcription factors, in embryonic stem cells (ESC), adult fibroblasts, and fibroblast-derived induced-pluripotent stem cells (iPSC). Dataset is curated from the submission by Liu et al. (2011a) to the public Gene Expression Omnibus (GEO) repository (GDS3892, `http://www.ncbi.nlm.nih.gov/sites/GDSbrowser`). Arrows indicate the interactions of outside-in signaling components from matrix to nucleus.

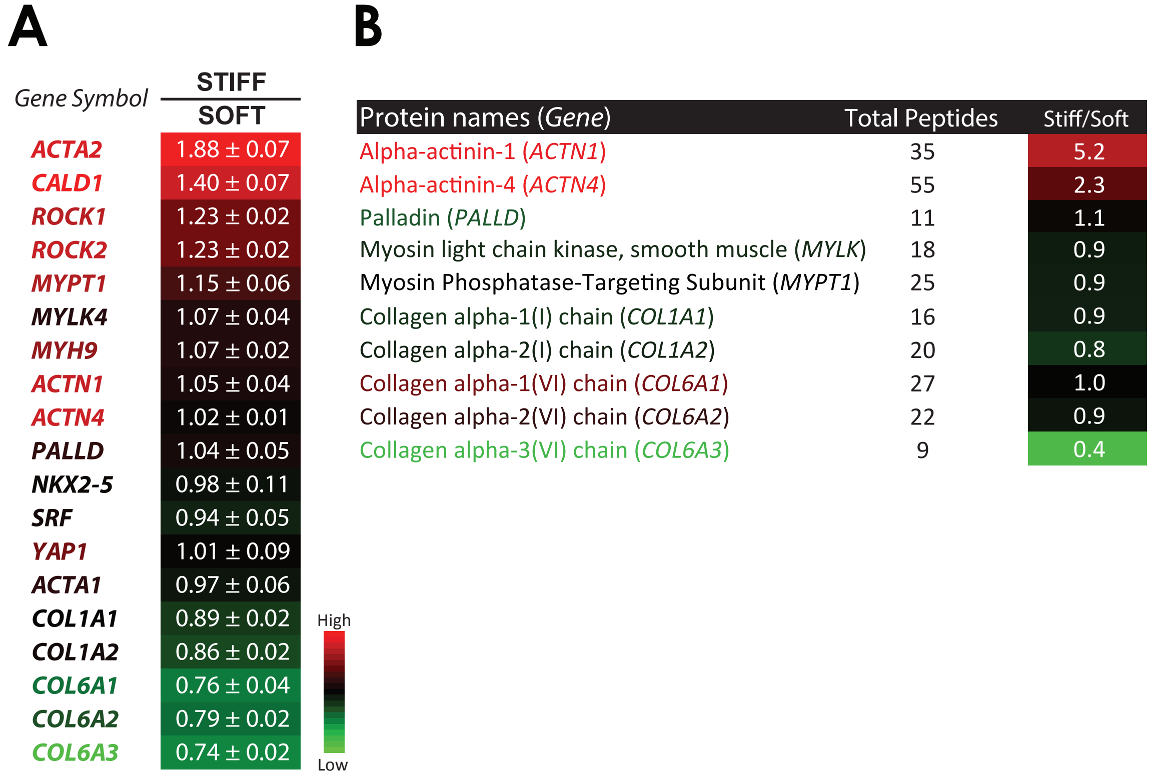

Gene Symbol	STIFF / SOFT
ACTA2	1.88 ± 0.07
CALD1	1.40 ± 0.07
ROCK1	1.23 ± 0.02
ROCK2	1.23 ± 0.02
MYPT1	1.15 ± 0.06
MYLK4	1.07 ± 0.04
MYH9	1.07 ± 0.02
ACTN1	1.05 ± 0.04
ACTN4	1.02 ± 0.01
PALLD	1.04 ± 0.05
NKX2-5	0.98 ± 0.11
SRF	0.94 ± 0.05
YAP1	1.01 ± 0.09
ACTA1	0.97 ± 0.06
COL1A1	0.89 ± 0.02
COL1A2	0.86 ± 0.02
COL6A1	0.76 ± 0.04
COL6A2	0.79 ± 0.02
COL6A3	0.74 ± 0.02

Protein names (*Gene*)	Total Peptides	Stiff/Soft
Alpha-actinin-1 (*ACTN1*)	35	5.2
Alpha-actinin-4 (*ACTN4*)	55	2.3
Palladin (*PALLD*)	11	1.1
Myosin light chain kinase, smooth muscle (*MYLK*)	18	0.9
Myosin Phosphatase-Targeting Subunit (*MYPT1*)	25	0.9
Collagen alpha-1(I) chain (*COL1A1*)	16	0.9
Collagen alpha-2(I) chain (*COL1A2*)	20	0.8
Collagen alpha-1(VI) chain (*COL6A1*)	27	1.0
Collagen alpha-2(VI) chain (*COL6A2*)	22	0.9
Collagen alpha-3(VI) chain (*COL6A3*)	9	0.4

Figure 3.2. Transcriptomic and proteomic profiles of MSCs on gels. **A**, Microarray profiling of contractility- and matrix-relevant mRNA expression levels from MSCs cultured for 1 day on soft (0.3 kPa) or stiff (40 kPa) collagen-1 coated PA gels. **B**, Proteomic profiling of 2-day MSC cultures on PA gels. Cell lysates were run on SDS-PAGE and gel bands in the range of ∼110–160 kDa were run on the mass spectrometer. Colors of gene/protein symbols indicate gene abundance, while those of ratios indicate up- or downregulation relative to soft-gel cultures.

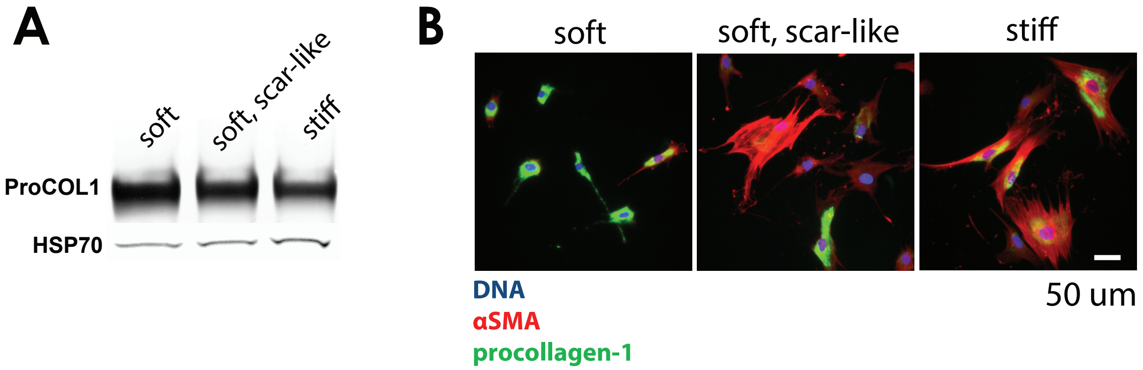
A
soft
soft, scar-like
stiff
ProCOL1
HSP70
B
soft
soft, scar-like
stiff
DNA
αSMA
procollagen-1
50 um

Figure 3.3. Matrix stiffness downregulates collagen-I matrix synthesis in MSCs. **A**, Immunofluorescence staining of α-smooth muscle actin (red) and procollagen-1 (green) in MSCs cultured for 2 days on soft, scar-like (0.3 kPa, with embedded collagen), and stiff gels. Hoechst 33342 for DNA stain, blue. Scale bar, 50 μm. **B**, Western blot of procollagen-1 levels of MSCs cultured for 7 days on gels; HSP70 was used as normalization control.

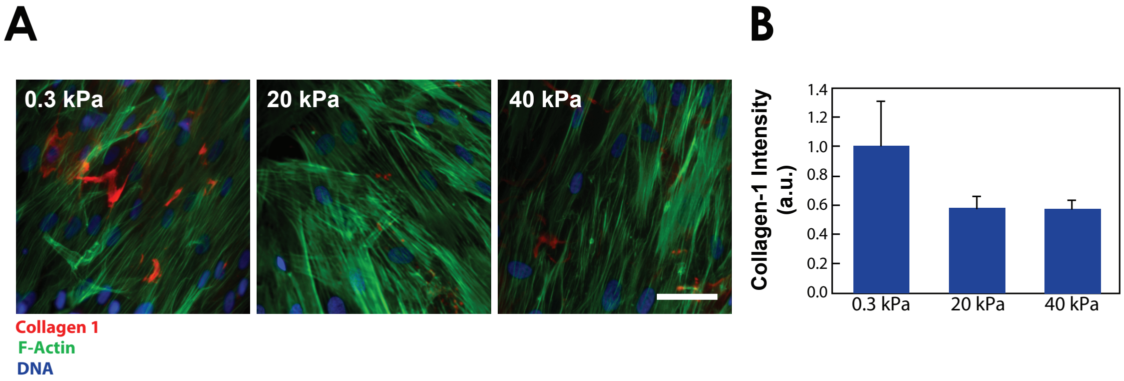
A
B
0.3 kPa
20 kPa
40 kPa
Collagen 1
F-Actin
DNA
Collagen-1 Intensity (a.u.)
1.4
1.2
1.0
0.8
0.6
0.4
0.2
0.0
0.3 kPa
20 kPa
40 kPa

Figure 3.4. Stiff gels coated with collagen-2 reduced collagen-1 in MSCs. A, Mesenchymal stem cells cultured on collagen-2 coated PA gels for 7 days, labeled for collagen-1 (red), F-actin (green) and DNA (blue). **B**, Quantification of collagen-1 production on gels showed decrease with gel stiffness. Scale bar, 50 μm.

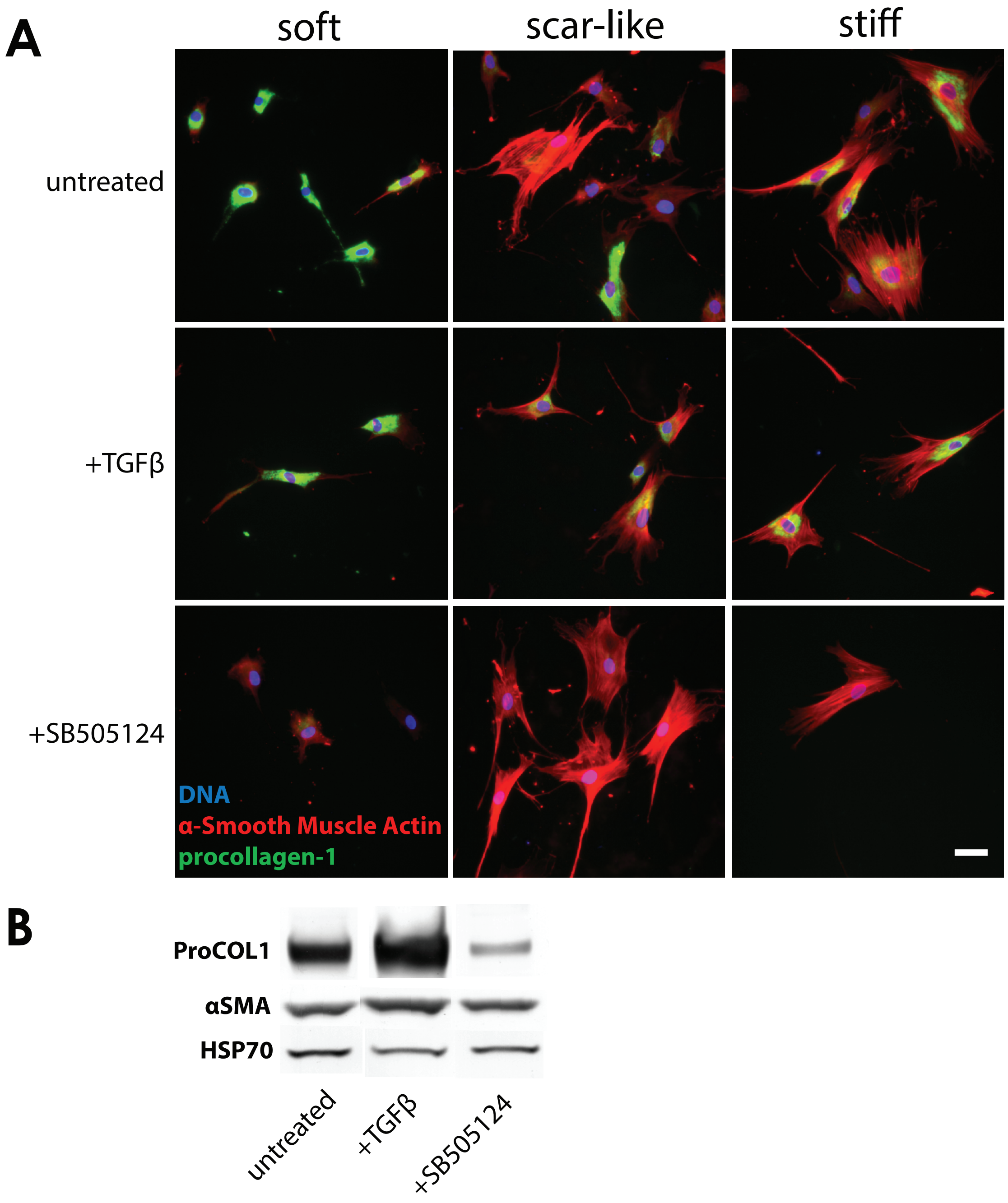
A
soft
scar-like
stiff
untreated
+TGFβ
+SB505124
DNA
α-Smooth Muscle Actin
procollagen-1
B
ProCOL1
αSMA
HSP70
untreated
+TGFβ
+SB505124

Figure 3.5. TGF-β is sufficient but not necessary for α-smooth muscle actin expression. **A**, Immunofluorescence staining of procollagen-1 (green) and α-smooth muscle actin (red) in mesenchymal stem cells cultured on soft (0.3 kPa), scar-like, and stiff (40 kPa) gel for 2 days (top panel), with TGF-β1 (10 ng/mL) (middle), or with TGF-β receptor inhibitor (10 μM SB505124, bottom). Hoechst 33342 for DNA, blue. **B**, Western analysis of the abovementioned conditions with Hsp-70 as normalization control.

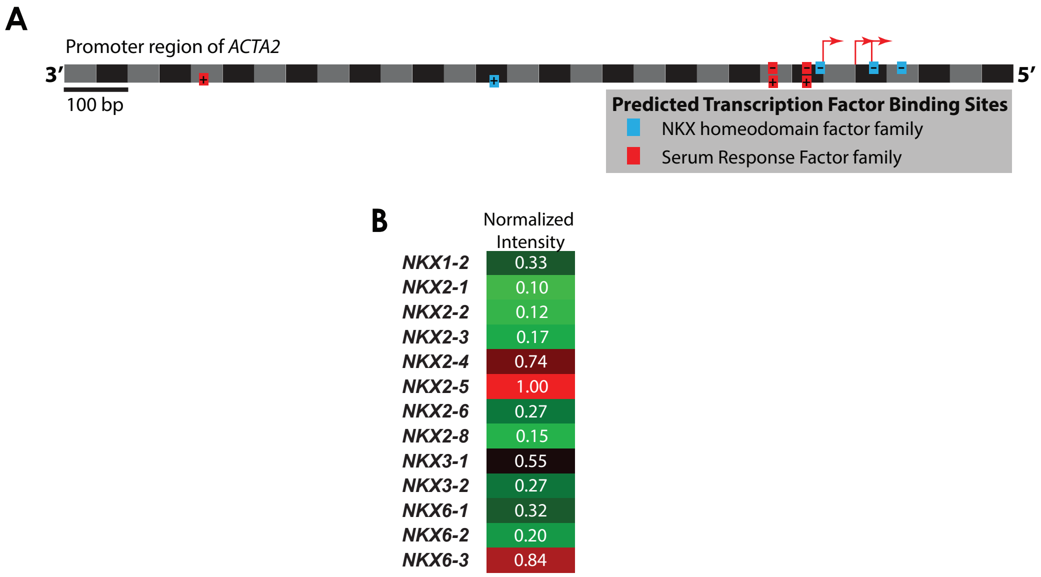
A
Promoter region of *ACTA2*
3′
5′
100 bp
+
-
Predicted Transcription Factor Binding Sites
NKX homeodomain factor family
Serum Response Factor family
B
Normalized Intensity

	Normalized Intensity
NKX1-2	0.33
NKX2-1	0.10
NKX2-2	0.12
NKX2-3	0.17
NKX2-4	0.74
NKX2-5	1.00
NKX2-6	0.27
NKX2-8	0.15
NKX3-1	0.55
NKX3-2	0.27
NKX6-1	0.32
NKX6-2	0.20
NKX6-3	0.84

Figure 3.6. NKX family of transcription factors: promoter binding and gene abundance. **A**, Analyses of promoter binding by NKX and Serum Response Factors families using the MatInspector tool (`www.genomatix.de`; Cartharius et al., 2005) on ∼1200 base-pairs upstream of transcription start sites (red arrows) of *ACTA2* (also see Table 3.1). **B**, Relative abundances within the NKX family transcriptome derived from human MSCs revealed *NKX2-5* to be the most abundant.

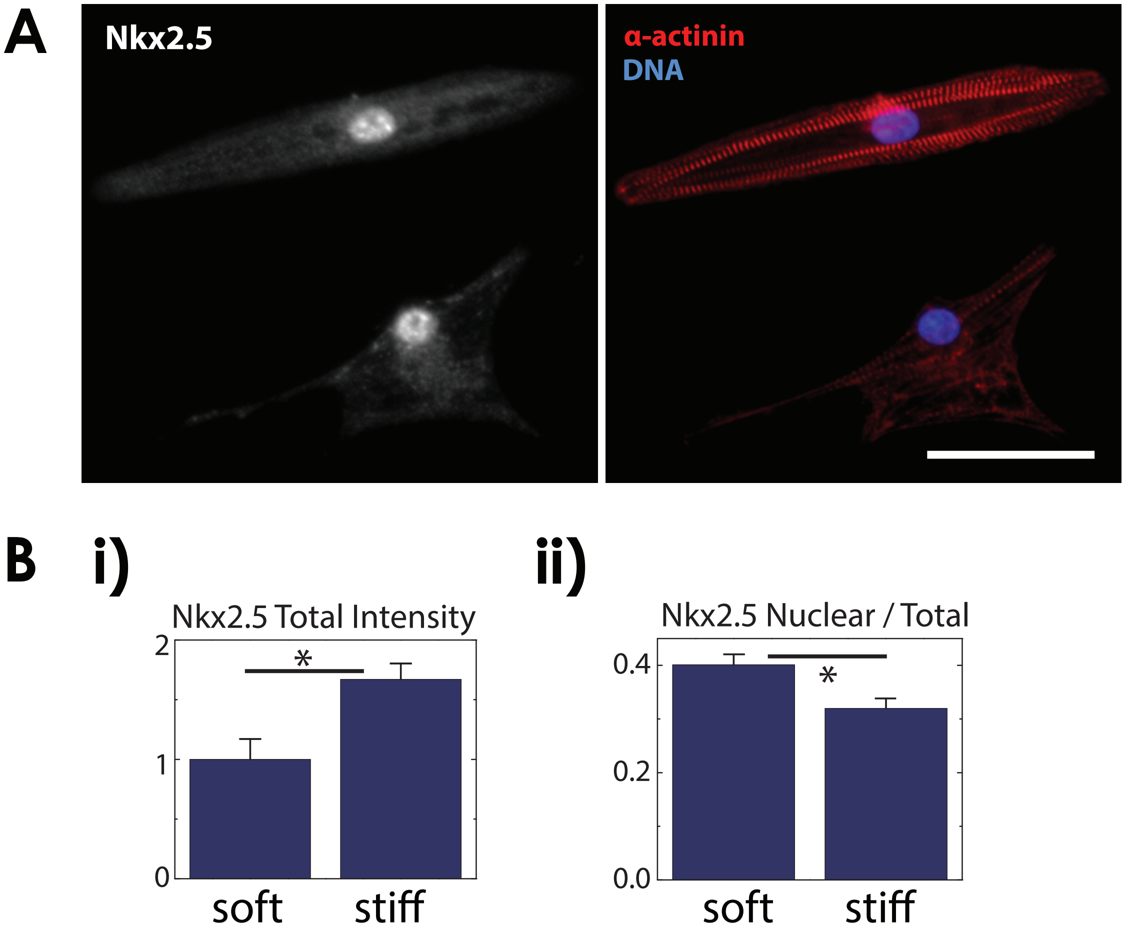
A
Nkx2.5
α-actinin
DNA
B
i)
Nkx2.5 Total Intensity
2
1
0
*
soft
stiff
ii)
Nkx2.5 Nuclear / Total
0.4
0.2
0.0
*
soft
stiff

Figure 3.7. Matrix stiffness modulates Nkx2.5 expression in embryonic cardiomyocytes. **A**, Immunofluorescence staining of Nkx2.5 (left) and sarcomeric α-actinin (right, red) in embryonic day-5 (E5) chick cardiomyocytes plated on 6 kPa PA gels for 3 days. Hoechst 33342 for DNA, blue. Scale bar, 50 μm. **B**, Quantification of i) total Nkx2.5 intensity and ii) nuclear-to-total Nkx2.5 intensity in E5 chick cardiomyocytes cultured on soft (0.3 kPa) and stiff (40 kPa) gels for 3 days. $^*p < 0.05$.

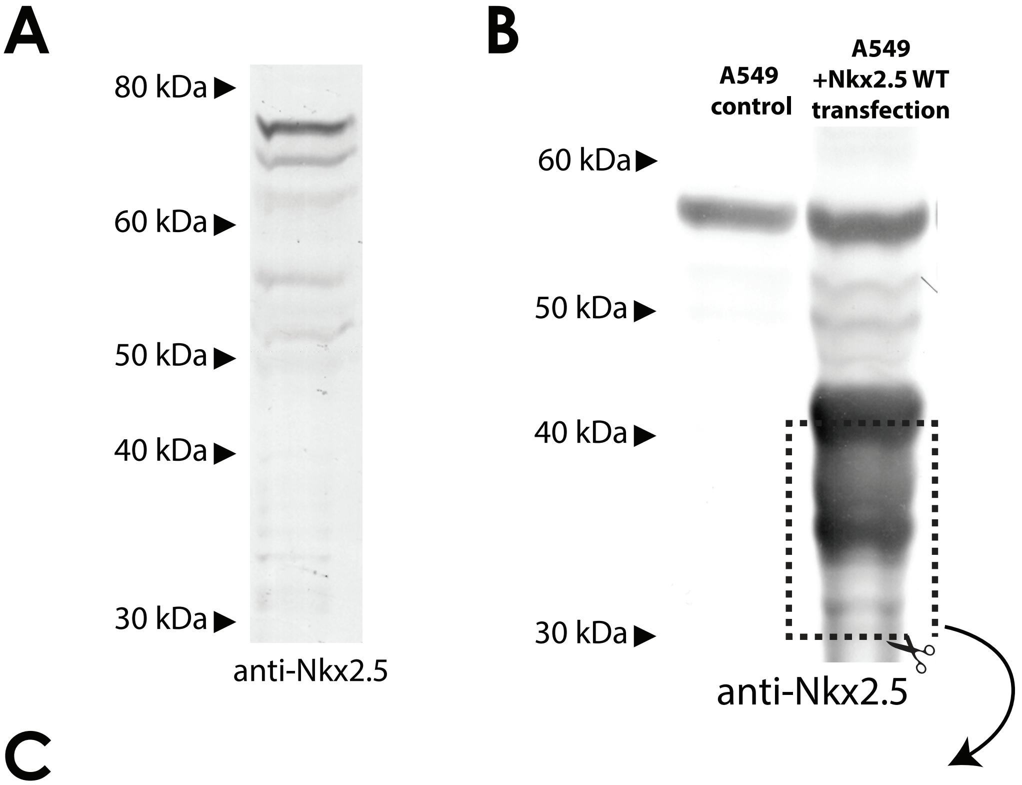

C

Major Nkx2.5 peptides detected by Mass Spectrometry

Protein IDs	Protein	# of unique Peptides (Rank)	Peptide sequences (relative to full length)	Sequence coverage	Median Intensity (Rank)
Q925V3; P42582	Nkx2.5	7 (134/496)	MFPSPALTPTPFSVKDILNLEQQQRSLASGDLSARLEATLAPASCMLAAFKPEAYSGPEAAASGLAELRAEMGPAPSPPKCSPAFPAAPTFYPGAYGDPDPAKDPRADKKELCALQKAVELDKAETDGAERPRARRRRKPRVLFSQAQVYELERRFKQQRYLSPAERDQLASVLKLTSTQVKIWFQNRRYKCKRQRQDQTLELLGPPPPPARRIAVPVLVRDGKPCLGDPAAYAPAYGVGLNAYGYNAYPYPSYGGAACSPGYSCAAYPAAPPAAHAPAASANSNFVNFGVGDLNTVQSPGMPQGNSGVSTLHGIRAW	28.6%	1.7x10^8 (50/496)

Figure 3.8. MSCs express NKX2.5 with some modifications. A, Western analysis of NKX2.5 in MSCs revealed multiple band shifts. **B**, Western analysis of wild-type Nkx2.5 overexpressed in A549 cells, with the expected molecular weight of 35 kDa, as well as bands that may be post-translationally modified. **C**, Mass spectrometry analysis of proteins in the 30–40-kDa range from Nkx2.5-overexpressing A549s confirmed Nkx2.5-antibody specificity with the detection of 7 peptides unique to Nkx2.5 and their abundance ranking relative to other proteins in that range.

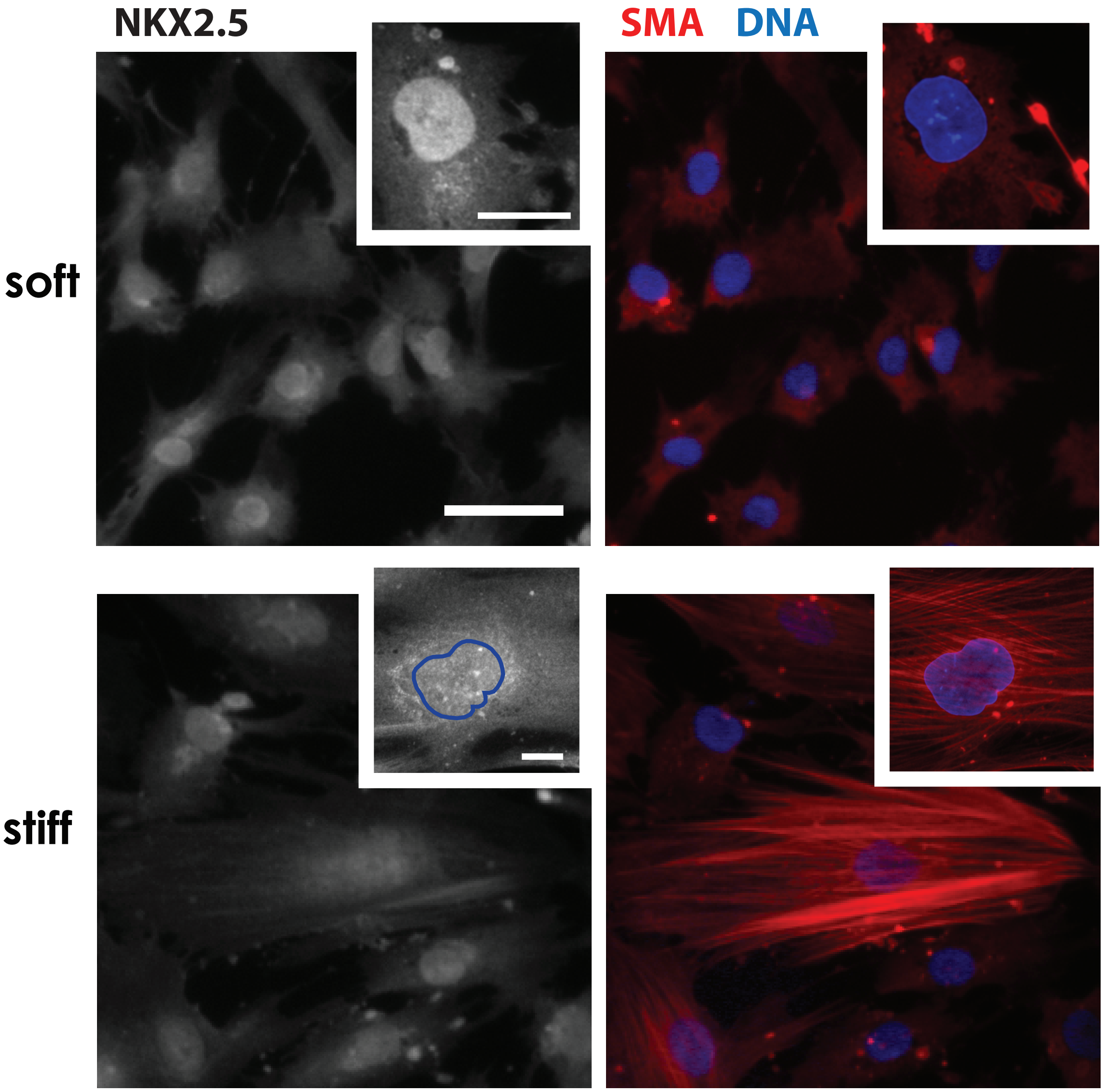

Figure 3.9. Matrix stiffness modulates NKX2.5 localization in MSCs., Immunofluorescence staining of NKX2.5 (top) and α-smooth muscle actin (bottom, red) in MSCs on soft (0.3 kPa, left) and stiff (40 kPa, right) PA gels for 7 days. Scale bar, 50 μm. Insets: Magnified images of nuclei; scale bars, 20 μm. Hoechst 33342 for DNA, blue.

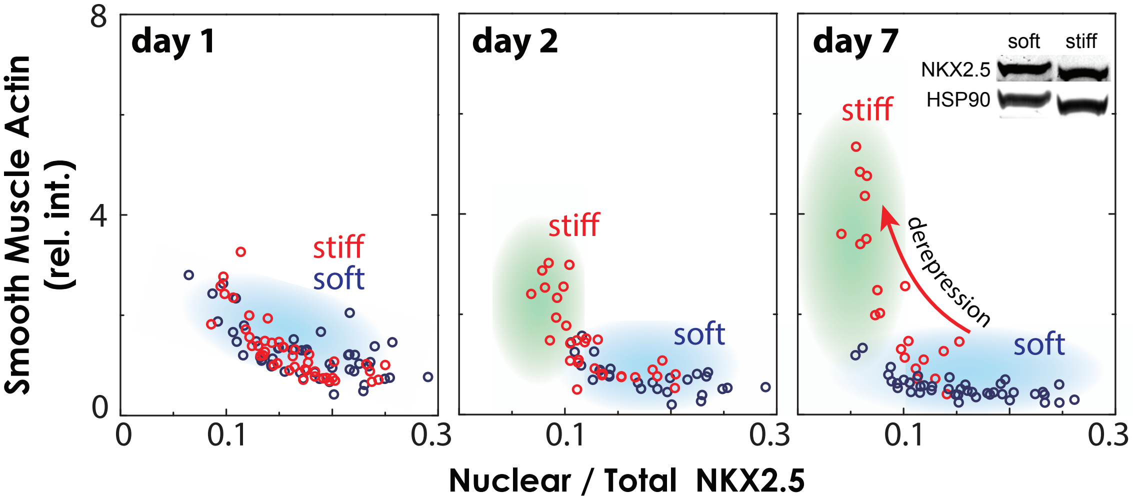

Figure 3.10. NKX2.5 is a slow-acting mechanorepressor of α-smooth muscle actin. MSCs cultured for 1 (left), 2 (middle) or 7 days (right) on soft (0.3 kPa, blue) or stiff (40 kPa, red) gels differed in their dynamic range of SMA expression. NKX2.5 depletion from the nucleus took several days and led to $\sim$8-fold upregulation of SMA in stiff-gel cultures. Inset: Western blot of NKX2.5 from soft- and stiff-gel cultures. HSP90 as loading control.

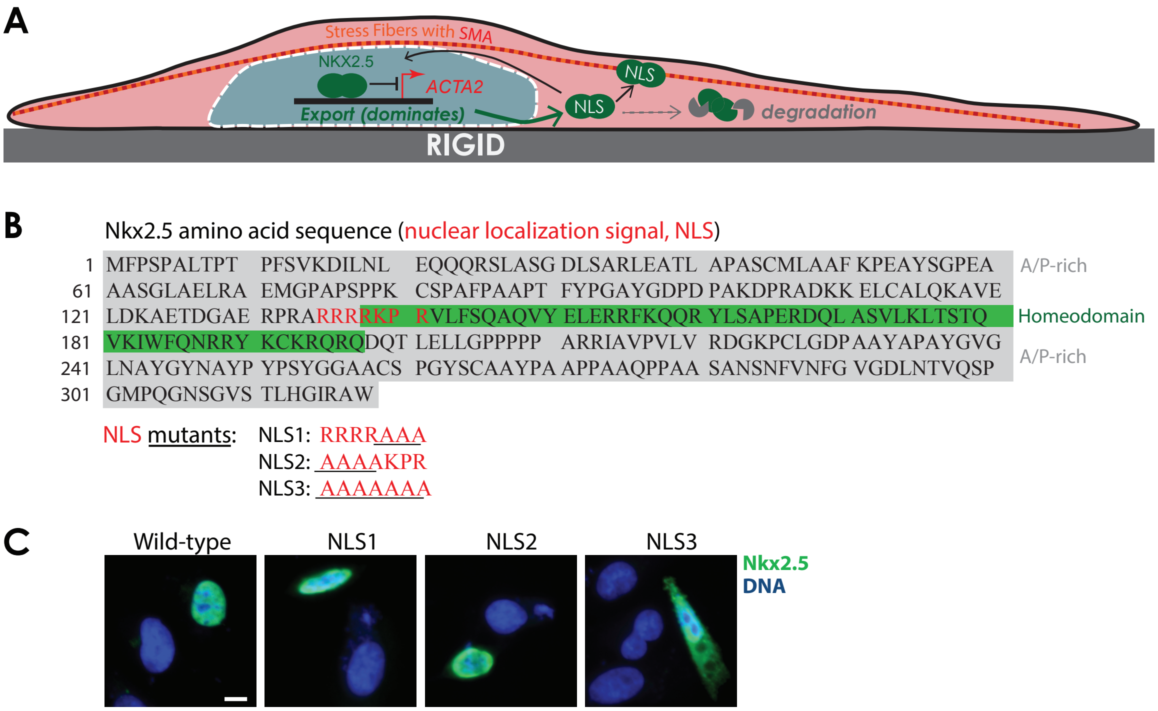
A
Stress Fibers with SMA
NKX2.5
ACTA2
Export (dominates)
NLS
NLS
degradation
RIGID
B
Nkx2.5 amino acid sequence (nuclear localization signal, NLS)
1 MFPSPALTPT PFSVKDILNL EQQQRSLASG DLSARLEATL APASCMLAAF KPEAYSGPEA
61 AASGLAELRA EMGPAPSPPK CSPAFPAAPT FYPGAYGDPD PAKDPRADKK ELCALQKAVE
121 LDKAETDGAE RPRARRRRKP RVLFSQAQVY ELERRFKQQR YLSAPERDQL ASVLKLTSTQ
181 VKIWFQNRRY KCKRQRQDQT LELLGPPPPP ARRIAVPVLV RDGKPCLGDP AAYAPAYGVG
241 LNAYGYNAYP YPSYGGAACS PGYSCAAYPA APPAAQPPAA SANSNFVNFG VGDLNTVQSP
301 GMPQGNSGVS TLHGIRAW
A/P-rich
Homeodomain
A/P-rich
NLS mutants:
NLS1: RRRRAAA
NLS2: AAAAKPR
NLS3: AAAAAAA
C
Wild-type
NLS1
NLS2
NLS3
Nkx2.5
DNA

Figure 3.11. Subcellular localization of Nkx2.5 by mutating its nuclear localization signal (NLS). A, MSCs on rigid substrates leads to nuclear export of NKX2.5, which can interact with stress fibers or otherwise degrades. **B**, Amino acid sequence of mouse Nkx2.5 with highlighted alanine- and proline- (A/P) rich regions (gray) and DNA-binding homeodomain region (green). The NLS sequence (red) is mutated in NLS1, NLS2 and NLS3 versions of Nkx2.5 as indicated. **C**, A549 cells were transfected with wild-type and NLS-mutated Nkx2.5 plasmids and immunolabeled 2 days after transfection with anti-Nkx2.5 antibody (green). Only NLS3 mutant localized in the cytoplasm. Hoechst 33342 for DNA, blue. Scale bar, 10 μm.

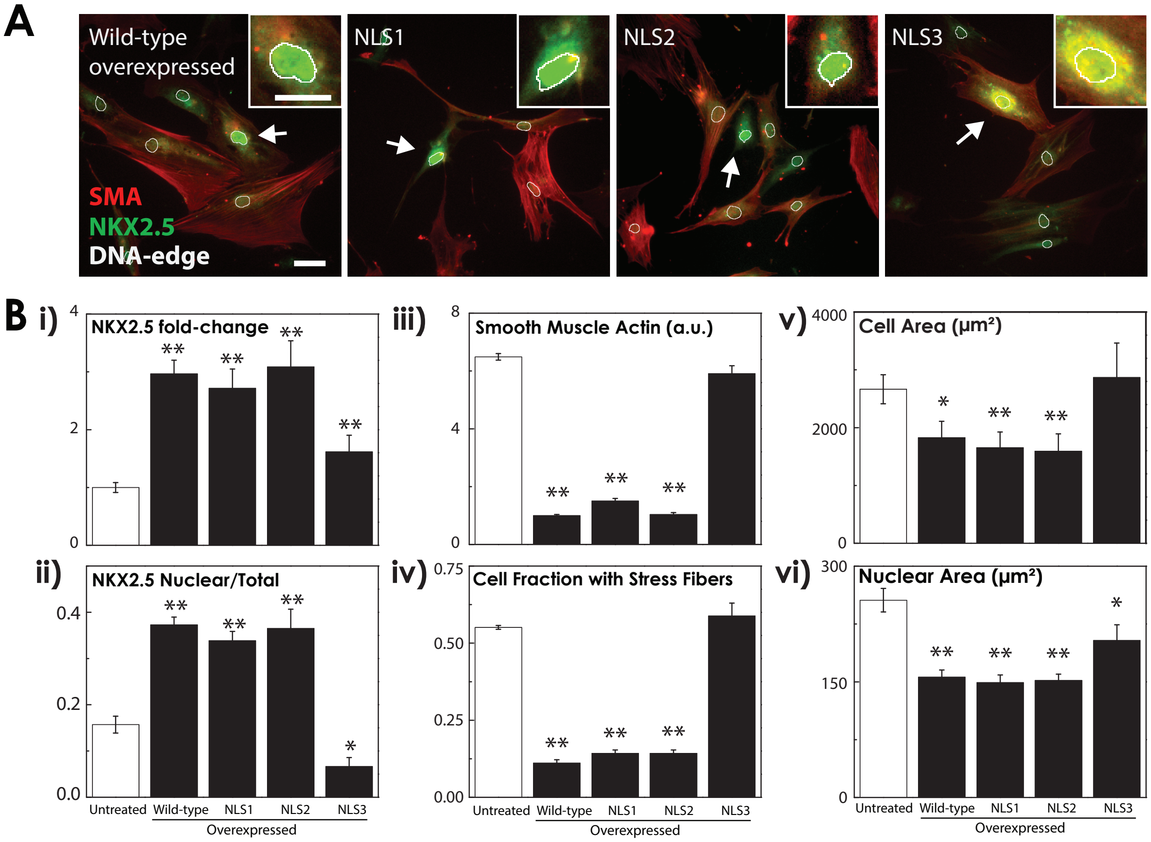

Figure 3.12. NKX2.5 can reprogram the stiff phenotype of MSCs. A, Overexpression of wild-type and NLS-mutated Nkx2.5 (green) in MSCs (white arrows) cultured on rigid plastic. Insets: Magnified nuclei with overexpressed NKX2.5. DNA-edge (white) is superimposed. Scale bars, 50 μm. **B**, i) Fold-changes in Nkx2.5 intensity upon overexpression; ii) Nuclear/total ratio of Nkx2.5 was increased in NLS1 and NLS2, but reduced in NLS3; iii) SMA expression is abrogated with overexpressed nuclear-localized Nkx2.5 iv) with concomitant reduction of stress fiber count, v) cell and vi) nuclear areas. Mean ± s.e.m. $^{*}p < 0.05$, $^{**}p < 0.01$ when compared to untreated control.

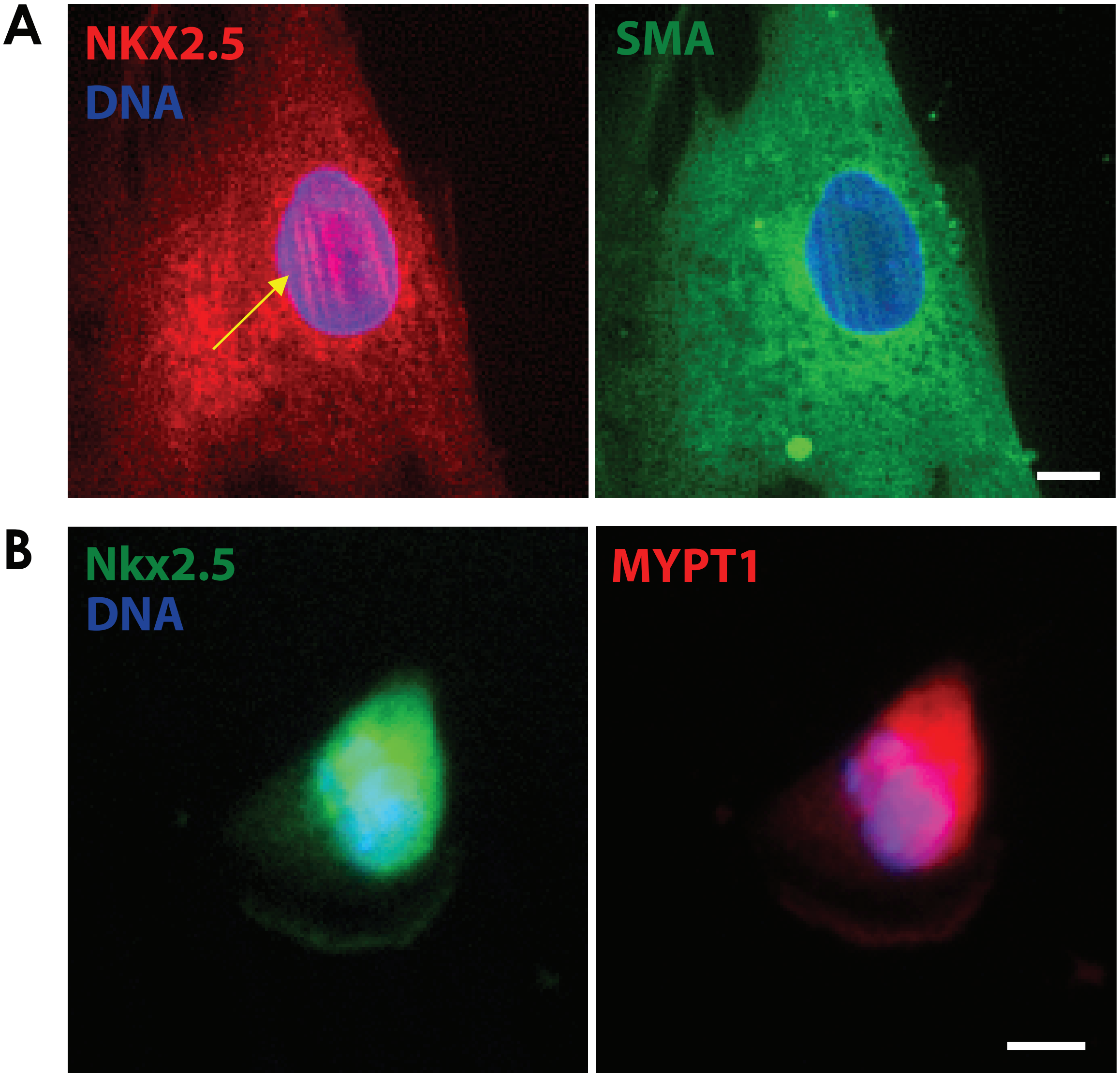

Figure 3.13. Extranuclear localization of NKX2.5. **A**, Immunofluorescence of NKX2.5 (red) in MSCs showed localization to stress fibers as visualized by α-smooth muscle actin (green). **B**, NKX2.5 was found to localize in lamellipodia with myosin phosphatase-1 (MYPT1) in A549 cells. Scale bars, 10 μm.

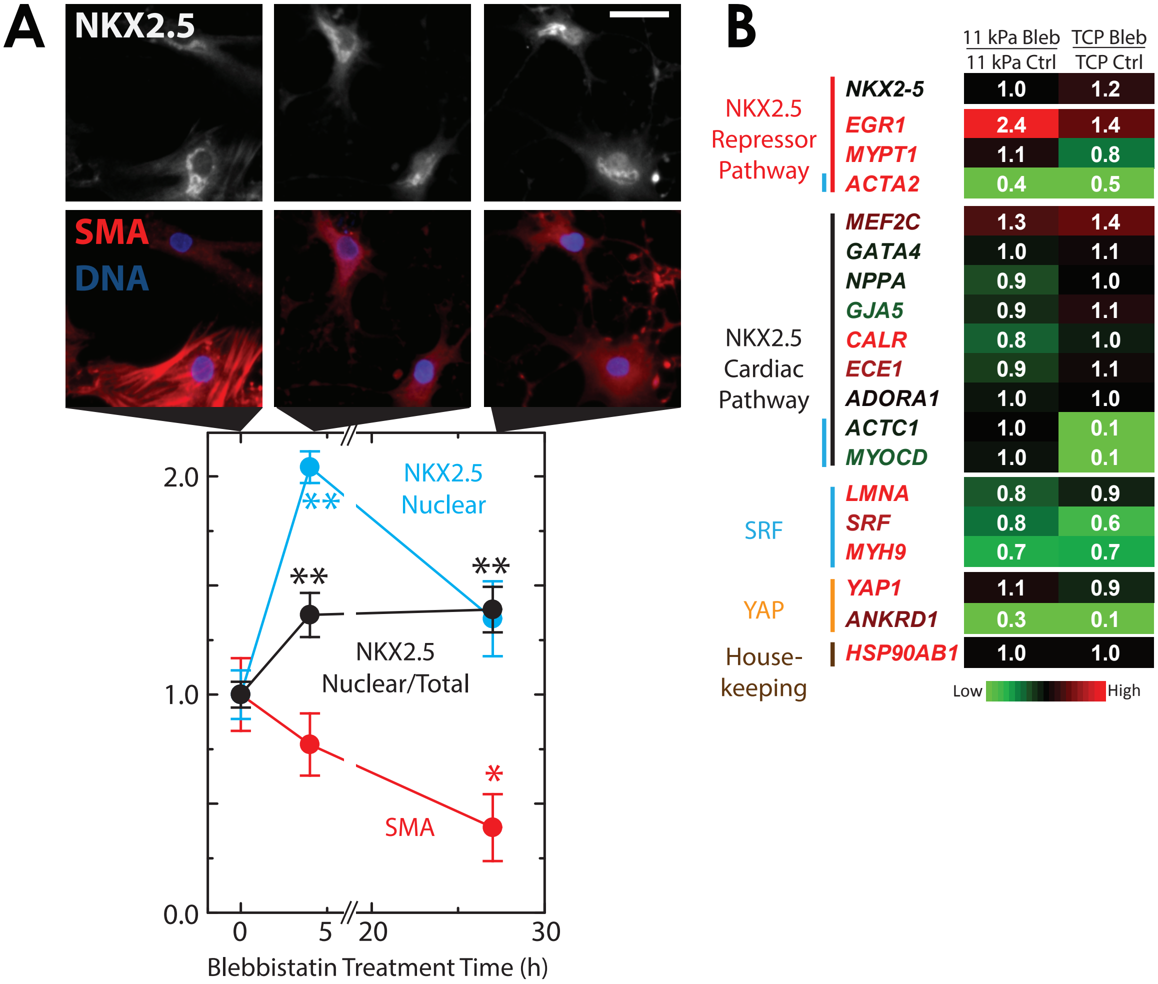

		11 kPa Bleb / 11 kPa Ctrl	TCP Bleb / TCP Ctrl
NKX2.5 Repressor Pathway	*NKX2-5*	1.0	1.2
	EGR1	2.4	1.4
	MYPT1	1.1	0.8
	ACTA2	0.4	0.5
NKX2.5 Cardiac Pathway	*MEF2C*	1.3	1.4
	GATA4	1.0	1.1
	NPPA	0.9	1.0
	GJA5	0.9	1.1
	CALR	0.8	1.0
	ECE1	0.9	1.1
	ADORA1	1.0	1.0
	ACTC1	1.0	0.1
	MYOCD	1.0	0.1
SRF	*LMNA*	0.8	0.9
	SRF	0.8	0.6
	MYH9	0.7	0.7
YAP	*YAP1*	1.1	0.9
	ANKRD1	0.3	0.1
House-keeping	*HSP90AB1*	1.0	1.0

Figure 3.14. Blebbistatin rescues NKX2.5 depletion from the nucleus in stiff-gel cultures. **A**, Kinetics of NKX2.5 expression and localization in MSCs cultured on rigid plastic and treated with blebbistatin for 4—27 h revealed loss of SMA (red) and nuclear enrichment of NKX2.5 (gray). Hoechst 33342 for DNA, blue. Scale bar, 50 μm. Mean ± s.e.m. $^{*}p < 0.05$, $^{**}p < 0.01$ when compared to untreated control. **B**, Transcriptomic profiling of MSCs treated with blebbistatin on 11 kPa gels or rigid plastic (TCP) for 24 h revealed decreased *SRF* and SRF-target levels (e.g. *ACTA2*). Downstream targets of NKX2.5 related to cardiac specification were downregulated and/or lowly-expressed.

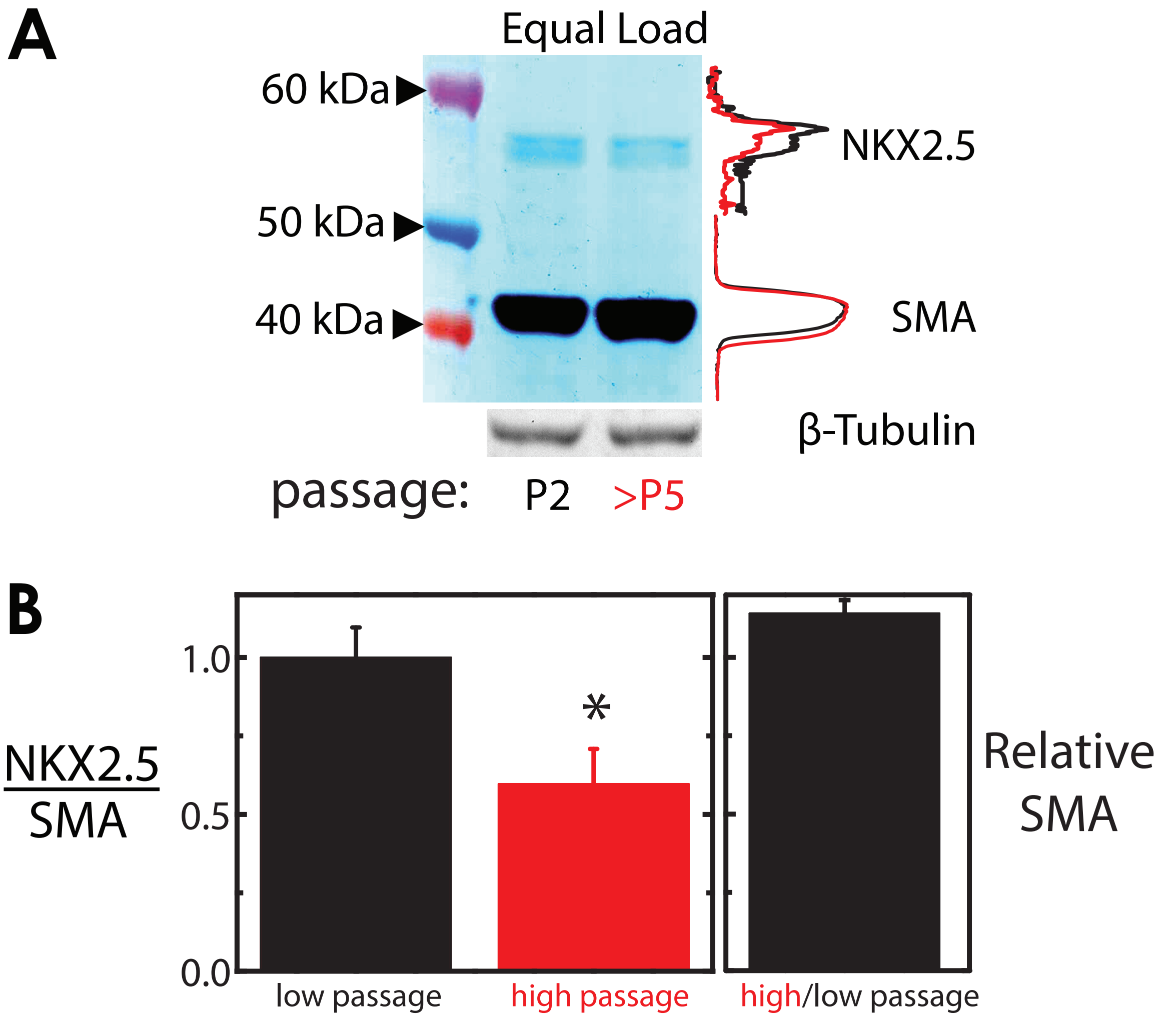

Figure 3.15. NKX2.5 decreases with long-term stiff-substrate cultures of MSCs. A, Long-term culture (high passage, >P5) of MSCs on tissue culture plastic leads to decreased levels of NKX2.5, while SMA levels are maintained. β-tubulin as loading control. **B**, Quantitation of Western blot. Mean ± s.e.m. $^*p < 0.05$, compared to low-passage MSCs.

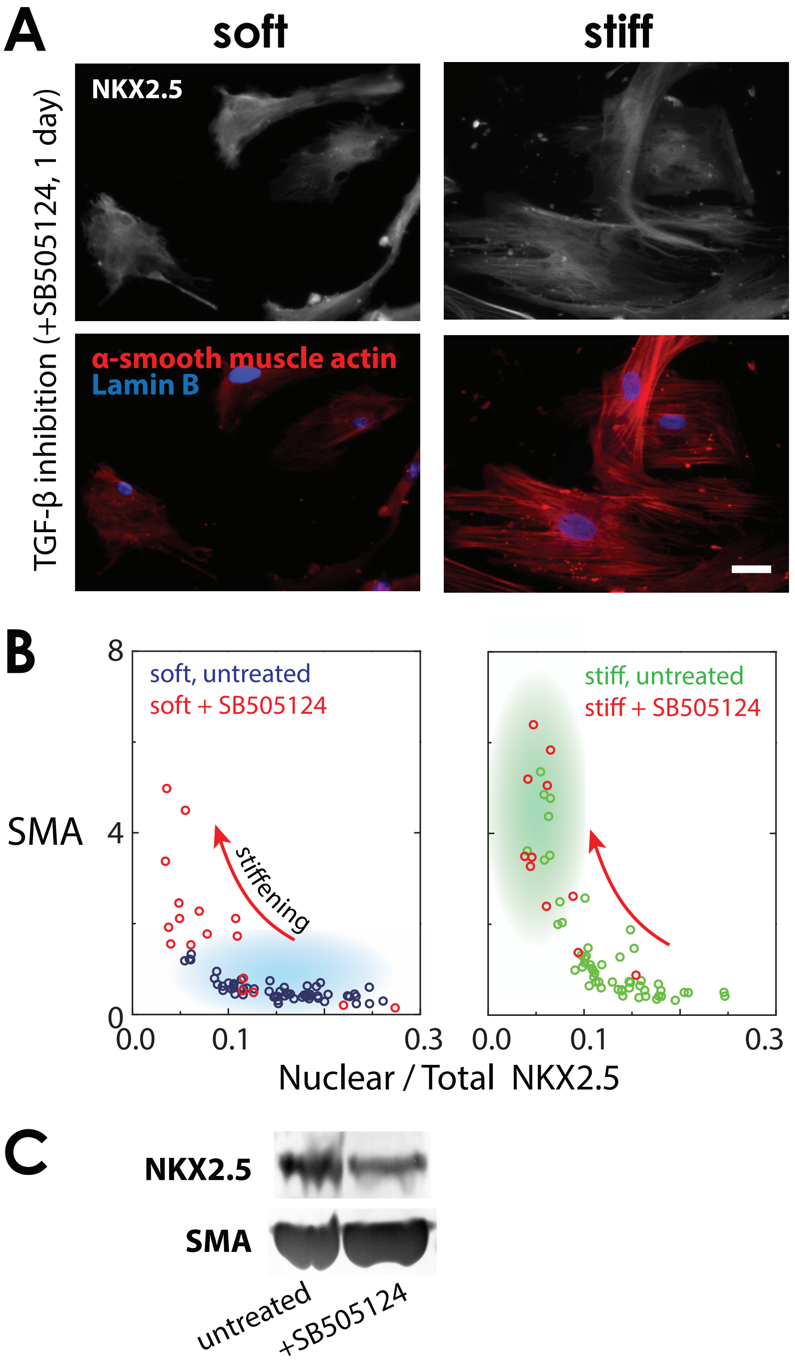
A
soft
stiff
TGF-β inhibition (+SB505124, 1 day)
NKX2.5
α-smooth muscle actin
Lamin B
B
soft, untreated
soft + SB505124
stiffening
stiff, untreated
stiff + SB505124
SMA
8
4
0
0.0
0.1
0.3
0.0
0.1
0.3
Nuclear / Total NKX2.5
C
NKX2.5
SMA
untreated
+SB505124

Figure 3.16. TGF-β inhibition recapitulates matrix stiffness-induced nuclear exit of NKX2.5. A, Inhibition of TGF-β pathway (1-day treatment with SB505124, 10 μM; 7-day culture) depleted NKX2.5 (top) from nuclei of MSCs cultured on both soft (0.3 kPa, left) and stiff (40 kPa, right) gels, and increased SMA (bottom). Hoechst 33342 for DNA, blue. Scale bar, 50 μm. **B** Scatterplots of SMA intensity vs nuclear/total NKX2.5 in MSCs on soft vs stiff matrices with or without TGF-β inhibition (1-day treatment, 7-day culture). **C**, Sustained treatment (3 days) of SB505124 reduced NKX2.5 but increased SMA levels in MSCs.

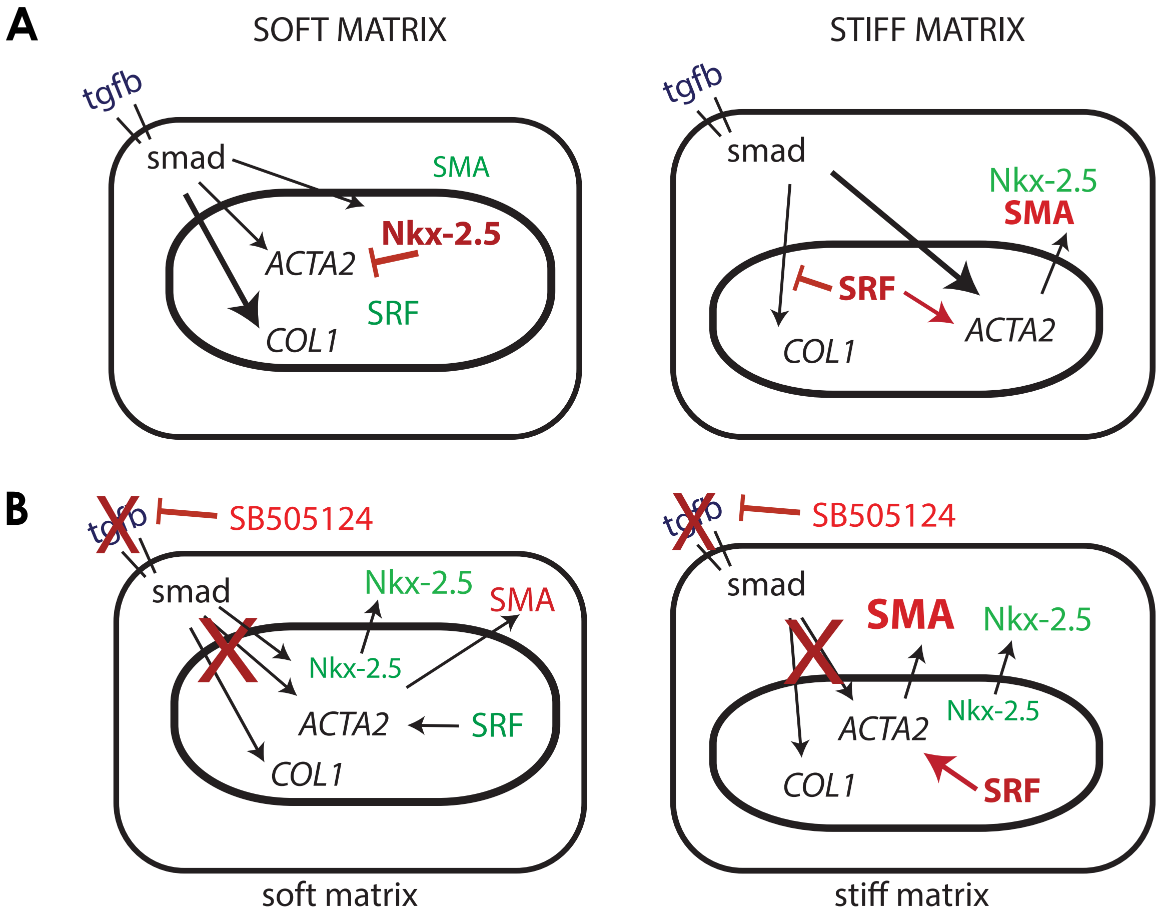
A
SOFT MATRIX
tgfb
smad
SMA
Nkx-2.5
ACTA2
SRF
COL1
STIFF MATRIX
tgfb
smad
Nkx-2.5
SMA
SRF
ACTA2
COL1
B
tgfb
SB505124
smad
Nkx-2.5
SMA
Nkx-2.5
ACTA2
SRF
COL1
soft matrix
tgfb
SB505124
smad
SMA
Nkx-2.5
Nkx-2.5
ACTA2
COL1
SRF
stiff matrix

Figure 3.17. Crosstalk of NKX2.5 and Serum Response Factor (SRF) with TGF-β signaling. A, At basal TGF-β and SRF activity, soft matrix-induced nuclear localization of NKX2.5 represses *ACTA2*, while stiff matrix induces high SRF activity (Swift et al., 2013b) that could then inhibit TGF-β induction of collagen-1 (Lee et al., 2007). **B**, Inhibiting TGF-β (i.e. with SB505124 treatment) prevents collagen-1 but not SMA, due to basal SRF activity on soft matrix, or to enhanced SRF activity and nuclear exit of NKX2.5 on stiff matrix. Sustained TGF-β inhibition also reduces total NKX2.5 expression leading to further SMA expression.

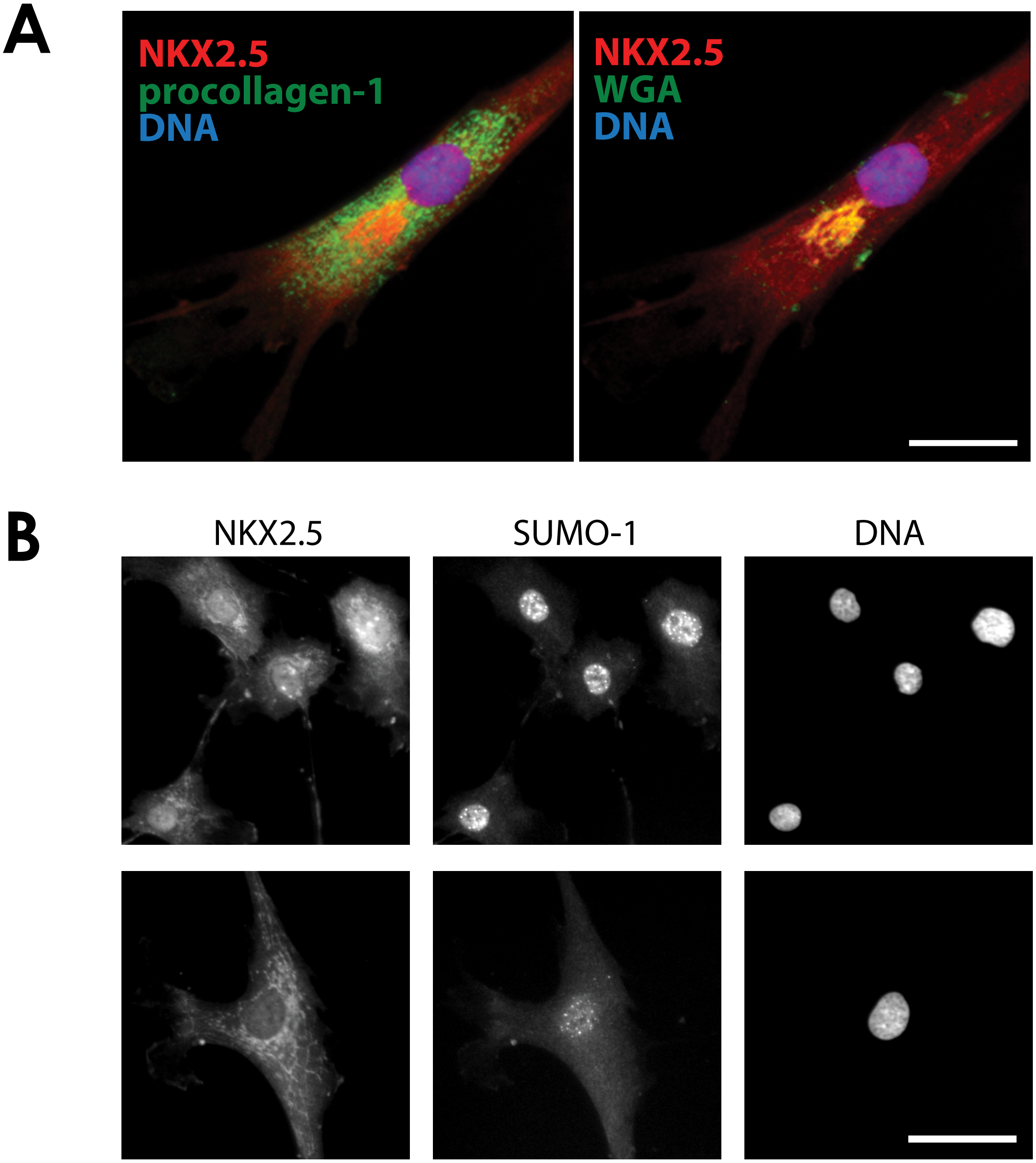

Figure 3.18. Post-translational modifications of NKX2.5. A, NKX2.5 was also found in the Golgi apparatus, as visualized by fluorescein-labeled wheat germ agglutinin (WGA; right, green). In contrast, procollagen-I staining (left, green) is predominantly in the endoplasmic reticulum. DNA, blue. Scale bar, 10 μm. **B**, Colocalization of NKX2.5 and SUMO-1 in MSC nuclei. (Top) MSCs with small spread areas had nuclear NKX2.5 (left) and enhanced nuclear SUMO-1 intensities (middle), but not in highly spread MSCs with NKX2.5-depleted nuclei (bottom). Hoechst 33342 staining for DNA (right). Scale bar, 50 μm.

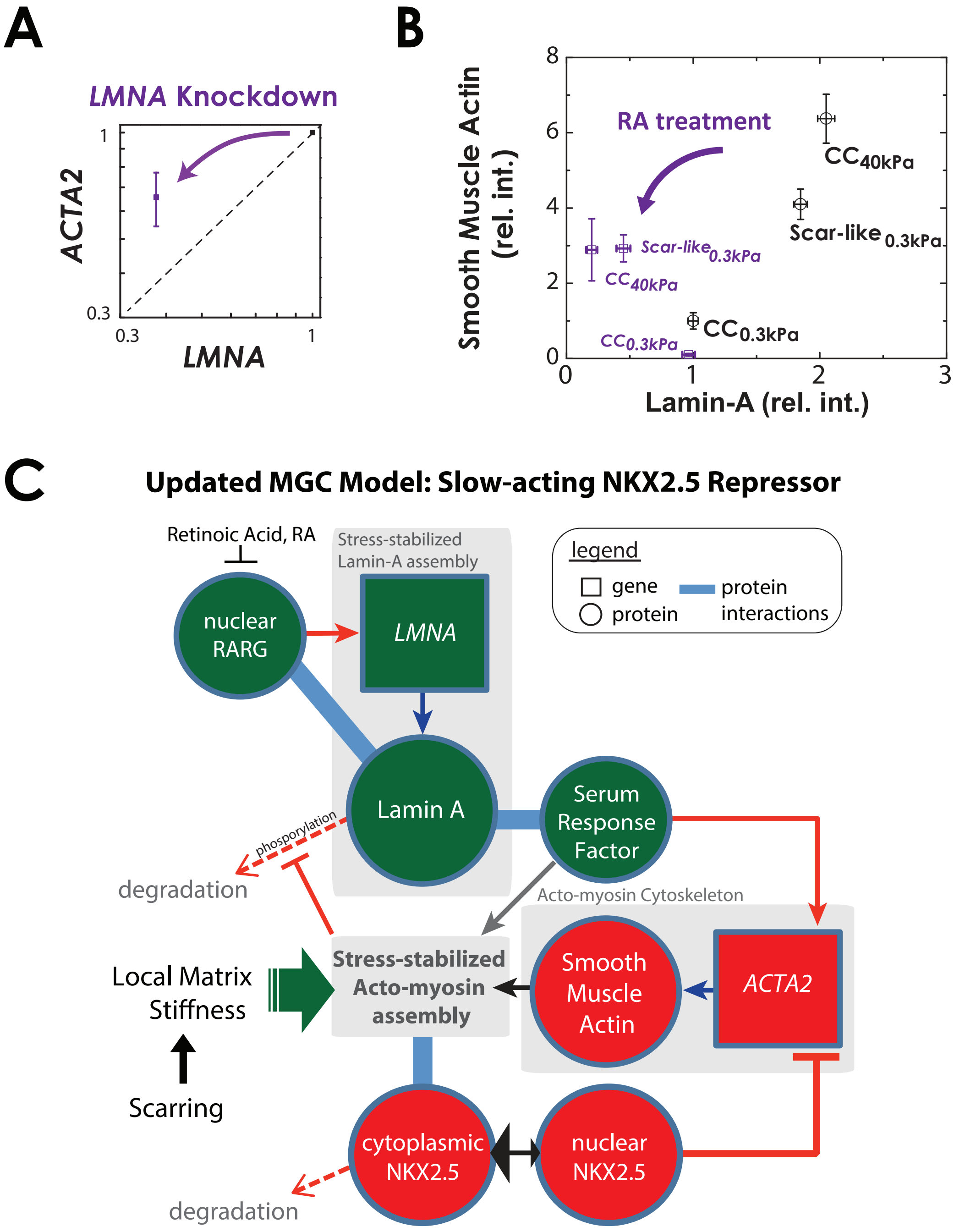

Figure 3.19. NKX2.5 de-repression on stiff matrix, which couples SMA and Lamin-A upregulation, is independent of retinoic acid/Lamin-A/SRF axis. **A**, Effect of *LMNA* knockdown to *ACTA2* levels in MSCs. **B**, Quantitative immunofluorescence of lamin A and α-smooth muscle actin (SMA) levels in MSCs cultured on gels with or without Retinoic Acid (RA, 1 μM) treatment for 7 days (mean $\pm$ s.e.m.). **C**, Retinoic acid (RA) disrupts stress-stabilized lamin-A assembly (but only partially disrupts downstream SMA) through retinoic acid receptor-γ (RARG) (Swift et al., 2013b), as NKX2.5 functions independently as a slow-acting, mechanosensitive repressor of SMA.

Chapter 4

Systems Mechanobiology: Tension-inhibited protein turnover is sufficient to physically control gene circuits

Portions of this work appear in *Science* 341:1240104, 2013 and *Current Biology* 24:R1-R7, 2014.

Abstract

Mechanotransduction pathways convert forces that stress and strain structures within cells into gene expression levels that impact development, homeostasis, and disease. The levels of some key structural proteins in the nucleus, cytoskeleton, or extracellular matrix have been recently reported to scale with tissue- and cell-level forces or mechanical properties, and so the mathematics of mechanotransduction becomes important to understand. Here, we show that if a given structural protein positively regulates its own gene expression, then stresses need only inhibit degradation of that protein in order to achieve stable, mechanosensitive gene expression. This basic 'use it or lose it' module is illustrated by application to meshworks of nuclear lamin A, mini-filaments of myosin II, and extracellular matrix collagen fibers – all of which possess filamentous coiled-coil/supercoiled structures. Past experiments not only suggest that tension suppresses protein degradation mediated and/or initiated by an enzyme, but also that transcript levels vary with protein levels as key transcription factors are regulated indirectly by these structural proteins. Coupling between modules occurs within single cells and between cells in tissue, as illustrated during embryonic heart development where cardiac fibroblasts make collagen that cardiomyocytes contract. With few additional assumptions, the basic module has sufficient physics to control key structural genes in both development and disease.

4.1 Introduction

Polymer physics provides fundamental explanations for how elasticity and viscosity of diverse polymer systems often scale as power laws with polymer concentration (Rouse, 1953), even when the polymers interact or assemble (Doi and Edwards, 1978). Living organisms are of course built from biopolymers (**Figure 4.1**A), and assembling proteins such as extracellular matrix (ECM) collagens, which are the most abundant proteins in metazoans, exhibit gel elasticities that indeed scale with concentration when purified and reconstituted (Yang et al., 2009). Not surprisingly perhaps, tissue stiffness not only scales with collagen levels, but is actually dictated by the amount of collagen with soft tissues such as brain having much less collagen than stiffer tissues such as muscle (Swift et al., 2013b). However, biopolymers that include many other key structural proteins within cells and tissues are subject to a variety of enzymatic processes of degradation and synthesis on time scales that can be only hours or days (Schwanhausser et al., 2011; Eden et al., 2011). How the mechanics of a tissue or cell reaches or maintains a steady state is therefore a fundamental question of biopolymer physics that impacts the form, function, and dysfunction of cells and tissues in general.

Some of the earliest examples of tension-mediated protein stability were demonstrated in cyclically beating neonatal rat heart cells, where components of the contractile myofibril assembly such as cardiac actin (Sharp et al., 1993) and myosin heavy chain (Byron et al., 1996) were found degraded when contractile activity was reduced. For collagen, recent evidence suggests mechanical strain stabilizes against enzymatic degradation (Flynn et al., 2010). High matrix stiffness is further associated with an increased stress or tension in the cell (Discher et al., 2005), and the key contractile protein, myosin II, responds to matrix stiffness by assembling into stress fibers and increasing in amount (Rehfeldt et al., 2012; Engler et al., 2006). More recently, we have shown that nucleoskeletal lamin-A level scales with tissue microelasticity E, with higher lamin A levels giving physically stiffer nuclei in stiffer tissues (Swift et al., 2013b). Lamin A and myosin II thus seem to mechanically couple to the collagenous matrix (Figure 4.1A) in ways that are prescribed by polymer physics. These coiled-coil proteins that assemble into structural networks are prime candidates as biological tension sensors, transducing similar mechanical signals from the ECM to the nucleus (Wang et al., 2009).

Genome-wide measurements of the production and degradation dynamics of mRNA as well as protein in mouse fibroblasts (NIH 3T3) in standard cultures (Schwanhausser et al., 2011) have shown that mRNA and protein half-lives are fairly uniform within structural groupings of collagens, integrins, and actomyosin components (Figure 4.1B). Collagen and actomyosin modules differ significantly in half-lives, and the integrins exhibit intermediate half-lives consistent perhaps with these membrane proteins serving as intermediary linkages between ECM and the cytoskeleton. Even structural proteins on the nuclear envelope such as lamins exhibit largely coordinated expression as a single module, with half-lives similar to those for the actomyosin module. This seems consistent with mechanically coordinated responses of the nuclear lamina to cytoskeletal stresses (Houben et al., 2007). Regardless, for a given structural gene (S) and its corresponding protein (s) in a module, the typical rate equations are:

$$\frac{dS}{dt} = \alpha - \beta \tag{4.1}$$

$$\frac{ds}{dt} = \gamma - \delta \tag{4.2}$$

where α and γ are synthesis rates, and β and δ are degradation rates for mRNA and protein, respectively. Any of these terms could in principle be functions of S, s and other factors such as tension. The goal here is to identify a possible minimal model that fits the current understanding of tension coupling to gene expression.

Tension on coiled-coil assemblies has been shown to suppress the affinity of a phosphorylating kinase/protease that initiates enzymatic solubilization/degradation (Flynn et al., 2010; Raab et al., 2012; Swift et al., 2013b; Buxboim et al., 2014). Like pulling on a wet rope to wring out water, tension squeezes out free volume or sterically shields a binding site via coiled-coil assembly to prevent enzyme access. Single-molecule studies of collagen have suggested tension-enhanced degradation (Adhikari et al., 2011), but such short polymers tend to unwind under tension, whereas rope-like polymers would tend to tighten their coils and knots. Regardless of the mechanism, the rate of degradation can be generally represented by Michaelis-Menten kinetics (Michaelis and Menten, 1913) as

$$\delta(s) = \frac{\delta_0 s^n}{K_s^n + s^n} \tag{4.3}$$

where δ_0 is the maximum degradation rate at saturating concentrations of substrate s, such as a coiled-coil protein assembly. K_s is an enzyme affinity for the substrate and is also a surrogate for tension; n is a cooperativity coefficient ≥ 2 that is typical of multimeric interactions. By incorporating Equation (4.3) to Equation (4.2) and by including an experimentally supported mechanism for transcriptional control, we solve the system of differential equations at steady state and arrive at a relationship between S, s and tension-surrogate K_s.

Starting with the model above applied to lamin A, we then extend the model to two structural modules that couple the nucleoskeleton to the cytoskeleton. Dynamics on the tissue-level is then illustrated with a ‘two-cell type’ model of embryonic heart development. Our parsimonious models thus likely elaborate systems-level behavior of structural modules that respond to mechanical stress. These results have implications for both the physiology and pathophysiology of diseases involving structural proteins, from early cardiac development to stress-dependent aging.

4.2 Results and Discussion

4.2.1 Tension-inhibited degradation of coiled-coil proteins

With lamin-A as a representative mechanosensitive protein, we predicted systems-level trends by constructing a parsimonious model of its gene circuit that takes into account transcription (α) to be regulated by its own protein and protein turnover (δ) to be tension-dependent (**Figure 4.2**A). For simplicity, synthesis of messenger RNA (mRNA) and protein as well as degradation of mRNA were all assumed to be linear with rate constants of order unity (to eliminate bias on one biological process). Other variations for the reaction orders of α, β, and γ in Equations (4.2) and (4.3) were explored further in Appendix B, and only first-order rates can sufficiently recapitulate experimental observations. Kinetic measurements of lamin-A changes with mechanical perturbations are clearly needed to further develop the model. Nonetheless, Lamin-A protein is known to feed back on its own message as it positively regulates it own transcription factor, retinoic acid receptor-γ (RARG) (Swift et al., 2013b), such that the respective rate equations for lamin-A mRNA (L) and protein (l) are:

$$\frac{dL}{dt} = \tilde{\alpha} \cdot l - \tilde{\beta} \cdot L \tag{4.4}$$

$$\frac{dl}{dt} = \tilde{\gamma} \cdot L - \delta(l) \tag{4.5}$$

where $\tilde{\alpha}$ is a first-order protein-induced mRNA-production rate constant, $\tilde{\beta}$ is a first-order mRNA-degradation rate constant, $\tilde{\gamma}$ is a first-order mRNA-translational rate constant, and δ is a tension-dependent protein-degradation rate, as described in Equation (4.1).

Time evolution of protein (l) and mRNA (L) can be analytically solved with example trajectories in Figure 4.2B as a phase plot of $l(t)$ versus $L(t)$ converging to $\{l_{ss}, L_{ss}\}$. The phase plot suggests a stable steady-state node, lending both mathematical consistency and biophysical relevance to the parsimonious model. It also suggests that the initial protein and mRNA levels dictate expression dynamics. For example, for lamin A and the nucleoskeletal module, which have stable protein levels but unstable mRNA levels (Schwanhausser et al., 2011), protein dynamics for a given tension set point (K) are predictably well-controlled and stabilize linearly towards steady-state (Figure 4.2B, upper left quadrant). Lamin A is of course known for tethering heterochromatin near the nuclear envelope, and thus, may need a relatively stable protein expression. Other gene groups with unstable mRNAs include RNA-binding proteins (Schwanhausser et al., 2011). On the other hand, the ECM module has the opposite trend (Figure 4.1B); the kinetics of the model predicts that for highly stable mRNA but short-lived protein levels, the dynamics are nonlinear (Figure 4.2B, lower right quadrant). That is, protein levels would overshoot prior to stabilizing at a steady-state level. The kinetics of this regime was verified by tracking collagen protein expression in mesenchymal stem cells over time from suspension to attachment, starting at low collagen protein levels but with *COL1* mRNA levels remaining relatively stable among structural genes (Figure 4.1B). With an initially high mRNA level (Figure 4.2B, lower right quadrant), collagen protein tended to overshoot prior to stabilizing at a lower steady-state concentration, as was observed experimentally over 7 days (**Figure 4.3**). Other gene groups in this regime include those involved in defense response and homeostasis

(Schwanhausser et al., 2011).

Ultimately, tension dictates lamin-A (and *LMNA*) levels regardless of initial conditions, such that at steady state,

$$\frac{dl}{dt} = 0, \quad \frac{dL}{dt} = 0 \tag{4.6}$$

Equations (4.4) and (4.5) can be analytically solved for $n = 2$ to yield nonzero steady-state values for l and L,

$$\{l_{ss}, L_{ss}\} = \left\{ \frac{1}{2}\left(\frac{\tilde{\beta}\delta_0}{\tilde{\gamma}\tilde{\alpha}}\right) - \frac{1}{2}\sqrt{\left(\frac{\tilde{\beta}\delta_0}{\tilde{\gamma}\tilde{\alpha}}\right)^2 - 4K_l}, \quad \frac{\tilde{\alpha} l_{ss}}{\tilde{\beta}} \right\} \tag{4.7}$$

Based on the steady-state analysis above, a solution only exists if

$$\left(\frac{\tilde{\beta}\delta_0}{\tilde{\gamma}\tilde{\alpha}}\right)^2 - 4K_l > 0 \tag{4.8}$$

Although steady-state values depend on the various rate constants, we assumed all to be important and of order ~1 as we focus on K_l: at high stresses where lamin-A assembly is favored, K_l increases so that phosphorylation-mediated lamin-A degradation (Buxboim et al., 2014) decreases. Plotting steady-state lamin-A levels l_{ss} against different values for K_l fit a power-law $l_{ss} \sim K_l^2$ (for $n = 2$). As a test of whether such a model could capture key experimental trends, computational results showed that if K_l = (Tension)$^{0.3}$, then $l_{ss} \sim$ (Tension)$^{0.7}$ (Figure 4.2C), which parallels the scaling of lamin A with tissue microelasticity E (noting that Tension $\sim E$; Swift et al., 2013b). The set of equations and trends delineated above also applies obviously to collagen as it defines tissue E itself, and it was found to scale more strongly experimentally ($E^{1.5}$; Swift et al., 2013b).

4.2.2 Mechanical coupling of coiled-coil modules in series

We further developed our model by coupling two coiled-coil modules, e.g. cytoskeleton and nucleoskeleton, with nonmuscle myosin (e.g. MYH9) and lamin A as representatives in their respective modules. Lamin-A $\{L, l\}$ and nonmuscle-myosin $\{M, m\}$ message and protein circuitry is schematically presented in **Figure 4.4**A. In particular, expression kinetics were described as coupled rate equations for the respective transcripts $\{L, M\}$ and proteins $\{l, m\}$:

$$\frac{dL}{dt} = \tilde{\alpha}_1 \cdot l - \tilde{\beta}_1 \cdot L \tag{4.9}$$

$$\frac{dl}{dt} = \tilde{\gamma}_1 \cdot L - \underbrace{\delta_1 \cdot \frac{l^{n_l}}{K_l^{n_l} + l^{n_l}}}_{\text{coupled to myosin}} \tag{4.10}$$

$$\frac{dM}{dt} = \tilde{\alpha}_2 \cdot m - \tilde{\beta}_2 \cdot M \tag{4.11}$$

$$\frac{dm}{dt} = \tilde{\gamma}_2 \cdot M - \underbrace{\delta_2 \cdot \frac{m^{n_m}}{K_m^{n_m} + m^{n_m}}}_{\text{coupled to matrix } E} \tag{4.12}$$

Again for simplicity, mRNA degradation and translation rates were assumed of first order. Lamin-A protein positively regulates one of its transcription factors (*RARG*; Swift et al., 2013b) as does MYH9 with one of its transcription factors (*SRF*; Miralles et al., 2003) so that each enhances its own transcription (with rate constants, $\tilde{\alpha}_1$ and $\tilde{\alpha}_2$, respectively). Mechanical regulation of protein phosphorylation and turnover has been demonstrated in recent studies (Raab et al., 2012; Swift et al., 2013b; Buxboim et al., 2014), and so we described lamin-A and myosin turnover with suitable Hill functions (rate constants δ_1, δ_2). Specifically, lamin-A turnover is dictated by $K_l = m^{x/n_l}$ for some x that dictates sensitivity of lamin-A degradation to myosin-generated stress. Myosin protein turnover depends on matrix elasticity as simply $K_m = E^{y/n_m}$ for some y that represents the affinity for myosin degradation. Both K_m and K_l effectively couple matrix mechanics to cytoskeletal stress, which in turn tenses the nucleoskeleton (Figure 4.1A; Wang et al., 2009).

Equations (4.9) to (4.12) above were solved numerically at steady state (all derivatives $= 0$; see Appendix B.3). Rate constants and free parameters were adjusted collectively within an order of magnitude of each other (Appendix B.1.2) to reflect the observed similar half-lives of the modules (Figure 4.1B). In the simplest case, we first assumed synthesis and degradation rate constants to be equal ($\tilde{\alpha}_1 = \tilde{\alpha}_2; \tilde{\beta}_1 = \tilde{\beta}_2; \tilde{\gamma}_1 = \tilde{\gamma}_2; n_m = n_l; x = y$) and observed that, for any given E, the range of expression for myosin is larger than that for lamin A (Figure 4.4B). This likely reflects the matrix-cytoskeleton-nucleoskeleton assembly in series (Figure 4.1A). Nonetheless, as matrix and cell tension suppresses protein phosphorylation and turnover, steady-state levels monotonically increase with matrix E, consistent with coupled mechanoregulation of lamin A and myosin (Buxboim et al., 2014), just as with SMA and lamin A (Figure 2.12A).

If we consider a first-order effect of lamin-A protein on MYH9 transcription via SRF pathway (Swift et al., 2013b), then we can modify Equation (4.11) as:

$$\frac{dM}{dt} = \tilde{\alpha}_2 \cdot m + \tilde{\alpha}_3 \cdot l - \tilde{\beta}_2 \cdot M \tag{4.13}$$

In this case, numerical analysis showed that the dynamic range of myosin increased further due to matrix E and lamin-A contributions, but not the relative slope of the myosin–lamin-A response to matrix E (Figure 4.4C). The relative sensitivity of each module is instead dependent on x and y. If sensitivity of lamin A to degradation (x) is increased (or decreased), then more (lesser) myosin protein is required to generate the same stress that maintains the original lamin-A protein level (**Figure 4.5**A). Reducing x is similar to decoupling nucleoskeletal and cytoskeletal modules, as was done experimentally by ectopic expression of SUN2, a nuclear membrane protein that connects the nucleoskeleton to the cytoskeleton, which led to reduced lamin-A levels (Swift et al., 2013b). On the other hand, if sensitivity of myosin to degradation (y) is increased, then at low E the steady-state levels of myosin (and indirectly, lamin A) is much lower; at sufficiently high matrix E, myosin (and lamin) levels remain relatively unperturbed (Figure 4.5B). Experiments that observed this prediction include phosphomimetic mutants of nonmuscle myosin IIA that enrich myosin in the soluble pool, and nonphosphorylatable mutants that promote myosin-rich stress fibers (Raab et al., 2012).

4.2.3 Logistic coupling between collagen and myosin in cardiac development

Systems biology can potentially build an integrated understanding of the electrophysiological and physical processes involved in cardiac physiology and pathophysiology. It might also help identify therapeutic targets. Understanding how the balance between mechanical stiffness and contractile ability of the myocardium is achieved with age and pathological changes ultimately requires a systems-level model to guide hypotheses. The expression of actomyosin contractility proteins and collagen, among hundreds of abundant proteins, parallel myocardial stiffening in development (Majkut et al., 2013). Both static/cyclic and uniaxial/biaxial strains encourage collagen matrix deposition by cardiac fibroblasts (MacKenna et al., 2000), as passive and active contraction increase throughout cardiac development. However, as contractility (or myosin levels) increasingly strains the developing heart tissue, we postulate that fibroblast proliferation is ultimately limited by the stiffness of their environment, which correlates strongly with collagen-1 levels (Majkut et al., 2013; Swift et al., 2013b). The various components of the developing heart matrix and cytoskeleton, and any other functionally relevant signaling proteins must be integrated into a realistic physical model of the observed mechanics. Thus, we considered using our simplified model that focuses on the mechanical interaction between the collagenous matrix deposited by cardiac fibroblasts and the contractile activity of cardiomyocytes.

To explore possible general mechanisms, a coupled network of myosin $\{M, m\}$ and collagen $\{C, c\}$ mRNAs and proteins can be modeled within the developing myocardium (**Figure 4.6**A). With collagen produced primarily by cardiac fibroblasts, the rate of collagen mRNA production is assumed to be proportional to the fibroblast population, which is in turn limited by tissue stiffness imparted by collagen matrix density, such that:

$$\frac{dC}{dt} = \underbrace{\tilde{\alpha}_1 \cdot \frac{c^{n_f - 1}}{k_f^{n_f} + c^{n_f}}}_{\text{fibroblast crowding}} - \tilde{\beta}_1 \cdot C \tag{4.14}$$

The collagen mRNA production rate of fibroblasts increases at low collagen matrix densities up to a critical collagen concentration (and hence matrix stiffness), then it decreases thereafter; the amplitude and critical point of this biphasic behavior are modulated by n_f and k_f, respectively (Figure 4.6B).

The concept of tension-mediated degradation is again applied here for collagen protein. Collagen matrices have been shown to be stabilized (against degradation) by applied tension (Flynn et al., 2010), such that:

$$\frac{dc}{dt} = \tilde{\gamma}_1 \cdot C - \underbrace{\tilde{\delta}_1 \cdot \frac{c^{n_c}}{K_c^{n_c} + c^{n_c}}}_{\text{coupled to myosin}} \tag{4.15}$$

Cardiomyocytes are of course the primary contributors of myosin-mediated tension in cardiac tissue, such that $K_c = m^{x/n_c}$ for some x that dictates the extent of myosin-mediated collagen degradation. Additionally, myosin-II molecules under tension remain assembled and abundant (Majkut et al., 2013; Swift et al., 2013b), with some evidence of tension-suppressed phosphorylation of nonmuscle myosin-II suggesting an intermediate step (Raab et al., 2012). Striated muscle myosin-II is certainly turned-over *in vivo* (Ball et al., 1987), and its disuse probably favors degradation and muscle atrophy. Thus, the transcript (M) and protein (m) rate equations for myosin are coupled to collagen such that:

$$\frac{dM}{dt} = \alpha_2 \cdot m - \beta_2 \cdot M \tag{4.16}$$

$$\frac{dm}{dt} = \gamma_2 \cdot M - \underbrace{\delta_2 \cdot \frac{m^{n_m}}{K_m^{n_m} + m^{n_m}}}_{\text{coupled to collagen}} \tag{4.17}$$

where $K_m = c^{y/n_m}$, for some y.

With rate constants and free parameters adjusted within an order of magnitude of each other Appendix B.1.3, Equations (4.14) to (4.17) were solved numerically Appendix B.4 and obtained best agreement with the reported experimental results. By representing the basic assumptions on fibroblast population crowding (Equation 4.14) and tension-stabilized proteins (Eqs. 4.15

and 4.17), the model was able to recapitulate the logistic growth kinetics (Figure 4.6C) observed experimentally for myosin and collagen protein levels in a developing heart (Majkut et al., 2013). The model also predicted, perhaps not surprisingly, that mRNA levels should exhibit the same trends as the protein counterparts (Figure 4.6C).

4.3 Conclusion

The detailed molecular mechanism for tension-mediated stabilization of rope-like coiled-coil polymers is not yet known, but tension in polymer fibers and a polymer network is thought to sterically or conformationally prevent protease binding to collagen fibers (Flynn et al., 2010) or kinase binding to myosin minifilaments (Raab et al., 2012) and lamin-A meshwork (Swift et al., 2013b). Regardless of mechanism, turnover of key structural proteins appears to be mechano-regulated.

In the models presented here, membrane-bound integrins were implicitly overlooked. Overexpressing integrin receptors does not change the ability of a cell to spread, as observed experimentally (Engler et al., 2004b). On the other hand, perturbations to the Linker of Nucleoskeleton and Cytoskeleton (LINC) complex are understandably more complicated with observed cellular genotypic effects as it influences chromatin architecture. Nonetheless, the LINC complex is implicitly included in the x coefficient, as it couples cytoskeletal and nucleoskeletal responses. Indeed by applying force to nesprin-1, an isolated nucleus with an intact nuclear lamina stiffens (Guilluy et al., 2014).

To date, most experimental techniques in developmental biology come short of characterizing a systems-level landscape. Our modeling analysis of collagen and myosin levels in cardiac tissue development (Figure 4.6) demonstrates that coupled structural modules are sufficient to recapitulate the dynamics of tissue-level architecture. Given the highly interconnected signaling pathways in mammalian biology, our work distills the essential mechanobiological circuits that govern not just intracellular but also tissue-level observations.

The inherent difficulty of detailing these circuits with accurate rate constants and functional forms will be addressed by developing more sophisticated “-omic” approaches.

4.4 Methods

The sets of ordinary differential equations (ODEs) that describe the various mechanobiological systems modeled here are explicitly written in Appendix B. The analytical results were also derived where applicable. Numerical integration of systems of ODE were performed in Mathematica (version 8, Wolfram Research). The values of the various rate constants, initial conditions, etc. used in each model are also included in Appendix B.

Steady-state measurements were obtained by allowing the system to run until the levels of each species stabilize.

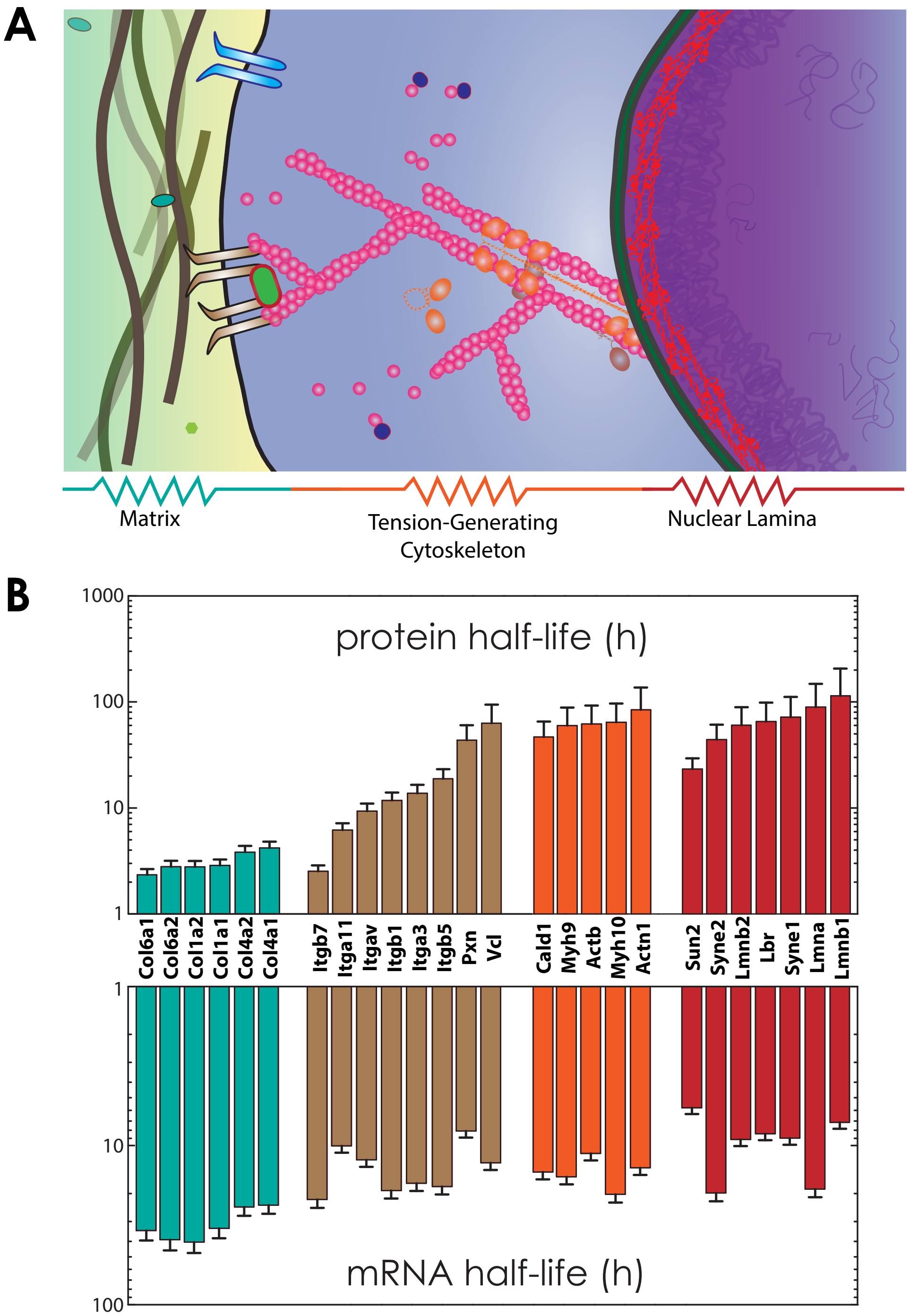

Figure 4.1. Systems-level view of structural molecules involved in mechanotransduction. **A**, A living cell and its microenvironment are built from biopolymers that provide structure; these molecules assemble and are interconnected to resist stress that arises from development or disease. **B**, Protein (top) and mRNA (bottom) half-lives of collagens (teal) membrane-bound integrins (brown), actomyosin (orange), and nuclear envelope components (red) measured in NIH3T3 mouse fibroblasts (Schwanhausser et al., 2011). Half-lives are fairly constant within structural groups suggesting similar dynamics within groups.

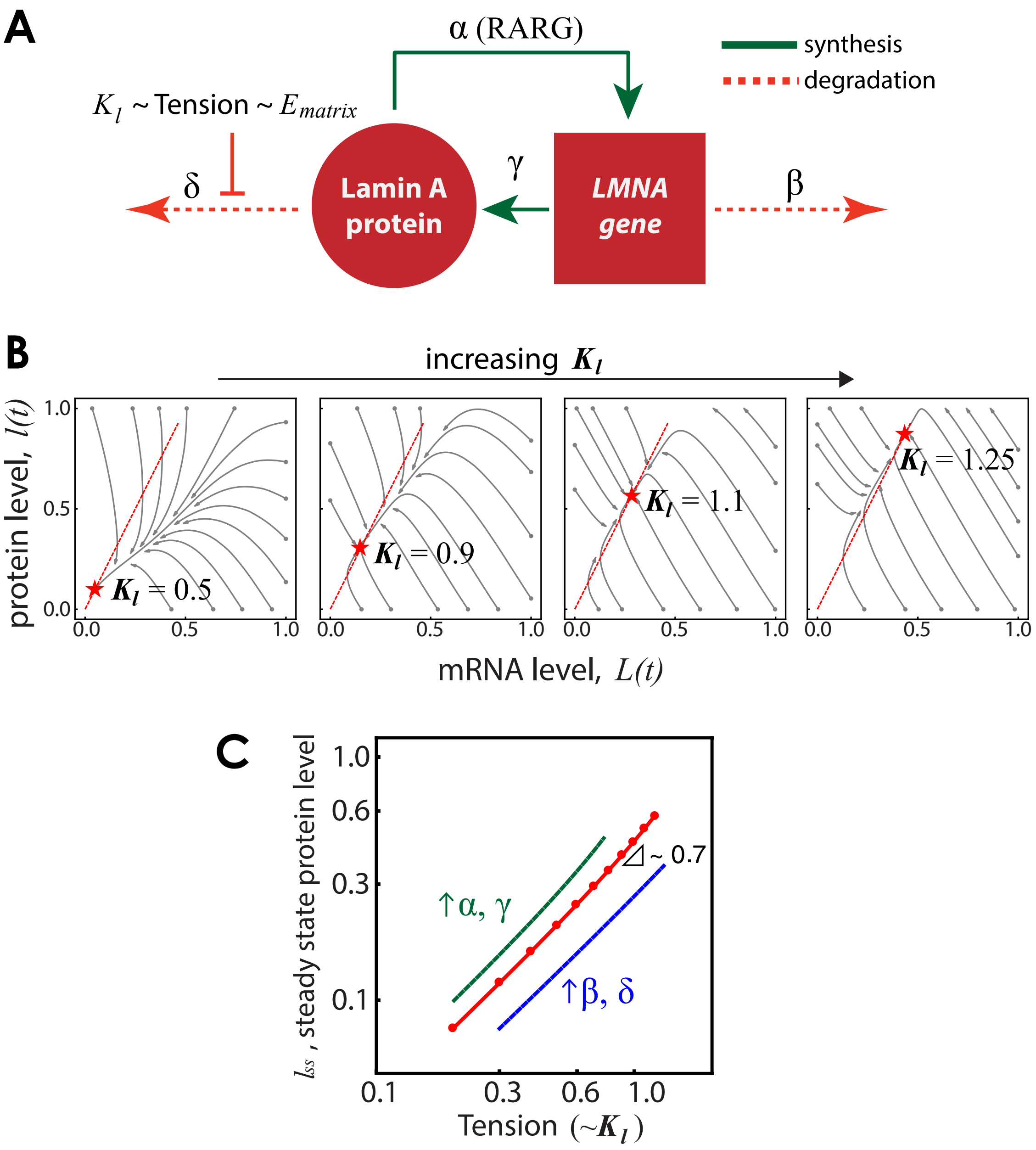

Figure 4.2. Feedback-based mechanobiological gene circuit model for lamin A exhibits polymer-physics scaling if cell tension suppresses protein turnover. **A**, Nucleoskeletal Lamin A protein regulates its own message (*LMNA*) and assembles in response to tension from matrix elasticity (E_{matrix}), which inhibits protein degradation. **B**, Trajectories of lamin-A message and protein as the model converges from a range of initial conditions to a single steady-state solution appropriate to the tension. **C** Setting the kinase/protease binding coefficient, K_l, to be proportional to $(\text{Tension})^{0.3}$ allows the model to generate steady-state scaling with tension, consistent with tissue-level scaling of lamin A (Swift et al., 2013b). Increasing the synthesis (α, γ) or degradation (β, δ) rates shifts lamin-A levels higher or lower, respectively.

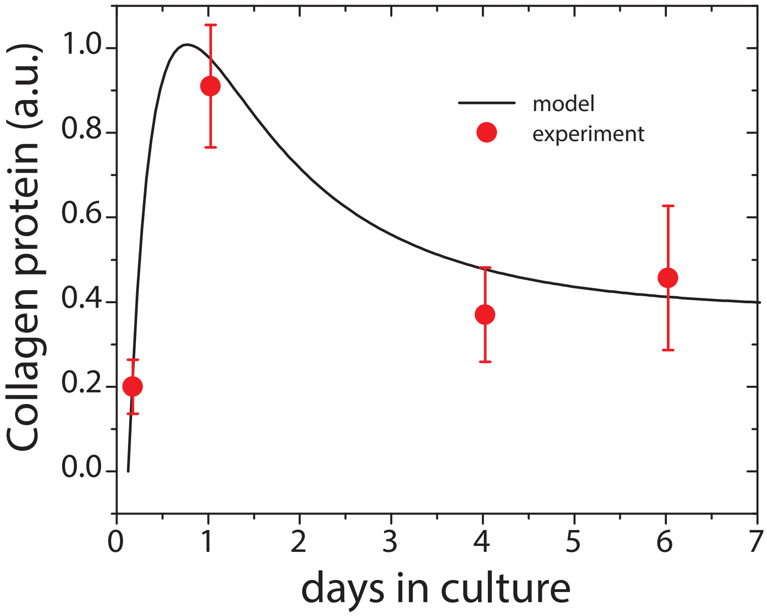

Figure 4.3. Dynamic behavior of collagen-1 produced by mesenchymal stem cells. Procollagen-1 expression in mesenchymal stem cells over 7 days was tracked by immunolabeling and quantified (red). Stem cells adhere and spread on a substrate and start to synthesize collagen matrix, which stabilizes over time. The biphasic response can be recapitulated by the model that assumes tension-based inhibition of collagen protein degradation rate.

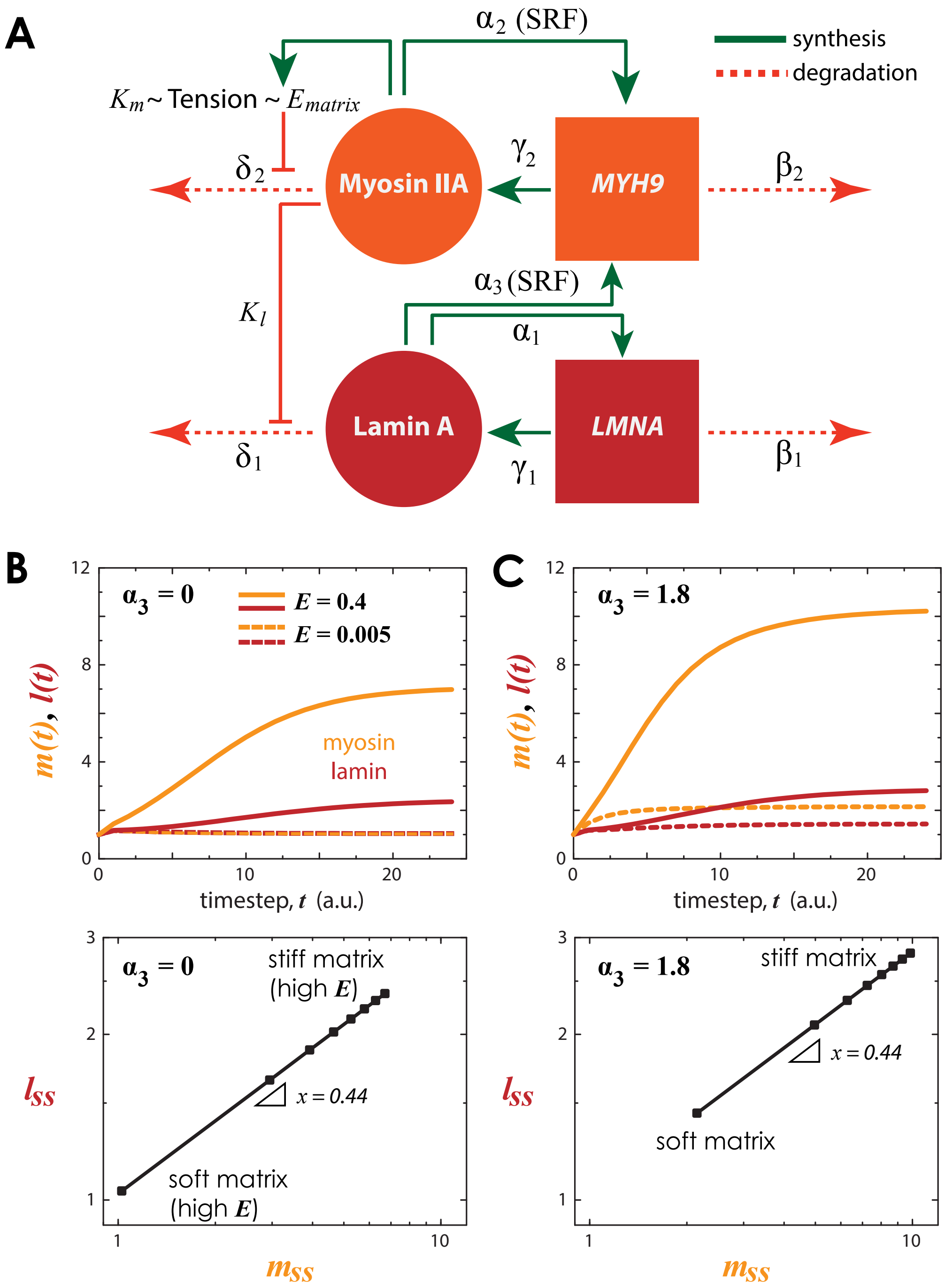
A
α2 (SRF)
synthesis
degradation
Km ~ Tension ~ Ematrix
δ2
Myosin IIA
γ2
MYH9
β2
α3 (SRF)
K_l
α1
Lamin A
LMNA
δ1
γ1
β1
B
α3 = 0
E = 0.4
E = 0.005
myosin
lamin
m(t), l(t)
timestep, t (a.u.)
0
4
8
12
0
10
20
C
α3 = 1.8
m(t), l(t)
timestep, t (a.u.)
α3 = 0
stiff matrix
(high E)
x = 0.44
soft matrix
(high E)
l_ss
m_ss
1
2
3
1
10
α3 = 1.8
stiff matrix
x = 0.44
soft matrix
l_ss
m_ss

Figure 4.4. Matrix stiffness-coupled lamin A and MYH9 turnover. **A**, Cytoskeletal myosin and nucleoskeletal lamin A is coupled where each regulates their own message and follows a tension-inhibited degradation mechanism. Lamin A has also been shown to regulate SRF-target genes (α_3), such as *MYH9* (Swift et al., 2013b). **B**, Kinetics (top) and steady-state (bottom) myosin (m, orange)and lamin A (l, red) protein levels, assuming $\alpha_3 = 0$, at low ($E = 0.005$) or high ($E = 0.4$) tension. **C**, With the known feedback of lamin A on myosin transcription ($\alpha_3 >$ 0), both myosin and lamin levels are increased.

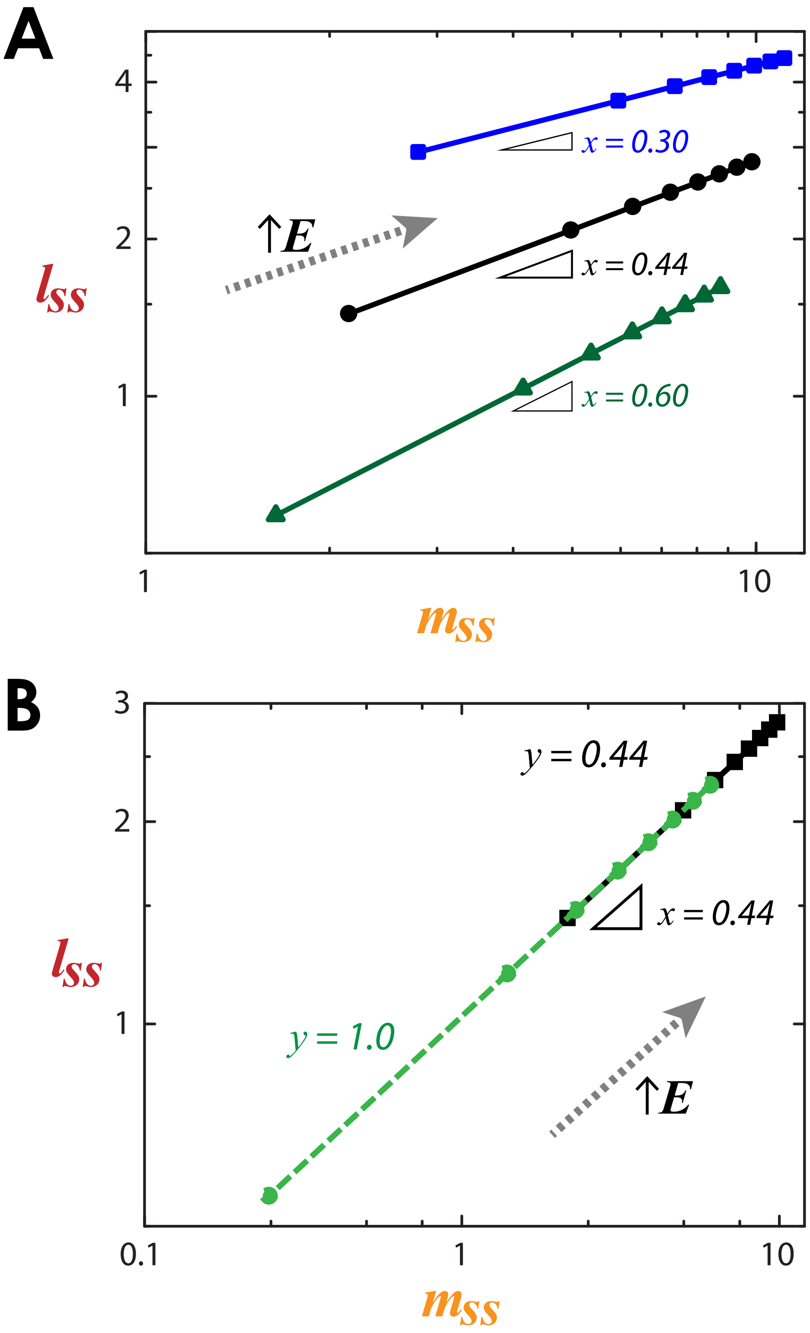

Figure 4.5. Sensitivity analysis of coupled structural modules. A, By varying x, we can perturb the (slope) sensitivity of lamin A to degradation in response to myosin-generated stress. **B**, Varying y perturbs the degradation sensitivity of myosin, but not its coupling with lamin A.

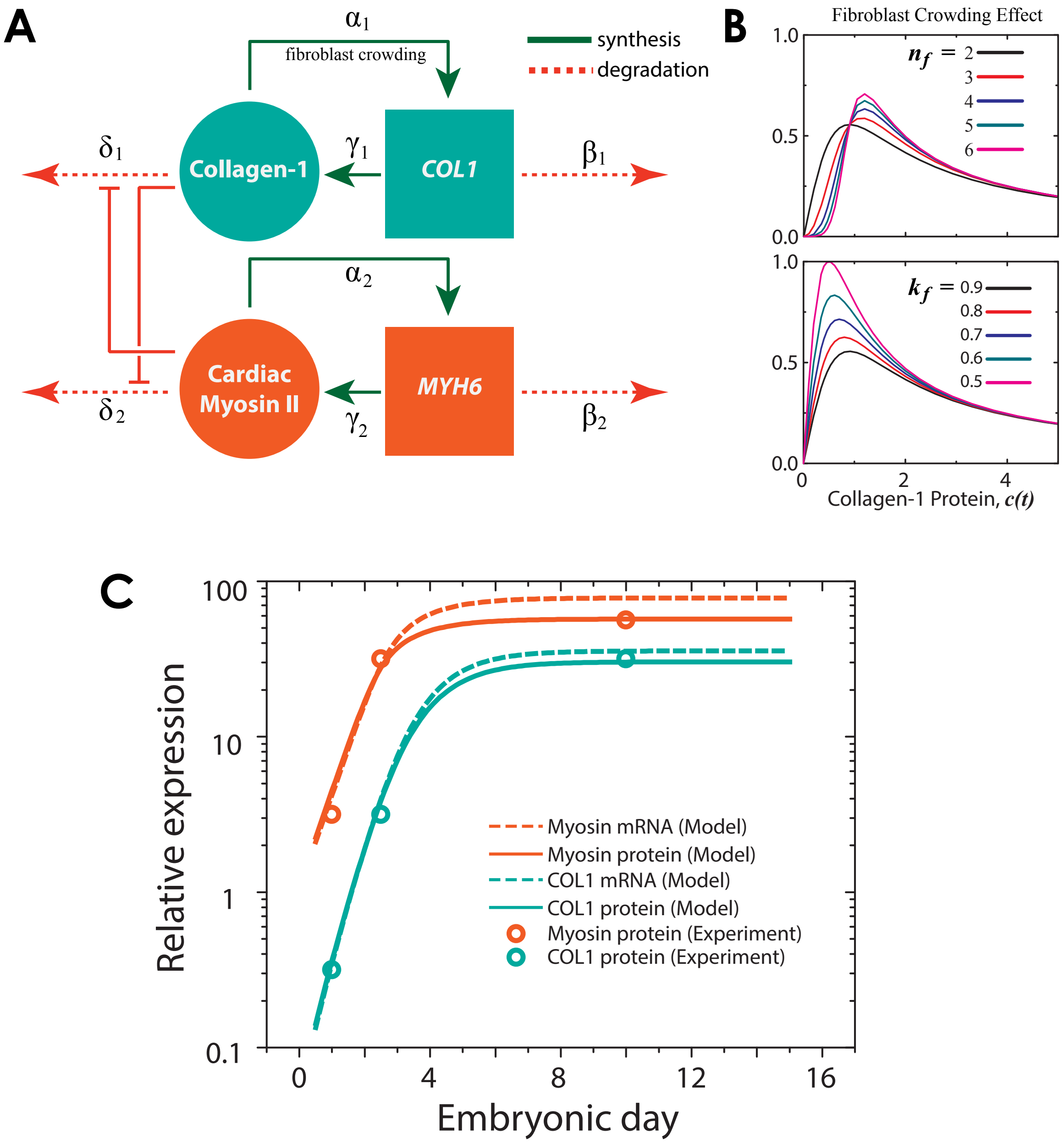

Figure 4.6. Cardiomyocytes and fibroblasts balance contraction and matrix production during heart development. A, Assumptions in matrix stiffness limiting fibroblast population α_1 (and hence, collagen expression), while encouraging myofibril organization in cardiomyocytes (and hence, myosin expression) are incorporated in a model where tension derived from each module inhibits degradation of the other. **B**, Fibroblast crowding is modeled by a Hill function (Equation 4.14) with n_f and k_f as the critical point and amplitude, respectively, of the collagen message production in response to collagen protein (and hence tension). **C**, Experimentally measured changes in both collagen-1 (COL1, teal) and cardiac myosin-II (red) expression (circles) in a developing embryonic chick heart (Majkut et al., 2013) can be recapitulated by the model (protein, lines; mRNA, dashed lines).

Chapter 5

Future challenges in characterization and mechanochemical control of stem cell fate

Portions of this work appear in *Current Opinion of Biotechnology* 28:46-50, 2014 as the cover article.

Abstract

Recent experiments have revealed that stem cells respond to biophysical cues as well as numerous biochemical factors. Nanoscale properties at the cell-matrix interface that appear to affect adherent stem cells range from matrix elasticity to porosity-dependent matrix tethering and geometry of adhesive linkages. Some stem cells can also remodel their immediate environment to influence phenotype, but this depends also on matrix-material properties such as covalent bonding and soft versus hard materials. Efforts to combine both matrix instructions and active cell feedback are required to properly direct stem cell behavior.

5.1 Introduction

Within the last ten years, stem cell approaches have become conceivable or even realized for each of the roughly 200 differentiated cell types in humans. Since most tissue cells are anchorage dependent – meaning that adhesion to a solid is necessary for cell survival – it is only sensible that the mechanochemical nature of the support can influence stem cell fate (Discher et al., 2009). Substrate stiffness, geometry, porosity, and topography are now understood to influence stem cells, perhaps as much as biochemical factors. Molecular pathways of cellular mechanotransduction that ultimately affect both cell phenotype and genotype are slowly becoming clear. Matrix stiffness-dependent lineage commitment of stem cells has been suggested to involve YAP/TAZ, which are transcription factors previously known to influence proliferation; newer evidence suggests they are also nuclear mechano-transducers regulated by Rho GTPase and cytoskeletal tension independent of the canonical Hippo pathway (Dupont et al., 2011). More recently, mass spectrometry-based scaling between tissue stiffness and the nuclear envelope structural protein, lamin A, has been reported to co-regulate YAP and SRF, among other transcription factors, suggesting that increased matrix rigidity leads to nuclear stiffening as a homeostatic response in all tissue types, including stem cells (Swift et al., 2013b; Pajerowski, 2007). In Chapter 3, a novel mechano-repressor NKX2.5 was identified via bioinformatics analysis and was found to maintain long-term maintenance of stem-cell response to matrix stiffness . More pathways are likely to emerge as the field gains control over systems-level technologies and precision design of micro/nano-environments for stem-cell culture *in vitro* and *in vivo*.

Virtually every organ in the body contains resident stem cells or progenitors that contribute to organ homeostasis or repair. Exploiting stem cells for regeneration of damaged tissue has spurred research into their multipotentiality as well as immunocompatibility. Therapeutics is limited in part by *in vitro* cell expansion as well as materials issues that include the design of biocompatible scaffolds for co-transplantation. Since many stem cells are anchorage dependent, injection *in vivo* should work best if the cells adhere quickly and adequately, but it is clear in many trials with mesenchymal stem cells (MSCs) that the vast majority of injected cells die rather than contribute to tissue (Berry et al., 2006). Recapitulating the various stem cell niches *ex vivo* is extremely challenging as it involves spatiotemporal regulation of biostimuli that extend to extracellular matrix architecture (Chapter 1). Nonetheless, understanding the niche *in vitro* might help in translation to *in vivo* (Stevens and George, 2005). In a diseased setting, engrafted stem cells encounter an inflammatory (early-stage) or fibrotic (late-stage) environment; a minimal scar-like model described in Chapter 2 recapitulated the heterogeneity and stiffness of fibrotic tissues, and how different cell types respond to it.

Recent advances as well as challenges in the material control of stem cell multipotency and lineage commitment are described in this Chapter. By “stem cell”, we refer to cited studies on MSCs (mesenchymal), NSCs (neural), ESCs (embryonic), iPSC (induced pluripotent), etc., but we emphasize the generality merely with “stem cell” as mechanochemical rules seem to apply for all types (see Chapter 1). We attempt to highlight in more detail how the field is beginning to formulate materials design rules for stem cell cultures down to the nanoscale in terms of fabrication and/or physical characterization. Approaches are crudely split into soft materials such as hydrogels that are as soft as most tissues or else hard materials in which the softest thing in culture is the cell. Remarkably, there seem to be ways – i.e. rules — to manipulate ‘boundary conditions’ in order to fool cells into responding to a hard material in a manner similar to that on a much softer material, and vice versa.

5.2 Soft matter control

Tissue stiffness or elasticity is dictated by the extracellular matrix (ECM). Even a few minutes of incubation with collagenase can soften a tissue dramatically (Majkut et al., 2013). ECM is comprised of a network of fibrous proteins, such as collagens, that are crosslinked in a homophilic or heterophilic manner. A hierarchical polymeric network of variable density allows for a broad range of characteristic microelasticities for tissues: brain (Georges et al., 2006) and fat (Patel et al., 2005) are hundreds of Pascals in stiffness whereas cartilage (Guilak et al., 2005) and pre-calcified bone (Engler et al., 2006) are dozens of kiloPascals or even stiffer on larger length scales. Precise regulation of physical properties of the ECM seems to match and couple to the applied mechanical forces that contribute to specific cell differentiation programs in adult tissue and likely in the embryo. A differential cell response to both ECM elasticity and dimensionality (i.e. 2D vs 3D) – termed ECM mechanosensing — has been observed *in vitro* through various materials approaches, particularly with natural (Rehfeldt et al., 2012) and synthetic (Engler et al., 2006) hydrogels. Naturally derived polymers such as silk (Wang et al., 2006), collagen and hyaluronic acid matrices (Nicodemus and Bryant, 2008) are currently used as delivery vehicles for cell transplantation. Synthetic scaffolds are chosen based on properties that range from biostability or biocompatibility to biodegradability and porosity. Inert synthetic hydrogels are used *in vitro* for studying cell behavior such as migration, proliferation, and differentiation. Indeed, due to the chemistry that can sometimes be very simple, physical parameters such as elastic and viscous moduli can be precisely tuned to mimic biological tissues.

5.2.1 Synthesis, Functionalization and Characterization

The basic components for polymer hydrogel synthesis are a monomer, a crosslinker, and an initiator of polymerization. The ratio and concentration of monomer and crosslinker are varied to achieve desired viscoelastic properties, perhaps to mimic a normal or diseased tissue or perhaps to be distinct from a tissue. For example, a myocardial infarct stiffens two- to three-fold more than a normal heart tissue (∼20kPa; Berry et al., 2006). Rheological methods provide measures of a material's complex modulus or stiffness (G^*) composed of both an elastic modulus (G') and a viscous modulus (G''). These can be measured as a function of frequency of oscillatory shear with a rheometer, and one typically considers that the 1-Hz beating of the heart is close to the high frequency limit of biological relevance. Solid tissues are mostly elastic, with G' values ranging from 0.1–100 kPa (Engler et al., 2006). Material-dependent cell responses are thus strongly influenced by the elastic component of a hydrogel, at least when G'' is two orders of magnitude lower than G'. Viscous matrix effects on cell morphology are nonetheless interesting based on recent examples in the literature (Murrell et al., 2011; Cameron et al., 2011).

Control of hydrogel chemistry can extend to spatiotemporal control of polymerization (Kloxin et al., 2009) and micropatterning (Marklein and Burdick, 2010). Non-uniform substrates might, for example, mimic a heterogeneous cell microenvironment, but in such a case, rheological measurements must be done at the cellular scale. One particularly attractive method is atomic force microscopy (AFM): a cantilever probe reflects a laser onto a photodiode detector that measures small variations in cantilever deflection as it indents a substrate. For such heterogeneous substrates, an AFM cantilever can probe and create a viscoelastic map along a preset path. For example, we examined "durotaxis" in Chapter 2, which is a phenomenon in which a cell migrates toward increasing matrix stiffness (Lo et al., 2004), and so we and others made hydrogels with stiffness gradients and used AFM to measure the steepness of those gradients (Raab et al., 2012; Isenberg et al., 2009).

Most hydrogels require some form of functionalization to promote favorable cell-material interactions. This can be done by linking cell-adhesive moieties into the polymer backbone, via functional side group chemistry. The well-known integrin-binding tripeptide RGD can be incorporated into a methacrylated polymer backbone (e.g. methacrylated polyethylene glycol) via a Michael-type addition reaction between thiol (from a cysteine moiety in the cell-adhesive peptide) and methacrylate groups (Marklein and Burdick, 2010). Large matrix proteins like fibronectin and collagen can also be covalently crosslinked into an amide-containing hydrogel backbone via a heterobifunctional crosslinker that contains a primary amine-reactive succinimidyl ester and a photoactivatable nucleophilic azide (e.g. Sulfo-SANPAH) (Pelham and Wang, 1997). Conventional matrix functionalization of hydrogel systems involves copious coverage of the cell-material interface with cell-adhesive molecules, to ensure that cell attachment is not adhesion ligand-limited and that any differential cellular response is due to physical properties of the matrix.

5.2.2 Advances in Soft Matter Research

Whereas past studies of the cell-material interface have focused on the effects of relatively homogeneous and weakly varying materials on stem cells, recent efforts have begun to address some aspects of matrix micro-/nano-heterogeneity. Tools that allow non-invasive in situ measurements of cell-material interaction at the small scales could ultimately clarify governing principles for cell-material interface design. Fabrication approaches are equally important as they should allow for systematic nanoscale control of substrate topography and functionalization. A great deal of effort is spent in (**1**) understanding how matrix ligand is presented at the interface, (**2**) how a cell adheres and applies ligand- and stiffness-dependent traction forces to a material, and (**3**) how a cell remodels or secretes adhesion-relevant molecules or other factors presented at its interface.

Insight into the first two issues above has been obtained from integrin clustering that occurs when a cell exerts traction forces in response to stiff matrix. Huebsch et al. (2010) found that increasing matrix resistance to adhesion ligand displacement leads to a greater ability of a cell to exert traction forces that allow for more stable integrin-ligand bonds (Kong et al., 2005) and ultimately, greater propensity toward osteogenic commitment. They encapsulated stem cells in 3D non-degradable, RGD-modified alginate gels for which elastic modulus (2.5–110 kPa) was varied by the extent of ionic crosslinking. In contrast to 2D studies where cells spread more in response to increased matrix rigidity, encapsulation in 3D nanoporous hydrogels maintained a rounded shape. The ability of encapsulated cells to rearrange integrin-RGD linkages in the ionically crosslinked alginates is estimated by fluorescence resonance energy transfer (FRET) of rhodamine- and fluorescein-labelled RGD peptides clustering near the cell membrane (Kong et al., 2005) and appeared to depend on matrix stiffness and seemed optimal at an intermediate stiffness ($\sim$20–30 kPa), where integrin receptors were estimated to probe 50 nm into the surrounding environment. In contrast, Khetan et al. (2013) made 3D, covalently crosslinked, methacrylated hyaluronic acid (MeHA) hydrogels (G' = 4–95kPa) and found a lack of matrix elasticity dependence, with most cells driven toward adipogenic commitment. Differences between the two systems start with the nature of crosslinking and could extend to how growth factors in serum differentially bind the gels or permeate gel pores; differentiation-relevant factors in serum include TGF-β, which is in a large latent complex that must immobilize near a cell in order for traction forces to release the active growth factor (Buscemi et al., 2011). Determination of traction-dependent stiffness sensing involves assumptions about matrix stiffness at the cell interface and is difficult to assess when cells are embedded in 3D. Yet stiffness sensing seems essential for osteogenic commitment and appears dysregulated in cells entrapped within overly restrictive microenvironments. Moreover, dynamically fluctuating tractions in and around focal adhesions are necessary for matrix rigidity sensing (Plotnikov et al., 2012).

The third issue mentioned above is how stem cells release their own matrix and other factors or else modify pre-existing factors. Minimizing cell- or serum-derived matrix deposition has been investigated to some extent on ultra-low fouling substrates that are zwitterionic in nature (Jiang and Cao, 2010). In all such studies, proteomic scale analysis of substrates is increasingly needed to define cell and serum responses to manufactured microenvironments; using antibodies to assess whether serum fibronectin or vitronectin adsorbs or not is just a start.

Once measurements are made, however, efforts to prevent adsorption of proteins either from cells or serum can also point the way toward preventing foreign body reactions if materials are to be taken *in vivo* (Zhang et al., 2013). In a study of 3D PEG hydrogels tethered with small-molecule functional groups, stem cell fate had been found to be directed toward adipogenic or osteogenic differentiation with respective functionalization of the gels by t-butyl or phosphate (Benoit et al., 2008). The effects of such small functional moieties have been speculated to reflect differences in cell-derived, lineage-specific matrix molecules which accumulate at the cell-matrix interface and ultimately direct differentiation. In the RGD-modified MeHA hydrogels cited above (Khetan et al., 2013), local matrix changes due to cell-derived matrix did not seem to impede RGD-integrin signaling, but no measurements of matrix were pursued — obviously, 3D microenvironments require deeper and more careful characterization than 2D, at least because of the complexity of protein entrapment through the depth of a gel. When the ability of a cell to probe its surrounding matrix is constrained by complexities of adsorption or encapsulation within covalently crosslinked gels, matrix rigidity (or other physical property) effects on stem cell fate might also be limited.

It must be noted that while promoting cell attachment with matrix-immobilized RGD peptides ensures direct matrix sensing, there are subtle, yet still confounding differences with tethering actual matrix proteins. For example, fibronectin contains an RGD motif, among other motifs, that seems to activate other signaling pathways within the cell, and at least affect cell migration differently from the minimal sequence (Maheshwari et al., 2000). Matrix tethering is an issue raised recently by Trappmann et al. (2012). In contrast to utilizing RGD peptides, which do not involve the tethering issues in 3D, collagen fibrils were functionalized on 2D polyacrylamide (PA) gels or polydimethylsiloxane (PDMS) elastomers. While stem cells differentiated as expected on soft versus stiff PA gels, the apparent stiffness of PDMS had no effect. Unfortunately, soft PDMS is well-known to be difficult to make and requires careful nanoscale characterization; it is often accompanied by increased viscosity (or even fluid-solid heterogeneity), which was not characterized but could adversely affect stem cell differentiation (Cameron et al., 2011) as well as epithelial cell sheet motion (Murrell et al., 2011). Additional studies by Trappmann et al. (2012) involved decreasing the collagen anchoring points on stiff gels by lowering sulfo-SANPAH crosslinker concentration with the effect of inducing a soft gel phenotype that prevented epidermal stem cell differentiation. Ligand density is likely decreased as sulfo-SANPAH is lowered (see Figure 2.4C), and cells simply do not spread on stiff PA gels when adhesive ligand is limiting (Engler et al., 2004a). Nonetheless, the idea of decoupling material stiffness and cell-matrix interactions may have application, as was attempted in our ‘scar in a dish’ model (see Chapter 2).

5.3 Hard matter approaches

The ligands, assembly, and overall architecture of ECM can all influence cell behavior. Parsing some aspects of cell-matrix interaction at the molecular level might be addressed with precision nano-fabrication of hard materials as used in the semiconductor industry. An array of nanotechnology-driven *in vitro* cell culture platforms has been reviewed recently (Kshitiz et al., 2011), and so we highlight here a couple of key advances in nanotopography design principles that are inspired from ECM (Kim et al., 2010) and/or inspire precise control of ECM (Dalby et al., 2007b; Kilian and Mrksich, 2012) in directing cell fate. Nanoscale patterning of cell adhesion ligands is problematic with soft materials because many cell types generate sufficient traction strain to rearrange any ligand pattern.

A minimal adhesive matrix unit required for cell attachment, spreading and migration is an important research question that is addressed with nanopatterned RGD surfaces. Schvartzman et al. (2011) varied RGD ligand spacing, density and cluster size, and found that a spacing of 60 nm in a cluster with a minimum of 4 RGD ligands is sufficient to support cell spreading. Although ligand surface density might have a role, they speculated that talin, an integrin-binding scaffolding protein that has 4 potential binding sites, is involved in the integrin clustering-derived cell response. Focal adhesion formation was indeed enhanced for a ligand spacing of $\sim$50 nm, concomitant with increased cell attachment, migration (Maheshwari et al., 2000) and stiffening (Selhuber-Unkel et al., 2010). In the alginate gel studies by Huebsch et al. (2010), the highest

RGD density is roughly $\sim$1 RGD ligand per 70×70 nm^2 surface patch on an entrapped stem cell of 10-μm radius. This might explain why matrix rigidity-dependent traction forces enhance clustering. In addition, highly ordered 120 nm ligand pits spaced 300 nm apart in a square lattice have been shown for 'best' maintaining adult stem cell multipotency for several weeks, whereas the exquisite sensitivity of stem cells to a pit placement offset of <50 nm leads to differentiation (Dalby et al., 2007b; McMurray et al., 2011). Integrin clustering is thus likely to be a key to some pathways that signal intracellular changes from cytoskeleton to nucleus (Swift et al., 2013b; Dalby et al., 2007a). Epigenetic state and cell reprogramming can also be affected by nanopatterns in recent studies by Downing et al. (2013), which indicate how much more we need to learn about the cell-matrix interface.

5.4 Conclusion

In the heterogeneous microenvironments referred to as stem cell niches, various mechanical and biomolecular cues are integrated to maintain pluripotency or induce differentiation. Biological applications of both soft and hard matter systems to elucidate cell-material interactions have certainly increased our understanding of the stem cell-matrix interface, but there is much more to learn. Soft matter substrates are more tissue-mimetic than hard substrates, but precise nanoscale control of the cell-matrix interface provides powerful tools for understanding and directing a wide range of cell behaviors. Cell-derived molecules are generally overlooked when designing and using many of these materials, whether hard or soft, and 2D or 3D, although some stem cell types express lesser matrix than others. Controlling endogenous expression of such factors by methods such as siRNA knockdown is one approach. Ultimately, new design rules that are emerging for material control of stem cell fate could help with *in vitro* cultures as well as implantable scaffolds for more stem cell-based therapies.

Appendix A

Supplementary Information for Chapter 2

A.1 Adhesion and Thin-film Corrections for scar-like$_{0.3kPa}$ gel

In order to create 2D hydrogel substrates for cell culture, polyacrylamide (PA) gels were sandwiched between an allysilanated bottom coverslip and a nonreactive top coverslip (18- and 25-mm in diameter, respectively; Fisher). Embedding fibrous collagen in polyacrylamide hydrogels exhibited tackiness to the gel surface post-polymerization. That is, removal of the top coverslip required more force than without the fibers. This again provided evidence for interfacial localization of the fibers. To correct for tackiness of scar-like$_{0.3kPa}$ gel, the force required to remove the top coverslip was measured with a custom-made and calibrated polystyrene cantilever (spring constant, k_{sp} = 804.6 N/m), attached at one end to a syringe pump (RS-232, Harvard Apparatus) and the other to a nylon string, which in turn was firmly attached to the top coverslip of a stage-immobilized gel. Syringe pump was set to 'pump mode' pulling the cantilever-string-coverslip setup at an effective velocity of 0.4 mm/s. The removal process was observed with a side-view camera to determine when the pulling string should be stopped and maintained at constant force (zero velocity). Maximal deflection of the cantilever (translated to maximal force of the pulling string) was observed just before coverslip was fully detached (or just before cantilever relaxes back to zero deflection) and used to calculate gel adhesion force. Adhesion force on scar-like$_{0.3kPa}$ gels was found to be 84 $\pm$ 20% higher than on pristine 0.3-kPa gels ($n = 5$).

The effective elasticity can be derived from rigid cylinder (i.e. coverslip of length a) pulling from a soft elastic thin film by assuming non-uniform Boussinesq-type stress distribution at the interface. The force per unit length F/a (along x) or P that propagates from the edge of the coverslip can be derived as (Chung and Chaudhury, 2005):

$$P = D\frac{\partial^3 u_z}{\partial x^3} \tag{A.1}$$

where u_z is displacement field in the z-direction, D is bending stiffness of the coverslip. Since coverslip bending is coupled to the deformation of the hydrogel below it, the characteristic stress decay length, ε, from the edge of contact is (Ghatak et al., 2004):

$$\varepsilon \sim \left(\frac{Dh_1^3}{E_1}\right)^{1/6} \tag{A.2}$$

where h_1 and E_1 is the height and Young's modulus of the thin film, respectively. By taking $u_z \sim \delta_2$, where δ_2 is the thin film extension length at the applied pull-off force, F, and $x \sim \varepsilon$, we can analyze equation (A.1) with (A.2) at the scaling level:

$$P \sim \frac{F}{a} \sim \frac{D\delta_2}{\varepsilon^3} \sim \frac{D^{1/2}E_1^{1/2}\delta_2}{h_1^{3/2}} \tag{A.3}$$

or simply (by removing material-property constants),

$$E_1 \sim \left(\frac{F}{\delta_2}\right)^2 \tag{A.4}$$

for which we can estimate elasticity increase with addition of embedded collagen. Assuming adhesion work is constant (related to surface tension and interfacial area), δ_2 is thus inversely correlated to E_1, which can be derived to scale as $\delta_2 \sim E_1^{-1/3}$ (Chung and Chaudhury, 2005). From equation (A.4), this leads simply to

$$E_1 \sim F^6 \tag{A.5}$$

Thus, surface elasticity of scar-like$_{0.3kPa}$ gels, with a first approximation due to tackiness, is

$$E_{scar-like_{0.3kPa}} \sim E_{0.3kPa}(1.84 \pm 0.2)^6 \sim 5.8 - 22 \text{ kPa} \tag{A.6}$$

AFM measurements of scar-like$_{0.3kPa}$ gel in Figure 2.4ii was corrected based on this adhesion considerations.

A fluorescence microscopy-based elasticity approximation can also be used to correct for the observed thin film (Figure 2.2B) of embedded collagen fibers near the gel interface. For pure collagen gels, storage modulus G' (Pa) is a function of temperature and concentration, c (mg/mL). At 37°C, this was found to scale as (Yang et al., 2009)

$$G' \approx 22\ c^{2.1} \tag{A.7}$$

From confocal stack reconstruction, we found embedded collagen localization within 10 microns near the surface of scar-like$_{0.3kPa}$ PA gel of ~80-micron thickness (Figure 2.2B). Since the embedded fibers are putatively stiffer than the compliant PA around them, Equation (A.7) was assumed to still apply at least in the regions near fiber bundles. For scar-like$_{0.3kPa}$ gels, surface coverage is ~30% based on Sirius red and/or collagen immunofluorescence staining, which matches that of *mdx* and DMD skeletal muscle tissue cross-sections (~20–30%; Turgeman et al., 2008; Mann et al., 2011). This leads to a corrected collagen concentration from the nominal value of 0.4 mg/mL to an effective c = 11.6 mg/mL. Plugging this value into Equation (A.7), and assuming Young's modulus $(E) = 2.9G'$, we predicted an effective EC fiber stiffness of $E_{eff} \sim$ 11 kPa.

A.2 Theoretical analysis of lateral pulling curves

For an elastic substrate medium bounded on one side by a plane (e.g. PA gel on coverslip) with a point force F on applied on its free surface, the distribution of displacement, u, along the surface ($z = 0$) has been determined in equilibrium by Landau and Lifshitz (1986) as:

$$u_x = \frac{1+\sigma}{E} \cdot \frac{1}{r} \left\{ -\frac{(1-2\sigma)x}{r} F_z + 2(1-\sigma)F_x + \frac{2\sigma x}{r^2}(xF_x + yF_y) \right\} \tag{A.8}$$

where E is Young's modulus of the medium, σ is Poisson's ratio, and $r = \sqrt{x^2 + y^2}$. A similar formula for u_y was also found. We assumed that the lateral pulling force was applied to a small region and that the measured displacement profiles were obtained at large distances away from the initial loading point to satisfy Equation (A.8). In the simplest case (of a Boussinesq approximation) where $x = r, (y = 0)$, displacement far enough from the loading point scales as $u_r = a_B/r$, for some Boussinesq constant, a_B. Since such scaling leads to infinite displacement at $x = r = 0$, we also fit exponential scaling ($u_r = a_0 e^- br$, for some characteristic decay constant b; Figure 2.5ii) to set the approximate maximum displacement at the initial loading point, a_0. Both scalings agree well ($R^2 > 0.9$), as evidenced by the fitted scaling constants in Figure 2.5B.

Appendix B

Supplementary Information for Chapter 4

B.1 Mechanobiological gene circuits: systems of ordinary differential equations

We consider tension-mediated stabilization of polymeric, structural proteins as the basis for systems mechanobiology – as explored here mathematically for single, coupled and population-coupled modules. To incorporate the stabilizing effect of tension (K_s) on protein (s) we define degradation term δ as a Hill function as in Equation (4.3) in the main text:

$$\delta(s) = \frac{\delta_0 s^n}{K_s^n + s^n}$$

Structural proteins of the extracellular matrix, cytoskeleton, or nucleoskeleton are understandably polymeric, but in an effort to parsimoniously define a mechanobiological gene circuit, tension-mediated turnover is assumed to depend simply on total protein level, as one might assume for proteasomal degradation of monomeric proteins. This also assumes that polymerization and depolymerization rates are relatively rapid compared to the rates defined here.

B.1.1 Single-module gene circuits: reaction-order stability

A single module refers to a particular gene and its corresponding protein and is described by general rate equations that define what factors affects synthesis and turnover. The set of ordinary differential equations (ODEs) for a single module is simply:

$$\frac{dS}{dt} = \alpha - \beta$$
$$\frac{ds}{dt} = \gamma - \delta$$

S and s represent the gene and protein, respectively, whose synthesis (α, γ) and degradation (β, δ) rates describe their expression levels. Ultimately, the value of K_l (and hence, E) dictates the steady state values, regardless of the initial condition; while the functional forms of the various rates dictate the stability and dynamics of the system. For the given Hill-functional form of δ above, we explored the various reaction-order forms of the other rates that converge to a steady state solution. As discussed in the following sections, none of the other functional forms properly recapitulate the matrix elasticity-dependence of structural proteins unless the protein degradation rate is tension-dependent, and protein positively regulates its own gene expression.

***Rate-order forms by Schwanhausser* et al.**

Schwanhausser et al. (2011) quantified proteomic and transcriptomic half-lives under the following rate equations:

$$\frac{dS}{dt} = \tilde{\alpha} - \tilde{\beta} \cdot S$$
$$\frac{ds}{dt} = \tilde{\gamma} \cdot S - \tilde{\delta} \cdot s$$

where $\tilde{\alpha}, \tilde{\beta}, \tilde{\gamma}, \tilde{\delta}$ are rate constants. A phase plot below of protein (s) and mRNA (S), while varying relative protein synthesis/degradation rates ($\tilde{\gamma}/\tilde{\delta}$) and the relative mRNA synthesis/degradation rates ($\tilde{\alpha}/\tilde{\beta}$), shows that mRNA-relevant rates scale mRNA and protein levels (blue line), but protein-relevant parameters do not (red line). This was expected from

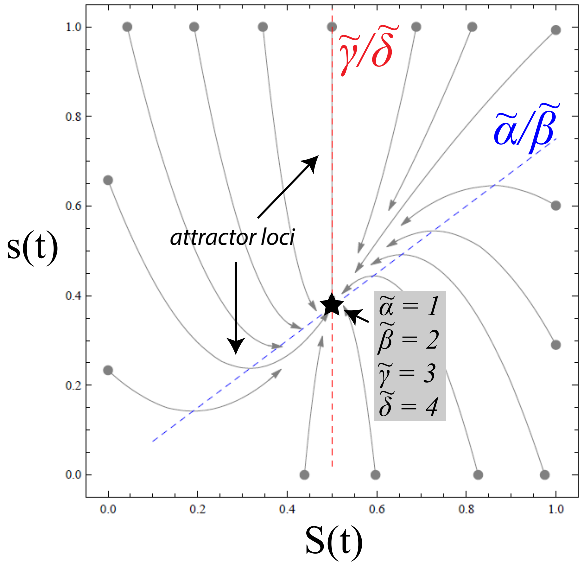

the chosen forms of the rate equations above as the protein kinetics does not affect its mRNA. Thus, in the search for the appropriate forms of the rate equations that capture the variations in structural protein expression with matrix elasticity, E, the ones described by Schwanhausser *et al.* are *not* sufficient.

Zeroth-order α, tension-dependent δ

Now if we consider changing degradation rate to be tension-dependent, keeping others similar to above:

$$\frac{dS}{dt} = \tilde{\alpha} - \tilde{\beta} \cdot S$$
$$\frac{ds}{dt} = \tilde{\gamma} \cdot S - \frac{\delta_0 s^n}{K_s^n + s^n}$$

In this case, we get the following phase plot where varying K_s, and hence protein levels, does not affect mRNA levels. This is again not physically relevant as we expect that both mRNA and protein levels should respond to K_s (or E).

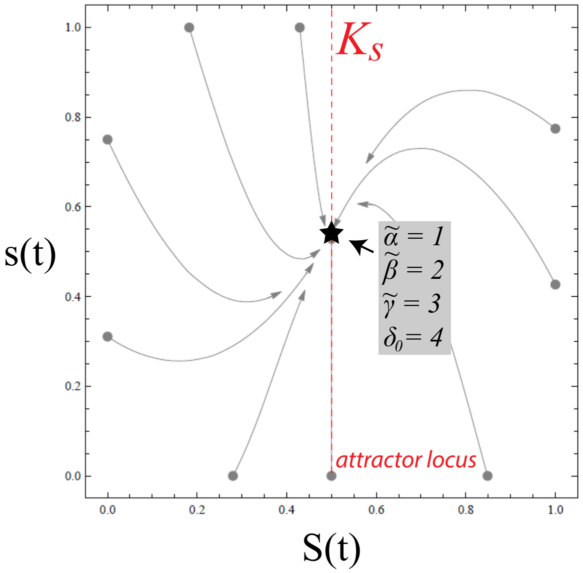

First-order rates, tension-dependent δ

First-order rates were chosen for the main text as they recapitulate experimental observations for the mechanobiological gene circuit of lamin A (Swift et al., 2013b).

$$\frac{dS}{dt} = \tilde{\alpha} \cdot s - \tilde{\beta} \cdot S$$
$$\frac{ds}{dt} = \tilde{\gamma} \cdot S - \frac{\delta_0 s^n}{K_s^n + s^n}$$

With the lack of precise values for rate constants published in literature, we chose $O(1)$ values for the parameters. For the purposes of display in Figure 4.2 of the main text, we used the following values for each of the rate constants:

Parameter	Value
$\tilde{\alpha}$	1
$\tilde{\beta}$	2
$\tilde{\gamma}$	3
δ_0	4
n	2

Protein and mRNA levels were initialized in the range $\{0, 1\}$, as shown in the phase plot in

Figure 4.2.

Unstable steady states: higher-order rates

The following higher-order ($p \geq 2$) cases have divergent steady states, and hence not biologically relevant:

- $\alpha = \tilde{\alpha} \cdot s^p$; $\beta = \tilde{\beta} \cdot S$; $\gamma = \tilde{\gamma} \cdot S$;
- $\alpha = \tilde{\alpha} \cdot s$; $\beta = \tilde{\beta} \cdot S$ $\gamma = \tilde{\gamma} \cdot S^p$;
- $\alpha = \tilde{\alpha} \cdot s^p$; $\beta = \tilde{\beta} \cdot S^p$ $\gamma = \tilde{\gamma} \cdot S^p$;

B.1.2 Two-Module Gene Circuit

Assuming first-order rates (except for protein degradation rates), the set of ODEs for coupled two-module gene circuit is:

$$\begin{aligned}
\frac{dL}{dt} &= \tilde{\alpha}_1 \cdot l - \tilde{\beta}_1 \cdot L \\
\frac{dl}{dt} &= \tilde{\gamma}_1 \cdot L - \delta_1 \cdot \frac{l^{n_l}}{K_l^{n_l} + l^{n_l}} \\
\frac{dM}{dt} &= \tilde{\alpha}_2 \cdot m \ \ (+\tilde{\alpha}_3 \cdot l) - \tilde{\beta}_2 \cdot M \\
\frac{dm}{dt} &= \tilde{\gamma}_2 \cdot M - \delta_2 \cdot \frac{m^{n_m}}{K_m^{n_m} + m^{n_m}}
\end{aligned}$$

where $K_s = f(s)$ and $K_s = f(tension)$, for some functional form (e.g. power-law). For lamin-myosin coupling, we chose $K_l = m^{x/n_l}$ and $K_m = E^{y/n_m}$.

The following values for rate constants were used in the simulations presented in Figure 4.4B, C of the main text:

Parameter	Value
$\{\tilde{\alpha_1}, \tilde{\alpha_2}\}$	$\{1.1, 1.1\}$
$\{\tilde{\beta_1}, \tilde{\beta_2}\}$	$\{5, 5\}$
$\{\tilde{\gamma_1}, \tilde{\gamma_2}\}$	$\{1.2, 1.2\}$
$\{\delta_1, \delta_2\}$	$\{5, 5\}$
$\{n_l, n_m\}$	$\{2, 2\}$
$\{x, y\}$	$\{0.44, 0.44\}$

with $E = 0.003 - 0.4$, to represent the order of magnitude range elasticities in cell-on-gels experiments (0.3–40 kPa; Swift et al., 2013b). The different molecular species were all initialized as $L(0) = l(0) = m(0) = M(0) = 0.005$.

B.1.3 Two-Module, Tissue-level Mechanobiological Gene Circuit

The set of ODEs for population-level coupling of two modules (e.g. collagen and myosin levels in a developing heart) are:

$$\begin{aligned}
\frac{dC}{dt} &= \tilde{\alpha}_1 \cdot \frac{c^{n_f - 1}}{k_f^{n_f} + c^{n_f}} - \tilde{\beta}_1 \cdot C \\
\frac{dc}{dt} &= \tilde{\gamma}_1 \cdot C - \tilde{\delta}_1 \cdot \frac{c^{n_c}}{K_c^{n_c} + c^{n_c}} \\
\frac{dM}{dt} &= \alpha_2 \cdot m - \beta_2 \cdot M \\
\frac{dm}{dt} &= \gamma_2 \cdot M - \delta_2 \cdot \frac{m^{n_m}}{K_m^{n_m} + m^{n_m}}
\end{aligned}$$

where $K_c = m^{x/n_c}$ for some x, $K_m = c^{y/n_m}$, for some y.

The following values for rate constants were used in the simulations in Figure 4.6 (unless otherwise specified):

Parameter	Value
$\{\tilde{\alpha_1}, \tilde{\alpha_2}\}$	$\{5.2, 4.1\}$
$\{\tilde{\beta_1}, \tilde{\beta_2}\}$	$\{5, 3\}$
$\{\tilde{\gamma_1}, \tilde{\gamma_2}\}$	$\{3, 1.5\}$
$\{\delta_1, \delta_2\}$	$\{6.5, 7\}$
$\{n_f, n_c, n_m\}$	$\{2, 1.6, 3.7\}$
$\{x, y, a_0\}$	$\{0.51, 0.39, 0.89\}$

The different molecular species were initialized with the following values:

Species	Initial Value
C	0.00051
c	0.00051
M	0.011
m	0.011

B.2 Analytical Solution for Single-Module Gene Circuit

For the case that δ is tension-dependent and all other rates are first-order (B.1.1), as in the main text, such that at steady state we have:

$$\frac{dS}{dt} = 0 = \tilde{\alpha} \cdot s - \tilde{\beta} \cdot S \tag{B.1}$$

$$\frac{ds}{dt} = 0 = \tilde{\gamma} \cdot S - \frac{\delta_0 s^n}{K_s^n + s^n} \tag{B.2}$$

For the simplest case of $n = 2$ and substituting Eq. (B.2) to Eq. (B.1), we get (after removing null solution):

$$s^3 - \frac{\tilde{\beta}\delta_0}{\tilde{\gamma}\tilde{\alpha}} s^2 + \tilde{\gamma} K^2 s = 0 \tag{B.3}$$

$$s^2 - \frac{\tilde{\beta}\delta_0}{\tilde{\gamma}\tilde{\alpha}} s + \tilde{\gamma} K^2 = 0 \tag{B.4}$$

Equation (B.4) is simply a quadratic equation, which has two solutions:

$$s_{1,2} = \frac{1}{2}\left(\frac{\tilde{\beta}\delta_0}{\tilde{\gamma}\tilde{\alpha}}\right) \pm \frac{1}{2}\sqrt{\left(\frac{\tilde{\beta}\delta_0}{\tilde{\gamma}\tilde{\alpha}}\right)^2 - 4K_l} \tag{B.5}$$

Stability analysis shows that the larger solution is an unstable node, such that we only have one biologically relevant, non-zero steady state:

$$\{s_{ss}, S_{ss}\} = \left\{\frac{1}{2}\left(\frac{\tilde{\beta}\delta_0}{\tilde{\gamma}\tilde{\alpha}}\right) - \frac{1}{2}\sqrt{\left(\frac{\tilde{\beta}\delta_0}{\tilde{\gamma}\tilde{\alpha}}\right)^2 - 4K_s}, \quad \frac{\tilde{\alpha} s_{ss}}{\tilde{\beta}}\right\} \tag{B.6}$$

where the rate constants must have values that obey the following:

$$\left(\frac{\tilde{\beta}\delta_0}{\tilde{\gamma}\tilde{\alpha}}\right)^2 - 4K_s > 0 \tag{B.7}$$

B.3 Numerical Solution for Two-Module Gene Circuit

For the coupled mechanobiological gene circuit (in **??**), we employed a numerical solver (Mathematica; version 8, Wolfram Research) to conduct kinetic and steady-state analyses. The outputs for the code below are found in Figure 4.4B (plot of E = 0.4 kinetics, and steady-state plot). To obtain Figure 4.4C plots, we changed the value of J (in code; equivalent to $\tilde{\alpha}_3$ in **??**) from 0 to 1.8. To obtain plots for the case of $E = 0.003$, we changed the upper limit of the **For** loop to i < 0.0031.

```
test = Partition[
  Flatten[Reap[
     For[i = .003, i < .4, i = i + .05, Clear[a, b, h, g, s, L, l, m, M, J, j, t, x, y, A1, A2
       , E1, q, r];
         a = 1.10; b = 5; g = 1.20; h = 5; x = .440; y = .44; J = 0; j = 1.1; q = 5; r = 1.20;
             s = 5; A1 = 2.0; A2 = 2.0; E1 = i; Ko = 9.2;
         s = NDSolve[{l'[t] == a*L[t] − b*l[t],
          L'[t] == g*l[t] − h*L[t]^A1/(M[t]^x + L[t]^A1),
          m'[t] == J*L[t] + j*M[t] − q*m[t],
          M'[t] == r*m[t] − s*M[t]^A2/(E1^y + M[t]^A2),
          l[0] == .005, L[0] == .005, m[0] == .005, M[0] == .005}, {l, L, m, M}, {t, 0, 1000}];
         Plot[Evaluate[{l[t], L[t], m[t], M[t]} /. s], {t, 0, 1000}, PlotRange −> {{0, 15},
             {0.00001, 1.1}}, PlotStyle −> Thick] Sow[{L[1000] /. s, l[1000] /. s, M[1000] /. s,
            m[1000] /. s }]];[[2, 1]]], 4]; Lss = test[[All, 1]]; lss = test[[All, 2]]; Mss =
            test[[All, 3]]; mss = test[[All, 4]];
Plot[Evaluate[{200 L[t], 200 M[t]} /. s], {t, 0, 100},P lotRange −> {{0, 25}, {0., 10}},
    PlotStyle −> Thick, PlotLegends −> {"Lamin␣protein", "Myosin␣protein"}]
 ListLogLogPlot[{Partition[Riffle[200 Lss, 200 Mss], 2]}, PlotRange −> {{0.5, 20}, {0.5,
     20}}]
```

B.4 Numerical Solution for Tissue-level Coupled Gene Circuit

The code listed below refers to **??** on modeling of the mechano-regulated dynamics of collagen production (by cardiac fibroblasts) and myosin expression and hence contraction levels (by cardiomyocytes), which prints out Figure 4.6C:

```
Clear[a, b, h, g, u, s, F, f, M, m, J, j, t, T, x, y, k0]
a = 5.2; b = 5; g = 3; h = 6.5; x = .51; j = 4.1; q = 3; r = 1.5; s = 7;
A1 = 1.6; A2 = 3.7; y = .39; z = 2; k0 = .89;
s = NDSolve[{F'[t] == a*f[t]^(z - 1)/(k0^z + f[t]^z) - b*F[t],
     f '[ t ] == g*F[t] - h*f[t]^A1/(m[t]^x + f[t]^A1),
     M'[t] == j*m[t] - q*M[t],
     m'[t] == r*M[t] - u*m[t]^A2/(f[t]^y + m[t]^A2),
     F[0] == .00051, f[0] == 0.00051, M[0] == 0.011, m[0] == 0.011},
     {F, f, M, m}, {t, 0, 1000}];
LogPlot[Evaluate[{100 F[t], 100 f[t ], 100 M[t], 100 m[t]} /. s], {t, 0.5, 1000},
          PlotRange -> {{0, 15}, {0.1, 100.}}]
```

Appendix C

Standard biological laboratory protocols and reagents used

C.1 Cell culture

Cell cultures were kept in 5% CO_2 humidified incubators and maintained at 37 °C. Cells were passaged at 70–80% confluence using 0.05% trypsin-EDTA solution and fed every 2–3 days for cell lines (e.g. A549 cells) or 3–4 days for primary cell cultures.

Human mesenchymal stem cells (MSCs), isolated from human donor bone marrows (anonymous donors with Institutional Review Board approvals), were obtained from Stem Cell and Xenograft Core, University of Pennsylvania School of Medicine, and cultured using standard methods (Pittenger et al., 1999). Cells were expanded on tissue culture flasks (Corning, Inc.) in low-glucose (1 g/L) Dulbecco's Modified Eagle Medium (DMEM) supplemented with 10% fetal bovine serum (FBS) and 100 μg/ml penicillin and 100 μM streptomycin (P/S) and used at passages 3–5 for all cell-on-gel cultures. All reagents were purchased from Gibco (Life Technologies) unless otherwise specified.

C.2 Quantitative Immunofluorescence Microscopy

For immunofluorescence staining, cells were fixed with 3.7% formaldehyde (Sigma) in PBS for 15 min at RT and washed with PBS twice for 5 min. Blocking was done for 1 hr with 1% BSA in PBS. All primary antibodies (see Table C.6 for specifications) in PBS with 0.025% Tween-20 (PBST) were incubated at RT for 1 hour or overnight at 4 °C. All donkey secondary antibodies (at 1:1000 dilution, Alexa series from Invitrogen) were used to stain primary antibody-labeled fixed cells for 1 hour at RT in PBST. Actin filament (F-actin) staining was done in PBS with 100 ng/ml TRITC-phalloidin (Sigma) for 20 min at RT. Hoechst 33342 (Invitrogen) was used at a concentration of 1 μg/ml in PBS to stain for DNA for 5 min at RT. Quantitative immunofluorescence of immunolabeled proteins of interest and their localization was performed using an inverted microscope (IX-71, Olympus) with a 20× LCACh objective (NA 0.40) and a Cascade CCD camera (Photometrics). Image acquisition was performed under Image-Pro Plus software (Media Cybernetics, Inc.) and image analysis was done using ImageJ software. For quantitative immunofluorescence microscopy, samples were imaged under the same specifications of exposure times and gains. If two different exposure times were necessary for quantification between samples, both exposure times were performed for those samples to ensure that images were in the linear range of fluorescence intensities with respect to exposure times. Control samples incubated only with secondary antibody (no primary-antibody incubation) were also imaged as negative control under the same specifications and used as background-intensity subtraction during image processing.

C.3 Cell Morphometrics

Intensity analyses and cell-morphology quantification were performed in ImageJ software. From images acquired from immunofluorescent samples, F-actin and myosin IIB rear/front polarization ratios were determined by splitting the cell into two equal areas (rear and front) and plotting the fluorescence vs length. For nuclear-localized stains (e.g. of NKX2.5), a dedicated channel for Hoechst 33342-stained nuclear DNA was used to delineate nuclear versus cytoplasmic/whole-cell regions. The ratio is the total integrated fluorescence of the rear half over the front half of the cell. Cell area and aspect ratio were quantified from myosin IIA or F-actin immunofluorescence (since they consistently stain the whole cell body).

Before comparing different sample conditions, integrated intensity of a particular protein was normalized to background value (secondary antibody-only control).

C.4 Transfection protocol

For transfecting plasmid DNA and siRNA into cell cultures, Lipofectamine 2000 Reagent was used according to Invitrogen's instructions. After 4–24 h post-transfection, culture media was freshly replaced. Western analysis of transfection efficiency was performed on cell lysates 48 h post-transfection.

C.5 Western Blotting and Analysis

Adherent cells such as MSCs, THP1-derived macrophages, and A549 cells were trypsinized, then pelleted and washed in cold PBS twice prior to addition of RIPA lysis buffer (1.0 vol% NP40, 2 mM EDTA, 150 mM NaCl, 50 mM Tris-HCL, 0.1 wt% SDS, 0.5 wt% sodium deoxycholate) at 4 °C for 30 minutes. During incubation, the pellet solution was sonicated to fully break down cell particulates. The pellet solution is then centrifuged at 12,000 rpm at 4 °C for 20 min and the collected supernatant lysate can be stored at –80 °C or immediately used. LDS (4×, Thermo Scientific) / β-mercaptoethanol solution at 11:1 v/v is then added at 36% of lysate volume and boiled at 90 °C for 10 min prior to gel electrophoresis. Boiled lysates were cooled at RT, loaded onto 3–8% NuPAGE Novex Tris-Acetate gels (Life Technologies); after gel-run, the gel-immobilized protein bands were transferred to blotting paper (iBlot PVDF, Life Technologies) using an iBlot gel transfer device (Life Technologies) set at P3 for 7 min. Blots were blocked with 5% non-fat milk (American Bioanalytical) in TBST for 1 hour at RT and then desired primary antibodies in TBS were added overnight at 4 °C. HRP-conjugated secondary antibodies (ECL™, GE Healthcare) in TBST with 5% milk were added for 1 hour at RT. Two 10-min TBST washes were performed in between above steps, and a final TBS wash before precipitate development. Chromosensor (GenScript), a chromogenic substrate, was finally added to generate a precipitate for the ECL reaction that should appear visible within 5–10 min.

C.6 Statistical Analyses

An independent samples t-test was used when there were only two different sample means. One-way ANOVA was used for matrix elasticity effects on cell morphometrics, protein expression, etc. Two-way Analysis of Variance (ANOVA) with Tukey post-hoc test was used for time-lapse cell migration experiments with time-dependent displacement values between conditions. Statistical significance was determined at α = 0.05 level. All statistics analyses were done in Microsoft Excel.

Table C.1. Polyacrylamide gel precursor formulations#

Nominal Elasticity (kPa)	Volume (μL) of 40% Acrylamide stock	Volume (μL) of 1.5% w/v Bis-Acrylamide stock	Volume (μL) of distilled water
0.3	75	47	874.84
3.0	112	70	812.86
10	150	93	750.68
20	200	93	696.00
40	250	200	539.47

#1 μL of N,N,N',N'-Tetramethylethylenediamine (Sigma) and 10 μL of 10% w/v Ammonium Persulfate (Sigma) was added to a ~1 mL gel formulation to initiate polymerization.

Table C.2. Primary antibody specifications[#]

Antigen	Host species and Reactivity	Clone, Catalog number, Vendor	Concentration/Dilution and Application
β-Actin	mouse anti-β-Actin IgG1	C4, sc-47778, Santa Cruz Biotechnology	1 μg/mL (Western blot)
β-tubulin	goat anti-β-tubulin	ab21057, Abcam	1 μg/mL (Western blot)
Collagen-1	mouse anti-collagen type I IgG1[1]	COL-1, C2456, Sigma	1:1000 (Indirect immunofluorescence – IF)
Myosin IIB (MIIB)	rabbit anti-MIIB	3404, Cell Signaling Technology	1:1000 (Western blot), 1:200 (IF)
Myosin IIA (MIIA)	rabbit anti-MIIA	M8064, Sigma	1:200 (IF)
Myosin phosphatase-1 (MYPT1)	rabbit anti-MYPT1	ab24670, Abcam	1:10000 (Western blot), 1:2000 (IF)
NKX2.5	rabbit anti-NKX2.5	H-114, sc-14033, Santa Cruz Biotechnology	1 μg/mL (Western blot, IF)
Lamin A,C	mouse anti-lamin A,C IgG2b	636, sc-7292, Santa Cruz Biotechnology	1 μg/mL (Western blot, IF)
Lamin B	goat anti-lamin B1	sc-6217, Santa Cruz Biotechnology	1 μg/mL (Western blot, IF)
Heat shock protein 90 (HSP90)	mouse anti-HSP90	AC88, ab13492, Abcam	1 μg/mL (Western blot)
Heat shock protein 70 (HSP70)	mouse anti-HSP70	C92F3A-5, ab47455, Abcam	1 μg/mL (Western blot)
Pro-collagen type I	mouse anti-pro-collagen type I IgG1	M-38, Developmental Studies Hybridoma Bank (DSHB)	1 μg/mL (Western blot, IF)
Sarcomeric α-actinin	mouse anti-sarcomeric α-actinin IgG1	EA-53, MA1-22863, Sigma	1 μg/mL (IF)
α-Smooth Muscle Actin (SMA)	mouse anti-SMA IgG2a	1A4, A2547, Sigma	1:1000 (Western blot, IF)
SUMO-1	mouse anti-SUMO-1 IgG1	21c7, DSHB	1 μg/mL (Western blot, IF)

[#] reactive to human antigen, unless otherwise specified; [1] used to stain rat collagen-1, also reactive to human.

Bibliography

Abad, M., Mosteiro, L., Pantoja, C., Canamero, M., Rayon, T., Ors, I., Grana, O., Megias, D., Dominguez, O., Martinez, D., Manzanares, M., Ortega, S., and Serrano, M. (2013). Reprogramming in vivo produces teratomas and ips cells with totipotency features. *Nature*, 502(7471):340–5.

Abdallah, B. M. and Kassem, M. (2009). The use of mesenchymal (skeletal) stem cells for treatment of degenerative diseases: Current status and future perspectives. *Journal of Cellular Physiology*, 218(1):9–12.

Achterberg, V. F., Buscemi, L., Diekmann, H., Smith-Clerc, J., Schwengler, H., Meister, J. J., Wenck, H., Gallinat, S., and Hinz, B. (2014). The nano-scale mechanical properties of the extracellular matrix regulate dermal fibroblast function. *J Invest Dermatol*, 134(7):1862–72.

Adhikari, A. S., Chai, J., and Dunn, A. R. (2011). Mechanical load induces a 100-fold increase in the rate of collagen proteolysis by mmp-1. *Journal of the American Chemical Society*, 133(6):1686–1689.

Ahamed, J., Burg, N., Yoshinaga, K., Janczak, C. A., Rifkin, D. B., and Coller, B. S. (2008). In vitro and in vivo evidence for shear-induced activation of latent transforming growth factor-beta1. *Blood*, 112(9):3650–60.

Allenby, G., Bocquel, M. T., Saunders, M., Kazmer, S., Speck, J., Rosenberger, M., Lovey, A., Kastner, P., Grippo, J. F., Chambon, P., and et al. (1993). Retinoic acid receptors and retinoid x receptors: interactions with endogenous retinoic acids. *Proc Natl Acad Sci U S A*, 90(1):30–4.

Alvarez-Buylla, A. and Lim, D. A. (2004). For the long run: maintaining germinal niches in the adult brain. *Neuron*, 41(5):683–6.

Bakay, M., Zhao, P., Chen, J., and Hoffman, E. P. (2002). A web-accessible complete transcriptome of normal human and dmd muscle. *Neuromuscul Disord*, 12 Suppl 1:S125–41.

Ball, R. D., Krus, D. L., and Alizadeh, B. (1987). Myosin degradation fragments in skeletal muscle. *J Mol Biol*, 193(1):47–56.

Banerjee, A., Arha, M., Choudhary, S., Ashton, R. S., Bhatia, S. R., Schaffer, D. V., and Kane, R. S. (2009). The influence of hydrogel modulus on the proliferation and differentiation of encapsulated neural stem cells. *Biomaterials*, 30(27):4695–9.

Benoit, D. S., Schwartz, M. P., Durney, A. R., and Anseth, K. S. (2008). Small functional groups for controlled differentiation of hydrogel-encapsulated human mesenchymal stem cells. *Nat Mater*, 7(10):816–23.

Bentzinger, C. F., Wang, Y. X., von Maltzahn, J., Soleimani, V. D., Yin, H., and Rudnicki, M. A. (2013). Fibronectin regulates wnt7a signaling and satellite cell expansion. *Cell Stem Cell*, 12(1):75–87.

Berry, M. F., Engler, A. J., Woo, Y. J., Pirolli, T. J., Bish, L. T., Jayasankar, V., Morine, K. J., Gardner, T. J., Discher, D. E., and Sweeney, H. L. (2006). Mesenchymal stem cell injection after myocardial infarction improves myocardial compliance. *Am J Physiol Heart Circ Physiol*, 290(6):H2196–203.

Biswas, S., Guix, M., Rinehart, C., Dugger, T. C., Chytil, A., Moses, H. L., Freeman, M. L., and Arteaga, C. L. (2007). Inhibition of tgf-beta with neutralizing antibodies prevents radiation-induced acceleration of metastatic cancer progression. *Journal of Clinical Investigation*, 117(5):1305–1313.

Boiani, M. and Scholer, H. R. (2005). Regulatory networks in embryo-derived pluripotent stem cells. *Nat Rev Mol Cell Biol*, 6(11):872–84.

Breitbach, M., Bostani, T., Roell, W., Xia, Y., Dewald, O., Nygren, J. M., Fries, J. W., Tiemann, K., Bohlen, H., Hescheler, J., Welz, A., Bloch, W., Jacobsen, S. E., and Fleischmann, B. K. (2007). Potential risks of bone marrow cell transplantation into infarcted hearts. *Blood*, 110(4):1362–9.

Brohl, D., Vasyutina, E., Czajkowski, M. T., Griger, J., Rassek, C., Rahn, H. P., Purfurst, B., Wende, H., and Birchmeier, C. (2012). Colonization of the satellite cell niche by skeletal muscle progenitor cells depends on notch signals. *Dev Cell*, 23(3):469–81.

Buscemi, L., Ramonet, D., Klingberg, F., Formey, A., Smith-Clerc, J., Meister, J. J., and Hinz, B. (2011). The single-molecule mechanics of the latent tgf-beta 1 complex. *Current Biology*, 21(24):2046–2054.

Buxboim, A., Rajagopal, K., Brown, A. E., and Discher, D. E. (2010). How deeply cells feel: methods for thin gels. *J Phys Condens Matter*, 22(19):194116.

Buxboim, A., Swift, J., Irianto, J., Spinler, K. R., Dingal, P. C. D. P., Athirasala, A., Kao, Y.-R. C., Cho, S., Harada, T., Sin, J.-W., and Discher, D. E. (2014). Matrix elasticity regulates lamin-a,c phosphorylation and turnover with feedback to actomyosin. *Current Biology*. In press.

Byron, K. L., Puglisi, J. L., Holda, J. R., Eble, D., and Samarel, A. M. (1996). Myosin heavy chain turnover in cultured neonatal rat heart cells: Effects of [ca2+](i) and contractile activity. *American Journal of Physiology-Cell Physiology*, 271(5):C1447–C1456.

Cai, Y., Biais, N., Giannone, G., Tanase, M., Jiang, G., Hofman, J. M., Wiggins, C. H., Silberzan, P., Buguin, A., Ladoux, B., and Sheetz, M. P. (2006). Nonmuscle myosin iia-dependent force inhibits cell spreading and drives f-actin flow. *Biophys J*, 91(10):3907–20.

Cameron, A. R., Frith, J. E., and Cooper-White, J. J. (2011). The influence of substrate creep on mesenchymal stem cell behaviour and phenotype. *Biomaterials*, 32(26):5979–93.

Cartharius, K., Frech, K., Grote, K., Klocke, B., Haltmeier, M., Klingenhoff, A., Frisch, M., Bayerlein, M., and Werner, T. (2005). MatInspector and beyond: promoter analysis based on transcription factor binding sites. *Bioinformatics*, 21(13):2933–2942.

Celiz, A. D., Smith, J. G. W., Langer, R., Anderson, D. G., Winkler, D. A., Barrett, D. A., Davies, M. C., Young, L. E., Denning, C., and Alexander, M. R. (2014). Materials for stem cell factories of the future. *Nature Materials*, 13(6):570–579.

Chanda, B., Ditadi, A., Iscove, N. N., and Keller, G. (2013). Retinoic acid signaling is essential for embryonic hematopoietic stem cell development. *Cell*, 155(1):215–27.

Chen, J., Yuan, K., Mao, X., Miano, J. M., Wu, H., and Chen, Y. (2012). Serum response factor regulates bone formation via igf-1 and runx2 signals. *J Bone Miner Res*, 27(8):1659–68.

Chen, T., Yuan, D., Wei, B., Jiang, J., Kang, J., Ling, K., Gu, Y., Li, J., Xiao, L., and Pei, G. (2010). E-cadherin-mediated cell-cell contact is critical for induced pluripotent stem cell generation. *Stem Cells*, 28(8):1315–25.

Chenn, A. and McConnell, S. K. (1995). Cleavage orientation and the asymmetric inheritance of notch1 immunoreactivity in mammalian neurogenesis. *Cell*, 82(4):631–41.

Chowdhury, F., Li, Y., Poh, Y. C., Yokohama-Tamaki, T., Wang, N., and Tanaka, T. S. (2010a). Soft substrates promote homogeneous self-renewal of embryonic stem cells via downregulating cell-matrix tractions. *PLoS One*, 5(12):e15655.

Chowdhury, F., Na, S., Li, D., Poh, Y. C., Tanaka, T. S., Wang, F., and Wang, N. (2010b). Material properties of the cell dictate stress-induced spreading and differentiation in embryonic stem cells. *Nat Mater*, 9(1):82–8.

Chung, J. Y. and Chaudhury, M. K. (2005). Soft and hard adhesion. *Journal of Adhesion*, 81(10-11):1119–1145.

Clark, R. J., McDonough, P. M., Swanson, E., Trost, S. U., Suzuki, M., Fukuda, M., and Dillmann, W. H. (2003). Diabetes and the accompanying hyperglycemia impairs cardiomyocyte calcium cycling through increased nuclear o-glcnacylation. *Journal of Biological Chemistry*, 278(45):44230–44237.

Colter, D. C., Class, R., DiGirolamo, C. M., and Prockop, D. J. (2000). Rapid expansion of recycling stem cells in cultures of plastic-adherent cells from human bone marrow. *Proceedings of the National Academy of Sciences of the United States of America*, 97(7):3213–3218.

Colton, C. K. (1995). Implantable biohybrid artificial organs. *Cell Transplant*, 4(4):415–36.

Corr, D. T., Gallant-Behm, C. L., Shrive, N. G., and Hart, D. A. (2009). Biomechanical behavior of scar tissue and uninjured skin in a porcine model. *Wound Repair and Regeneration*, 17(2):250–259.

Dalby, M. J., Gadegaard, N., Herzyk, P., Sutherland, D., Agheli, H., Wilkinson, C. D. W., and Curtis, A. S. G. (2007a). Nanomechanotransduction and interphase nuclear organization influence on genomic control. *Journal of Cellular Biochemistry*, 102(5):1234–1244.

Dalby, M. J., Gadegaard, N., Tare, R., Andar, A., Riehle, M. O., Herzyk, P., Wilkinson, C. D., and Oreffo, R. O. (2007b). The control of human mesenchymal cell differentiation using nanoscale symmetry and disorder. *Nat Mater*, 6(12):997–1003.

Dembo, M. and Wang, Y. L. (1999). Stresses at the cell-to-substrate interface during locomotion of fibroblasts. *Biophys J*, 76(4):2307–16.

Discher, D. E., Janmey, P., and Wang, Y. L. (2005). Tissue cells feel and respond to the stiffness of their substrate. *Science*, 310(5751):1139–1143.

Discher, D. E., Mooney, D. J., and Zandstra, P. W. (2009). Growth factors, matrices, and forces combine and control stem cells. *Science*, 324(5935):1673–1677.

Doi, M. and Edwards, S. F. (1978). Dynamics of concentrated polymer systems .1. brownian-motion in equilibrium state. *Journal of the Chemical Society-Faraday Transactions Ii*, 74:1789–1801.

Domke, J. and Radmacher, M. (1998). Measuring the elastic properties of thin polymer films with the atomic force microscope. *Langmuir*, 14(12):3320–3325.

Downing, T. L., Soto, J., Morez, C., Houssin, T., Fritz, A., Yuan, F. L., Chu, J. L., Patel, S., Schaffer, D. V., and Li, S. (2013). Biophysical regulation of epigenetic state and cell reprogramming. *Nature Materials*, 12(12):1154–1162.

Dupont, S., Morsut, L., Aragona, M., Enzo, E., Giulitti, S., Cordenonsi, M., Zanconato, F., Le Digabel, J., Forcato, M., Bicciato, S., Elvassore, N., and Piccolo, S. (2011). Role of yap/taz in mechanotransduction. *Nature*, 474(7350):179–83.

Eden, E., Geva-Zatorsky, N., Issaeva, I., Cohen, A., Dekel, E., Danon, T., Cohen, L., Mayo, A., and Alon, U. (2011). Proteome half-life dynamics in living human cells. *Science*, 331(6018):764–8.

Engler, A., Bacakova, L., Newman, C., Hategan, A., Griffin, M., and Discher, D. (2004a). Substrate compliance versus ligand density in cell on gel responses. *Biophys J*, 86(1 Pt 1):617–28.

Engler, A. J., Carag-Krieger, C., Johnson, C. P., Raab, M., Tang, H. Y., Speicher, D. W., Sanger, J. W., Sanger, J. M., and Discher, D. E. (2008). Embryonic cardiomyocytes beat best on a matrix with heart-like elasticity: scar-like rigidity inhibits beating. *J Cell Sci*, 121(Pt 22):3794–802.

Engler, A. J., Griffin, M. A., Sen, S., Bonnetnann, C. G., Sweeney, H. L., and Discher, D. E. (2004b). Myotubes differentiate optimally on substrates with tissue-like stiffness: pathological implications for soft or stiff microenvironments. *Journal of Cell Biology*, 166(6):877–887.

Engler, A. J., Rehfeldt, F., Sen, S., and Discher, D. E. (2007). Microtissue elasticity: measurements by atomic force microscopy and its influence on cell differentiation. *Methods Cell Biol*, 83:521–45.

Engler, A. J., Sen, S., Sweeney, H. L., and Discher, D. E. (2006). Matrix elasticity directs stem cell lineage specification. *Cell*, 126(4):677–89.

Esnault, C., Stewart, A., Gualdrini, F., East, P., Horswell, S., Matthews, N., and Treisman, R. (2014). Rho-actin signaling to the mrtf coactivators dominates the immediate transcriptional response to serum in fibroblasts. *Genes Dev*, 28(9):943–58.

Espuny-Camacho, I., Michelsen, K. A., Gall, D., Linaro, D., Hasche, A., Bonnefont, J., Bali, C., Orduz, D., Bilheu, A., Herpoel, A., Lambert, N., Gaspard, N., Peron, S., Schiffmann, S. N., Giugliano, M., Gaillard, A., and Vanderhaeghen, P. (2013). Pyramidal neurons derived from human pluripotent stem cells integrate efficiently into mouse brain circuits in vivo. *Neuron*, 77(3):440–56.

Eto, M., Kirkbride, J. A., and Brautigan, D. L. (2005). Assembly of mypt1 with protein phosphatase-1 in fibroblasts redirects localization and reorganizes the actin cytoskeleton. *Cell Motility and the Cytoskeleton*, 62(2):100–109.

Flynn, B. P., Bhole, A. P., Saeidi, N., Liles, M., DiMarzio, C. A., and Ruberti, J. W. (2010). Mechanical strain stabilizes reconstituted collagen fibrils against enzymatic degradation by mammalian collagenase matrix metalloproteinase 8 (mmp-8). *Plos One*, 5(8).

Fuentealba, L. C., Obernier, K., and Alvarez-Buylla, A. (2012). Adult neural stem cells bridge their niche. *Cell Stem Cell*, 10(6):698–708.

Georges, P. C., Hui, J. J., Gombos, Z., McCormick, M. E., Wang, A. Y., Uemura, M., Mick, R., Janmey, P. A., Furth, E. E., and Wells, R. G. (2007). Increased stiffness of the rat liver precedes matrix deposition: implications for fibrosis. *Am J Physiol Gastrointest Liver Physiol*, 293(6):G1147–54.

Georges, P. C., Miller, W. J., Meaney, D. F., Sawyer, E. S., and Janmey, P. A. (2006). Matrices with compliance comparable to that of brain tissue select neuronal over glial growth in mixed cortical cultures. *Biophysical Journal*, 90(8):3012–3018.

Ghatak, A., Mahadevan, L., Chung, J. Y., Chaudhury, M. K., and Shenoy, V. (2004). Peeling from a biomimetically patterned thin elastic film. *Proceedings of the Royal Society a-Mathematical Physical and Engineering Sciences*, 460(2049):2725–2735.

Ghiaur, G., Yegnasubramanian, S., Perkins, B., Gucwa, J. L., Gerber, J. M., and Jones, R. J. (2013). Regulation of human hematopoietic stem cell self-renewal by the microenvironment's control of retinoic acid signaling. *Proc Natl Acad Sci U S A*, 110(40):16121–6.

Gilbert, P. M., Havenstrite, K. L., Magnusson, K. E., Sacco, A., Leonardi, N. A., Kraft, P., Nguyen, N. K., Thrun, S., Lutolf, M. P., and Blau, H. M. (2010). Substrate elasticity regulates skeletal muscle stem cell self-renewal in culture. *Science*, 329(5995):1078–81.

Godwin, J. W., Pinto, A. R., and Rosenthal, N. A. (2013). Macrophages are required for adult salamander limb regeneration. *Proc Natl Acad Sci U S A*, 110(23):9415–20.

Grigoriadis, A. E., Heersche, J. N., and Aubin, J. E. (1988). Differentiation of muscle, fat, cartilage, and bone from progenitor cells present in a bone-derived clonal cell population: effect of dexamethasone. *J Cell Biol*, 106(6):2139–51.

Guilak, F., Alexopoulos, L. G., Haider, M. A., Ting-Beall, H. P., and Setton, L. A. (2005). Zonal uniformity in mechanical properties of the chondrocyte pericellular matrix: Micropipette aspiration of canine chondrons isolated by cartilage homogenization. *Annals of Biomedical Engineering*, 33(10):1312–1318.

Guilluy, C., Osborne, L. D., Van Landeghem, L., Sharek, L., Superfine, R., Garcia-Mata, R., and Burridge, K. (2014). Isolated nuclei adapt to force and reveal a mechanotransduction pathway in the nucleus. *Nat Cell Biol*, 16(4):376–81.

Gurtner, G. C., Werner, S., Barrandon, Y., and Longaker, M. T. (2008). Wound repair and regeneration. *Nature*, 453(7193):314–21.

Harada, T., Swift, J., Irianto, J., Shin, J. W., Spinler, K. R., Athirasala, A., Diegmiller, R., Dingal, P. C., Ivanovska, I. L., and Discher, D. E. (2014). Nuclear lamin stiffness is a barrier to 3d migration, but softness can limit survival. *J Cell Biol*, 204(5):669–82.

Hare, J. M., Traverse, J. H., Henry, T. D., Dib, N., Strumpf, R. K., Schulman, S. P., Gerstenblith, G., DeMaria, A. N., Denktas, A. E., Gammon, R. S., Hermiller, J. B., J., Reisman, M. A., Schaer, G. L., and Sherman, W. (2009). A randomized, double-blind, placebo-controlled, dose-escalation study of intravenous adult human mesenchymal stem cells (prochymal) after acute myocardial infarction. *J Am Coll Cardiol*, 54(24):2277–86.

Hart, G. W., Housley, M. P., and Slawson, C. (2007). Cycling of o-linked beta-n-acetylglucosamine on nucleocytoplasmic proteins. *Nature*, 446(7139):1017–1022.

Hashimoto, Y., Kagechika, H., and Shudo, K. (1990). Expression of retinoic acid receptor genes and the ligand-binding selectivity of retinoic acid receptors (rar's). *Biochem Biophys Res Commun*, 166(3):1300–7.

Heissig, B., Hattori, K., Dias, S., Friedrich, M., Ferris, B., Hackett, N. R., Crystal, R. G., Besmer, P., Lyden, D., Moore, M. A., Werb, Z., and Rafii, S. (2002). Recruitment of stem and progenitor cells from the bone marrow niche requires mmp-9 mediated release of kit-ligand. *Cell*, 109(5):625–37.

Heldin, C. H., Miyazono, K., and ten Dijke, P. (1997). Tgf-beta signalling from cell membrane to nucleus through smad proteins. *Nature*, 390(6659):465–71.

Hinz, B. (2007). Formation and function of the myofibroblast during tissue repair. *J Invest Dermatol*, 127(3):526–37.

Hinz, B., Celetta, G., Tomasek, J. J., Gabbiani, G., and Chaponnier, C. (2001). Alpha-smooth muscle actin expression upregulates fibroblast contractile activity. *Mol Biol Cell*, 12(9):2730–41.

Holst, J., Watson, S., Lord, M. S., Eamegdool, S. S., Bax, D. V., Nivison-Smith, L. B., Kondyurin, A., Ma, L., Oberhauser, A. F., Weiss, A. S., and Rasko, J. E. (2010). Substrate elasticity provides mechanical signals for the expansion of hemopoietic stem and progenitor cells. *Nat Biotechnol*, 28(10):1123–8.

Houben, F., Ramaekers, F. C. S., Snoeckx, L. H. E. H., and Broers, J. L. V. (2007). Role of nuclear lamina-cytoskeleton interactions in the maintenance of cellular strength. *Biochimica Et Biophysica Acta-Molecular Cell Research*, 1773(5):675–686.

Huebsch, N., Arany, P. R., Mao, A. S., Shvartsman, D., Ali, O. A., Bencherif, S. A., Rivera-Feliciano, J., and Mooney, D. J. (2010). Harnessing traction-mediated manipulation of the cell/matrix interface to control stem-cell fate. *Nat Mater*, 9(6):518–26.

Imayoshi, I., Sakamoto, M., Yamaguchi, M., Mori, K., and Kageyama, R. (2010). Essential roles of notch signaling in maintenance of neural stem cells in developing and adult brains. *J Neurosci*, 30(9):3489–98.

Isenberg, B. C., Dimilla, P. A., Walker, M., Kim, S., and Wong, J. Y. (2009). Vascular smooth muscle cell durotaxis depends on substrate stiffness gradient strength. *Biophys J*, 97(5):1313–22.

Jiang, S. Y. and Cao, Z. Q. (2010). Ultralow-fouling, functionalizable, and hydrolyzable zwitterionic materials and their derivatives for biological applications. *Advanced Materials*, 22(9):920–932.

Kapoun, A. M., Gaspar, N. J., Wang, Y., Damm, D., Liu, Y. W., O'Young, G., Quon, D., Lam, A., Munson, K., Tran, T. T., Ma, J. Y., Murphy, A., Dugar, S., Chakravarty, S., Protter, A. A., Wen, F. Q., Liu, X. D., Rennard, S. I., and Higgins, L. S. (2006). Transforming growth factor-beta receptor type 1 (tgf beta ri) kinase activity but not p38 activation is required for tgf beta ri-induced myofibroblast differentiation and profibrotic gene expression. *Molecular Pharmacology*, 70(2):518–531.

Karumbayaram, S., Novitch, B. G., Patterson, M., Umbach, J. A., Richter, L., Lindgren, A., Conway, A. E., Clark, A. T., Goldman, S. A., Plath, K., Wiedau-Pazos, M., Kornblum, H. I., and Lowry, W. E. (2009). Directed differentiation of human-induced pluripotent stem cells generates active motor neurons. *Stem Cells*, 27(4):806–811.

Kasahara, H., Bartunkova, S., Schinke, M., Tanaka, M., and Izumo, S. (1998). Cardiac and extracardiac expression of csx/nkx2.5 homeodomain protein. *Circulation Research*, 82(9):936–946.

Kasahara, H. and Izumo, S. (1999). Identification of the in vivo casein kinase ii phosphorylation site within the homeodomain of the cardiac tissue-specifying homeobox gene product csx/nkx2.5. *Molecular and Cellular Biology*, 19(1):526–536.

Keith, B. and Simon, M. C. (2007). Hypoxia-inducible factors, stem cells, and cancer. *Cell*, 129(3):465–72.

Kent, W., Sugnet, C., Furey, T., Roskin, K., Pringle, T., Zahler, A., and Haussler, D. (2002). The human genome browser at ucsc. *Genome Research*, 12(6):996–1006.

Khetan, S., Guvendiren, M., Legant, W. R., Cohen, D. M., Chen, C. S., and Burdick, J. A. (2013). Degradation-mediated cellular traction directs stem cell fate in covalently crosslinked three-dimensional hydrogels. *Nat Mater*, 12(5):458–65.

Kilian, K. A. and Mrksich, M. (2012). Directing stem cell fate by controlling the affinity and density of ligand-receptor interactions at the biomaterials interface. *Angewandte Chemie-International Edition*, 51(20):4891–4895.

Kim, D. H., Lipke, E. A., Kim, P., Cheong, R., Thompson, S., Delannoy, M., Suh, K. Y., Tung, L., and Levchenko, A. (2010). Nanoscale cues regulate the structure and function of macroscopic cardiac tissue constructs. *Proceedings of the National Academy of Sciences of the United States of America*, 107(2):565–570.

Kim, E. Y., Chen, L., Ma, Y. L., Yu, W., Chang, J., Moskowitz, I. P., and Wang, J. (2011). Expression of sumoylation deficient nkx2.5 mutant in nkx2.5 haploinsufficient mice leads to congenital heart defects. *Plos One*, 6(6).

Kim, H. S., Woo, J. S., Joo, H. J., and Moon, W. K. (2012). Cardiac transcription factor nkx2.5 is downregulated under excessive o-glcnacylation condition. *Plos One*, 7(6).

Kloxin, A. M., Kasko, A. M., Salinas, C. N., and Anseth, K. S. (2009). Photodegradable hydrogels for dynamic tuning of physical and chemical properties. *Science*, 324(5923):59–63.

Kocic, M., Lazovic, M., Mitkovic, M., and Djokic, B. (2010). Clinical significance of the heterotopic ossification after total hip arthroplasty. *Orthopedics*, 33(1):16.

Kokovay, E., Goderie, S., Wang, Y., Lotz, S., Lin, G., Sun, Y., Roysam, B., Shen, Q., and Temple, S. (2010). Adult svz lineage cells home to and leave the vascular niche via differential responses to sdf1/cxcr4 signaling. *Cell Stem Cell*, 7(2):163–73.

Kong, H. J., Polte, T. R., Alsberg, E., and Mooney, D. J. (2005). Fret measurements of cell-traction forces and nano-scale clustering of adhesion ligands varied by substrate stiffness. *Proceedings of the National Academy of Sciences of the United States of America*, 102(12):4300–4305.

Kshitiz, Kim, D. H., Beebe, D. J., and Levchenko, A. (2011). Micro- and nanoengineering for stem cell biology: the promise with a caution. *Trends in Biotechnology*, 29(8):399–408.

Kuang, S., Kuroda, K., Le Grand, F., and Rudnicki, M. A. (2007). Asymmetric self-renewal and commitment of satellite stem cells in muscle. *Cell*, 129(5):999–1010.

Kuang, S. and Rudnicki, M. A. (2008). The emerging biology of satellite cells and their therapeutic potential. *Trends Mol Med*, 14(2):82–91.

Labbaye, C., Valtieri, M., Testa, U., Giampaolo, A., Meccia, E., Sterpetti, P., Parolini, I., Pelosi, E., Bulgarini, D., Cayre, Y. E., and et al. (1994). Retinoic acid downmodulates erythroid differentiation and gata1 expression in purified adult-progenitor culture. *Blood*, 83(3):651–6.

Laflamme, M. A., Chen, K. Y., Naumova, A. V., Muskheli, V., Fugate, J. A., Dupras, S. K., Reinecke, H., Xu, C., Hassanipour, M., Police, S., O'Sullivan, C., Collins, L., Chen, Y., Minami, E., Gill, E. A., Ueno, S., Yuan, C., Gold, J., and Murry, C. E. (2007). Cardiomyocytes derived from human embryonic stem cells in pro-survival factors enhance function of infarcted rat hearts. *Nat Biotechnol*, 25(9):1015–24.

Landau, L. D. and Lifshitz, E. M. (1986). *Theory of elasticity*. Course of theoretical physics. Pergamon Press, Oxford Oxfordshire ; New York, 3rd english edition.

Leask, A. and Abraham, D. J. (2004). Tgf-beta signaling and the fibrotic response. *Faseb Journal*, 18(7):816–827.

Lee, H. J., Yun, C. H., Lim, S. H., Kim, B. C., Baik, K. G., Kim, J. M., Kim, W. H., and Kim, S. J. (2007). Srf is a nuclear repressor of smad3-mediated tgf-beta signaling. *Oncogene*, 26(2):173–185.

Leor, J., Rozen, L., Zuloff-Shani, A., Feinberg, M. S., Amsalem, Y., Barbash, I. M., Kachel, E., Holbova, R., Mardor, Y., Daniels, D., Ocherashvilli, A., Orenstein, A., and Danon, D. (2006). Ex vivo activated human macrophages improve healing, remodeling, and function of the infarcted heart. *Circulation*, 114(1 Suppl):I94–100.

Levental, K. R., Yu, H., Kass, L., Lakins, J. N., Egeblad, M., Erler, J. T., Fong, S. F., Csiszar, K., Giaccia, A., Weninger, W., Yamauchi, M., Gasser, D. L., and Weaver, V. M. (2009). Matrix crosslinking forces tumor progression by enhancing integrin signaling. *Cell*, 139(5):891–906.

Li, T. S., Komota, T., Ohshima, M., Qin, S. L., Kubo, M., Ueda, K., and Hamano, K. (2008). Tgf-beta induces the differentiation of bone marrow stem cells into immature cardiomyocytes. *Biochem Biophys Res Commun*, 366(4):1074–80.

Lichtman, M. A. and Kearney, E. (1970). Cellular deformability during maturation of the myeloblast. possible role in marrow egress. *N Engl J Med*, 283(18):943–8.

Lien, C. L., McAnally, J., Richardson, J. A., and Olson, E. N. (2002). Cardiac-specific activity of an nkx2-5 enhancer requires an evolutionarily conserved smad binding site. *Developmental Biology*, 244(2):257–266.

Liu, F., Mih, J. D., Shea, B. S., Kho, A. T., Sharif, A. S., Tager, A. M., and Tschumperlin, D. J. (2010). Feedback amplification of fibrosis through matrix stiffening and cox-2 suppression. *Journal of Cell Biology*, 190(4):693–706.

Liu, G. H., Barkho, B. Z., Ruiz, S., Diep, D., Qu, J., Yang, S. L., Panopoulos, A. D., Suzuki, K., Kurian, L., Walsh, C., Thompson, J., Boue, S., Fung, H. L., Sancho-Martinez, I., Zhang, K., Yates, J., and Belmonte, J. C. I. (2011a). Recapitulation of premature ageing with ipscs from hutchinson-gilford progeria syndrome. *Nature*, 472(7342):221–225.

Liu, H., Kim, Y., Sharkis, S., Marchionni, L., and Jang, Y. Y. (2011b). In vivo liver regeneration potential of human induced pluripotent stem cells from diverse origins. *Science Translational Medicine*, 3(82).

Liu, H., Wen, J., Xiao, Y., Liu, J., Hopyan, S., Radisic, M., Simmons, C. A., and Sun, Y. (2014). In situ mechanical characterization of the cell nucleus by atomic force microscopy. *ACS Nano*.

Liu, J., Tan, Y., Zhang, H., Zhang, Y., Xu, P., Chen, J., Poh, Y. C., Tang, K., Wang, N., and Huang, B. (2012). Soft fibrin gels promote selection and growth of tumorigenic cells. *Nat Mater*, 11(8):734–41.

Lo, C. M., Buxton, D. B., Chua, G. C., Dembo, M., Adelstein, R. S., and Wang, Y. L. (2004). Nonmuscle myosin iib is involved in the guidance of fibroblast migration. *Mol Biol Cell*, 15(3):982–9.

Lolmede, K., Campana, L., Vezzoli, M., Bosurgi, L., Tonlorenzi, R., Clementi, E., Bianchi, M. E., Cossu, G., Manfredi, A. A., Brunelli, S., and Rovere-Querini, P. (2009). Inflammatory and alternatively activated human macrophages attract vessel-associated stem cells, relying on separate hmgb1- and mmp-9-dependent pathways. *J Leukoc Biol*, 85(5):779–87.

Loulier, K., Lathia, J. D., Marthiens, V., Relucio, J., Mughal, M. R., Tang, S. C., Coksaygan, T., Hall, P. E., Chigurupati, S., Patton, B., Colognato, H., Rao, M. S., Mattson, M. P., Haydar, T. F., and Ffrench-Constant, C. (2009). beta1 integrin maintains integrity of the embryonic neocortical stem cell niche. *PLoS Biol*, 7(8):e1000176.

MacKenna, D., Summerour, S. R., and Villarreal, F. J. (2000). Role of mechanical factors in modulating cardiac fibroblast function and extracellular matrix synthesis. *Cardiovascular Research*, 46(2):257–263.

MacQueen, L., Sun, Y., and Simmons, C. A. (2013). Mesenchymal stem cell mechanobiology and emerging experimental platforms. *J R Soc Interface*, 10(84):20130179.

Maheshwari, G., Brown, G., Lauffenburger, D. A., Wells, A., and Griffith, L. G. (2000). Cell adhesion and motility depend on nanoscale rgd clustering. *Journal of Cell Science*, 113(10):1677–1686.

Majkut, S., Idema, T., Swift, J., Krieger, C., Liu, A., and Discher, D. E. (2013). Heart-specific stiffening in early embryos parallels matrix and myosin expression to optimize beating. *Curr Biol*, 23(23):2434–9.

Mann, C. J., Perdiguero, E., Kharraz, Y., Aguilar, S., Pessina, P., Serrano, A. L., and Munoz-Canoves, P. (2011). Aberrant repair and fibrosis development in skeletal muscle. *Skelet Muscle*, 1(1):21.

Marklein, R. A. and Burdick, J. A. (2010). Spatially controlled hydrogel mechanics to modulate stem cell interactions. *Soft Matter*, 6(1):136–143.

Martin, P. (1997). Wound healing–aiming for perfect skin regeneration. *Science*, 276(5309):75–81.

McMurray, R. J., Gadegaard, N., Tsimbouri, P. M., Burgess, K. V., McNamara, L. E., Tare, R., Murawski, K., Kingham, E., Oreffo, R. O. C., and Dalby, M. J. (2011). Nanoscale surfaces for the long-term maintenance of mesenchymal stem cell phenotype and multipotency. *Nature Materials*, 10(8):637–644.

McNamara, L. E., McMurray, R. J., Biggs, M. J., Kantawong, F., Oreffo, R. O., and Dalby, M. J. (2010). Nanotopographical control of stem cell differentiation. *J Tissue Eng*, 2010:120623.

McWhorter, F. Y., Wang, T., Nguyen, P., Chung, T., and Liu, W. F. (2013). Modulation of macrophage phenotype by cell shape. *Proc Natl Acad Sci U S A*, 110(43):17253–8.

Mei, Y., Saha, K., Bogatyrev, S. R., Yang, J., Hook, A. L., Kalcioglu, Z. I., Cho, S. W., Mitalipova, M., Pyzocha, N., Rojas, F., Van Vliet, K. J., Davies, M. C., Alexander, M. R., Langer, R., Jaenisch, R., and Anderson, D. G. (2010). Combinatorial development of biomaterials for clonal growth of human pluripotent stem cells. *Nat Mater*, 9(9):768–78.

Melkoumian, Z., Weber, J. L., Weber, D. M., Fadeev, A. G., Zhou, Y., Dolley-Sonneville, P., Yang, J., Qiu, L., Priest, C. A., Shogbon, C., Martin, A. W., Nelson, J., West, P., Beltzer, J. P., Pal, S., and Brandenberger, R. (2010). Synthetic peptide-acrylate surfaces for long-term self-renewal and cardiomyocyte differentiation of human embryonic stem cells. *Nat Biotechnol*, 28(6):606–10.

Mendez-Ferrer, S., Lucas, D., Battista, M., and Frenette, P. S. (2008). Haematopoietic stem cell release is regulated by circadian oscillations. *Nature*, 452(7186):442–7.

Mendez-Ferrer, S., Michurina, T. V., Ferraro, F., Mazloom, A. R., Macarthur, B. D., Lira, S. A., Scadden, D. T., Ma'ayan, A., Enikolopov, G. N., and Frenette, P. S. (2010). Mesenchymal and haematopoietic stem cells form a unique bone marrow niche. *Nature*, 466(7308):829–34.

Michaelis, L. and Menten, M. L. (1913). Die kinetik der invertinwirkung. *Biochem. z*, 49(333-369):352.

Miralles, F., Posern, G., Zaromytidou, A. I., and Treisman, R. (2003). Actin dynamics control srf activity by regulation of its coactivator mal. *Cell*, 113(3):329–42.

Morrison, S. J. and Scadden, D. T. (2014). The bone marrow niche for haematopoietic stem cells. *Nature*, 505(7483):327–34.

Mosser, D. M. and Edwards, J. P. (2008). Exploring the full spectrum of macrophage activation. *Nat Rev Immunol*, 8(12):958–69.

Mu, X., Usas, A., Tang, Y., Lu, A., Wang, B., Weiss, K., and Huard, J. (2013). Rhoa mediates defective stem cell function and heterotopic ossification in dystrophic muscle of mice. *FASEB J*, 27(9):3619–31.

Munster, S., Jawerth, L. M., Leslie, B. A., Weitz, J. I., Fabry, B., and Weitz, D. A. (2013). Strain history dependence of the nonlinear stress response of fibrin and collagen networks. *Proc Natl Acad Sci U S A*, 110(30):12197–202.

Murrell, M., Kamm, R., and Matsudaira, P. (2011). Substrate viscosity enhances correlation in epithelial sheet movement. *Biophys J*, 101(2):297–306.

Nahrendorf, M., Swirski, F. K., Aikawa, E., Stangenberg, L., Wurdinger, T., Figueiredo, J. L., Libby, P., Weissleder, R., and Pittet, M. J. (2007). The healing myocardium sequentially mobilizes two monocyte subsets with divergent and complementary functions. *J Exp Med*, 204(12):3037–47.

Nicodemus, G. D. and Bryant, S. J. (2008). Cell encapsulation in biodegradable hydrogels for tissue engineering applications. *Tissue Engineering Part B-Reviews*, 14(2):149–165.

O'Brien, L. E., B. D. (2013). Beyond the niche: Tissue-level coordination of stem cell dynamics. *Annual Review of Cell and Developmental Biology*, 29:107–136.

Olins, A. L., Herrmann, H., Lichter, P., Kratzmeier, M., Doenecke, D., and Olins, D. E. (2001). Nuclear envelope and chromatin compositional differences comparing undifferentiated and retinoic acid- and phorbol ester-treated hl-60 cells. *Exp Cell Res*, 268(2):115–27.

Olsen, A. L., Bloomer, S. A., Chan, E. P., Gaca, M. D. A., Georges, P. C., Sackey, B., Uemura, M., Janmey, P. A., and Wells, R. G. (2011). Hepatic stellate cells require a stiff environment for myofibroblastic differentiation. *American Journal of Physiology-Gastrointestinal and Liver Physiology*, 301(1):G110–G118.

Olson, E. N. and Nordheim, A. (2010). Linking actin dynamics and gene transcription to drive cellular motile functions. *Nat Rev Mol Cell Biol*, 11(5):353–65.

Orlic, D., Kajstura, J., Chimenti, S., Jakoniuk, I., Anderson, S. M., Li, B., Pickel, J., McKay, R., Nadal-Ginard, B., Bodine, D. M., Leri, A., and Anversa, P. (2001). Bone marrow cells regenerate infarcted myocardium. *Nature*, 410(6829):701–5.

Pajerowski, D. (2007). Nuclear plasticity physically defined. *Biophysical Journal*, pages 51a–51a.

Patel, P. N., Gobin, A. S., West, J. L., and Patrick, C. W. (2005). Poly(ethylene glycol) hydrogel system supports preadipocyte viability, adhesion, and proliferation. *Tissue Engineering*, 11(9-10):1498–1505.

Peled, A., Kollet, O., Ponomaryov, T., Petit, I., Franitza, S., Grabovsky, V., Slav, M. M., Nagler, A., Lider, O., Alon, R., Zipori, D., and Lapidot, T. (2000). The chemokine sdf-1 activates the integrins lfa-1, vla-4, and vla-5 on immature human cd34(+) cells: role in transendothelial/stromal migration and engraftment of nod/scid mice. *Blood*, 95(11):3289–96.

Pelham, R. J. and Wang, Y. L. (1997). Cell locomotion and focal adhesions are regulated by substrate flexibility. *Proceedings of the National Academy of Sciences of the United States of America*, 94(25):13661–13665.

Pfeffer, M. A. and Braunwald, E. (1990). Ventricular remodeling after myocardial infarction. experimental observations and clinical implications. *Circulation*, 81(4):1161–72.

Pittenger, M. F., Mackay, A. M., Beck, S. C., Jaiswal, R. K., Douglas, R., Mosca, J. D., Moorman, M. A., Simonetti, D. W., Craig, S., and Marshak, D. R. (1999). Multilineage potential of adult human mesenchymal stem cells. *Science*, 284(5411):143–7.

Plotnikov, S. V., Pasapera, A. M., Sabass, B., and Waterman, C. M. (2012). Force fluctuations within focal adhesions mediate ecm-rigidity sensing to guide directed cell migration. *Cell*, 151(7):1513–1527.

Prokhorova, T. A., Harkness, L. M., Frandsen, U., Ditzel, N., Schroder, H. D., Burns, J. S., and Kassem, M. (2009). Teratoma formation by human embryonic stem cells is site dependent and enhanced by the presence of matrigel. *Stem Cells Dev*, 18(1):47–54.

Purton, L. E., Dworkin, S., Olsen, G. H., Walkley, C. R., Fabb, S. A., Collins, S. J., and Chambon, P. (2006). Rargamma is critical for maintaining a balance between hematopoietic stem cell self-renewal and differentiation. *J Exp Med*, 203(5):1283–93.

Raab, M., Swift, J., Dingal, P. C., Shah, P., Shin, J. W., and Discher, D. E. (2012). Crawling from soft to stiff matrix polarizes the cytoskeleton and phosphoregulates myosin-ii heavy chain. *J Cell Biol*, 199(4):669–83.

Raj, A., van den Bogaard, P., Rifkin, S. A., van Oudenaarden, A., and Tyagi, S. (2008). Imaging individual mrna molecules using multiple singly labeled probes. *Nat Methods*, 5(10):877–9.

Ramachandran, P., Pellicoro, A., Vernon, M. A., Boulter, L., Aucott, R. L., Ali, A., Hartland, S. N., Snowdon, V. K., Cappon, A., Gordon-Walker, T. T., Williams, M. J., Dunbar, D. R., Manning, J. R., van Rooijen, N., Fallowfield, J. A., Forbes, S. J., and Iredale, J. P. (2012). Differential ly-6c expression identifies the recruited macrophage phenotype, which orchestrates the regression of murine liver fibrosis. *Proc Natl Acad Sci U S A*, 109(46):E3186–95.

Ramalho-Santos, M., Yoon, S., Matsuzaki, Y., Mulligan, R. C., and Melton, D. A. (2002). "stemness": transcriptional profiling of embryonic and adult stem cells. *Science*, 298(5593):597–600.

Rao, B. M. and Zandstra, P. W. (2005). Culture development for human embryonic stem cell propagation: molecular aspects and challenges. *Curr Opin Biotechnol*, 16(5):568–76.

Rehfeldt, F., Brown, A. E., Raab, M., Cai, S., Zajac, A. L., Zemel, A., and Discher, D. E. (2012). Hyaluronic acid matrices show matrix stiffness in 2d and 3d dictates cytoskeletal order and myosin-ii phosphorylation within stem cells. *Integr Biol (Camb)*, 4(4):422–30.

Rouse, P. E. (1953). A theory of the linear viscoelastic properties of dilute solutions of coiling polymers. *Journal of Chemical Physics*, 21(7):1272–1280.

Ryan, T., Shelton, M., Lambert, J. P., Malecova, B., Boisvenue, S., Ruel, M., Figeys, D., Puri, P. L., and Skerjanc, I. S. (2013). Myosin phosphatase modulates the cardiac cell fate by regulating the subcellular localization of nkx2.5 in a wnt/rho-associated protein kinase-dependent pathway. *Circulation Research*, 112(2):257–+.

Saha, K., Keung, A. J., Irwin, E. F., Li, Y., Little, L., Schaffer, D. V., and Healy, K. E. (2008). Substrate modulus directs neural stem cell behavior. *Biophys J*, 95(9):4426–38.

Saha, K., Mei, Y., Reisterer, C. M., Pyzocha, N. K., Yang, J., Muffat, J., Davies, M. C., Alexander, M. R., Langer, R., Anderson, D. G., and Jaenisch, R. (2011). Surface-engineered substrates for improved human pluripotent stem cell culture under fully defined conditions. *Proc Natl Acad Sci U S A*, 108(46):18714–9.

Saha, S., Ji, L., de Pablo, J. J., and Palecek, S. P. (2006). Inhibition of human embryonic stem cell differentiation by mechanical strain. *J Cell Physiol*, 206(1):126–37.

Sakurai, K., Talukdar, I., Patil, V. S., Dang, J., Li, Z., Chang, K. Y., Lu, C. C., Delorme-Walker, V., Dermardirossian, C., Anderson, K., Hanein, D., Yang, C. S., Wu, D., Liu, Y., and Rana, T. M. (2014). Kinome-wide functional analysis highlights the role of cytoskeletal remodeling in somatic cell reprogramming. *Cell Stem Cell*, 14(4):523–34.

Schofield, R. (1983). The stem-cell system. *Biomedicine & Pharmacotherapy*, 37(8):375–380.

Schvartzman, M., Palma, M., Sable, J., Abramson, J., Hu, X., Sheetz, M. P., and Wind, S. J. (2011). Nanolithographic control of the spatial organization of cellular adhesion receptors at the single-molecule level. *Nano Lett*, 11(3):1306–12.

Schwanhausser, B., Busse, D., Li, N., Dittmar, G., Schuchhardt, J., Wolf, J., Chen, W., and Selbach, M. (2011). Global quantification of mammalian gene expression control. *Nature*, 473(7347):337–342.

Selhuber-Unkel, C., Erdmann, T., Lopez-Garcia, M., Kessler, H., Schwarz, U. S., and Spatz, J. P. (2010). Cell adhesion strength is controlled by intermolecular spacing of adhesion receptors. *Biophysical Journal*, 98(4):543–551.

Sharp, W. W., Terracio, L., Borg, T. K., and Samarel, A. M. (1993). Contractile activity modulates actin synthesis and turnover in cultured neonatal rat-heart cells. *Circulation Research*, 73(1):172–183.

Shimono, K., Tung, W. E., Macolino, C., Chi, A. H., Didizian, J. H., Mundy, C., Chandraratna, R. A., Mishina, Y., Enomoto-Iwamoto, M., Pacifici, M., and Iwamoto, M. (2011). Potent inhibition of heterotopic ossification by nuclear retinoic acid receptor-gamma agonists. *Nat Med*, 17(4):454–60.

Shin, J. W., Buxboim, A., Spinler, K. R., Swift, J., Christian, D. A., Hunter, C. A., Leon, C., Gachet, C., Dingal, P. C., Ivanovska, I. L., Rehfeldt, F., Chasis, J. A., and Discher, D. E. (2014). Contractile forces sustain and polarize hematopoiesis from stem and progenitor cells. *Cell Stem Cell*, 14(1):81–93.

Shin, J. W., Spinler, K. R., Swift, J., Chasis, J. A., Mohandas, N., and Discher, D. E. (2013). Lamins regulate cell trafficking and lineage maturation of adult human hematopoietic cells. *Proc Natl Acad Sci U S A*, 110(47):18892–7.

Shin, J. W., Swift, J., Spinler, K. R., and Discher, D. E. (2011). Myosin-ii inhibition and soft 2d matrix maximize multinucleation and cellular projections typical of platelet-producing megakaryocytes. *Proc Natl Acad Sci U S A*, 108(28):11458–63.

Stevens, M. M. and George, J. H. (2005). Exploring and engineering the cell surface interface. *Science*, 310(5751):1135–1138.

Storm, C., Pastore, J. J., MacKintosh, F. C., Lubensky, T. C., and Janmey, P. A. (2005). Nonlinear elasticity in biological gels. *Nature*, 435(7039):191–194.

Sullivan, G. J., Hay, D. C., Park, I. H., Fletcher, J., Hannoun, Z., Payne, C. M., Dalgetty, D., Black, J. R., Ross, J. A., Samuel, K., Wang, G., Daley, G. Q., Lee, J. H., Church, G. M., Forbes, S. J., Iredale, J. P., and Wilmut, I. (2010). Generation of functional human hepatic endoderm from human induced pluripotent stem cells. *Hepatology*, 51(1):329–335.

Sullivan, K. E., Quinn, K. P., Tang, K. M., Georgakoudi, I., and Black, L. D., r. (2014). Extracellular matrix remodeling following myocardial infarction influences the therapeutic potential of mesenchymal stem cells. *Stem Cell Res Ther*, 5(1):14.

Swift, J., Harada, T., Buxboim, A., Shin, J. W., Tang, H. Y., Speicher, D. W., and Discher, D. E. (2013a). Label-free mass spectrometry exploits dozens of detected peptides to quantify lamins in wildtype and knockdown cells. *Nucleus*, 4(6):450–459.

Swift, J., Ivanovska, I. L., Buxboim, A., Harada, T., Dingal, P. C., Pinter, J., Pajerowski, J. D., Spinler, K. R., Shin, J. W., Tewari, M., Rehfeldt, F., Speicher, D. W., and Discher, D. E. (2013b). Nuclear lamin-a scales with tissue stiffness and enhances matrix-directed differentiation. *Science*, 341(6149):1240104.

Takahashi, K., Tanabe, K., Ohnuki, M., Narita, M., Ichisaka, T., Tomoda, K., and Yamanaka, S. (2007). Induction of pluripotent stem cells from adult human fibroblasts by defined factors. *Cell*, 131(5):861–72.

Tenney, R. M. and Discher, D. E. (2009). Stem cells, microenvironment mechanics, and growth factor activation. *Curr Opin Cell Biol*, 21(5):630–5.

Tidball, J. G. and Wehling-Henricks, M. (2007). Macrophages promote muscle membrane repair and muscle fibre growth and regeneration during modified muscle loading in mice in vivo. *J Physiol*, 578(Pt 1):327–36.

Tomita, S., Li, R. K., Weisel, R. D., Mickle, D. A., Kim, E. J., Sakai, T., and Jia, Z. Q. (1999). Autologous transplantation of bone marrow cells improves damaged heart function. *Circulation*, 100(19 Suppl):II247–56.

Trappmann, B., Gautrot, J. E., Connelly, J. T., Strange, D. G., Li, Y., Oyen, M. L., Cohen Stuart, M. A., Boehm, H., Li, B., Vogel, V., Spatz, J. P., Watt, F. M., and Huck, W. T. (2012). Extracellular-matrix tethering regulates stem-cell fate. *Nat Mater*, 11(7):642–9.

Tropepe, V., Hitoshi, S., Sirard, C., Mak, T. W., Rossant, J., and van der Kooy, D. (2001). Direct neural fate specification from embryonic stem cells: a primitive mammalian neural stem cell stage acquired through a default mechanism. *Neuron*, 30(1):65–78.

Tsai, R. K. and Discher, D. E. (2008). Inhibition of "self" engulfment through deactivation of myosin-ii at the phagocytic synapse between human cells. *J Cell Biol*, 180(5):989–1003.

Tse, J. R. and Engler, A. J. (2011). Stiffness gradients mimicking in vivo tissue variation regulate mesenchymal stem cell fate. *PLoS One*, 6(1):e15978.

Turgeman, T., Hagai, Y., Huebner, K., Jassal, D. S., Anderson, J. E., Genin, O., Nagler, A., Halevy, O., and Pines, M. (2008). Prevention of muscle fibrosis and improvement in muscle performance in the mdx mouse by halofuginone. *Neuromuscul Disord*, 18(11):857–68.

Ulrich, T. A., de Juan Pardo, E. M., and Kumar, S. (2009). The mechanical rigidity of the extracellular matrix regulates the structure, motility, and proliferation of glioma cells. *Cancer Res*, 69(10):4167–74.

Urciuolo, A., Quarta, M., Morbidoni, V., Gattazzo, F., Molon, S., Grumati, P., Montemurro, F., Tedesco, F. S., Blaauw, B., Cossu, G., Vozzi, G., Rando, T. A., and Bonaldo, P. (2013). Collagen vi regulates satellite cell self-renewal and muscle regeneration. *Nat Commun*, 4:1964.

Vader, D., Kabla, A., Weitz, D., and Mahadevan, L. (2009). Strain-induced alignment in collagen gels. *Plos One*, 4(6).

Wang, A. J., Tang, Z. Y., Park, I. H., Zhu, Y. Q., Patel, S., Daley, G. Q., and Li, S. (2011). Induced pluripotent stem cells for neural tissue engineering. *Biomaterials*, 32(22):5023–5032.

Wang, D. J., Park, J. S., Chu, J. S. F., Krakowski, A., Luo, K. X., Chen, D. J., and Li, S. (2004). Proteomic profiling of bone marrow mesenchymal stem cells upon transforming growth factor beta 1 stimulation. *Journal of Biological Chemistry*, 279(42):43725–43734.

Wang, J., Zhang, H., Iyer, D., Feng, X. H., and Schwartz, R. J. (2008). Regulation of cardiac specific nkx2.5 gene activity by small ubiquitin-like modifier. *Journal of Biological Chemistry*, 283(34):23235–23243.

Wang, N., Tytell, J. D., and Ingber, D. E. (2009). Mechanotransduction at a distance: mechanically coupling the extracellular matrix with the nucleus. *Nature Reviews Molecular Cell Biology*, 10(1):75–82.

Wang, X. L., Liu, S. X., and Wilcken, D. E. L. (1997). Circulating transforming growth factor beta 1 and coronary artery disease. *Cardiovascular Research*, 34(2):404–410.

Wang, Y. Z., Kim, H. J., Vunjak-Novakovic, G., and Kaplan, D. L. (2006). Stem cell-based tissue engineering with silk biomaterials. *Biomaterials*, 27(36):6064–6082.

Watanabe, K., Ueno, M., Kamiya, D., Nishiyama, A., Matsumura, M., Wataya, T., Takahashi, J. B., Nishikawa, S., Nishikawa, S., Muguruma, K., and Sasai, Y. (2007). A rock inhibitor permits survival of dissociated human embryonic stem cells. *Nat Biotechnol*, 25(6):681–6.

Wipff, P. J., Rifkin, D. B., Meister, J. J., and Hinz, B. (2007). Myofibroblast contraction activates latent tgf-beta1 from the extracellular matrix. *J Cell Biol*, 179(6):1311–23.

Worley, J. R., Baugh, M. D., Hughes, D. A., Edwards, D. R., Hogan, A., Sampson, M. J., and Gavrilovic, J. (2003). Metalloproteinase expression in pma-stimulated thp-1 cells. effects of peroxisome proliferator-activated receptor-gamma (ppar gamma) agonists and 9-cis-retinoic acid. *J Biol Chem*, 278(51):51340–6.

Xu, Y., Zhu, X., Hahm, H. S., Wei, W., Hao, E., Hayek, A., and Ding, S. (2010). Revealing a core signaling regulatory mechanism for pluripotent stem cell survival and self-renewal by small molecules. *Proc Natl Acad Sci U S A*, 107(18):8129–34.

Yamazaki, S., Ema, H., Karlsson, G., Yamaguchi, T., Miyoshi, H., Shioda, S., Taketo, M. M., Karlsson, S., Iwama, A., and Nakauchi, H. (2011). Nonmyelinating schwann cells maintain hematopoietic stem cell hibernation in the bone marrow niche. *Cell*, 147(5):1146–58.

Yang, C., Tibbitt, M. W., Basta, L., and Anseth, K. S. (2014). Mechanical memory and dosing influence stem cell fate. *Nat Mater*.

Yang, J. H., Sakamoto, H., Xu, E. C., and Lee, R. T. (2000). Biomechanical regulation of human monocyte/macrophage molecular function. *Am J Pathol*, 156(5):1797–804.

Yang, Y. L., Leone, L. M., and Kaufman, L. J. (2009). Elastic moduli of collagen gels can be predicted from two-dimensional confocal microscopy. *Biophys J*, 97(7):2051–60.

Yu, D. X., Marchetto, M. C., and Gage, F. H. (2013). Therapeutic translation of ipscs for treating neurological disease. *Cell Stem Cell*, 12(6):678–88.

Zemel, A., Rehfeldt, F., Brown, A. E., Discher, D. E., and Safran, S. A. (2010). Optimal matrix rigidity for stress fiber polarization in stem cells. *Nat Phys*, 6(6):468–473.

Zhang, L., Cao, Z., Bai, T., Carr, L., Ella-Menye, J. R., Irvin, C., Ratner, B. D., and Jiang, S. (2013). Zwitterionic hydrogels implanted in mice resist the foreign-body reaction. *Nat Biotechnol*, 31(6):553–6.

Zhu, J., Heyworth, C. M., Glasow, A., Huang, Q. H., Petrie, K., Lanotte, M., Benoit, G., Gallagher, R., Waxman, S., Enver, T., and Zelent, A. (2001). Lineage restriction of the raralpha gene expression in myeloid differentiation. *Blood*, 98(8):2563–7.